Modèle multi-échelle de la fatigue des lignes d'ancrage câblées pour l'éolien offshore flottant

Federico Bussolati

université PARIS-SACLAY

école normale supérieure paris-saclay

NNT : NNT2019SACLN041

Thèse de doctorat

Multi-scale modeling of the fatigue of mooring wire ropes for floating offshore wind turbines

Thèse de doctorat de l'Université Paris-Saclay
préparée à Ecole normale supérieure Paris-Saclay

Ecole doctorale n°ED579 Sciences mécanique et énérgetique, matériaux et géosciences (SMEMAG)
Spécialité de doctorat : Solides, structures, matériaux

Thèse présentée et soutenue à Cachan, le 26 Septembre 2019, par

FEDERICO BUSSOLATI

Composition du Jury :

Peter Wriggers Professeur, Leibniz Universität Hannover	Président
Laura De Lorenzis Professeur, Technische Universität Braunschweig	Rapporteur
Patrick Massin Directeur de recherche, ENSTA Paris	Rapporteur
Fikri Hafid Chercheur associé, Centre des Mathématiques et de Leurs Applications	Examinateur
Olivier Allix Professeur, ENS-Paris-Saclay (LMT)	Directeur de thèse
Pierre-Alain Guidault Maître de Conférence, ENS-Paris-Saclay (LMT)	Co-encadrant
Martin Guiton Ingénieur chercheur, IFP Energies Nouvelles	Invité

Acknowledgments

Many people have contributed to this research project and I would like to express my appreciation to all concerned.

Special thanks are for Martin Guiton, my supervisor at IFPen. It has been a pleasure to work with him, especially because of the many interesting exchanges and discussion. I also really appreciated the help he gave me outside the research project, when I first arrived in France and when I came back to Lyon after my stay at the LMT.

Many thanks are for my supervisors at the LMT, Pierre-Alain Guidault and Olivier Allix. It is has been a great pleasure to work with them, because of their great competences, commitment to research and positive attitude. Pierre-Alain, in particular, has to be also acknowledged for its great contribution to the development of the contact element.

I would like to thank to the other members of the jury, particularly the reviewers prof. Massin and prof. De Lorenzis for having accepted the task and for their valuable remarks.

Yann Poirette, Michael Martinez, Sebastien Lalonde and Imanol Martinez Perez are gratefully acknowledged for their help and availability. Baudin-Chateauneuf company is also acknowledged, for having provided the data that inspired the six-layer wire rope model.

I want to express my gratitude to IFPen for the financial support and for having enabled me to carry on this study, together with the possibility of participating to study trips that I very much enjoyed.

I feel very grateful to many people I met at LMT and at IFPen for the good times spent together, that made these three years really pleasant. I wish the best to all of them and I hope I will stay in touch with many.

Last but not least, I greatly thank Rana for her constant support and love.

Contents

General introduction

Industrial context

The depletion of fossil fuels and consequent environmental pollution has been elevating concerns about sustainable green energy sources. This situation has driven the industry to the development of new sustainable technologies for supplying the energy demand, which according to recent forecasts will continue to increase (Fig. 1).

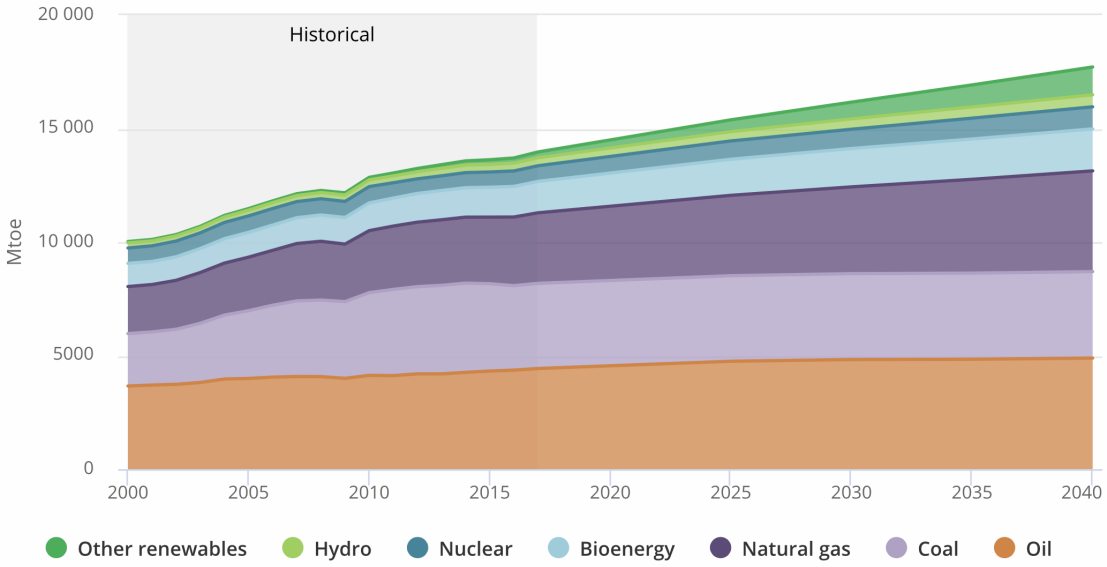

Figure 1: Forecast of worldwide energy consumption, measured by Million Tonnes of Oil Equivalent (from IEA/World Energy Outlook 2018).

In the current context of energy transition, wind energy has been one of the main and fastest-growing sources of renewable energy and has contributed significantly to the decarbonization of the electric sector. A recent development area aims to extend the exploitable wind sites by means of floating offshore wind turbines.

Although there is a sizable wind resource that can be developed with the fixed-bottom foun-

dation technology (fixed-foundation offshore wind turbines can be installed up to a sea depth of about 50 meters), the material and installation requirements of these foundations, along with the amount of additional wind resource at at higher water depths, drive significant interest in floating offshore wind, since it open up new and possibly better wind resource areas. The interest in exploiting sites with deep water depth of several hundreds meters is growing fast, due to better cost-performance trade-off, higher average wind speed and reduction of environmental issues regarding noise, visual and space constraints [109].

Little is known about the long-term cost implications of moving to floating offshore platforms; however, floating offshore foundations offer the potential for less foundation material relative to deep-water fixed-bottom foundations and the installations and decommissioning are greatly simplified [53]. Moreover, the long-term survivability of floating structures has already been technically demonstrated by the marine and offshore oil industries over many decades [11].

Floating offshore wind turbines (FOWT) are basically constituted by a wind turbine installed on a floater, which is linked to the seabed by means of mooring lines. The mooring system has the function of limiting excessive displacements and rotations to preserve the power-cables and other wind turbines installed nearby and to ensure suitable production conditions for the turbine.

Engineers must consider several limit states, in particular ultimate limit state (ULS) and fatigue limit state (FLS), to design the mooring system [31]. For the FLS on which we will focus in this thesis, mooring lines have to resist the cyclic loading induced by the floater movements during the whole structural lifespan, with a sufficient safety margin defined by offshore regulations [32].

Despite the offshore mooring technology is used since many years, still nowadays mooring line failure events are elevating concerns in the Oil&Gas industry (a FOWT industry still has to develop), since a failure at a key structural connection of the mooring leg to the floating unit can require significantly complex repair operations [76].

Statistics of mooring line failures are available regarding oil exploitation. In [45] mooring failure data collected from a survey involving industrial operators and contractors are reported. Based on the survey results, the annual rate of single line failure turns out to be of the order of $2.5 \cdot 10^{-3}$ per mooring line per year and $2.1 \cdot 10^{-2}$ per facility per year. This failure rate for FPS mooring systems (Fig. 2) is exceeding the nominal design failure rate by an order of magnitude [76].

For what concerns wire ropes, the chart in Figure 3 shows that a greater part of failure events is linked to rope damaging during installation. From defects and microcracks which originates in the installation phase, fatigue cracks take place in the early years of life of the structure. These early line failures are grouped in a failure case named *Infant Mortality*. Even without the initial damaging, fatigue represents an important cause of failure. The greater part of the failures occurs near the socket, where the wire rope movements are restrained. Nevertheless, in this work we will focus our analysis on mooring part far from these restraints.

For the FLS, current offshore standards predict fatigue life of mooring lines just considering results from laboratory fatigue tests on a rope sample, mostly limited to tension-tension tests [30]. The goal of this study is to build a tool which takes into account tension and bending

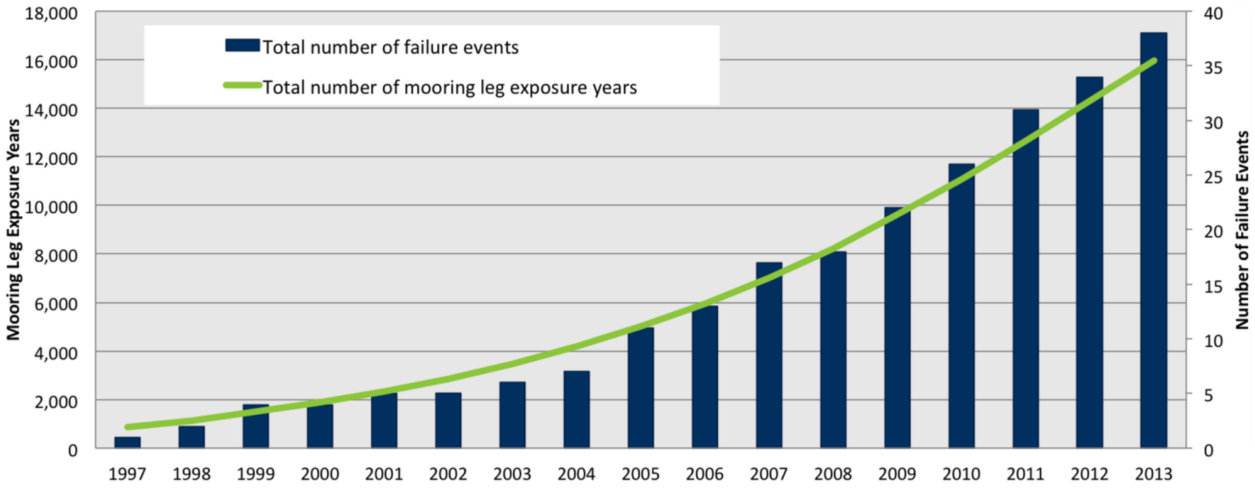

Figure 2: Cumulative failure events versus number of mooring leg exposure years per year from 1997 to 2013 [45].

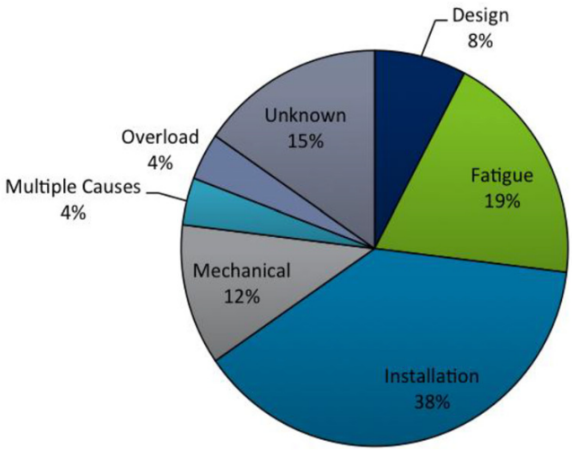

Figure 3: Causes of failure events for wire ropes [45].

and predict the fatigue damage along each mooring line, considering local stress variations linked to the contact interactions between the wires. To our knowledge, the industry still lacks of this kind of tool.

Proposed approach

The approach which has been chosen in order to reach the goal of the thesis is described by the flowchart in Fig. 4.

At the top of the flowchart there is the global model, which in our case is implemented in the dedicated industrial software Deeplines^{TM}. It models the mechanical response of the global wind turbine system, i.e. the floating structure and the mooring lines, under the

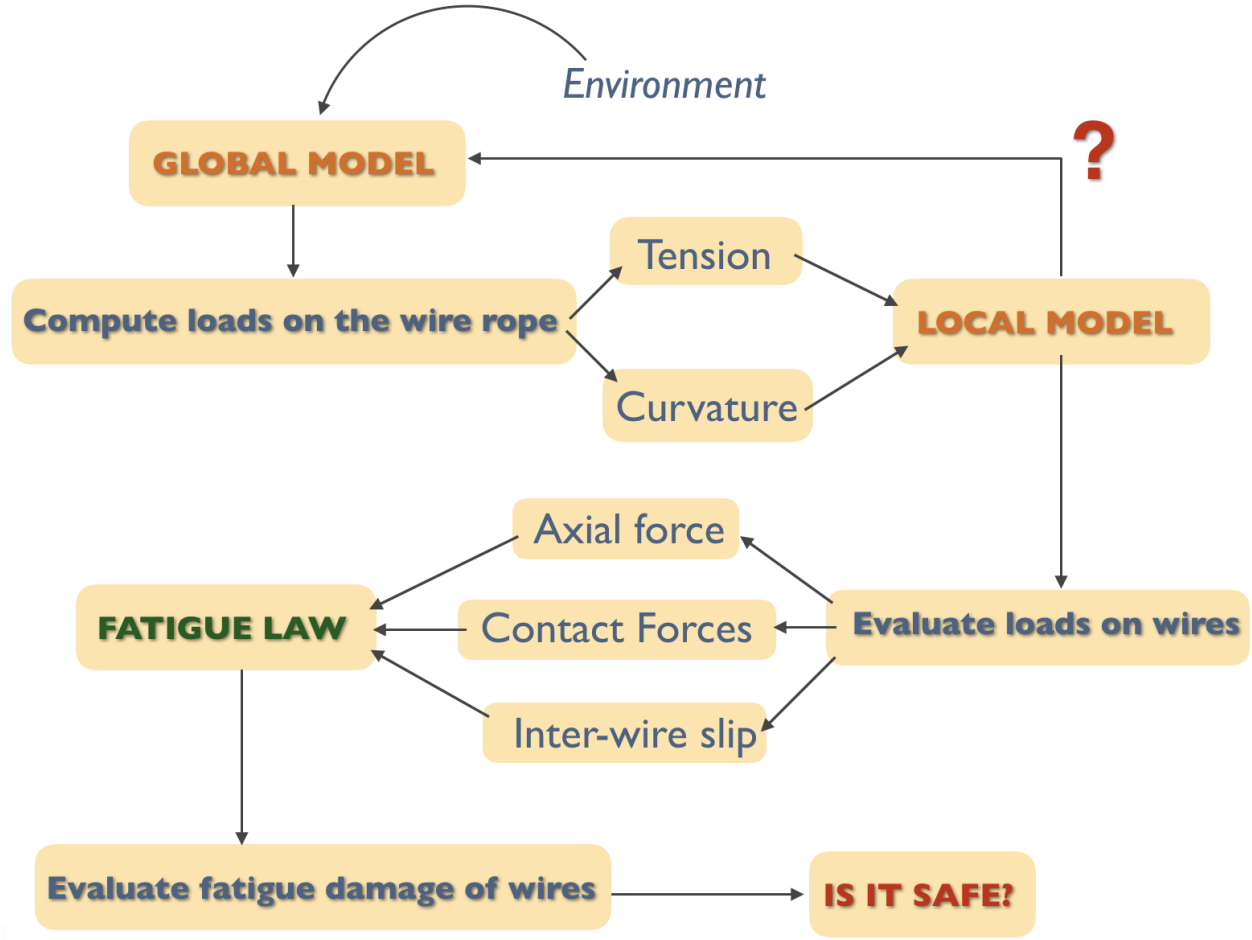

Figure 4: Flowchart of the thesis.

environmental loading. When a solution is computed, the global quantities of interest are obtained, namely the tension and the curvature histories along the mooring lines.

These global quantities are transferred to a local model, whose task is to estimate the local forces at the wires level. The aim is therefore to obtain generalized stresses in each wire, the contact forces and the relative movements among the wires. Moreover, thanks to this local model the mechanical behavior of the wire rope can be deduced, and the mechanical properties of the beam elements in the global model can be updated, mostly for what concerns the bending behavior. The red question mark in Fig. 4 stands for the fact that is not clear if this updating would affect or not the results of the global model.

The local quantities feed a fatigue law, to be identified in the literature. The fatigue damage will then be obtained for each environmental state. According to the probability of occurrence of each environmental state, the fatigue damage expectation in the structural lifespan can be estimated.

Finally, if considering a safety factor for uncertainty or embedding the flowchart in a reliable analysis, the mooring system configuration can be declared safe or unsafe with respect to the

FLS.

Scientific challenges

There are several scientific challenges to face in order to accomplish the purpose of the thesis.

- First of all, there is the need to develop a numerical model able to properly estimate what happens inside a wire rope subjected to tension and bending, balancing accuracy and computational cost. This finite element model has to manage contact among multiple deformable bodies (the steel wires), many of them with very small contact surfaces.
- Since with the wire rope model we simulate the behavior of a wire rope portion, the boundary conditions have to be specified in order to model the continuity of the rope, avoiding as much as possible any artificial edge effect. This ensures the coupling between the macro and the micro scales, for the critical global zones of interest.
- Several fatigue laws will be proposed and the influence of the choice of the fatigue criterion on the final results will be evaluated.

One of the major challenges of the thesis is associated to the complex geometry of the wire rope and to the computational cost of a 3D modeling which allows to compute the sliding among a high number of wires and along a representative length of the rope. Another difficulty is associated to the complexity of modeling a high number of localized contacts, which results in a highly nonlinear model.

The prohibitive computational cost of a Finite Element analysis which employs 3D elements led us to prefer a simplified model of the wires, namely by describing the rope as an assembly of beam elements having rigid sections. Despite this simplification, we noted that the computational cost can still be considerable.

The results of computationally expensive models allowed us to take further hypotheses about the contact kinematics. These have been the starting point for the development of a new simplified model feasible for the fatigue analysis of mooring wire ropes, both for its computational cost and its accuracy.

Even if some specialized softwares have been developed to deal with wire rope modeling [37], a concern in this thesis is to be able to use a legacy code, which is a prerequisite if one wishes the developed approach to be actually used for design.

Thesis outline

The thesis is organized into different parts.

1. The first part presents the state of the art of all the fields that have been covered during this work. It is subdivided into four chapters, going from the global scale to the local one. Namely it starts from the description of FOWT installations, in which particular emphasis is given to characterization of the environment and to the structural modeling. In the second chapter, the literature concerning wire ropes is reported, both concerning their modeling and the experimental results. In the third chapter, some notions about fatigue are given, particularly regarding multiaxial and fretting fatigue. In the last chapter, general aspects of computational contact mechanics are treated.
2. The second part presents the developments and results which have been obtained during this thesis. It begins with a chapter that deals with the global model, in which the characteristics of the case study are presented and the wire rope profile is chosen in order to satisfy the ultimate limit state requirements. The following chapter regards the first attempts in the wire rope modeling, using tools already available in Abaqus®/Standard. In chapter 7, the formulation of a new element for the frictional contact between beam elements assuming small sliding and finite rotations is presented. In chapter 8 numerical simulations are performed in order to compare the results of this new frictional contact element to analytical solutions, and to numerical solutions of standard beam-to-beam and surface-to-surface contact algorithms. In the last chapter, the analysis on a mooring wire rope portion is performed considering a severe sea state among the fatigue environmental cases. It constitutes a preliminary attempt of a detailed fatigue analysis.
3. In the third part, some conclusions are drawn and directions for further research will be proposed.
4. The final part is constituted by appendices, giving to the interested reader some notions on finite rotations theory and on the linearizations involved in the contact element described in chapter 7.

Part I

State of the art

Chapter 1

Floating wind turbines

Floating wind turbines are particular structures, which are composed of a turbine, a tower, a floater linked to the seabed by mooring lines, and a power cable.
The design of a FOWT involves many difficulties. First of all, its physical modeling requires:

- to evaluate the action of the sea waves on the floater and the effect of water on the motion of the mooring lines by means of hydrodynamic calculations;
- to estimate the action of wind on the turbine and on the tower by means of aerodynamic calculations;
- to include control strategies, in particular on the blade orientation, to ensure the structural safety and optimize the production;
- to solve a highly nonlinear structural dynamic problem.

Secondly, the random nature of the environmental loads adds first-order uncertainties on the analyses output, in addition to other sources of uncertainty: material properties, model parameters, real installation configuration, etc...

1.1 Characterization of the environment

Offshore structures of all types are subjected to cycle loading from wind, current and waves acting simultaneously. These environmental phenomena are of random nature and for each of them it is possible to define a statistical distribution by making some preliminary assumptions. The set of possible environmental conditions is defined by including the joint probability of the different load parameters. However, even with a coarse discretization of the parameter space, the number of loading conditions can easily exceed 10^4. Since the calculations are usually time-consuming, engineers developed strategies in order to deal with a further limited set of environmental loading [107], in particular for FLS calculations. On the other hand, this drives interest for the development of faster numerical models.

1.1.1 Modeling of the sea state

For what concerns the sea waves, they may be distinguished in two main categories:

- wind sea, generated by the direct action of the local winds on the sea;
- swell, caused by distant weather systems.

For the sake of simplification, we assume that the main load contribution is due to swell, neglecting the local action of the wind sea on the structure (which is less easy to describe). Swell can be modeled as superposition of many harmonic components, having different frequencies and directions.

In general, the observed sea elevation at a certain location $\underline{x} = \underline{x}_0$ at time t, $\psi(\underline{x}_0, t)$, can be considered as a realization of a non-stationary stochastic process Ψ, whose characteristic parameters vary slowly in time [140, 99].

In order to characterize the sea elevation at a given position from a stochastic point of view, we make reference to two different time scales, a short-term and a long-term one.

Short-term statistical distribution

For short term periods (few hours) the sea surface $\Psi(\underline{x}, t)$ is assumed to be a zero-mean ergodic (and therefore stationary) Gaussian process.

The ergodicity assumption implies that, from a statistical point of view, it's the same to look one realization in time of the stochastic process or fix a time instant and look to all the realizations. Therefore an ergodic stochastic process can be described by looking to a single realization. For the sea state, this assumption is by convention considered for a time interval of three hours [99]. However, in practice engineers often consider a simulation time of one hour only, following the requirement of the standard [67].

The spectral density $S(\omega)$ is the Fourier transform of the autocorrelation function and represents the energy distribution of waves according to the different pulsations ω_i. The link between spectrum and wave amplitudes A_i is defined by the following equation:

$$A_i^2 = 2S(\omega_i)d\omega_i \tag{1.1}$$

in which $d\omega_i$ is the difference between two consecutive frequencies.

Hence from the spectral density it's possible to define infinite realizations, expressed by Fourier series:

$$\psi(t) = \sum_i A_i \cos(\omega_i t + \phi_i) = \sum_i \sqrt{2S(\omega_i)d\omega_i}\cos(\omega_i t + \phi_i) \tag{1.2}$$

by changing the phase angles ϕ_i, which is done by choosing a different *stochastic seed* for each realization.

Many types of spectra could be defined in order to characterize the energy distribution of the wave components. In this thesis, we use the *JONSWAP spectrum*:

$$S_J(\omega) = \alpha \frac{\omega_p^4}{\omega^5} H_s^2 \exp\left(-\frac{5}{4}\left(\frac{\omega_p}{\omega}\right)^4\right) \gamma^{\exp\left(-\frac{1}{2}\left(\frac{\omega-\omega_p}{\sigma_{JON}\omega_p}\right)^2\right)} \tag{1.3}$$

which was originally set for North Sea sites but has been generalized in offshore applications. In (1.3)

- H_s is the significant wave height;
- ω is the wave pulsation and ω_p is the peak pulsation;
- γ is the peak enhancement factor, which basically defines the spreading of the spectrum;
- α is chosen such that

$$\frac{H_s^2}{16} = \int S_J(\omega) d\omega \tag{1.4}$$

while

$$\sigma_{JON} = \begin{cases} 0.07 & for \quad \omega \leq \omega_p \\ 0.09 & for \quad \omega > \omega_p \end{cases} \tag{1.5}$$

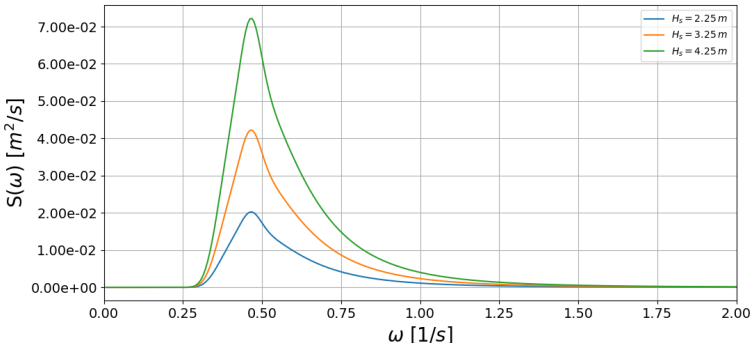

Figure 1.1: JONSWAP spectra obtained with $T_p = 13.5\,s$, $\gamma = 1.3$ for different values of H_s.

.

The shape of the spectrum (Fig. 1.1) depends on three parameters: H_s, ω_p (or equivalently $T_p = \frac{2\pi}{\omega_p}$) and γ.

Long-term statistical distribution

The characterization of the sea state in the long-term is given by the percentage of occurrence of each short-term sea states.
The metocean data (records of the time evolution of the height of the sea level) are hence used to build the so-called *Wave Scatter Diagram* (WSD), as the one reported in Figure 1.2.

1.1.2 Wind action

The action of the wind is also a stochastic phenomenon, which hence adds uncertainty to the physical model. According to [31], time wind climate is represented by the 10-minute mean wind speed U_{10} and the standard deviation σ_U, both referred to a certain height above the mean sea level. This time interval corresponds to a stationary assumption, with constant values of U_{10} and σ_U.

Percentage of occurrence of height of swell (m) in rows versus peak period of swell (s) in columns

	lower	2	3	4	5	6	7	8	9	10	11	12	13	14	15	16	17	18	19	20	21	22	23	24	
lower	upper	3	4	5	6	7	8	9	10	11	12	13	14	15	16	17	18	19	20	21	22	23	24	25	total
0	0,5	0	0,005	0,003	0,037	0,166	0,318	0,555	0,658	0,634	0,51	0,446	0,303	0,22	0	0,182	0,149	0	0,075	0	0,036	0	0,019	0	4,316
0,5	1	0	0	0	0,072	0,308	0,825	1,117	1,302	1,117	0,801	0,618	0,346	0,2	0	0,099	0,033	0	0,007	0	0	0	0	0	6,845
1	1,5	0	0	0,003	0,039	0,282	0,542	1,148	1,62	1,6	1,191	0,869	0,45	0,193	0	0,104	0,043	0	0,009	0	0,002	0	0	0	8,097
1,5	2	0	0	0	0,002	0,08	0,252	0,671	1,03	1,528	1,335	1,052	0,537	0,166	0	0,111	0,026	0	0,01	0	0,002	0	0	0	6,802
2	2,5	0	0	0	0	0,003	0,072	0,277	0,527	0,963	1,354	1,28	0,633	0,216	0	0,094	0,012	0	0,007	0	0	0	0	0	5,438
2,5	3	0	0	0	0	0	0,012	0,062	0,202	0,477	0,883	1,068	0,664	0,187	0	0,074	0,019	0	0	0	0	0	0	0	3,646
3	3,5	0	0	0	0	0	0	0,014	0,072	0,27	0,607	0,963	0,601	0,144	0	0,056	0,01	0	0,002	0	0	0	0	0	2,74
3,5	4	0	0	0	0	0	0	0	0,015	0,121	0,286	0,671	0,618	0,156	0	0,033	0,01	0	0	0	0	0	0	0	1,91
4	4,5	0	0	0	0	0	0	0	0,002	0,026	0,176	0,448	0,423	0,214	0	0,034	0,015	0	0	0	0	0	0	0	1,338
4,5	5	0	0	0	0	0	0	0	0	0,012	0,056	0,33	0,347	0,238	0	0,077	0,017	0	0,003	0	0	0	0	0	1,081
5	5,5	0	0	0	0	0	0	0	0	0	0,019	0,147	0,291	0,149	0	0,06	0,009	0	0	0	0	0	0	0	0,674
5,5	6	0	0	0	0	0	0	0	0	0	0	0,063	0,099	0,115	0	0,058	0,019	0	0,003	0	0	0	0	0	0,358
6	6,5	0	0	0	0	0	0	0	0	0	0,002	0,01	0,063	0,096	0	0,077	0,015	0	0	0	0	0	0	0	0,264
6,5	7	0	0	0	0	0	0	0	0	0	0	0,005	0,015	0,058	0	0,039	0,005	0	0	0	0	0	0	0	0,123
7	7,5	0	0	0	0	0	0	0	0	0	0	0	0,012	0,019	0	0,022	0,009	0	0	0	0	0	0	0	0,062
7,5	8	0	0	0	0	0	0	0	0	0	0	0	0,005	0,005	0	0,019	0,003	0	0,002	0	0	0	0	0	0,034
8	8,5	0	0	0	0	0	0	0	0	0	0	0	0,003	0,003	0	0,009	0,005	0	0	0	0	0	0	0	0,021
8,5	9	0	0	0	0	0	0	0	0	0	0	0	0,003	0	0	0,007	0	0	0	0	0	0	0	0	0,01
9	9,5	0	0	0	0	0	0	0	0	0	0	0	0	0	0	0	0	0	0	0	0	0	0	0	0
total		0	0,005	0,007	0,15	0,84	2,021	3,844	5,429	6,749	7,219	7,972	5,415	2,378	0	1,155	0,399	0	0,117	0	0,039	0	0,019	0	43,758

Copyright ARGOSS, November 2012

Figure 1.2: WSD obtained by metocean data at a given site. Each column corresponds to a certain interval for the peak period T_p, while the rows define the intervals for the significant wave height H_s. Into each block is reported the percentage of occurrence of that specific 3 hours sea state. The sum of all the percentages is not 100% because this WSD refers to a certain azimuthal sector.

Wind speed U_{10} varies according to the height above the sea level. In [32] are reported two possible distributions: a logarithmic and a power-law one. In general, the wind speed gradient decreases rapidly with the height above the sea level (Fig. 1.3).

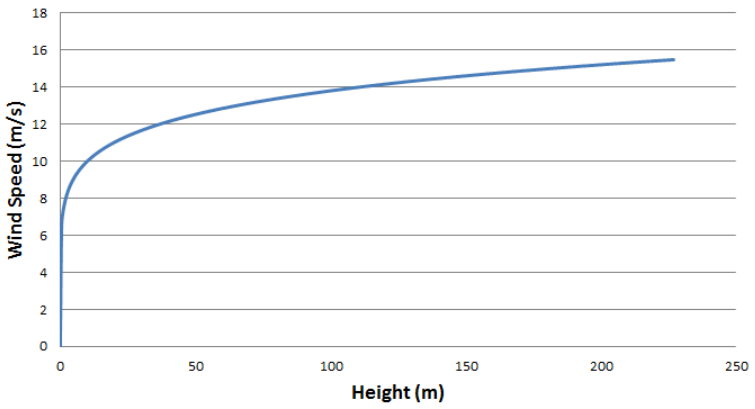

Figure 1.3: Power-law wind speed distribution.

In this thesis we neglect wind turbulence, assuming that its contribution on fatigue damage of mooring lines is small with respect to the one due to the sea waves and the steady part of the wind action. This assumption could for instance be supported by the comparison of the square root of the spectrum of the mooring line tension in [77] for the semi-submersible OC4 model of [132], with a steady wind and with an irregular wind. of the square root of the spectrum Moreover, for the sake of simplicity, the direction of the wind is assumed to be the same of the one of the sea waves.

1.2 Floating structure

The floating structure is composed of the floater, the tower and the turbine. It is subjected to the action of waves on the floater and wind on tower and turbine.

There exists several design typologies for the floating structure of offshore wind turbines. They may be classified according to the way in which the stability is achieved in three main categories, represented in Figure 1.4.

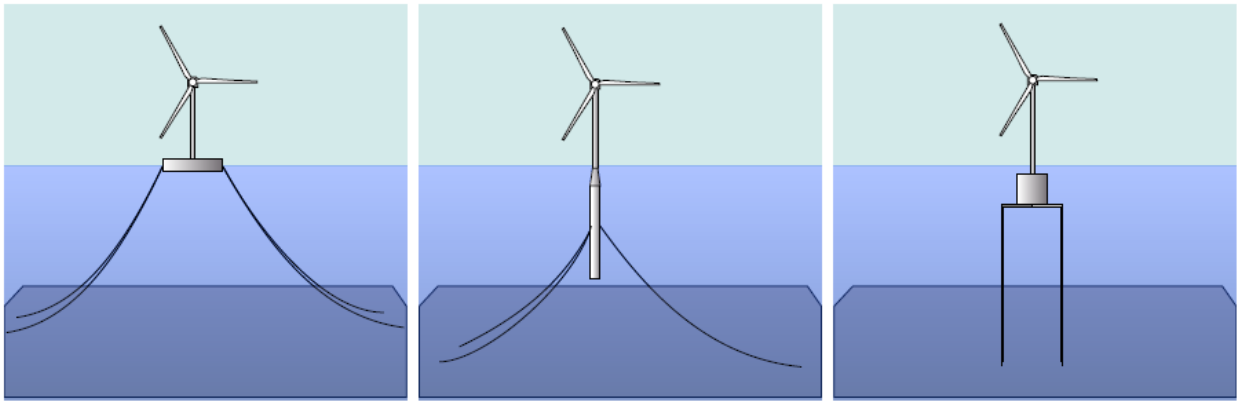

Figure 1.4: Possible floating wind turbine designs [54].

(a) The first one is a *buoyancy stabilized floater*. The idea is to use a floater with a large water-plane area. Thanks to this feature, the floater has an improved resistance for any kind of displacements which involves the vertical movement of the base, because of the greater contact surface with water.

(b) The second is the so-called *ballast stabilized floater*, in which hydro-static stability is pursued by lowering the platform's center of mass below the center of buoyancy, thanks to heavy ballast and large draft. In this case the water-plane area is minimal, which produces a lower susceptibility to wave-induced motions. On the other hand, the heavy weight of the ballast is achieved by addition of material, increasing the costs, and the large draft complicates the installation.

(c) Another possible design is represented by the *tension leg platform*. Here the system is stabilized with taut mooring lines, anchored in the sea ground and kept in tension thanks to excess buoyancy of the floater. The line tensioning together with a small water-plane area bestow on the system a very high stability, but increases the loads on the mooring lines and on the anchors.

The whole floating structure is often considered as a rigid body, since deformations in the platform are negligible if compared to its gross motion. Hence, its degrees of freedom, represented in Figure 1.5, are the six associated to rigid body motions:

- translation along the main wind direction (longitudinal direction), called *surge*,
- translation transversal to the wind direction, called *sway*,

- translation along the vertical axis, called *heave*,
- rotation about the longitudinal axis, called *roll*,
- rotation about the transverse axis, called *pitch*,
- rotation about the vertical axis, called *yaw*.

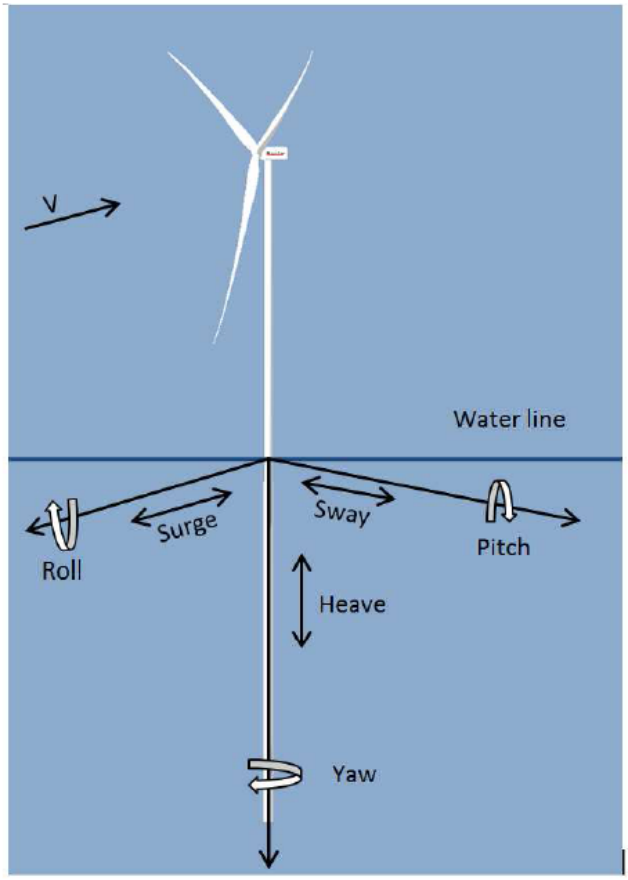

Figure 1.5: Degrees of freedom of a floater [31].

From a wind turbine design point of view, the use of a floating platform instead of a fixed foundation exposes the turbine to these significant new motions. Among them, the most problematic to a turbine is pitch, which is easily excited by both wave loading and wind thrust and which also generates additional bending moments in tower and blades, two of the most critical structural loads [54]. In order to limit the bending moment, for extreme loading, and also to optimize the electrical production in operational conditions, control strategies have been developed (Fig. 1.6).

1.2.1 Wave loads

Since the water is in relative movement with respect to the body, the physical problem to be faced is a hydrodynamic one. Neglecting for the moment non-linearity in dynamic equation

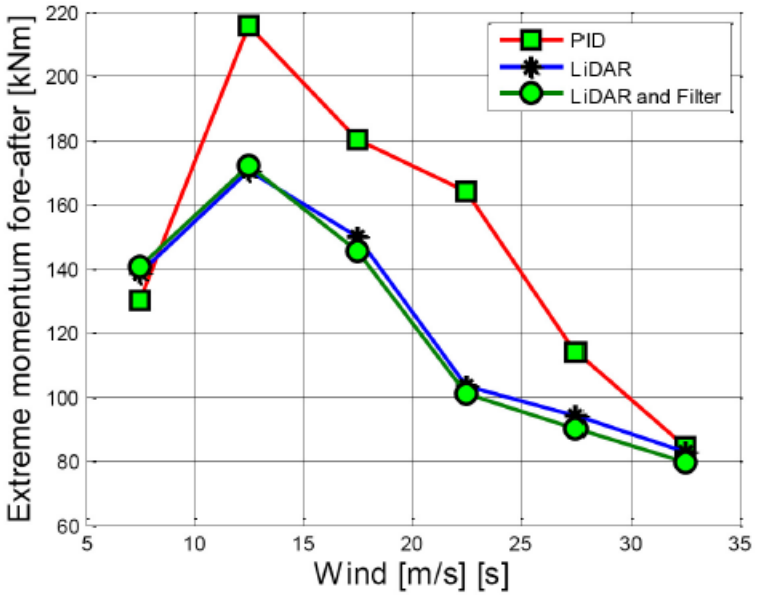

Figure 1.6: Maximum absolute moment in the fore-after direction as a function of wind speed and different control strategies, namely PID and LiDAR [52].

due for instance to finite rotation, in usual hydrodynamic problems the equation of motion has the form

$$\underline{\underline{M}} \cdot \ddot{\underline{u}} + \underline{\underline{B}}_0 \cdot \dot{\underline{u}} + \underline{\underline{B}}_1 \cdot (\dot{\underline{v}} - \dot{\underline{u}}) \|\dot{\underline{v}} - \dot{\underline{u}}\| + \underline{\underline{K}} \cdot \underline{u} = \underline{F} \tag{1.6}$$

in which $\underline{\underline{M}}$ is the mass matrix, $\underline{\underline{B}}_0$ is the damping matrix for linear drag, $\underline{\underline{B}}_1$ is the damping matrix for viscous drag, $\underline{\underline{K}}$ is the stiffness matrix and $\underline{F}$ is the force vector. The vectors $\underline{u}$ and $\underline{v}$ collect respectively the displacements of the solid body and of the surrounding fluid, while the dot upon the vectors denote the derivative with respect to time.

First of all, in order to define the tensors in the equation of motion, it is necessary to look at the dimensions of the bodies within the fluid. One has to distinguish between two situations, namely if the dimensions of the submerged body are small or not relatively to the wavelength. The reason is that in the first case the wave excitation forces can be calculated based on the undisturbed wave kinematics, while in the other case the presence of the body influences the wave profile.

The linear hydrodynamics approach is used when the dimension of the body, the floater in our case, is not negligible when compared to the wavelength. The hydrodynamic forces are considered as the superposition of the three following problems, as reported in Figure 1.7.

(a) Hydro-statics: it corresponds to the equilibrium between the own weight of the body and the Archimede buoyant force.

(b) Diffraction (or wave excitation): it's the loading on the platform exerted by incident waves. In this problem the system is studied without the body movement, on which the incoming waves diffract around it.

(c) Radiation: the body moves in still water, generating waves. If one neglects viscous drag, the forces that result from radiation can be split in two components: added mass, which

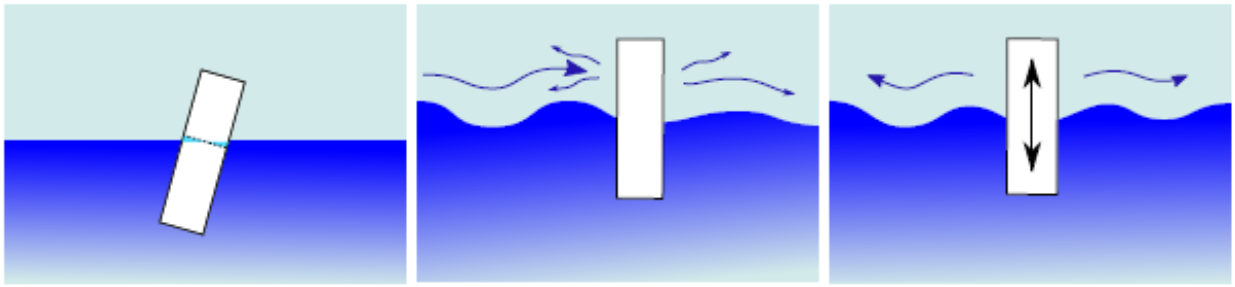

Figure 1.7: The components of linear hydrodynamics illustrated for a cylinder [54].

accounts for the mass of water that is accelerated by the floater, and wave-radiation damping, proportional to the velocity of the floater, whose power (neglecting viscous drag) is equal to the power radiated away in the generated waves. These waves influence the pressure field around the body, impacting its motion. Hence one can note that radiation has a memory effect: wave-radiation damping forces depend on past floater motions.

The hydrodynamic response of the floater is computed thanks to a dedicated software which performs linear hydrodynamic computations of diffraction and radiation (see Fig. 1.7), for different wave periods. The solutions are then superposed, creating the so-called Response Amplitude Operators (RAOs). These basically collect the value of Forces and Moments to be applied on the floater for waves with unitary amplitude, having different period and direction.

Moreover, any relative motion of body and water also produces viscous drag forces. Their effect can be estimated thanks to the *Keulegan-Carpenter number*

$$K_C = \frac{VT}{D_{body}} \tag{1.7}$$

where V is the amplitude of the velocity oscillations, T the oscillation period and D_{body} is a characteristic length of the body. If K_C is small the viscous effects can be neglected, conversely viscous drag effects are superior with respect to the inertial ones.

The viscous effects can be relevant, depending on the geometry of the floater. Namely, if it is characterized by the presence of sharp edges, these would generate a vortex shedding effect in the case of relative movement with respect to the surrounding fluid. This dissipates energy and has therefore the beneficial effect to reduce the mobility of the floater.

1.2.2 Wind loads

The aerodynamic loads depend on whether the turbine is rotating or not. Namely, the turbine rotation is prevented, i.e. it is shut down, in the following situations:

- when the wind speed is below a certain threshold, usually $3m/s$, since in this case the wind turbulence is too high and would cause important stress variations in the blades, with consequent fatigue issues;

- when the wind speed is above a certain threshold, usually $25m/s$, because the pitch of the blades is not sufficient to limit the rotational speed;
- during maintenance operations and curtailments.

If the turbine is shut down, two thrust forces applied on the tower and on the rotor of the turbine are introduced. Their value are given by the following expressions:

$$F_{rot} = \frac{1}{2}\rho_{air}(C_{d,nac}S_{nac} + C_{d,rot}S_{rot})V_{wind}^2 \tag{1.8}$$

$$F_{tow} = \frac{1}{2}\rho_{air}C_{d,tow}S_{tow}V_{wind}^2 \tag{1.9}$$

in which

- $C_{d,tow}$ is the drag coefficient of the tower
- S_{tow} is the tower surface exposed to the wind
- $C_{d,nac}$ and $C_{d,rot}$ are the drag coefficients of nacelle and rotor
- S_{nac} and S_{rot} is the surfaces of nacelle and rotor exposed to the wind

In the operational case, the force on the rotor is determined from aerodynamic simulations. Moreover, a torque around the turbine rotation axis is added. For the case study of the thesis, the load profile is reported in Figure 5.3.

1.2.3 Mooring system

The mooring lines have the function to link the floater to the seabed, lowering the loads on the floating structure by minimizing the motions of the platform. Moreover excessive displacements are avoided to preserve the power-cables and the other wind turbines, and to ensure suitable operational conditions.

Mooring lines may be constituted by *chains*, *synthetic cables* or *wire ropes*. Frequently, mooring lines are composed of different segments, with chains in the top part connecting to the floater, to facilitate tensioning, and on the part which lays on the seabed, to resist abrasion.

In general, according to their shape, mooring lines may be distinguished in two categories:

- *tension legs*, in which the lines are kept in tension by means of an excessive buoyancy of the floater ((c) in Fig. 1.4);
- *catenary*, which consists in long lines that sit on the seabed before reaching the anchor (Fig. 1.8).

In the considered case study, the shape of the lines is the catenary. The advantage of this configuration with respect to tension legs consists in the possibility to use cheaper anchors, because they are subjected to actions which are lower in magnitude, thanks to the longer length of the mooring lines. Most of the restoring forces of a catenary system is generated by the own weight of the lines.

According to the configuration of the lines with respect to wind direction, one can distinguish between leeward and windward lines, as shown in Figure 1.9. From inspections of existing

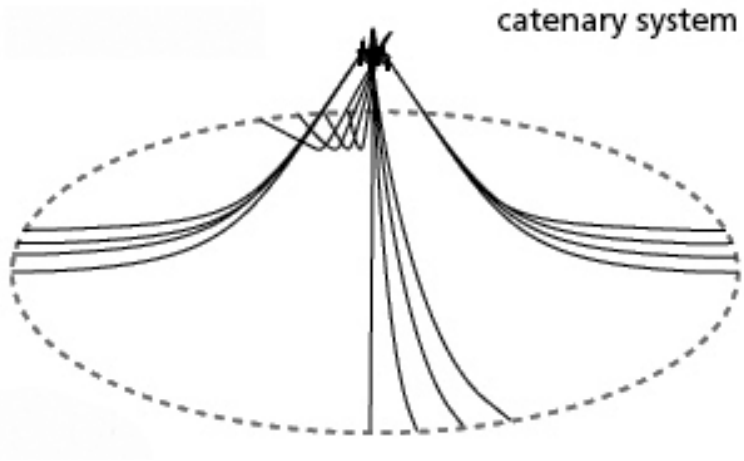

Figure 1.8: Catenary-shaped system (`www.dredgingengineering.com`).

offshore structures it has become clear that the less loaded leeward lines can be subjected to greater degradation than the windward lines; this seems to be due to greater bending in leeward lines since the line is typically under lower tension [106].

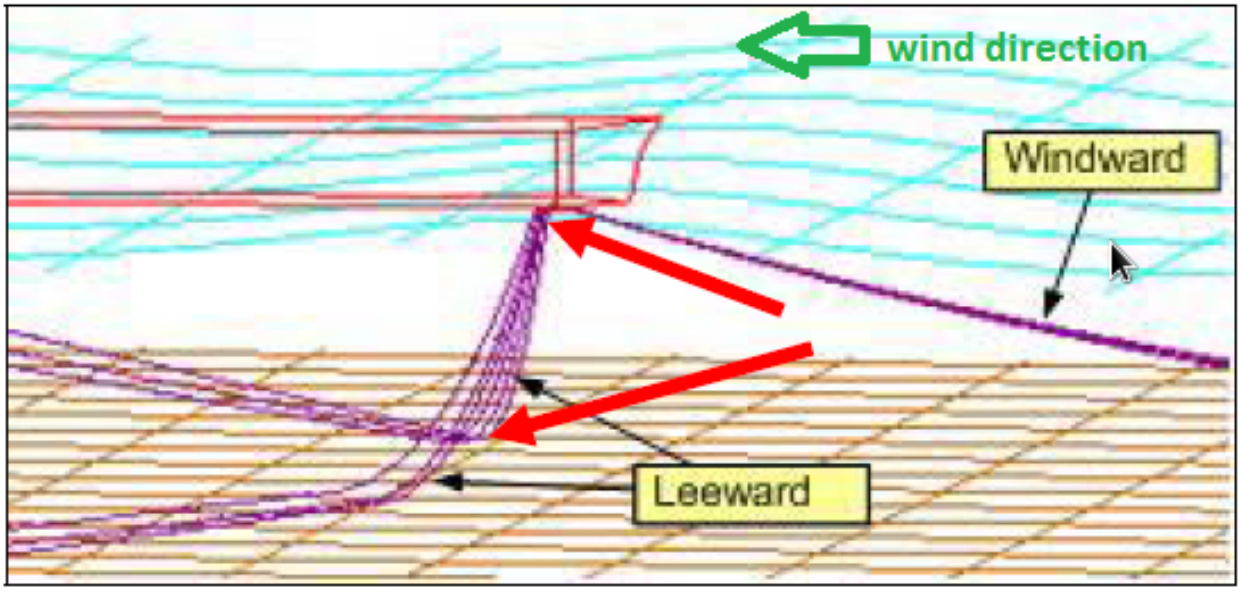

Figure 1.9: Sketch of windward and leeward lines for the case of an oil & gas FPSO. The red arrows indicates the key areas which should be inspected on a mooring line [106].

The mooring lines are loaded by the floater movements and, in their submerged parts, by hydrodynamic loading. Since the mooring lines are slender bodies, with diameter by far smaller than the wavelength, the Morison's equation is used.

The Morison's equation is a semi-empirical equation and it's written as follows:

$$\begin{aligned}\underline{f}_{Mor} =&\rho V\underline{\ddot{v}} + \rho V\left(C_{a\perp}(\underline{\ddot{v}}_{\perp} - \underline{\ddot{u}}_{\perp}) + C_{a//}(\underline{\ddot{v}}_{//} - \underline{\ddot{u}}_{//})\right) + \\ &\frac{1}{2}\rho A\left[C_{d\perp}(\underline{\dot{v}}_{\perp} - \underline{\dot{u}}_{\perp})\|\underline{\dot{v}}_{//} - \underline{\dot{u}}_{//}\| + C_{d//}(\underline{\dot{v}}_{//} - \underline{\dot{u}}_{//})\|\underline{\dot{v}}_{//} - \underline{\dot{u}}_{//}\|\right]\end{aligned} \tag{1.10}$$

in which $\underline{u}$ and $\underline{v}$ denote the displacement vectors of the body and fluid respectively, ρ is the density of the fluid, V is the volume of the body, A is the cross sectional area, $C_a = C_m - 1$ is the added mass coefficient (while C_m is the inertia coefficient), C_d is the drag coefficient. The subscripts $\perp$ and // denote that the correspondent quantity is computed respectively in direction normal and parallel to the rope axis. The first term of the equation is called *Froude-Krylov inertia force*, the second is the hydrodynamic mass force (added mass term) and the third term is the drag force.

Morison's equation relies on the following assumptions:

(a) Since it cannot handle coupling between different DOFs in added mass, it's only applicable to slender axisymmetric bodies.

(b) The body will have a negligible effect on the wave motion; the formalization of this assumption is given by G.I. Taylor's long wavelength approximation, which states that for bodies whose diameter is less than one-fifth the wavelength, diffraction of the wave around the body is minimal and consequently undisturbed wave kinematics is considered (the body is "transparent" to the wave).

(c) Since it includes only a viscous (quadratic) drag term, it's assumed that pressure drag from wave radiation is negligible.

Then, in order to characterize completely the action exerted on the lines by the surrounding fluid, the Archimede buoyant force has to be added to $\underline{f}_{Mor}$.

1.2.4 Global hydrodynamic problem

Applying the Morison's theory on the mooring lines and linear hydrodynamics on the floater, the equation of motion of the system takes the form

$$\begin{aligned}&\left(\underline{\underline{M}}_{system} + \underline{\underline{M}}^{radiation}_{floater}\right)\cdot\underline{\ddot{u}} + \underline{\underline{B}}^{radiation}_{floater}\cdot\underline{\dot{u}} + \underline{\underline{B}}_{mooring}\cdot(\underline{\dot{v}} - \underline{\dot{u}})\|\underline{\dot{v}} - \underline{\dot{u}}\| + \\ &\left(\underline{\underline{K}}^{hydro}_{floater} + \underline{\underline{K}}^{hydro}_{mooring} + \underline{\underline{K}}_{system}(\underline{u})\right)\cdot\underline{u} = \underline{F}^{wind} + \underline{F}^{diff}_{floater} + \underline{F}_{Mor}\end{aligned} \tag{1.11}$$

in which

- $\underline{\underline{M}}_{system}$ and $\underline{\underline{M}}^{radiation}_{floater}$ are the mass matrix of the system and added mass tensor of the floater, coming from radiation effects;
- $\underline{\underline{B}}^{radiation}_{floater}$ is the linear damping matrix of the floater, caused by radiation effects;
- $\underline{\underline{B}}_{mooring}$ is the viscous damping matrix coming from the Morison's equation applied on the mooring lines;
- $\underline{\underline{K}}^{hydro}_{floater}$ and $\underline{\underline{K}}^{hydro}_{mooring}$ are the hydrostatic matrices of floater and mooring lines;
- $\underline{\underline{K}}_{system}$ is the stiffness matrix, which takes into account the reactions given by the mooring system when the floater is subjected to displacements, while the presence of

electrical cables is neglected, assuming that their contribution to the overall stiffness is negligible;

- $\underline{F}^{wind}$, $\underline{F}^{diff}_{floater}$ $\underline{F}_{Mor}$ are the force vectors generated by the action of wind and sea on the structure. The first accounts for the wind action, the second is obtained by solving the diffraction problem on the floater while the third is computed by applying Morison's equation to mooring lines and collects all the terms in the Morison's equation which do not depend on solid displacements.

Finally, an implicit Newmark time integration scheme [105] is generally employed to relate time derivative terms to the degrees of freedom.

1.3 Conclusion

In this chapter, the main features characterizing the mechanical response of a FOWT system have been presented. These elements will be essential for the understanding of the global model, that will be presented in Chapter 5.

In Section 1.1, it has been shown how the environmental loading is described, with particular emphasis on the sea state. In the so-called short-term, it is defined as a superposition of harmonic components, according to a spectrum (Fig. 1.1) defined by three parameters. In the long-term, joint probability of two of these parameters defines the so-called wave scatter diagram (Fig. 1.2). For the sake of simplification, the wind turbulence in this work is neglected, assuming its contribution to the fatigue damage of the mooring system small with respect to the one of the sea waves. This assumption should not be relevant for specific FOWT configuration, in particular with taut mooring lines. By contrast with catenary lines, taut lines should not be in principle be subjected to bending and are not therefore considered in this thesis.

In Section 1.2, the main characteristics of a FOWT structural system (namely floater and mooring lines) have been briefly described. Some general concepts of hydrodynamics are given, in order to get a basic understanding of the computations performed by Deeplines^{TM}, i.e. the software used to performed the global model analysis in Chapter 5.

Chapter 2

Wire ropes

The mechanical analysis of wire ropes constitutes the core of this thesis. A large amount of research works concerning wire ropes can be found in the literature. In the following sections, the main findings from analytical models, experimental tests and numerical models will be detailed.

2.1 Description

Wire ropes consist in a complex assembly of steel wires. The wires are obtained after the wiredrawing operation, whose aim is the increases of the wire ultimate stress (Fig. 2.1) and a reduction of ductility (Fig. 2.2). Moreover residual stresses up to 300 MPa may develop in the wire axis direction [156, 144] (Fig. 2.3). The residual stresses may be originated by mechanical, thermal and thermo-chemical treatments, whose evolution with respect to time and temperature is different [4]. In general, the manufacturing process is developed in order to obtain a compression residual stress on the wire surface, which has the beneficial effect of closing the fatigue cracks during the initiation phase.

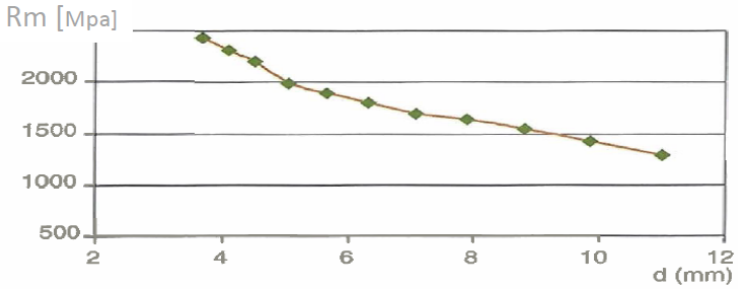

Figure 2.1: After 10 wiredrawing processes the wire diameter d reduces from 11 mm to 3.69 mm, while the ultimate stress R_m increases from 1300 MPa to 2400 MPa [9].

The wires can be wrapped together in different ways. In particular, there exists basically two categories of wire ropes: spiral strands (Fig. 2.4a) and stranded ropes (Fig. 2.4b). A

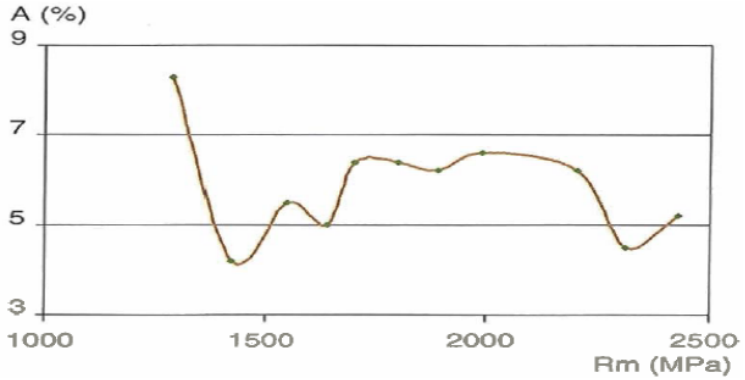

Figure 2.2: Axial strain at wire break as function of the ultimate stress [9].

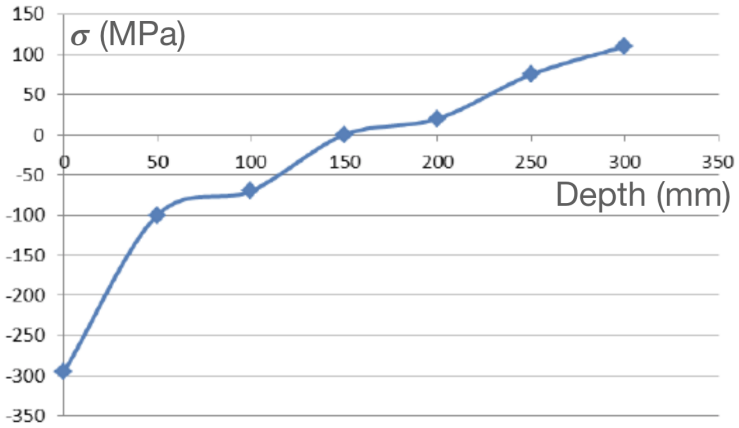

Figure 2.3: Residual stress at different depth below the wire surface (from `https://jacquesdubuisson.files.wordpress.com`).

spiral wire rope has layers of helical wires around a single core wire or a grouped wire core. A stranded wire rope will have normally six or eight strands or groups of wires helically wrapped around either an empty core or another single strand. The wire within a strand are double helices, i.e. and helix around and helix.

In offshore oil industry spiral strands are used for permanent applications, since they are more resistant than stranded wire ropes, which are conversely used for temporary application (as in the drilling phase). Six-strand ropes are less balanced in torsion with respect to spiral strand ones, in which the angle the wire make with its axis of revolution (called lay angle) of each layer is designed in such a way to minimize the traction-torsion coupling. Spiral strand constructions have also the advantage that a polymeric sheath can be more easily extruded over them to serve as a barrier to seawater.

The division of the load bearing capacity between many "parallel (in the sense of redundant load paths) wires has two essential benefits: it ensures the essential combination of high axial strength and stiffness with bending flexibility and allows the structural use of a brittle steel at very high stresses [15]. The lay angles involved in a particular wire rope architecture are

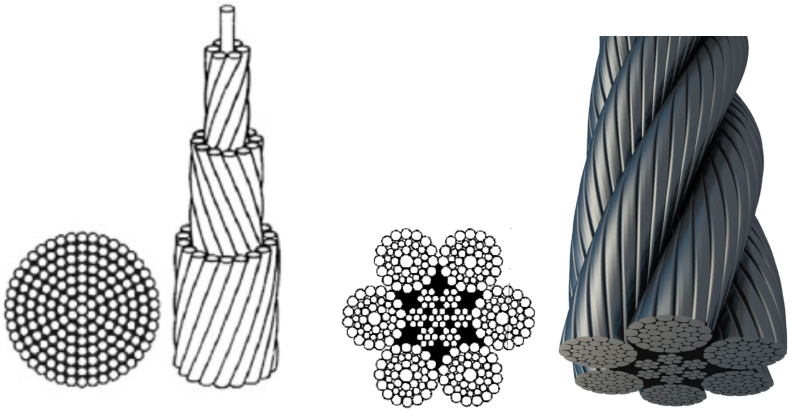

(a) (b)

Figure 2.4: (a) A spiral strand wire rope: it has layers of wires in circles around a single core wire or a grouped wire core [74]. (b) A six-strand wire rope: it is composed by strands wrapped helically.

chosen in such a way to minimize the length differences between the wires and, if possible, also to minimize the tension-torsion coupling, which arises because of the helical configuration.
Moreover spiral strands are designed in order to limit the lateral spacing between wires in the same layer. The geometric condition of lateral contact in the unloaded configuration has been given by Knapp [79]:

$$\sqrt{1+\frac{\tan^2\left(\frac{\pi}{2}-\frac{\pi}{n_i}\right)}{\cos^2\alpha_i}}=\frac{R_i}{r_i} \tag{2.1}$$

where r_i, R_i, n_i and α_i are respectively the wire radius, the layer radius, the number of wires and the lay angle associated to the layer i.

2.2 Helical geometry

The aim of the helical shape is to provide flexibility to the system. This feature is important in many application of wire ropes, since it limits the stress on the wires when the rope is subjected to bending [27]. The helical configuration reduces the axial deformation of wires when bending the cable, since each wire is located equally in both tension and compression side of the cross section. The flexibility is the result of the ability of the helical wires of different layers to slip with respect to each other as the rope axis bends. The amount of slip decreases with increasing lay angle of the wires [108].
The drawbacks of the helical structure are the losses in axial strength and axial stiffness, which increase with the lay angle. However, the helix structure is used even if the wires have to carry only tensile loads, since it creates the so-called *bundle coherence*, as wires are held together.

2.2.1 Helix with straight axis

The helix equation is given by the following parametric expression (Fig. 2.5):

$$\begin{cases} x = R_s \cos\theta_s \\ y = R_s \sin\theta_s \\ z = R_s \cot\alpha\, \theta \end{cases} \tag{2.2}$$

where

- R_s is the laying radius of the single helix;
- α is the lay angle (i.e. the angle between the helix tangent and its axis, Fig. 2.5);
- θ is the free parameter;
- θ_s represents the angular position of the helix center-line around the axis of the rope, which is given by

$$\theta_s = \theta + \theta_{s0} \tag{2.3}$$

with θ_{s0} the the single-helix phase angle, i.e. the angular position of the helix at the position $z = 0$.

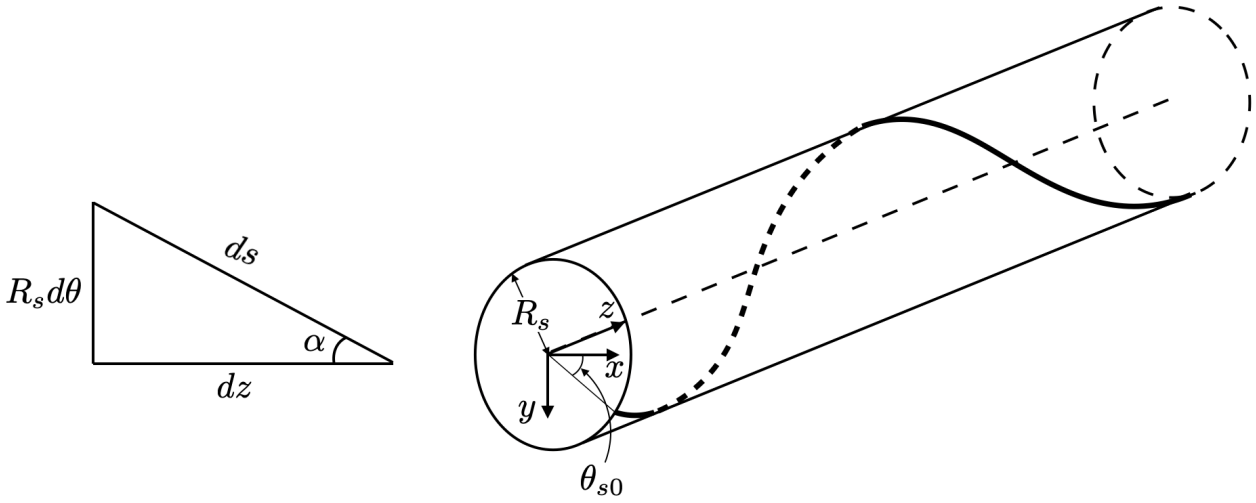

Figure 2.5: Planar and three-dimensional geometry of a helix with straight axis.

One can define the so-called Frenet-Serret reference system $(\underline{t}, \underline{n}, \underline{b})$ associated to each point along the helix center-line; $\underline{t}$ is the tangent vector, while $\underline{n}$ and $\underline{b}$ are the normal and the binormal vectors respectively. Naming $\underline{x}$ the position vector and s the curvilinear abscissa along the helix center-line, they are defined as

$$\underline{t} = \frac{d\underline{x}}{ds}, \qquad \underline{n} = \frac{\dfrac{d\underline{t}}{ds}}{\| \dfrac{d\underline{t}}{ds} \|}, \qquad \underline{b} = \underline{t} \wedge \underline{n} \tag{2.4}$$

These vectors are obtained by linking the variation of curvilinear abscissa with the variation of the parameter of the curve θ. From

$$ds = \sqrt{dx^2 + dy^2 + dz^2} = \sqrt{\left(\frac{dx}{d\theta}\right)^2 + \left(\frac{dy}{d\theta}\right)^2 + \left(\frac{dz}{d\theta}\right)^2} d\theta \tag{2.5}$$

one gets

$$d\theta = \frac{\sin\alpha}{R_s} ds \tag{2.6}$$

By then using the chain rule, the expression of the vectors composing the Frenet-Serret basis is obtained:

$$\underline{t} = \begin{pmatrix} -\sin(\alpha)\sin(\theta_s) \\ \sin(\alpha)\cos(\theta_s) \\ \cos(\alpha) \end{pmatrix}, \quad \underline{n} = \begin{pmatrix} -\cos(\theta_s) \\ -\sin(\theta_s) \\ 0 \end{pmatrix}, \quad \underline{b} = \begin{pmatrix} \cos\alpha\sin\theta_s \\ -\cos\alpha\cos\theta_s \\ \sin\alpha \end{pmatrix} \tag{2.7}$$

The vectors $(\underline{t}, \underline{n})$ define the osculating plane of the curve. The vector $\underline{n}$ points toward the center of rotation of the curve and, by definition, the curvature around $\underline{n}$ is null, i.e. $\kappa_n = 0$. Thus the Frenet formulas read

$$\frac{d}{ds}\begin{bmatrix} \underline{t} \\ \underline{n} \\ \underline{b} \end{bmatrix} = \begin{bmatrix} 0 & \kappa_b & 0 \\ -\kappa_b & 0 & \tau \\ 0 & -\tau & 0 \end{bmatrix} \begin{bmatrix} \underline{t} \\ \underline{n} \\ \underline{b} \end{bmatrix} \tag{2.8}$$

where κ_b is the curvature around the binormal, and corresponds to the total curvature, and τ is the torsion of the curve. From (2.8) one obtains

$$\kappa_b = \frac{d\underline{t}}{d\theta}\frac{d\theta}{ds} \cdot \underline{n} = \frac{\sin^2(\alpha)}{R_s} \tag{2.9}$$

$$\tau = -\frac{d\underline{b}}{d\theta}\frac{d\theta}{ds} \cdot \underline{n} = \frac{\cos(\alpha)\sin(\alpha)}{R_s} \tag{2.10}$$

Finally, it should be noted that in the case of a helix with straight axis, the Frenet-Serret basis coincides with the Darboux-Ribaucour basis associated with a cylinder having radius R_s and collinear with the helix axis.

It should be noted that the conventions used here are in agreement with the bibliography on wire ropes. These can differ from the one used by authors working with the Darboux-Ribeaucour basis, as [88], for which κ_b and κ_n are denoted respectively C_N and C_B, following the direction of variation of the tangent. Moreover, in this work the angle θ originates from the neutral plane, while in [88] $\theta = 0$ indicates the outer arc.

2.2.2 Helix with curved axis

Let us now consider a helix attached to a tore, i.e. a bent cylinder subjected to uniform curvature $\kappa_c = \dfrac{1}{\rho_c}$ on the y-z plane (Fig. 2.6). Keeping the same convention used in (2.2),

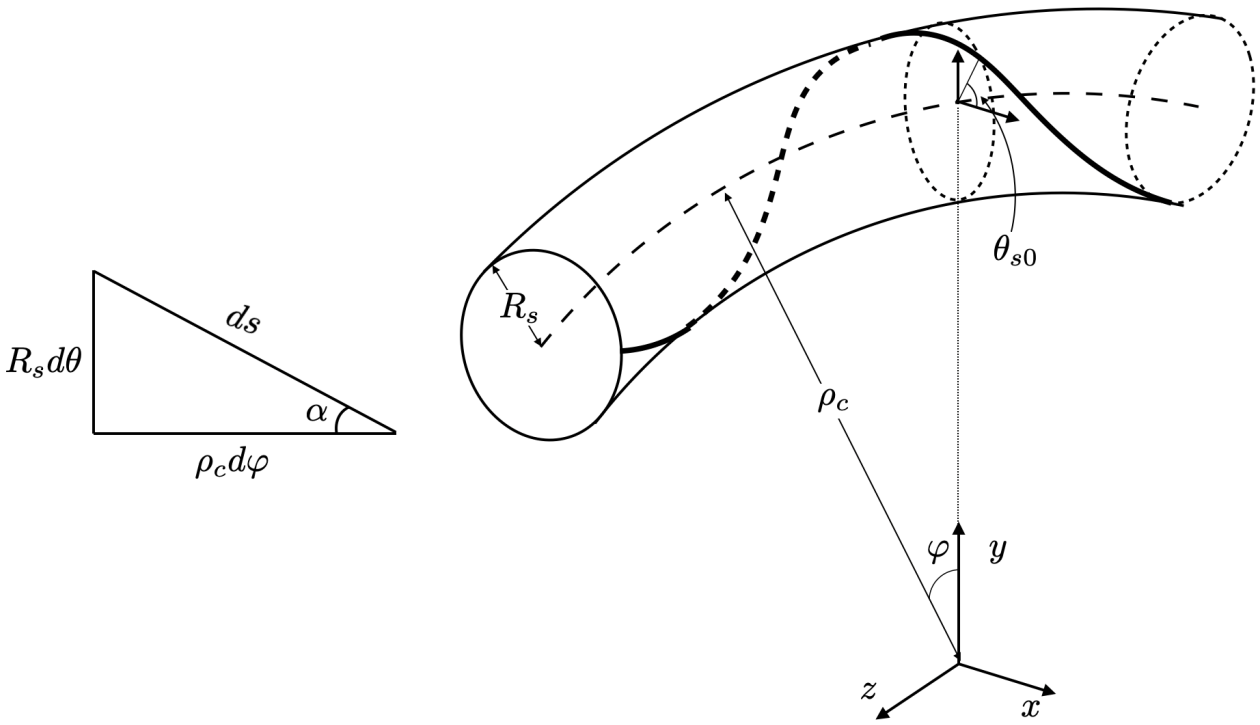

Figure 2.6: Planar and three-dimensional geometry of a helix with curved axis with constant curvature $\frac{1}{\rho_c}$ around the x axis.

$\theta_s = \dfrac{\pi}{2}$ and $\theta_s = -\dfrac{\pi}{2}$ define respectively the outside and inside generatrix of the tore. As shown for instance in [62], the parametric expression of the helix adherent on the surface of the tore is

$$\begin{cases} x = R_s \cos\theta_s \\ y = (\rho_c + R_s \sin\theta_s)\cos\varphi \\ z = (\rho_c + R_s \sin\theta_s)\sin\varphi \end{cases} \tag{2.11}$$

A three-dimensional surface is a function of two independent parameters, which in our case are θ and φ. A curve on this surface is defined once the relation between the two parameters is established. As shown in [88], the curvatures associated to the Darboux-Ribaucour basis and the derivative $\dfrac{ds}{d\theta}$ can be obtained once $\dfrac{d\varphi}{d\theta}$ is defined. It is assumed that the deformed helix can be described by

$$\frac{d\varphi}{d\theta} = \frac{\eta}{\tan\alpha}(1 + h(\theta, \eta)) \tag{2.12}$$

where $\eta = \dfrac{R}{\rho_c}$ and $h(\theta, \eta = 0) = 0$.

It is useful to represent the helix kinematics by considering the relative displacements with respect to a reference configuration, namely the kinematics that the helix would have if glued on the surface of the tore. We can decompose these relative displacements along characteristic directions. In particular we can choose to use the Darboux-Ribaucour basis or the directions

associated with the tore. In the first case, the components will be along the transverse and tangential directions, i.e. Δ_b and Δ_t respectively; otherwise we can use the components parallel to the tore axis and along its circumferential direction, respectively Δ_p and Δ_c. As shown in Figure 2.7, one can easily switch from a basis to the other.

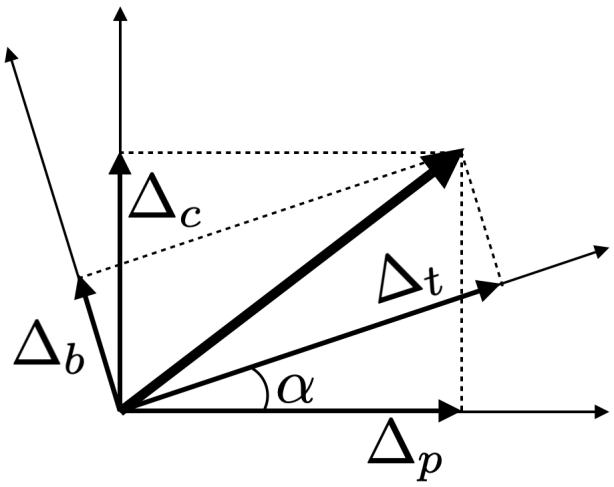

Figure 2.7: The total relative displacement decomposed along characteristic directions.

In [88] it is found that

$$h = \frac{1}{R_s}\left(\tan\alpha\frac{d\Delta_p}{d\theta} - \frac{d\Delta_c}{d\theta}\right) \tag{2.13}$$

One can define curves with particular distributions of Δ_p and Δ_c (or equivalently Δ_b and Δ_t). Namely

1. the *transposed* is the curve with no elongation and whose points can slip along the helix tangential direction only;
2. the *isomeridian* is the curve with no elongation and whose points can slip along the circumferential direction only;
3. the *geodesic* is the curve with minimum length and whose principal normal (i.e. the normal of the Frenet-Serret basis) is coincident with the normal to the surface (i.e. the normal of the Darboux-Ribaucour basis).

The expressions of Δ_p and Δ_c for these curves are the following

$$\begin{aligned}\Delta_c &= -R_s\cos^2\alpha(\zeta+1)\eta\cos(\theta)\\ \Delta_p &= \frac{R_s}{\tan\alpha}[(\zeta+1)\sin^2\alpha - 1]\eta\cos(\theta)\end{aligned} \tag{2.14}$$

where

- $\zeta = 0$ for the transposed curve;
- $\zeta = -1 + \dfrac{1}{\sin^2\alpha}$ for the isomeridian curve;
- $\zeta = -1 - \dfrac{1}{\sin^2\alpha}$ for the geodesic curve.

2.3 Mechanical behavior

One of the key aspects of the thesis is the modeling of the wire rope at the wire scale. In fact, being able to properly describe wire interactions at different load levels would allow to correctly characterize the stress variation and evaluate properly the risk of fatigue.

For what concerns the analytical models, it is important to distinguish between stranded ropes and spiral strands. For the first category, characterized by the presence of single and double helices, there are few available analytical models. They treat only the case of axial loading (tension and torsion without bending) and they assume no friction [167] or perfect adhesion [153]. We will not consider the case of stranded ropes in this thesis, as mooring cables for long time applications are mostly using spiral strands.

Conversely, in the literature there are analytical models for spiral strands including bending and finite friction. There exists two kinds of models:

- semi-continuous models, in which each layer is model as an orthotropic cylinder [59, 72];
- thin rod models, in which wires are considered individually [111, 62].

We chose to make use of the results from the second category, which are easier to be exploited since the quantities are directly associated to the single wires.

A vast quantity of experimental tests on wire ropes have been conducted, in order to study their behavior under several loading conditions. Some fatigue tests have also been performed, from which the researchers developed empirical fatigue laws (see section 3.4.4).

The numerical modeling of wire ropes started in more recent years, when the computational capabilities of modern calculators were sufficient to deal with the high number of contact interactions occurring between the wires. However, still nowadays their computational cost makes them unfeasible for practical design purposes.

2.3.1 Analytical Models - Tension

First of all, let us describe the behavior of the rope when it's subjected to a pure tensile load. This loading is of fundamental importance, since wire ropes are basically requested to bear tension. Moreover, before their usage, wire ropes are usually pretensioned, because a newly constructed wire rope has a lot of empty space between the wires and applying the load causes the cross section to contract until the wires are touching. This prevents large extension at a very low force when wire ropes are first loaded.

It is trivial saying that axial force T_{rope} applied to a wire rope induces an uniform elongation ε_c of the rope axis; because of the helical shape of the wires, a second effect arises, since tension induces an internal torque which tries to "unwind" the rope. According to the arrangements of the wires, this effect can be more or less pronounced. Therefore the total force acting on the rope is actually the sum of two contributions:

$$T_{rope} = (EA)_{rope}\frac{\Delta L}{L} + K_\theta \frac{\Delta \theta}{L} = (EA)_{rope}\varepsilon_c + K_\theta \tau_c \tag{2.15}$$

- The first term, in which $(EA)_{rope}$ is the axial stiffness of the rope, is the part of T_{rope}

which contributes to elongate the rope axis of a quantity ΔL. Note that the axial stiffness can be related to the radial contraction of the rope (see equation (2.30)).

- The second term is the part of force which makes the wires rotate of a quantity $\Delta\theta$ around the central axis of the rope; the quantity K_θ is linked to the torsional stiffness of the wire rope.

When a wire rope is loaded in tension, the total force T_{rope} distributes on each wire such that

$$\sum_{n}^{N_{wires}} S_n = T_{rope} \tag{2.16}$$

where S_n is the component in the direction of the rope axis of the force acting on the n-th wire.

As done by Papailiou [111] we now assume:

1. the change in the lay angle caused by the tensile load is negligible (it tends to decrease with tension);
2. radial contraction of wires cross sections, due to Poisson effect and contact pressure, is neglected;
3. the torsion τ_c of the rope cross section is null (i.e. the wire rope ends are restrained with respect to torsion);
4. shear forces acting on the wires are negligible with respect to the tensile force;
5. the helices are in line contact condition with the layer underneath (note that this is true only for the first layer).

With these hypotheses, by a simple geometrical consideration we can state that each wire in a layer i is subjected to the same tensile force T_i, whose components are represented in Figure 2.8. Its value is hence given by

$$T_i = \frac{S_i}{\cos\alpha_i} \tag{2.17}$$

in which S_i is the part of the tensile load taken by the wire. The other component of T_i, i.e. the transverse force U_i, is the one which prevents the rope to unwind.

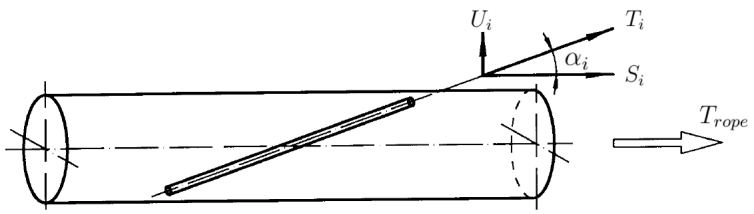

Figure 2.8: Tensile force decomposition in the individual wire [111].

Linearizing the Pythagorean relation from Figure 2.5, one obtains

$$\frac{ds}{s} = \sin^2\alpha\frac{d\theta}{\theta} + \cos^2\alpha\frac{dz_s}{z_s} \tag{2.18}$$

Because of the third assumption of this model, the torsion of the cross section (i.e. the second term of equation 2.15) is neglected, obtaining

$$\varepsilon_i = \cos^2 \alpha_i \varepsilon_c \tag{2.19}$$

in which ε_c is the axial strain of the rope axis. One could note immediately that the axial strain in helical wires is always lower than the one of the rope axis when the rope is subjected to pure tension.

Lanteigne [85] takes into account also the torsion of the rope cross section:

$$\varepsilon_i = \cos^2 \alpha_i \varepsilon_c + R_i \sin \alpha_i \cos \alpha_i \tau_c \tag{2.20}$$

By assuming a linear elastic behavior, with all the wires made by the same material characterized by Young Modulus E, the tensile force and the stress in the wire are respectively given by

$$T_i^{tens} = \frac{EA_i}{(EA)_{rope}} \cos^2 \alpha_i T_{rope} \tag{2.21}$$

where A_i is the area of the cross section of the wires in the i-th layer and $(EA)_{rope}$ is the axial stiffness of the rope, whose expression can be obtained by simple algebra from equations (2.15), (2.16), (2.17) and (2.19) as follows:

$$\begin{aligned} \textstyle\sum_i^L N_i T_i \cos \alpha_i &= (EA)_{rope} \varepsilon_c \\ \textstyle\sum_i^L [N_i (EA)_i \varepsilon_c \cos^2 \alpha_i] \cos \alpha_i &= (EA)_{rope} \varepsilon_c \\ (EA)_{rope} &= \textstyle\sum_i^L N_i (EA)_i \cos^3 \alpha_i \end{aligned} \tag{2.22}$$

with L the number of layers and N_i the number of wires in layer i.

It is important to notice that since the axial strain of the helical wires is constant, no friction in their longitudinal direction is expected. As a matter of fact, the Euler-Bernoulli axial equilibrium of a curved beam writes:

$$\frac{dT}{ds} - F\kappa + q = 0 \tag{2.23}$$

where s is the curvilinear abscissa, F is the shear force in the bending plane, κ is the beam curvature and q is the friction force per unit length. Therefore, according to the analytical results we have

$$\frac{dT}{ds} = 0; F \approx 0 \Rightarrow q = 0 \tag{2.24}$$

Since wires in adjacent layers are in contact with each other, this means that when a wire rope is uniformly extended there will be no slippage in the longitudinal direction (though there could be interwire slippage within each layer) and the stretched wires will retain the helix geometry with a reduced lay angle [62]. In this configuration each wire has constant curvature and tortuosity, depending on its lay angle and its distance from the cable centerline:

$$\begin{aligned} \Delta\kappa_n &= \kappa_n - \kappa_{n0} = 0 \\ \Delta\kappa_b &= \kappa_b - \kappa_{b0} = \frac{\sin^2 \alpha}{R_s} - \frac{\sin^2 \alpha_{s0}}{R_{s0}} \\ \Delta\tau &= \tau - \tau_0 = \frac{\cos \alpha \sin \alpha}{R_s} - \frac{\cos \alpha_{s0} \sin \alpha_{s0}}{R_{s0}} \end{aligned} \tag{2.25}$$

where subscript "0" refers to the quantity in the initial configuration, κ_n and κ_b are the wire curvature around the normal and binormal vector respectively (κ_n is null when the wire geometry is helical), τ is the wire tortuosity, R_s is the helix radius and α is the helix lay angle.
Actually, considering the real contact condition with the layer underneath, i.e. trellis contacts (see section 2.4), during tension microslips occur among adjacent layers [112]. According to [65] these microslips are responsible for the hysteretic behavior observed in tension tests, together with other slips that propagate from the cable ends.

Influence of radial contraction

Costello [21] considers the radial contraction due to the Poisson effect with the axial strain in the helical wires. The displacement vector of a point P on the helix centerline can be expressed as

$$\underline{u}(P) = \varepsilon_c z_P \underline{k} - \varepsilon_{ri} R_i \underline{n} \tag{2.26}$$

where $\underline{k}$ is the helix axis direction, z_P is the coordinate of point P along the rope axis and $\varepsilon_{ri} = \dfrac{\Delta R_i}{R_i}$. The axial strain in the helical wire is therefore given by

$$\varepsilon_i = \frac{d\underline{u}}{ds} \cdot \underline{t} = \varepsilon_c \cos^2 \alpha_i + \varepsilon_{ri} \sin^2 \alpha_i \tag{2.27}$$

According to Costello, for a layer i the radius contraction linked to the Poisson effect is

$$\varepsilon_{ri} = -\frac{\nu}{R_i} \left(r_0 \varepsilon_c + \sum_{j=1}^{i-1} 2 r_j \varepsilon_j \mu + r_i \varepsilon_i \right) \tag{2.28}$$

The axial strain each wire can then be expressed as follows:

$$\begin{aligned} \varepsilon_i &= a_i \varepsilon_c \\ a_i &= \frac{B_i}{A_i} - \frac{2\nu}{A_i R_i} \sin^2 \alpha_i \sum_{j=1}^{i-1} a_j r_j \\ A_i &= 1 + \nu \frac{r_0}{R_i} \sin^2 \alpha_i \\ B_i &= \cos^2 \alpha_i - \nu \frac{r_0}{R_i} \sin^2 \alpha_i \end{aligned} \tag{2.29}$$

Consequently the axial stiffness of the rope, which neglecting the Poisson effect is given by (2.22), by including the radial contraction effect becomes

$$(EA)_{rope} = \sum_{i}^{L} E_i g_i a_i \cos \alpha_i \tag{2.30}$$

with $g_i = \dfrac{n_i 2 r_i}{\sum_j^L n_j (2 r_j)^2}$.

Influence of lateral contact

Considering the contact between wires in the same layer, with the described kinematics previously described, one can notice that these wires exhibit a relative displacement (Fig. 2.9). This generates, in presence of friction, frictional forces and a shear deformation of the wires, which can be expressed as

$$\gamma_i = \frac{dU_i}{2r_i} = \varepsilon_i \tan\alpha_i = a_i \tan\alpha_i \varepsilon_c \tag{2.31}$$

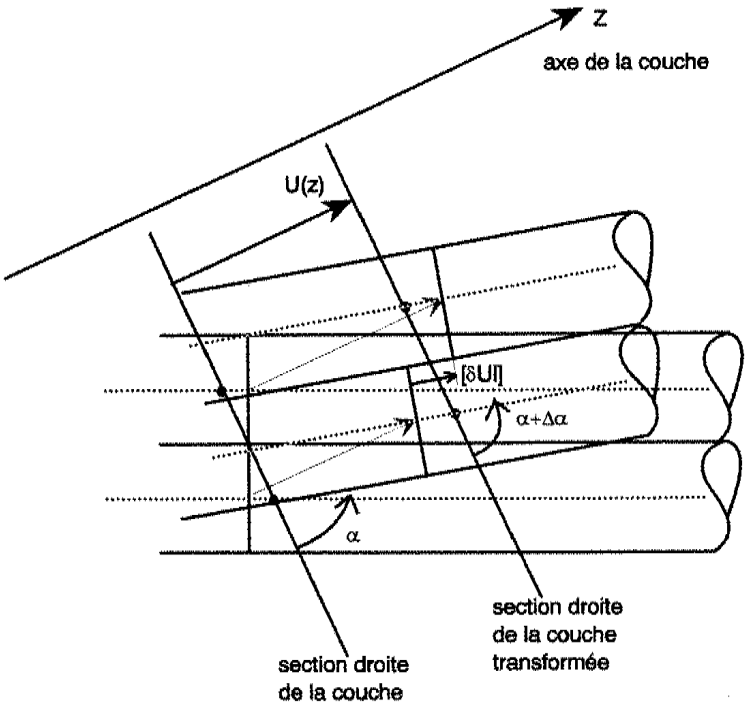

Figure 2.9: Sliding between the wires in the same layer caused by tension [139]

The critical shear deformation increment generating sliding among the wires is [139]

$$\Delta\gamma_i^{crit} = \frac{\mu p_0 b}{G 2r_i}\left(\log\left(\frac{2r_i}{b}\right) - \frac{1}{2}\right) \tag{2.32}$$

in which p_0 is the maximum normal contact pressure, b is the width of the contact area, μ is the friction coefficient and G is the shear modulus. The axial strain increment of the rope associated to the start of slip is at layer i is

$$\Delta\varepsilon_i^{crit} = \frac{\Delta\gamma_i^{crit}}{a_i \tan\alpha_i} \tag{2.33}$$

2.3.2 Analytical Models - Bending

Let us consider now the bending case. Now to the wire rope axis is also applied a uniform curvature κ_c.
As the cable is bent, the lay angle and, therefore, the curvature and tortuosity vary along each wire; consequently the wire configuration is no longer a helix. If the wires are under tension and there is no friction between them, then the wires freely slide toward a geodesic configuration. The configuration of a wire in a bent cable with friction is somewhere between the configuration without interlayer displacement and a geodesic curve [62].

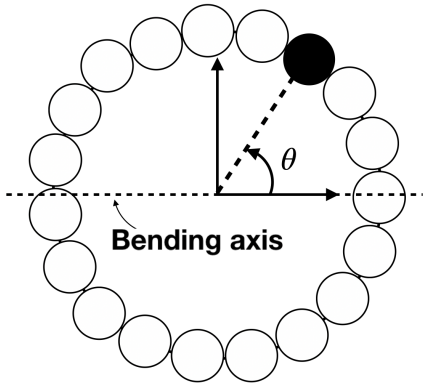

Figure 2.10: The angle θ identifies the position of the helical wire section with respect to the bending axis x.

When bending occurs, one can express the position of the helical wire at a given section by means of the angle θ (Fig. 2.10): $\theta = 0$ and $\theta = \pi$ correspond to the neutral axis, $\theta = \frac{\pi}{2}$ is the outer arc and $\theta = -\frac{\pi}{2}$ is the inner arc.
Let us consider frictional contact among the wires. During bending two different types of loading occur on a helical wire: wire elongation and wire bend around its own transverse axis (Fig. 2.11). The strain distribution caused by the second one can be simply obtained exploiting beam theory.
For what concerns wire elongation, one can distinguish between two limit situations.

1. When the curvature is sufficiently low, wires are in stick state. This means that no relative movements among them take place and the rope behaves as a beam, since sections remain plane in the deformed configuration.
2. After that rope curvature reaches a certain threshold, the helical wires are in complete slip state.

In order to explain this phenomenon, we first have to determine the contact pressure p_i that the helical wires in a layer i exert on the layer underneath $(i-1)$. Let us now assume line contact among the two layers.
The linear pressure p_i can be easily obtained by considering the transversal equilibrium of

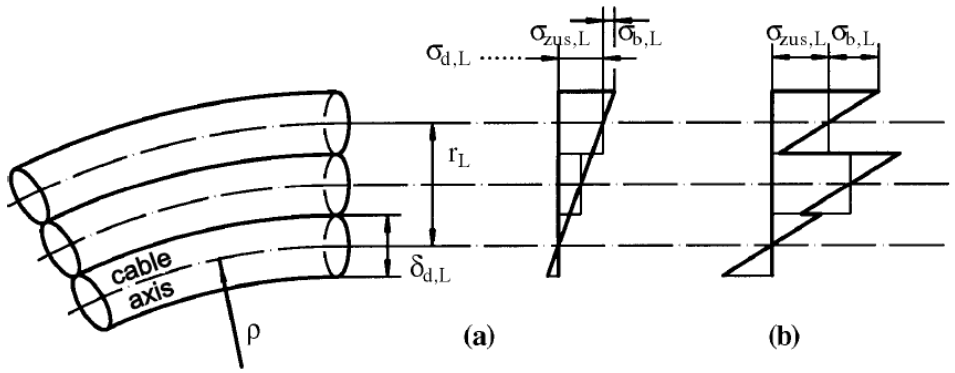

Figure 2.11: Wire stresses as the rope bends [111]: (a) wires not displaced, (b) wires displaced.

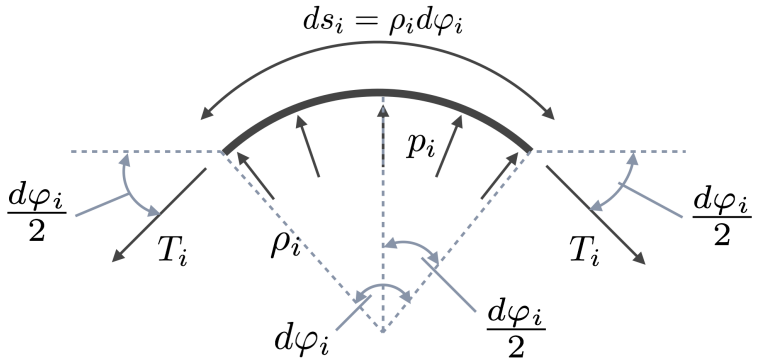

Figure 2.12: Transversal equilibrium of a curved wire element subjected to tension.

an infinitesimal wire element (Fig. 2.12). Neglecting higher order terms one obtains

$$p_i = \frac{T_i}{\rho_i} = T_i \kappa_{b,i} \tag{2.34}$$

in which ρ_i is the curvature radius of the helix. The radial force generated by p_i is

$$dN_i = p_i \rho_i d\varphi \tag{2.35}$$

where $d\varphi$ is the angle represented in Figure 2.12.
One should note that if the considered layer i is not the most external one, the pressure coming from the outer layers adds up to the value obtained from equation (2.34). Moreover, we will always consider that the helical wires are in tensile state. The absence of compression is a design requirement for a wire rope mooring system, since a compressed wire would immediately buckle, giving rise to a phenomenon known as birdcaging [21].
When the wires of a layer i are in complete stick state, the parametric description of their

axes are described by (2.11). Their axial deformation can be obtained as follows [62]:

$$\begin{aligned} ds &= \sqrt{dx^2+dy^2+dz^2} \\ &= ds_0\sqrt{\left(\frac{dx}{ds_0}\right)^2+\left(\frac{dy}{ds_0}\right)^2+\left(\frac{dz}{ds_0}\right)^2} \\ &= ds_0\sqrt{\left[\left(\frac{dx}{d\theta}\right)^2+\left(\frac{dy}{d\theta}\right)^2+\left(\frac{dz}{d\theta}\right)^2\right]\left(\frac{d\theta}{ds_0}\right)^2} \end{aligned} \tag{2.36}$$

Then, by using the relationship $R_i d\theta = ds_0 \sin\alpha_i$ (Fig. 2.6), after some algebra one obtains

$$ds = ds_0\sqrt{\left[R_i^2+(\rho_c+R_i\sin\theta)^2\left(\frac{d\varphi}{d\theta}\right)^2\right]\left(\frac{\sin\alpha_i}{R_i}\right)^2} \tag{2.37}$$

Since $dz = \rho_c d\varphi = (1+\varepsilon_c)dz_0$ and $\dfrac{dz_0}{d\theta} = R\cot\alpha_i$, one obtains

$$\frac{d\varphi}{d\theta} = (1+\varepsilon_c)\kappa_c^2 R_i^2\cot\alpha_i = (1+\varepsilon_c)\eta^2\cot\alpha_i \tag{2.38}$$

With reference to equation (2.12), for the adherent helix one gets

$$h_{adh}(\theta,\eta) = \eta(1+\varepsilon_c) - 1 \tag{2.39}$$

Finally the axial strain of the adherent wire is

$$\varepsilon_i = \frac{ds}{ds_0} - 1 = \sqrt{\sin^2\alpha_i + (1+\kappa_c R_i\sin\theta)^2(1+\varepsilon_c)^2\cos^2\alpha_i} - 1 \tag{2.40}$$

In the hypothesis of small curvature κ_c, the linearized expression of ε_i follows a sinusoidal distribution:

$$\varepsilon_i^{stick} = (\varepsilon_c + R_i\kappa_c\sin\theta)\cos^2\alpha_i \tag{2.41}$$

In addition to the axial strain, a bent helical wire is also subject to local bending and twisting. By projecting the acting bending vector in the Darboux-Ribaucour basis, in stick state the following curvatures are obtained [162]:

$$\begin{aligned} \kappa_b &= \kappa_c\cos\alpha_i\sin\theta \\ \kappa_n &= \kappa_c\cos\theta \\ \tau &= \kappa_c\sin\alpha_i\sin\theta \end{aligned} \tag{2.42}$$

When the most external layer L is in complete slip state, the axial elastic force, obtained after integrating the longitudinal equilibrium equation of a helical wire element and assuming that slippage only occurs along the axial direction of each wire, becomes

$$T_L(\theta) = T_L^{tens}e^{\mu_i\sin\alpha_L\theta}; \quad -\frac{\pi}{2} \le \theta \le \frac{\pi}{2} \tag{2.43}$$

where μ is the friction coefficient and T_L^{tens} is the tensile force due to tension in a wire belonging to the most external layer (equation (2.21)).
One can notice that after complete slippage is attained, a further increase of curvature would not change the tensile force on the helical wires and only the 'local' bending moment of the wire would increase.
Considering the fact that contact does not occur along lines, as in the case of two layers in contact with different lay angles, the normal force at contact points is given by [111]

$$P_i = 2T_i \sin\alpha_i \sin\left(\frac{\Delta\theta_i}{2}\right) \tag{2.44}$$

in which

$$\Delta\theta_i = \frac{2\pi}{b_i} \tag{2.45}$$

The quantity b_i is the number of contact points between layer i and $i-1$ per lay length i

$$b_i = N_{i-1}\left(\frac{R_i \tan\alpha_{i-1}}{R_{i-1}\tan\alpha_i} \pm 1\right) \tag{2.46}$$

in which the sign $'+'$ corresponds to the case of the adjacent layers having opposite lay sense.
The resulting axial strain and tension along the wires assumes stepwise variations. By increasing the number of contact points, the difference among this stepwise variation and the continuous one tends rapidly to become negliglible.
Considering a helix in a generic i-th layer in complete slip state, its axial force can be obtained thanks to the following equations [62]:

$$T_i^{slip}(\theta) = T_i^h(\theta) + T_i^p(\theta) \tag{2.47}$$

$$T_i^h(\theta) = C_i^h e^{\mu\theta\sin\alpha_i} \tag{2.48}$$

$$C_i^h(\theta) = EA_i\varepsilon_c\cos^2\alpha_i - \sum_{j=i+1}^{L} C_{i,j}^p \tag{2.49}$$

$$T_i^p(\theta) = \sum_{j=i+1}^{L} C_{i,j}^p e^{\mu\theta\sin\alpha_j} \tag{2.50}$$

$$C_{i,j}^p = \frac{2\sin\alpha_j \dfrac{R_i N_j \tan\alpha_j}{R_j N_i \tan\alpha_i} C_j^h + \displaystyle\sum_{k=i+1}^{j-1} \sin\alpha_k \frac{R_i N_k \tan\alpha_k}{R_k N_i \tan\alpha_i} C_{k,j}^p}{\sin\alpha_j - \sin\alpha_i} \quad 1 \le i < j \le L \tag{2.51}$$

The moment-curvature relation of a wire rope is nonlinear. Initially, all wires are in stick state and the cross sections remain plane (the wire rope follows beam kinematics). In this phase the bending stiffness is the maximum one:

$$(EI)_{max} = (EI)_{min} + (EI)_{II} = \sum_i^L N_i E\pi\frac{r_i^4}{4}\cos\alpha_i + \sum_i^L\sum_n^{N_i} E(R_i\sin\theta_n)^2 A_i\cos^3\alpha_i \tag{2.52}$$

- $(EI)_{min}$ is the bending stiffness contribution of the single wires which bends around their own axis (r_i is the wire radius in layer i); this is the bending stiffness of the wire rope when all the wires are in slip state and is the minimum one.
- $(EI)_{II}$ is the rigid cross section contribution caused by friction.

The slippage in a layer starts in the proximity of the neutral axis. The first layer to slip is the most external one, since the contact pressure involved is the lowest. For the internal layers the contribution of the external ones increases the contact pressure and consequently higher friction forces can take place.

For each layer, it is possible to determine which is the limit angle in $\theta_i^{\pm}$ in correspondence of slippage for a certain curvature of the rope axis. Differentiating the axial force in stick state (whose expression can be obtained from (2.41)) with respect to θ_i one obtains

$$dT_i^{stick} = EA_i\kappa_c R_i \cos^2\alpha_i \cos\theta_i d\theta_i \tag{2.53}$$

We now assume that the wire is in a state of impending slip. Consequently all the wires in outer layers in its sector must be in a slip state. The normal contact force increment on the wire is therefore

$$dP_i = \left(T_i^{stick}(\theta_i)\sin\alpha_i + 2\sum_{j=i+1}^{N} T_j^{slip}(\theta_i)\sin\alpha_j \frac{R_i N_j \tan\alpha_j}{R_j N_i \tan\alpha_i} \right) d\theta_i \tag{2.54}$$

Setting the imbalanced force equal to the maximum friction force at the boundary between the stick and slip states, identified by $\theta_i^{\pm}$, yields

$$EA_i\kappa_c R_i \cos^2\alpha_i \cos\theta_i^{\pm} = \mu \left(T_i^{stick}(\theta_i^{\pm})\sin\alpha_i + 2\sum_{j=i+1}^{N} T_j^{slip}(\theta_i^{\pm})\sin\alpha_j \frac{R_i N_j \tan\alpha_j}{R_j N_i \tan\alpha_i} \right) \tag{2.55}$$

This equation can be numerically solved to find the unknown boundary angles $\theta_i^{\pm}$. It is also possible to evaluate the curvature κ_c which activate slippage in layer i.

These equations allow to obtain numerically the moment-curvature diagram of the wire rope. A even more accurate modeling is proposed in [63], where shearing and micro-slipping (and ultimately the gross slipping) are taken into account at the inter-layer wire contact interfaces, as opposed to only considering a stick-slip system. However, we will consider the simplified approach proposed by Papailiou [111], which considers that each layer suddenly slips when a certain level of curvature is attained. The bending diagram takes therefore a multilinear shape.

The bending stiffness values at the kink points of the bending diagram are

$$(EI)_j = (EI)_{min} + \sum_{i}^{j}\sum_{n}^{N_i} E(R_i\sin\theta_n)^2 A_i \cos^3\alpha_i \tag{2.56}$$

The curvatures κ_m in correspondence of the stiffness changes are obtained as follows. Firstly, the bending moment generated by friction has to be obtained:

$$M_{R,j} = \sum_{i=L-j+1}^{L}\sum_{n=1}^{N_i} T_i^{slip}(\theta_n) R_i \sin\theta_n \cos\alpha_i \tag{2.57}$$

Then the curvatures κ_m are computed as

$$\kappa_{m,j} = \frac{M_{R,j}}{(EI)_j - (EI)_{j-1}} \tag{2.58}$$

It should be noted that the maximum friction force which can take place among the wires depends on the normal contact force. Consequently, it depends on the value of the traction force applied to the rope (see (2.21) and (2.34)). Therefore an important conclusion can be drawn: traction affects the bending stiffness of the rope.

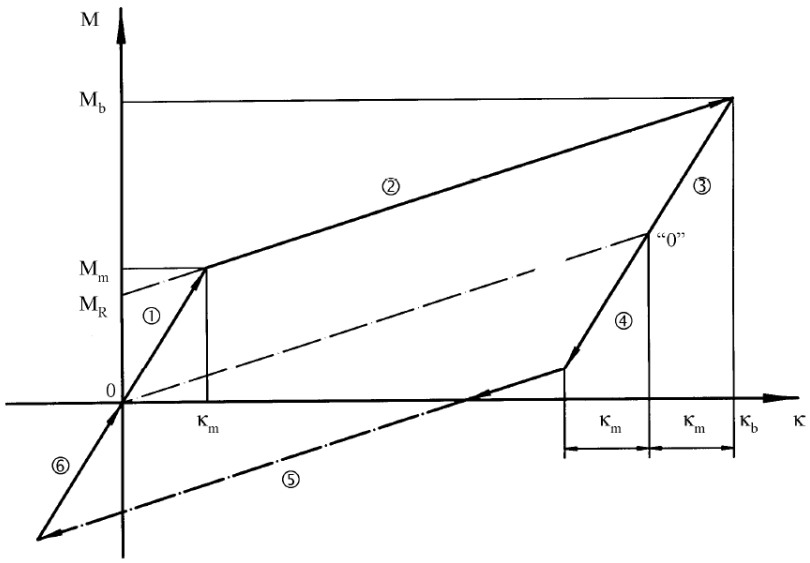

Figure 2.13: Moment-curvature diagram for a single layer strand in a loading-unloading cycle [111].

In the case of loading-unloading cycles, the behavior is hysteretic and it is represented in Figure 2.13. It is drawn in the hypothesis that no damage occurs among the contact surfaces of the wires. Branch 1 is characterized by perfect adhesion between the wires. At curvature k_m, wire slippage takes place and therefore in branch 2 the stiffness is reduced with respect to the initial one. In the unloading branches 3 and 4 there is again perfect adhesion between the wires. The point "0" can be seen as a new origin of the diagram. Branch 5 starts when the curvature computed form point "0" reaches the value k_m: the stiffness is the same of the one in branch 2 but wires slip in the opposite direction. Finally if the stress is again reversed the hysteresis loop closes with branch 6, whose slope is the initial one. It should be noted that it is possible to have a residual curvature with no bending moment.

2.3.3 Analytical Models - Torsion

Because of the helical pattern of the wires, when a wire rope is tensioned the wires can easily generate torque. In other words, wire ropes exhibit a tension-torsion coupling. The

mechanism is shown in Figure 2.14: the total tensile force is distributed equally to each wire, generating also a transverse force component whose magnitude depends on the lay angle α; these components are responsible of the generation of torque, given by

$$M_t = \sum_i^L N_i T_i \sin\alpha_i R_i \tag{2.59}$$

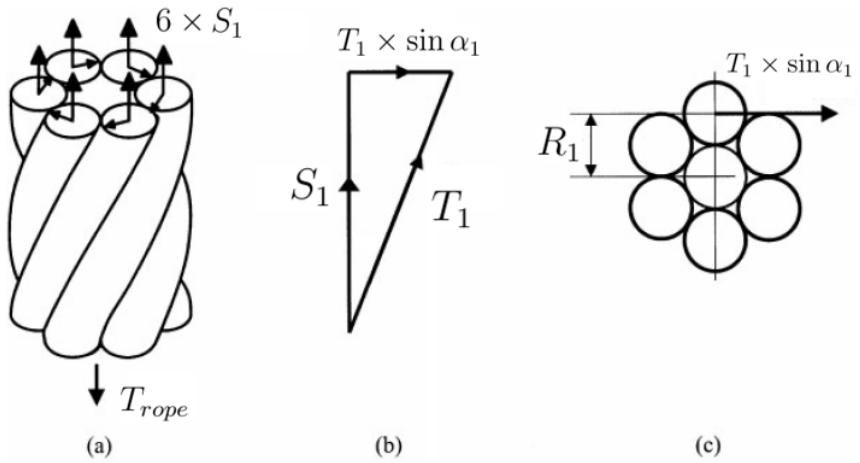

Figure 2.14: Torsional forces in a 6+1 wire rope structure under axial load [130].

In the literature, many procedures have been employed in order to quantify this coupling, which is assumed to be expressed linearly as follows:

$$\begin{bmatrix} T \\ M^t \end{bmatrix} = \begin{bmatrix} C_{11} & C_{12} \\ C_{21} & C_{22} \end{bmatrix} \begin{bmatrix} \varepsilon_c \\ \tau_c \end{bmatrix} \tag{2.60}$$

For instance, Lanteigne [85] obtain the coupling coefficient $C_{12} = C_{21}$ in accordance to what is shown in Figure 2.14. Therefore its expression is

$$C_{12} = C_{21} = \sum_i^L EA_i N_i R_i \sin\alpha_i \cos^2\alpha_i \tag{2.61}$$

2.3.4 Observations from experimental tests

Many experimental tests have been performed on steel wire ropes in order to assess their strength and resistance. The obtained results have also been used to assess the quality of analytical and numerical models.

In [154] Utting and Jones performed static axial tests in order to predict the behavior of 7-wire strand with different end restraints. The authors analyzed the local effects near terminations of steel wire ropes, which result in uneven loading between the wires and in a hysteretic behavior. In particular, they observed that whereas friction and wire flattening have very

little effect on estimates of the overall strand response, the axial deformation of individual wires can be significantly affected by the magnitude of friction and contact forces and the proximity of strand terminations.

In [125] tension-torsion static tests are conducted on spiral strands. The hysteretic torsional behavior is studied on a brand new rope and another one being on service for several years, highlighting differences among the two ropes. In [131] tension-torsion fatigue tests are performed on stranded ropes. In particular, an experimental test is designed in order to specifically analyze torsion induced when two mooring branches having different tension-torsion coupling are connected in series. At the connection the two branches rotate in order to match their torques and re-establish the equilibrium of the system. The magnitude of the rotation is a function of the rope constructions, the load and the relative lengths of the ropes [17].

In [78] bending fatigue tests on a curved support are performed. In offshore engineering, the situation is representative for the design of what occurs when a rope runs over a pulley and its characterization will not be tackled in this thesis.

In many works, for instance [58, 120, 122, 124, 89], free bending fatigue tests are conducted. The results obtained from these tests are very useful for the thesis project. The main outcome is that the first ruptures, which occur close to the rope termination, are not located at extreme fibers, where wire tension is higher, but they are located in correspondence of the neutral axis, where wire fretting is most important. Since fretting can be an important source of damage, these results highlight the need of building a model which predicts properly the friction and the relative movements between the wires.

In [20] the authors used strain gauges to measure the axial strain variation close to the termination of wire ropes subjected to bending. The importance of friction is here highlighted.

- When the friction coefficient is sufficiently high, they observed a negligible variation of the axial strain in correspondence of the neutral axis. The friction is sufficient for the rope to assume a Euler-Bernoulli kinematics, i.e. plane cross sections remain plane after bending.
- With low friction coefficient, the strain variations in the bending plane and at the neutral axis are comparable. The wires tend to slide in the zone close to the neutral axis, but the presence of the rope termination modifies the kinematics and hence the strain distribution.

Moreover, the authors observed that the first wire breakages can occur in the inner layers.

2.3.5 Numerical models in the literature

A lot of efforts have been produced by a considerable number of authors, in order to characterize the behavior of wire ropes by means of finite element models. Only some of them will be recalled here.

In [135] an eight degree-of-freedom curved beam element has been developed for the purpose of stress and slip analysis of flexible pipe armoring tendons.

In [111] a specific beam finite element is used in order to obtain the profile of the rope axis

when subjected to tension and bending.
In [78] the authors use Abaqus®/Explicit and model the wires of a multilayer spiral strand with linear brick elements (with reduced integration and hourglass control), in order to predict the three-dimensional stress state in the wires when the rope is bent over a rigid support. The same elements are used in [146] to simulate a pure tension test.
In [171] linear brick elements are used to determine the evolution of the bending stiffness of a single layer strand.
In [37] beam elements are used to model the fibers of a synthetic fiber rope bent over a rigid support. The beam elements are enriched to take into account the deformation of the cross section.
In [74] the authors used 3D elasto-plastic finite elements to model a multilayer spiral strand, implemented in the sofware LS-DYNA.

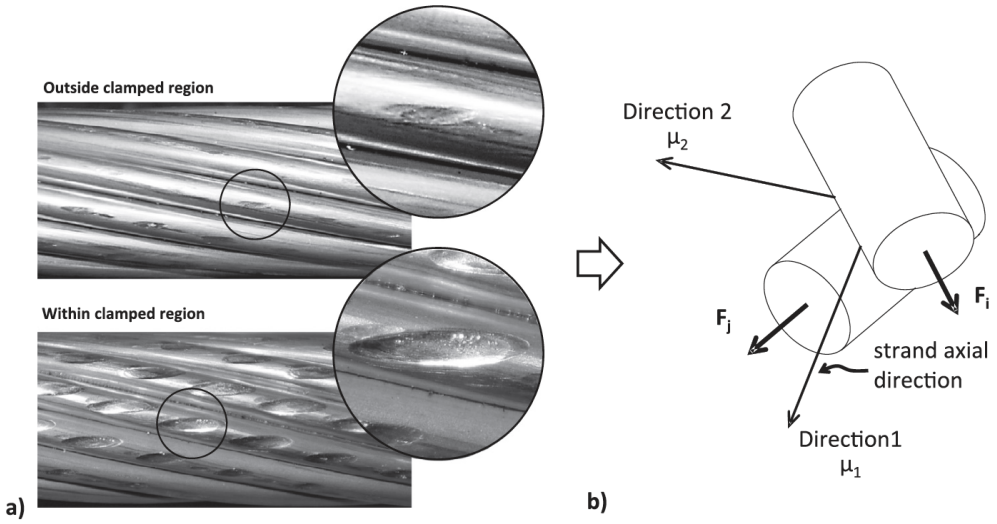

Figure 2.15: Indentation at interlayer contact positions between layers of a 19/54 ACSR Géant after being submitted to free-bending test and the interpretation with the anisotropic friction concept [84].

Recently in [84] the authors used the software ANSYS to model each wire of a multilayer electrical conductor with beam elements, managing the contact with the edge-to-edge contact elements implemented in the code. They used this model in [83] to compute the fatigue damage caused by wind-induced vibration (free bending fatigue) on an electrical conductor. The rope in this case is made by aluminum wires. Because of fretting, indentation at trellis contact position is observed (Fig. 2.15). To better model the phenomenon, the authors use an anisotropic friction law. However, no evidences of this phenomenon are reported for high strength steel wires.
Since in this thesis the goal is to compute the fatigue damage, the need is to evaluate the effects of a very high number of load cycles (see section 1.1. Therefore, it is fundamental to employ a numerical model which limit as much as possible the computational cost.

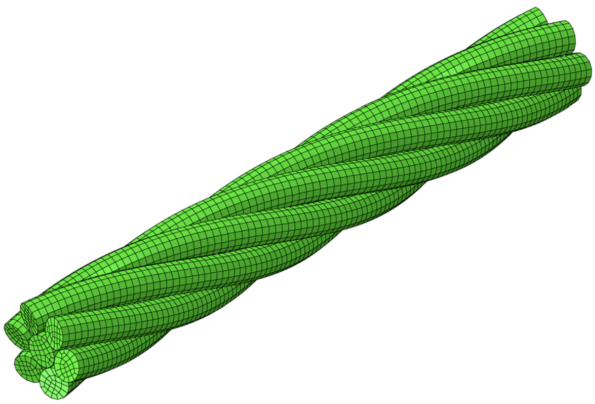

Figure 2.16: "Coarse" mesh used in [171] for the modeling of a 7-wire strand.

Consequently, it has been decided to model the wires behavior by means of beam elements. By looking at Figure 2.16, the use of 3D solid elements seems conversely not feasible in a reasonable computational time.

2.4 Interwire contact

The interwire contact phenomena in wire rope represent a key point in the understanding of their elastic, hysteretic and fatigue properties [60]. Gross sliding may occur at contact locations when the rope is bent, but even in a pure tension regime microslips take place [64]. The contact surfaces evolve during the fretting interaction and three phases can be distinguished [66].

1. During the first cycles, the formation of metal junctions causes the increase of the contact stresses, with consequent plastic deformations. This generates a metallurgic transformation of the surfaces.
2. Oxide debris with high hardness are formed between the surfaces. These particles accelerate the wear of the surfaces
3. A bed of small particles, the so-called third body, is created between the surfaces, which are flattened.

Clearly, the frictional properties change during the evolution of the contact surfaces. This effect will not be considered in the present work and could be an interesting perspective.

The contact area is a stress concentration zone and promotes crack nucleation. Consequently, the fatigue endurance with contact decreases by a factor of 2-5 with respect to the endurance limit determined by uniaxial tests [139]. Experimental observations (Fig. 2.17) confirm that crack initiation starts in correspondence of the interwire contact zone.

One can distinguish between two classes of interwire contact, which are shown in Figure 2.18.

A. *Line contact*: it is the contact within a given layer between adjacent wires and between the wires in the first layer and the central one. In terms of contact stress theory, this

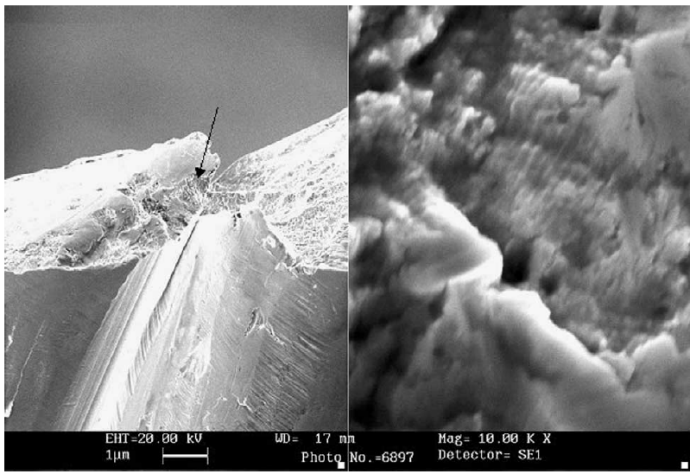

Figure 2.17: SEM images of crack initiation fatigue zone [49].

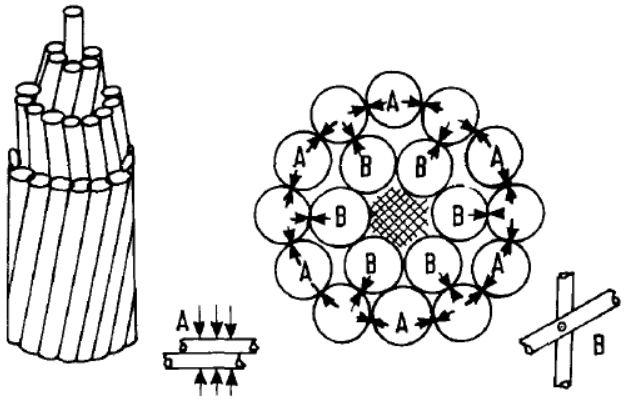

Figure 2.18: Interwire contacts in spiral strands: A- line contact within layers; B- trellis contact between layers [60].

class of contacts can be regarded as the line contact between parallel cylinders. It influences the overall axial, torsional and free bending stiffness. The contact area is rectangular.

B. *Trellis contact*: it occurs between the layers of a spiral strand, since wires belonging to adjacent layers cross at an oblique angle, producing a point rather than a line contact. Since it is localized, the contact stresses are much higher than on the line contacts within a layer. Trellis contacts play a central role in fatigue phenomena. The contact area in this case is elliptical.

The two contact types will be treated separately by means of Hertz and Mindlin theories. Namely, Hertz theory [56] relies on the following assumptions:

1. strains are small and within the elastic limit;
2. the surface are continuous (namely the body curvatures near the point of contact can be adequately represented by parabolas) and non-conforming, meaning that when the

bodies enter in contact at zero load they touch only at a point or along a line;
3. each body can be considered as an elastic half-space, i.e. their dimensions are much bigger with respect to the contact area;
4. the maximum diameter of the contact area is very small compared to the radii of curvature of the surfaces;
5. no friction.

We can then introduce friction in the analytical treatment if the materials in contact are "elastically similar", meaning

$$\frac{1-2\nu_1}{G_1} = \frac{1-2\nu_2}{G_2} \tag{2.62}$$

where ν and G are respectively the Poisson coefficient and the shear modulus. If the condition (2.62) is satisfied, the tangential contact problem can be decoupled from the normal contact problem [71].

The aim is to define the stress distribution which originates from the contact interaction among the two bodies, including friction. In particular, from the analytical stress distributions one notices that the most heavily loaded elements of material, and thus the site of initial plastic yielding and eventually crack initiation, lies not at the surface but a small distance beneath it. This confirms the experimental evidences showing that the fretting fatigue cracks initiate below the body surfaces.

2.4.1 Line contact

Line contact occurs between the central wire and the first layer and between wires in the same layer. By neglecting the contribution to the equilibrium in radial direction coming from contact between the adjacent wires (Fig 2.19), the line pressure central wire and the first layer is expressed by (2.34).

In the case of line contacts (Fig. 2.20), the contact patch will be of half-width [161]

$$b = \sqrt{\frac{2w\overline{r}}{\pi E^*}} \tag{2.63}$$

in which w is the load per unit length of the contact area, E^* is the contact modulus determined from

$$\frac{1}{E^*} = \frac{1-\nu_1^2}{E_1} + \frac{1-\nu_2^2}{E_2}$$

and $\overline{r}$ is the reduced radius of curvature is defined as

$$\frac{1}{\overline{r}} = \frac{1}{r_1} + \frac{1}{r_2}$$

with r_1 and r_2 the radii of the two cylinders.

The pressure distribution is

$$p(x) = p_0\sqrt{1-\frac{x^2}{b^2}} \tag{2.64}$$

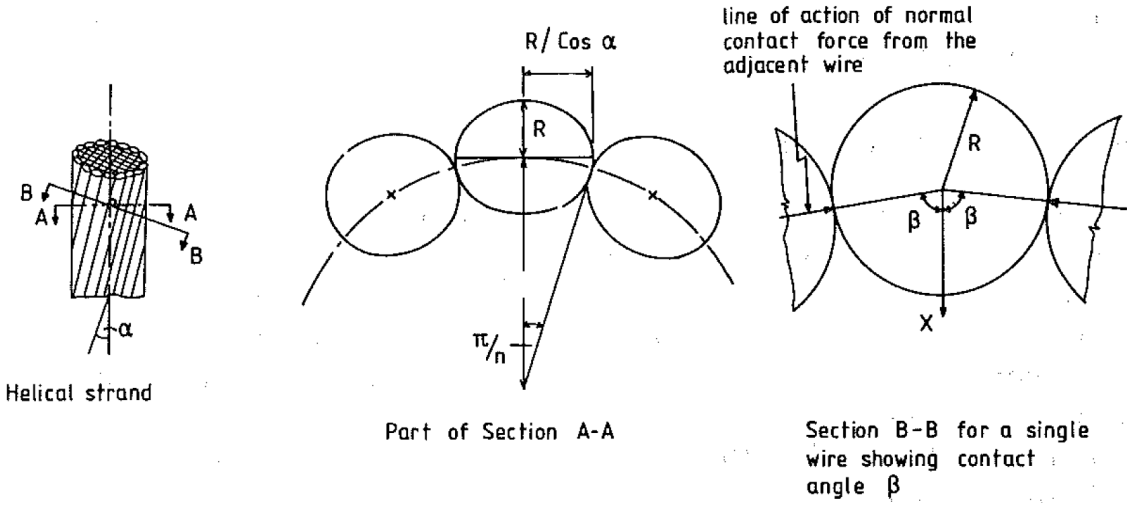

Figure 2.19: The normal contact force of adjacent wires have a nonzero component in radial direction [126].

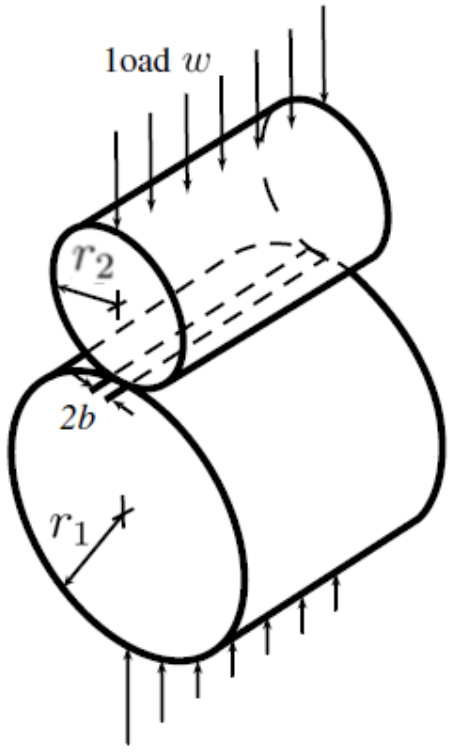

Figure 2.20: Parallel cylinders in contact [161].

where x is a coordinate measured in the direction perpendicular to the cylinder axes starting

from the center of the contact patch, while p_0 is the maximum pressure, given by

$$p_0 = \sqrt{\frac{wE^*}{\pi \overline{r}}} \tag{2.65}$$

The contact stress distribution which originates from line contact is given for instance in [8]. The tangential contact is included in the sliding case only, i.e. when $\tau(x) = \mu p(x)$, with μ the friction coefficient.

2.4.2 Trellis contact

The trellis contact geometry in a wire rope refers to cylinders with curved axis, with their axes inclined by an angle α (Fig. 2.21)). One assumes that the profile of each body closer to the origin of the contact position can be expressed as [161]

$$\begin{cases} z_1 = \dfrac{x_1^2}{2R_1'} + \dfrac{y_1^2}{2R_1''} \\ z_2 = \dfrac{x_1^2}{2R_2'} + \dfrac{y_1^2}{2R_2''} \end{cases}$$

The directions of the axes of each body are chosen to coincide with the principal curvatures. In particular, in our case R_i' and R_i'' denote respectively the minimum and maximum radius of curvature of body i. For a curved cylinder, the minimum radius of curvature is the cylindrical radius, while the maximum is the radius of curvature of the axis, which for a helix around a straight axis is obtained from (2.9). Negative values are taken for concave surfaces.
The contact area is elliptical (Fig. 2.22), whose dimensions can be computed assuming Hertzian contact [56, 71]. The major semi-axis a can be obtained from [151]

$$a = \left(\frac{3\mathcal{E}(e)P}{(A_{cp} + B_{cp})\, 2\pi E^* (1 - e^2)} \right) \tag{2.66}$$

in which

- $\mathcal{E}(e)$ is the elliptical integral of the second kind of argument $e = 1 - \left(\dfrac{b}{a}\right)^2$;
- $\dfrac{1}{E^*} = \dfrac{1-\nu_1^2}{E_1} + \dfrac{1-\nu_2^2}{E_2}$ with E_i and μ_i the Young modulus and the Poisson ratio of body i;
- A_{cp} and B_{cp} are curvature parameters, obtained as

$$A_{cp} = \frac{1}{2}(U - V) \quad B_{cp} = \frac{1}{2}(U + V) \tag{2.67}$$

with

$$U = \frac{1}{2}\left(\frac{1}{R_1'} + \frac{1}{R_1''} + \frac{1}{R_2'} + \frac{1}{R_2''} \right)$$

$$V = \frac{1}{2}\sqrt{\left(\frac{1}{R_1'} - \frac{1}{R_1''} \right)^2 + \left(\frac{1}{R_2'} - \frac{1}{R_2''} \right)^2 + 2\left(\frac{1}{R_1'} - \frac{1}{R_1''} \right)\left(\frac{1}{R_2'} - \frac{1}{R_2''} \right)\cos(2\alpha)}$$

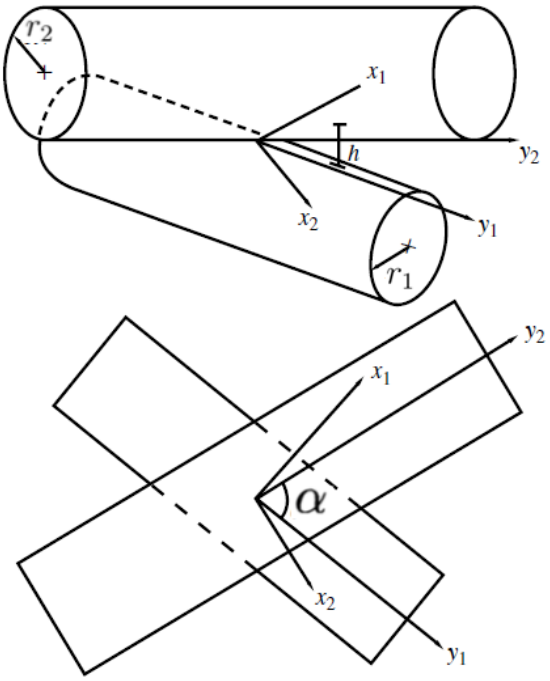

Figure 2.21: Inclined cylinders in elastic contact [161].

For moderately elliptical contact, meaning $\frac{A_{cp}}{B_{cp}} \leq 5$, the ellipticity can be approximated as [50]

$$\frac{b}{a} \approx \left(\frac{A_{cp}}{B_{cp}}\right)^{2/3}$$

As one can see, the points at the same distance are located along ellipses. Assuming that points coming into contact are points on the two surfaces that originally were equally distant from the tangent plane, one deduces that the obtained contact surface has an elliptical shape. When a load is applied, the point of contact spreads therefore into this area (Fig. 2.22), whose eccentricity, i.e. the ratio between its axes, depends on the ratio between the principal radii of relative curvature. The elliptical shape of the contact area has been observed experimentally in [139].
The angle γ formed by the ellipse minor axis and the direction x_1 in Figure 2.21 can be obtained considering the cylinders as straight, by solving [161]

$$\frac{r_2}{r_1}\sin(2\gamma) = \sin[2(\alpha - \gamma)] \tag{2.68}$$

After simple algebra one obtains

$$\gamma = \frac{1}{2}\tan^{-1}\left(\frac{\sin(2\alpha)}{\frac{r_2}{r_1} + \cos(2\alpha)}\right) \tag{2.69}$$

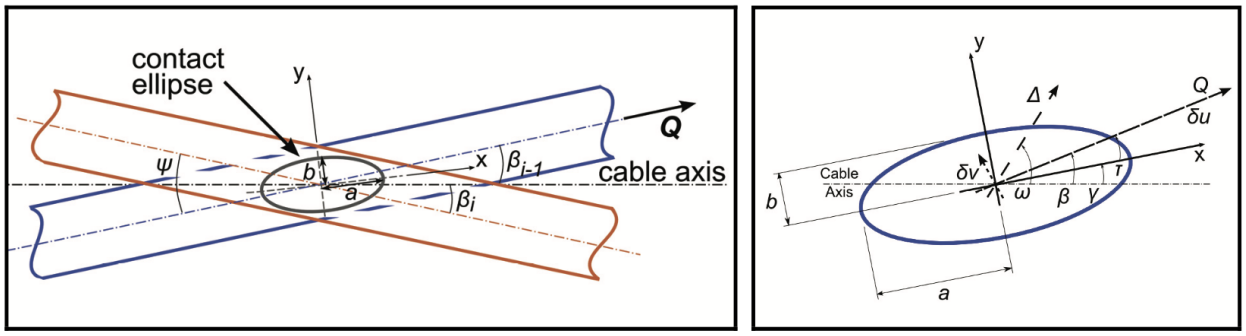

Figure 2.22: Contact ellipse geometry [112].

Normal contact

Considering the xy plane in Figure 2.22, the hertzian pressure distribution is

$$p(x,y) = p_0\sqrt{1-\frac{x^2}{a^2}-\frac{y^2}{b^2}} \tag{2.70}$$

The maximum pressure p_0 is given by

$$p_0 = \frac{3P}{\pi ab} \tag{2.71}$$

with P the value of the normal contact force.

Tangential contact

The expressions of the stresses linked to tangential contact depend on the slip conditions between the two bodies in contact. When gross slip occurs, the tangential stress τ_c on the contact surface is expected to be proportional to the value of the normal pressure (2.70):

$$\tau_c^{slip} = q_0\sqrt{1-\left(\frac{x}{a}\right)^2-\left(\frac{y}{b}\right)^2} \tag{2.72}$$

where $q_0 = \mu p_0$.
When the total tangential force is not sufficient to cause gross slip, the situation is more complicated. The problem was first studied when the two bodies are essentially at rest by Cattaneo [14]. In this case there is a central region, which in absence of rolling is homothetic with the contact patch, where slip does not occur, while in the surrounding region microslips take place.
In the microslip region, the tangential stresses on the surface are given by (2.72), whilst in the no-slip zone one has to add a reverse stress distribution:

$$\tau_c^{stick} = \tau_c^{slip} - \left(1-\frac{Q}{\mu P}\right)^{1/3} q_0\sqrt{1-\left(\frac{x}{a'}\right)^2-\left(\frac{y}{b'}\right)^2} \tag{2.73}$$

where P and Q are normal and tangential load respectively and

$$\frac{a'}{a} = \frac{b'}{b} = 1 - \frac{P}{Q}$$

The problem of rolling contact has been first studied in [69] and [92]. In this case the stick zone is no more homothetic with the contact patch and a considerable amount of additional calculations is necessary. Moreover, superposition may be used to represent the stick area, but since its shape differs from an ellipse the final solution will be inexact. [157] presents the result for the general case of elliptic contact patch.

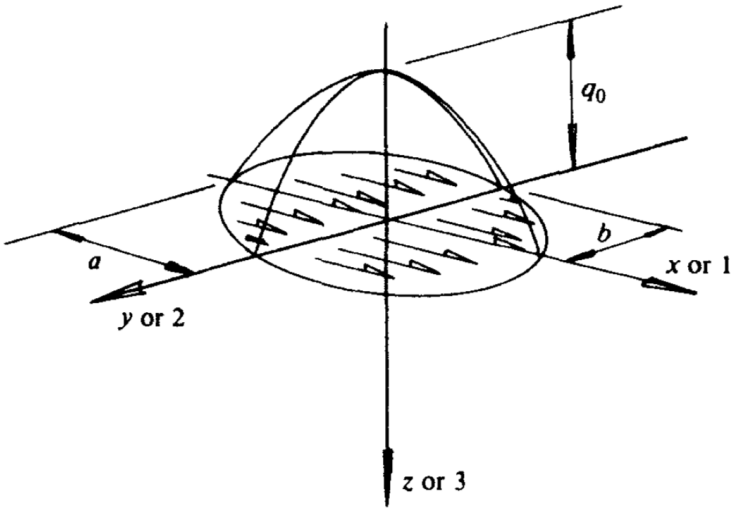

Figure 2.23: Orientation of tangential contact stresses [134].

In the absence of rolling, considering that shearing takes place in x direction (Fig. 2.23) the stress resultants are given in [134].

2.4.3 Validity of elastic contact

The analytical solutions for contact are obtained in the hypothesis of isotropic elastic material behavior. However, in the presence of high contact stresses the materials may in general exhibit plastic deformations. In this case, the contact area and the surface stress distribution changes with respect to the analytical prediction. Kapoor [75] and Johnson [70] suggest an increase of contact area if the residual stresses are not sufficient for attaining the elastic shakedown regime.

The increase in the contact area has been observed by Siegert [139], who carried out tension-bending tests on wire rope samples. This increase concerns mostly the line contact between the first wire layer and the central wire and the trellis contact positions where relative displacements are larger.

In [96] fretting wear is analyzed numerically. The results show that initially the contact stresses are very close to the ones predicted by Hertz's theory. Conversely with the onset of wear, the contact area increases and the peak contact pressure decreases dramatically to about 40% of the initial peak Hertzian value.

In general, we can therefore state that the hertzian solution loses progressively its validity with the onset of wear, which causes an increase on the contact area and a consequent reduction of the contact stresses. Therefore, it should be pointed out that the hertzian approximation is conservative.

2.5 Conclusion

The main features regarding spiral strand wire ropes, used for permanent mooring applications, have been presented in this chapter.

Some key elements concerning the helix kinematics have been given. In particular, the introduction of the reference cylinder concept (Sec. 2.2.2) will be useful for analyzing the performance of the numerical models in Chapters 6-8.

The main results from the literature concerning spiral strand have been reported in Section 2.3, with particular emphasis on tension and bending loading, on which we will focus our attention in Part II. The key-point is that the mechanical behavior of wire ropes is strongly related to the helical shape of the wires and to the inter-wire contact interactions. The results of this part will be extensively used in Chapters 5, 6 and 8.

The analytical models for the description of wire contacts have been detailed in Section 2.4, both considering line and trellis contacts. The limitations of these analytical models have been also pointed out.

Chapter 3

Fatigue

In essence the process of fatigue in metals involves crack propagation from some stress concentrating defect, by mechanisms which involve local plasticity at the crack tip under the influence of a fluctuating load. The result is that structural parts subjected to fluctuating loads may fail under a nominal stress much weaker than that necessary to cause fracture in a single application.
An enormous amount of papers is related to the study of fatigue. An extensive historical analysis is performed for instance in [137].

3.1 Asymptotic behavior

Considering an elastoplastic material with isotropic hardening subjected to cyclic loading, one can distinguish between three types of asymptotic behavior, represented in Figure 3.1.

1. *Elastic shakedown*: the material can experience some plastic strains in the first loading cycles, but the asymptotic behavior is elastic. High-cycle fatigue may occur.
2. *Plastic shakedown*: in its asymptotic behavior the material goes through a closed plastic strain loop. Low-cycle fatigue may occur.
3. *Ratchetting*: plastic strains continue to sum up, leading to a failure in few load cycles.

The static shakedown theorems [97, 81, 93] yield sufficient conditions for elastic shakedown. However, these conditions requires to look for a residual stress field $\underline{\underline{\rho}}^*$ that satisfies the global equilibrium with null applied forces. In practice, it is easier to verify if a "local" condition is satisfied. Let us express a plasticity criterion as

$$g(\underline{\underline{\sigma}} - C\underline{\underline{\varepsilon}}^P) - k^2(\alpha) \leq 0 \tag{3.1}$$

with $\underline{\underline{\sigma}}$ the stress tensor, C the hardening modulus, $\underline{\underline{\varepsilon}}^P$ the plastic strain tensor, α a hardening variable and k the elastic limit. A local condition for elastic shakedown consists in the following requirements:

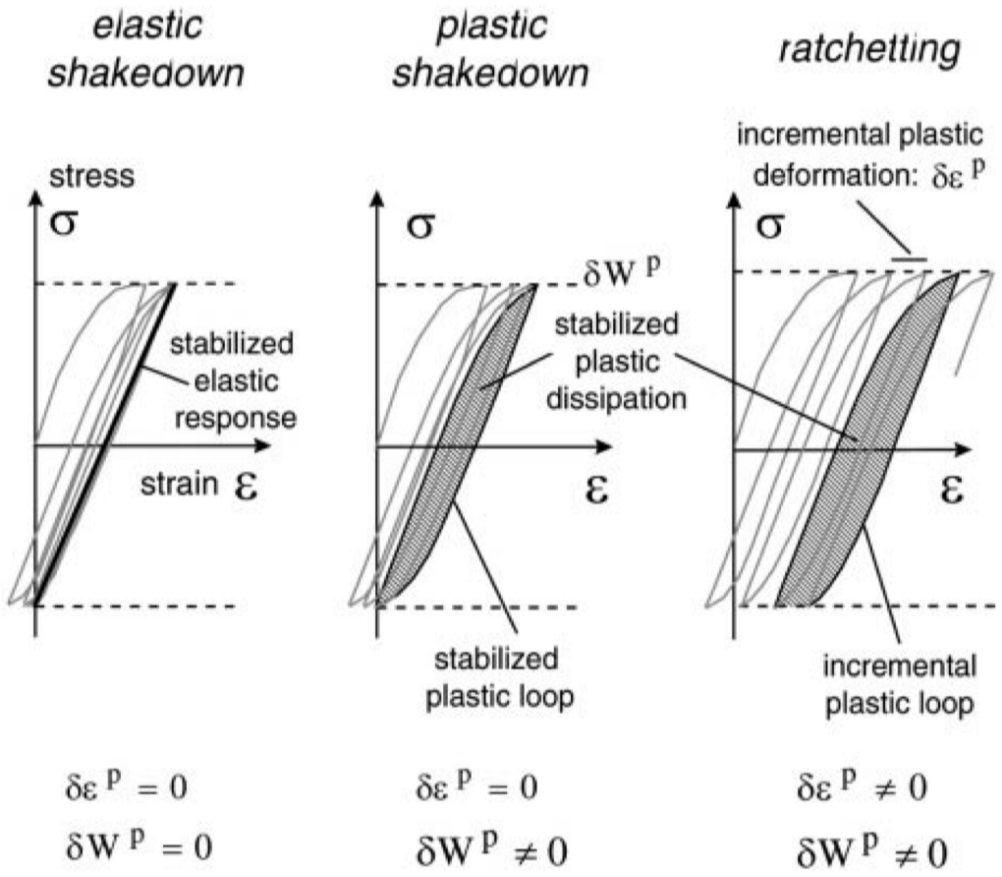

Figure 3.1: Possible asymptotic behavior of a material subjected to cyclic loading [164]. ε^P and W^P represent respectively the plastic strain and the energy dissipated by plasticity.

(a) there exists a steady stress field $\underline{\underline{\sigma}}^*$ such that

$$g(\underline{\underline{\sigma}}^{el}(M,t) - \underline{\underline{\sigma}}^*(M)) < k^2(\alpha_s) \quad \forall M, t > T \tag{3.2}$$

with M a point inside the material, t the time variable, $\underline{\underline{\sigma}}^{el}$ the elastic stress field and α_s the biggest value reached by α and compatible with the small deformation hypothesis;

(b) the difference between the stress field $\underline{\underline{\sigma}}^*$ and a self-balanced stress field $\underline{\underline{\rho}}^*$ is a field of the order of $C\alpha_s$;

(c) $\underline{\underline{\underline{\underline{M}}}} : (\underline{\underline{\rho}}^* - \underline{\underline{\rho}}_0)$ is small, with $\underline{\underline{\underline{\underline{M}}}}$ the elastic compliance matrix and $\underline{\underline{\rho}}_0$ an initial residual stress field.

3.2 Uniaxial fatigue

The first studies on fatigue dealt with uniaxial fatigue, i.e. cases in which the stress state can be expressed by a single number, that can be a tensile or a compression stress. The

first uniaxial fatigue law was formulated by O. H. Basquin [5] using Wöhler's stress data in [163]. Basquin proposed a bi-logarithmic relationship between the stress amplitude S and the number of cycles to failure N. These curves are known as Wöhler or S-N curves, which are expressed as

$$N(S) = S^{-m}K \tag{3.3}$$

where $N(S)$ is the number of cycles with zero mean and amplitude S leading to failure, while m and K are material parameters to be determined by linear regression from experimental data. The Goodman line, the Gerber parabola or the Soderberg line (Fig. 3.2) allow to take into account the effect of non-zero mean stress by determining an effective alternating stress.

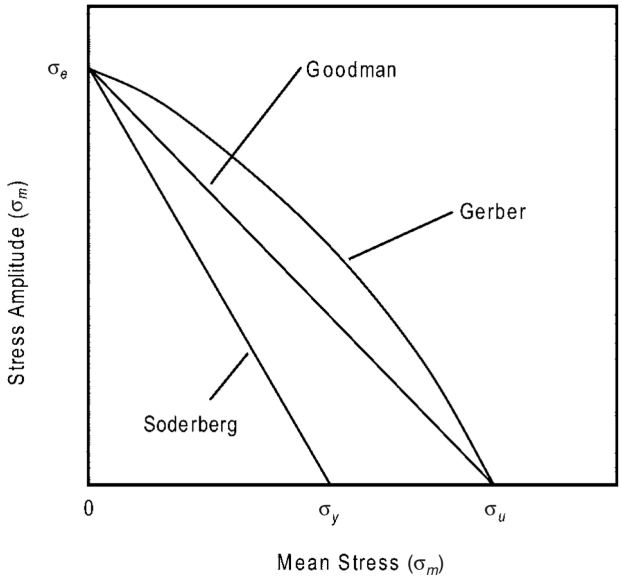

Figure 3.2: Comparison of Goodman, Gerber, and Soderberg models, relating the mean stress to an equivalent stress amplitude [117].

The Palmgren-Miner law, or linear damage hypothesis, states that when there are different stress magnitudes k in a spectrum, the total damage is given by

$$d = \sum_k \frac{n(S_k)}{N(s_k)} \tag{3.4}$$

where n and N are respectively the number of cycles in the spectrum and the number of cycles to failure. This approach, which is largely used in the industry, neglects the influence of the load sequence on the damage evolution.

When the load cycles are irregular, the rainflow algorithm can be used to switch from a stochastic irregular tension process obtained from the analyses to a number of equivalent stress cycles.

However, because of the contact interactions between the wires, a fatigue criterion based on cyclic tension tests on steel wires is not suitable for wire ropes.

3.3 Multiaxial and fretting fatigue

Most of the time, structural parts in real applications experience multiaxial stress states. In particular cases very localized surface stresses (e.g. in fretting) are linked with the initial stages of fatigue crack propagation.

Some criteria for multiaxial fatigue do not allow for a quantitative estimation of the fatigue damage, but allow to distinguish among the load paths the ones that produce or do not produce damage. In other words, they define in the space of stresses an endurance domain such that if the loading stays inside this domain, the material would not experience fatigue. It has to be noted that such approaches are therefore particularly conservative.

In the attempt of formulating a criterion for multiaxial fatigue, many studies focused on the propagation phase of a fatigue crack, which occurs in a shear plane. Consequently, these criteria are formulated in terms of shear and normal stresses associated to the choice of a maximum shear plane.

Fretting fatigue can be considered as a particular type of multiaxial fatigue. It is defined as the surface damage induced by small-amplitude oscillatory displacements between metal components in contact. This damage can either be wear or crack nucleation, depending on the prescribed forces or the displacements amplitude. Fretting fatigue mechanisms have gradually been identified with help of fracture mechanics approaches [148, 149], showing that the frictional forces on the contact surface play the dominant role both in crack initiation and propagation stages [102].

Many research works focused on the fretting issue, both from an experimental [139] and numerical [129] point of view. Experimentally, one may distinguish three regimes of fretting-fatigue, according to the amount of relative displacement experienced by the surfaces in contact (Fig. 3.3):

1. if the surfaces are always in stick state, no damage occurs (neither cracks nor wear);
2. in mixed stick-slip conditions, cracking can occur after a sufficient number of cycles;
3. in the case of gross slip, damage occurs in terms of wear, with the formation of debris on the surfaces.

The results obtained by Siegert [139] in fretting tests of steel wires confirm that fatigue cracks develop at small sliding regimes (Fig. 3.4).

In [159] and [158] the authors established a test methodology based on fretting maps (Fig. 3.5). These maps give the material response fretting map, in terms of no damage, crack nucleation or wear, according to the running condition, i.e. the slip regime. These results are very useful for a qualitative understanding of damage phenomena, but they cannot be exploited for other fretting problems [26].

In [139, 170, 160, 18] experimental tests are run on steel wires, in order to characterize wear and fretting. In [114] the influence of the aqueous environment on wear is analyzed.

In [26] is pointed out the high computational cost of fretting fatigue simulations. The direct cyclic method is proposed, which is based on the large time incremental method and on research of the solution in the space of periodic responses. The algorithm looks for mechanical fields which are cyclic, i.e. which have the same value at the end and at the beginning of the

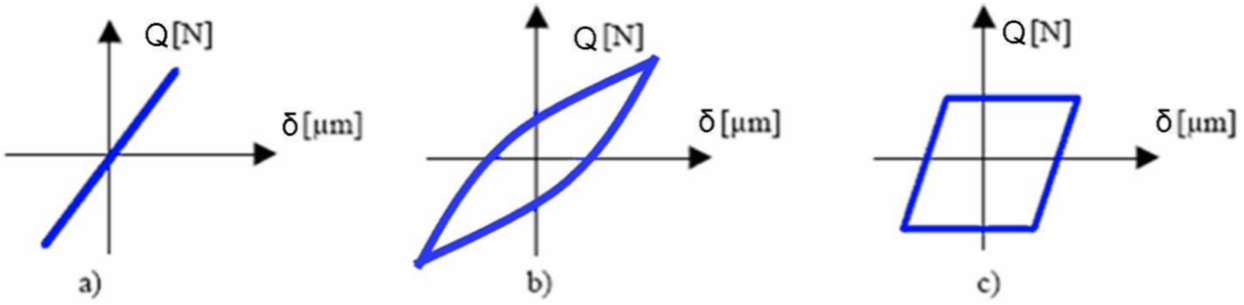

Figure 3.3: Hysteretic behavior in the tangential force (Q) - slip (δ) diagram for fretting cycles in three different regimes: a) elastic slip, b) partial slip and c) gross slip [98].

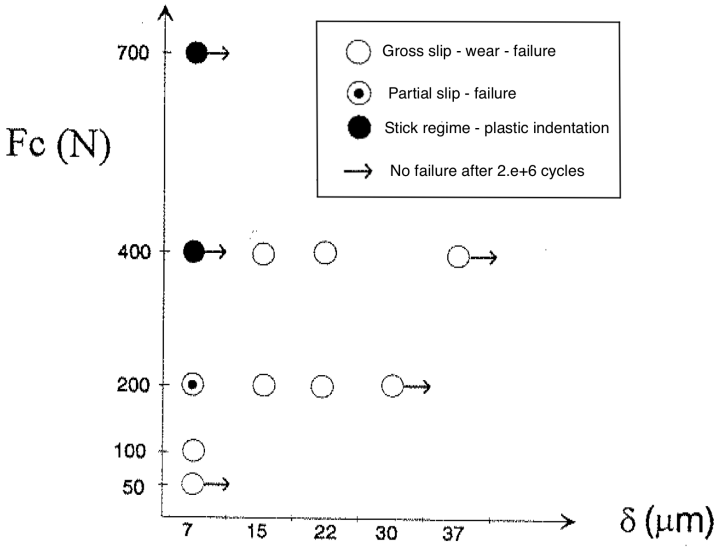

Figure 3.4: Results from fretting tests on steel wires (from [139]), in which δ represents the amplitude of the tangential displacement and F_C is the normal contact force.

loading cycle.

Since cracks propagate in mixed-mode conditions, their path are complex and also dependent on the material microstructure, namely because of the presence of grain boundaries. By considering the approach proposed by Siegert [139], one can estimate a crack critical crack length by looking where a multiaxial fatigue criterion (in this case the one of Dang Van, see Sec. 3.3.2) predicts the fatigue crack initiation. Then, the Extended Finite Element Method (X-FEM) allows to simulate the fatigue crack propagation [138, 40]. In [3], the X-FEM predictions of fretting fatigue crack growths are successfully compared to experimental results.

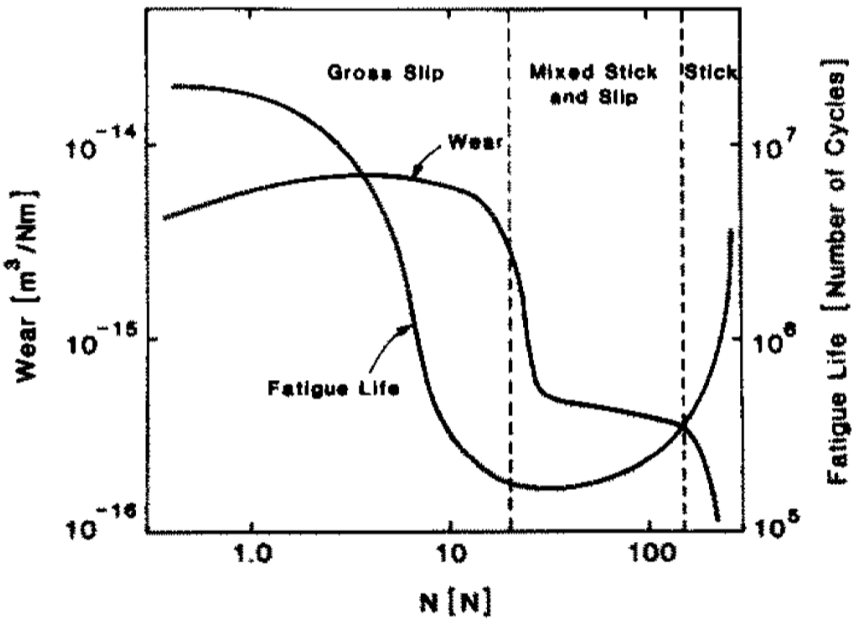

Figure 3.5: Fretting maps showing the variation in fretting fatigue life and fretting wear rate with applied normal force N for a constant displacement amplitude [159].

3.3.1 Sines and Crossland criteria

The criteria by Sines [143] and Crossland [22] identify conditions for unlimited endurance, i.e. they identify the endurance domain, and they can be easily implemented. The Sines criterion is expressed as

$$\mathcal{I}_a + a\mathcal{P}_m \leq b \tag{3.5}$$

where

- $$\mathcal{I}_a = \frac{1}{2\sqrt{2}} \max_{t_1} \left\{ \max_{t_2} \sqrt{[\underline{\underline{s}}(t_2) - \underline{\underline{s}}(t_1)] : [\underline{\underline{s}}(t_2) - \underline{\underline{s}}(t_1)]} \right\}$$
  with $\underline{\underline{s}}$ the deviatoric part of the stress tensor;
- $$\mathcal{P}_m = \frac{1}{2} \left[\max_t \mathcal{P}(t) + \min_t \mathcal{P}(t) \right]$$
  with $\mathcal{P}$ the hydrostatic part of the stress tensor;
- a and b are material parameters linked to the endurance limits f and t obtained respectively from repeated bending and alternate torsion tests.

The Crossland criterion is very similar to the previous one, since it reads

$$\mathcal{I}_a + a\mathcal{P}_{max} \leq b \tag{3.6}$$

where $\mathcal{P}_{max}$ is the maximum value of hydrostatic pressure attained during the load cycle. The parameters a and b are obtained from alternate bending and alternate torsion tests.

3.3.2 Dang Van criterion

The criteria presented so far rely on macroscopic quantities. In materials composed by grains distributed inside a matrix, experimental observations actually show that the fatigue crack propagation involves mechanisms that start at the mesoscopic scale, with the comparison of slip bands close to the most unfavorably oriented grains. For this reason, the criterion proposed by Dang Van [25, 23, 24] involves the passage from macroscopic to mesoscopic scales.

A representative elementary volume (REV) has first to be identified, in such a way that statistically all the sizes, shapes and orientations of the grains are represented. In general, the relationship which relies the macroscopic stress field at a point M, at the REV level, to a point m, inside the REV, can be expressed as

$$\underline{\underline{\sigma}}(m,t) = \underline{\underline{\underline{\underline{A}}}}(M,m)\underline{\underline{\Sigma}}(M,t) + \underline{\underline{\rho}}(m,t) \tag{3.7}$$

with $\underline{\underline{\sigma}}$ and $\underline{\underline{\Sigma}}$ respectively the mesoscopic and macroscopic stress fields, $\underline{\underline{\underline{\underline{A}}}}$ is the so-called localization tensor and $\underline{\underline{\rho}}$ is the mesoscopic residual stress field.

By assuming that the grains and the matrix share the same elastic isotropic behavior, (3.7) can be simplified as

$$\underline{\underline{\sigma}}(m,t) = \underline{\underline{\Sigma}}(M,t) + \underline{\underline{\rho}}(m,t) \tag{3.8}$$

where $\underline{\underline{\rho}} = -2\mu\underline{\underline{\varepsilon}}^P$. It is considered that elastic shakedown happens before crack initiation. This is expressed as

$$\underline{\underline{\sigma}}(t) = \underline{\underline{\Sigma}}(t) + \underline{\underline{\rho}}^* \tag{3.9}$$

with $\underline{\underline{\rho}}^*$ the mesoscopic residual stress field in the elastic shakedown phase, independent on time.

The calculation of $\underline{\underline{\sigma}}$ is done by computing separately its hydrostatic and deviatoric components. The hydrostatic pressure can be easily determined as

$$p(t) = \frac{1}{3}tr(\underline{\underline{\sigma}}(t)) = \frac{1}{3}tr(\underline{\underline{\Sigma}}(t)) = \mathcal{P}(t) \tag{3.10}$$

For the deviatoric part $dev(\underline{\underline{\sigma}})$, the residual mesoscopic stress state $\underline{\underline{\rho}}^*$ has to be evaluated. We have that according to the Mises plasticity function

$$\begin{array}{rcl} f(\underline{\underline{\sigma}}, C\underline{\underline{\varepsilon}}^P) & = & \sqrt{\frac{1}{2}[dev(\underline{\underline{\sigma}}) - C\underline{\underline{\varepsilon}}^P] : [dev(\underline{\underline{\sigma}}) - C\underline{\underline{\varepsilon}}^P]} - k(\alpha) \\ & = & \frac{1}{\sqrt{2}}\|dev(\underline{\underline{\sigma}}) - C\underline{\underline{\varepsilon}}^P\| - k(\alpha) \end{array} \tag{3.11}$$

there is adaptation if, at any point M,

$$\inf_{\underline{\underline{\sigma}}^1} \sup_t \frac{1}{\sqrt{2}}\|dev(\underline{\underline{\Sigma}}^{el}(M,t) - dev(\underline{\underline{\sigma}}_1))\| < k(\alpha) \tag{3.12}$$

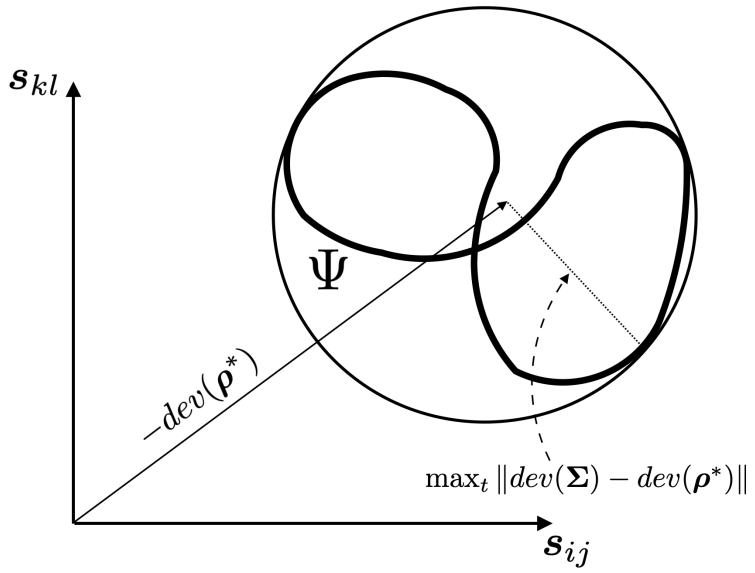

Figure 3.6: Smallest hypersphere circumscribing the load path Ψ.

and therefore we have that $dev(\underline{\underline{\rho}}^*)$ is the tensor $\underline{\underline{\sigma}}_1$ such that

$$\inf_{\underline{\underline{\sigma}}_1} \sup_t \|dev\left(\underline{\underline{\Sigma}}^{el}(M,t)\right) - dev(\underline{\underline{\sigma}}_1)\| \tag{3.13}$$

Geometrically, $dev(\underline{\underline{\rho}}^*)$ is the opposed of the center of the smallest hypersphere that circumscribe the elastic stress path in the space of the macroscopic stress deviators (Fig. 3.6). Once $\underline{\underline{\rho}}^*$ is determined, thanks to (3.9) the mesoscopic stress field $\underline{\underline{\sigma}}$ is computed.
From the stress tensor one can compute the stress vector on an inclined facet of normal $\underline{n}$

$$\underline{\sigma}(\underline{n},t) = \underline{\underline{\sigma}}(t)\underline{n} \tag{3.14}$$

and the normal and shear stress components

$$\sigma_n(\underline{n},t) = \underline{\sigma}(t) \cdot \underline{n} \tag{3.15}$$

$$\tau(\underline{n},t) = \sqrt{\|\underline{\sigma}\|^2 - [\sigma_n(\underline{n},t)]^2} \tag{3.16}$$

Finally, the Dang Van criterion yields the condition for unlimited endurance

$$\max_{\underline{n}}\{\max_t \tau(\underline{n},t) + a\mathcal{P}(t)\} \leq b \tag{3.17}$$

We can avoid the maximization with respect to the plane orientation given by $\underline{n}$ by assuming that the maximum mesoscopic shear stress is given by the greatest difference of the principal values of the mesoscopic stress deviator. Thus the condition (3.17) reads

$$\max_t\{\tau(t) + a\mathcal{P}(t)\} \leq b \tag{3.18}$$

The two constant a and b are material parameters, that identifies the line $\tau + a\mathcal{P} = b$ which defines the endurance domain (Fig. 3.7).

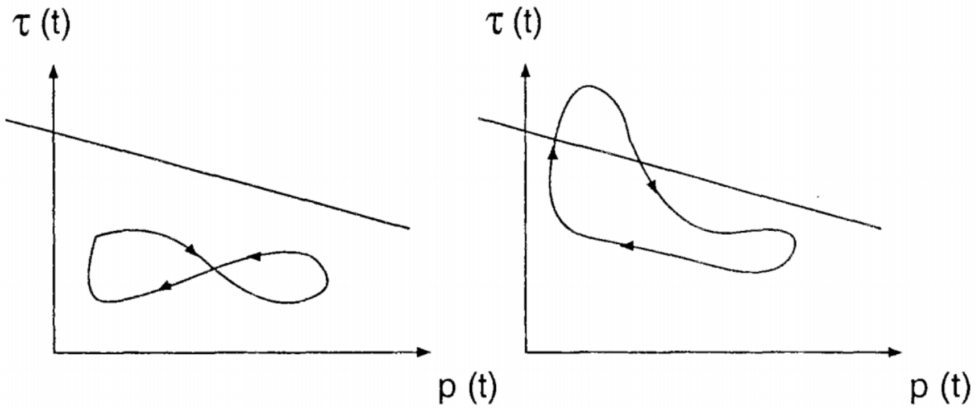

Figure 3.7: Loading paths represented on Dang Van diagrams. On the left, the loading is inside the endurance domain; on the right, a part of the load path is above the endurance domain and therefore it would generate fatigue cracks in a sufficient number of cycles [94].

3.3.3 Smith-Watson-Topper (SWT) criterion

This criterion has been applied satisfactorily by many researchers for the prediction of crack nucleation life and location in fretting fatigue loading conditions [150, 2].
The formulation of the SWT criterion starts from Basquin's equation for high-cycle fatigue and the Coffin-Manson's equation for low-cycle fatigue, which are respectively

$$\left(\frac{\Delta\varepsilon_e}{2}\right) = \frac{\sigma'_f}{E}(2N_f)^b \tag{3.19}$$

$$\left(\frac{\Delta\varepsilon_p}{2}\right) = \varepsilon'_f(2N_f)^c \tag{3.20}$$

in which σ'_f and b are respectively the fatigue strength coefficient and exponent, ε'_f and c are respectively the fatigue ductility coefficient and exponent, $2N_f$ is the number of reversals to failure (two per load cycle) and E is the Young Modulus. The parameters σ'_f, b, ε'_f and c are known as strain-life constants and are determined from uniaxial fatigue tests.
The total strain can then be related to life through the following strain-life equation which is simply the summation of (3.19) and (3.20):

$$\frac{\Delta\varepsilon_{tot}}{2} = \frac{\sigma'_f}{E}(2N_f)^b + \varepsilon'_f(2N_f)^c \tag{3.21}$$

However, this equation does not consider the effects of mean stress or strain on fatigue life. Thus, Smith et al. [145] used Basquin's formulation for the maximum stress and multiplied it by (3.21) to obtain the SWT parameter, $\sigma_{max}\Delta\varepsilon_a$:

$$SWT = \sigma_{max}\frac{\Delta\varepsilon_{tot}}{2} = \frac{(\sigma'_f)^2}{E}(2N_f)^{2b} + \sigma'_f\varepsilon'_f(2N_f)^{b+c} \tag{3.22}$$

The SWT parameter thus considers both elastic (HCF) and plastic (LCF) strain components and takes into account the effects of the mean stress.
Basically one has to find the global maximum SWT parameter, calculating the stress and strain fields for the complete loading cycle at each different location in the component. It is therefore assumed that crack nucleation occurs on the plane where the combination of the range of strain normal to the plane and maximum stress normal to the plane is most damaging. Then (3.22) is used to correlate the parameter to the life of the component. With an irregular load cycle, one can sum up the single contributions by using the Palmgren-Miner law.

3.3.4 Fatemi-Socie (FS) criterion

For situations where the cracks grow on planes of high shear strain, Fatemi and Socie [41] suggested the fatigue parameter

$$FS = \frac{\Delta\gamma}{2}\left(1 + \alpha\frac{\sigma_{max}}{\sigma_y}\right) \tag{3.23}$$

where $\Delta\gamma$ is the difference between maximum and minimum values of shear strain experienced during the cycle, σ_{max} is the maximum value of the stress normal to the chosen plane, σ_y is the yield strength, and α is a constant which approaches unity at long lives and is reduced at shorter lives. The ratio $\frac{\sigma_y}{\alpha}$ is often very close to the value of σ'_f.
Then an empirical equation fitted to the results of simple fully-reversed tests (this time under pure shear) can be used to correlate the FS fatigue parameter with life, yielding:

$$\frac{\Delta\gamma}{2}\left(1 + \alpha\frac{\sigma_{max}}{\sigma_y}\right) = \frac{\tau'_f}{G}(2N_f)^b + \gamma'_f(2N_f)^c \tag{3.24}$$

where G is the shear modulus and τ'_f, γ'_f, b and c are material constants.

3.4 Fatigue of wire ropes

In a mooring system, tension fluctuations induced by the movements of the floating structure are the dominant source of fatigue stresses.
In a wire rope, due to the loose coupling between wires, complete failure of the rope requires that many wires are broken in fairly close proximity. The fatigue of a single wire in the rope is invariably more than a simple matter of fluctuating stress in the direction parallel to the wire axis. There is usually some other process which exacerbates and accelerates the fatigue, and which localizes at specific locations. This process might be fretting between wires, or be linked to another degradation mechanism such as wear or corrosion. A study on the influence of the environmental condition on the life of wire ropes is reported in [115], where the mutual influence between corrosion and fretting fatigue is highlighted.

3.4.1 Fatigue loading in the mooring system

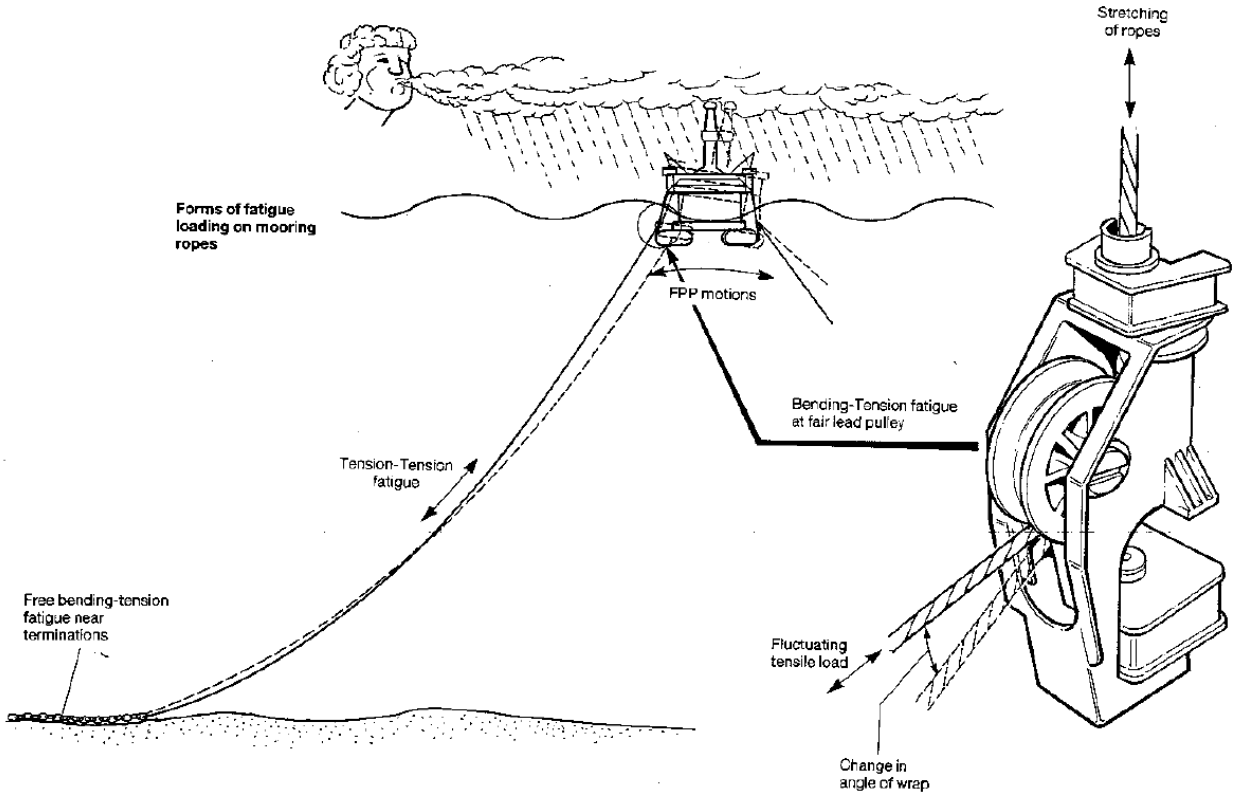

Figure 3.8: Mooring line motions and types of fatigue loading for a catenary moored platform [12].

In mooring lines, one can distinguish three types of fatigue loading [106] (Fig. 3.8).

(a) Tension-Tension (T-T) fatigue, which involves the whole line and consists in fluctuating line tensions about the mean tension, due to platform movement. According to [12], the Palmgren-Miner cumulative damage approach works well with wire ropes concerning T-T fatigue.

(b) Bending-Tension (B-T) fatigue, primarily located in the zones in which the line are subjected to a predetermined curvature (i.e. at the fairlead), consists in oscillation of bending and tension. The B-T fatigue is not treated in this work, since it is preferred to use chains instead of wire ropes at the fairleads.

(c) Free Bending-Tension (FB-T) fatigue, which is mainly the case of zone in proximity of contact with the seafloor and in correspondence of additional masses or buoyancy modules. It's a change in unsupported rope curvature in phase with the fluctuating line tension. In this case the radius of curvature varies since there are no sheaves, fairleads or other formers. According to [127], free bending-tension fatigue problems may be a source of concern with catenary moorings and in taut moorings for tethered buoyant platforms

where they originates from surge motions of the platform.

(d) Torsion fatigue, which occurs when cyclic tension generates a proportional cyclic torque in the rope and the adjoining components do not have sufficient torsional stiffness to prevent rotation. Life under these conditions is related to a combination of twist range and tension range [16].

Practical and economic solutions lead to a need to understand and quantify interactions between different modes of fatigue loading (simplistically: bending, tension and torsion) which are traditionally separated in laboratory testing [15]. For instance, wire rope bending generates a variation of the axial strain in the wire and fretting between the wires at contact positions. In dealing with fretting fatigue, it should be noticed that the Palmgren-Miner approach can be used only with SWT and FS criteria (Sec. 3.3.3-3.3.4).

3.4.2 Offshore regulations

During the design procedure, a designer has to consider several limit states, i.e. conditions beyond which the structure is no more able to fulfill the design requirements. One of these is the fatigue limit state.

As usual, to account for uncertainty in the design flowchart, a safety factor multiplying the estimated damage is introduced for a given design configuration. From the knowledge of reliable studies, the use of a specific fatigue safety factor γ_F for the mooring lines is recommended in [30]. It has the role of covering the uncertainties in the fatigue analysis. The design equation for the FLS is hence

$$1 - d_c \gamma_F \geq 0 \tag{3.25}$$

in which d_c is the computed fatigue damage accumulated as a result of cyclic loading during the design life time. The value of γ_F is established as follows:

$$\begin{aligned} \gamma_F &= 5 && if \quad d_F \leq 0.8 \\ \gamma_F &= 5 + 3\left(\frac{d_F - 0.8}{0.2}\right) && if \quad d_F > 0.8 \end{aligned} \tag{3.26}$$

where d_F is the adjacent fatigue damage ratio, which is the ratio between the characteristic fatigue damage d_c in two adjacent lines taken as the lower damage divided by the greater damage. Note that a more elaborated approach is to compute the failure probability with a reliability approach considering explicitly the uncertainties. In fact, safety factors can be related to the distance in parameter space between the nominal configuration and the most probable failure configuration.

The resistance against fatigue of a mooring line is normally given after fitting a distribution of experimental fatigue test results, in terms of a T-N curve (tension range vs number of cycles to failure) or alternately as S-N curve, with S for the stress range. In the latter case, S is computed as T divided by a nominal area which is $\pi \frac{D^2}{4}$ for wire rope, with D the outer diameter. The S-N curve gives the number of cycles to failure N versus the stress range S and

it is based on fatigue tests. S-N curve that provides 97.7% probability of survival is specified in the offshore standards [32].
In [30] the S-N fatigue law is given for different type of mooring, assuming that the rope will not be affected by corrosion. It takes the form

$$N_{cycles}(S) = a_D S^{-m} \tag{3.27}$$

in which N_{cycles} is the number of cycles to failure, S is the stress range, while a_D and m are structural parameters defined in table 3.1.

Wire rope type	m	$\mathbf{a_D}$
Stranded rope	4.0	$3.4 \cdot 10^{14}$
Spiral strand	4.8	$1.7 \cdot 10^{17}$

Table 3.1: Coefficient for the S-N fatigue law (3.27) in [30].

In [33] a fatigue damage law for steel wire rope is provided, after tension-tension tests as the following T-N curve:

$$N_{cycles}(T) = KT^{-m} \tag{3.28}$$

where m and K are structural parameters defined according to table 3.2, for a mean load equal to 30% of the rope minimum breaking strength.

Wire rope type	m	K
six/multi-strand	4.09	231
spiral strand	5.05	166

Table 3.2: Coefficient for the T-N fatigue law (3.28) in [33].

To resume, one can note that offshore regulations consider only 1D stress variation tangent to the rope axis (or tension) as indicator for the fatigue damage estimation.

3.4.3 Fatigue damage estimation

The mean fatigue damage per stress amplitude can be written as

$$\bar{D}_i = \int_0^{+\infty} D_i(s) p_S(s) ds \tag{3.29}$$

where D_i is obtained from a specific fatigue law, s is the stress amplitude and p_S is the probability density of the stress amplitudes.
The total damage D_{tot} can then be obtained by summing up the mean damage $\bar{D}_i$ over the service life of the structure, taking into account the long-term distribution of the sea states [140]. Its expression is hence

$$D_{tot} = \int_{\bar{\theta}} \int_{H_s} \int_{T_p} \frac{T_L}{T_{mp}(t,h,\theta)} \bar{D}_i(t,h,\theta) p_{T_p|H_s}(t \mid h) p_{H_s}(h) p_{\bar{\theta}}(\theta) dt\, dh\, d\theta \tag{3.30}$$

in which

- p_{H_s} is the marginal probability density function of the significant wave height H_s;
- $p_{T_p|H_s}$ is the conditional probability density function of the wave spectral period T_p, given H_s;
- $p_{\bar{\theta}}$ is the probability density function of the mean direction of wave propagation $\bar{\theta}$;
- T_L is the total service life;
- T_{mp} is the mean period of a stress cycle within the sea state.

Note that the joint probability choice considered here is arbitrary and could be replaced by another formulation depending on the metocean data available [147].

Since the long-term stochastic distribution of the sea state is defined by wave scatter diagrams representing the discretized joint probability (see Sec. 1.1.1), the computation of the fatigue damage is approximated by

$$D_{tot} \approx T \sum_{i=1}^{NSS} d\left(H_{si}, T_{pi}, \gamma_i, \theta_i, \xi_i\right) p_{sea}(H_{si}, T_{pi}, \gamma_i, \theta_i) \tag{3.31}$$

in which

- NSS is the number of sea states taken into account, i.e. the overall number of blocks of the WSDs;
- $\underline{H}_s, \underline{T}_p, \underline{\gamma}, \underline{\theta}, \underline{\xi}$ are the vectors collecting the NSS realizations of the stochastic variables associated to the sea state (to the ones already defined, are introduced also the directions $\underline{\theta}$ and the stochastic seeds $\underline{\xi}$, see section 1.1.1);
- the function d calculates, for each sea state, the fatigue damage per unit time;
- p_{sea} is the probability of occurrence of the sea state, defined thanks to the values in the blocks of WSDs;
- T is the total time.

The fatigue damage accumulation is based on the Palmgren-Miner law, hence neglecting loading history effects. However, it is necessary to switch from a stochastic irregular tension process obtained from the analyses to a number of equivalent stress cycles. The *rainflow technique* [47] is currently considered as the most accurate approximation to do so [30] (Fig. 3.9). To take into account of the non-zero mean stress, the classical Goodman approach can be used to compute an effective alternating stress. It is then possible to estimate the fatigue damage per unit time for each block in the WSD:

$$d(H_{si}, T_{pi}, \gamma_i, \theta_i, \xi_i) = \frac{1}{T_{analysis}} \sum_{k=1}^{N_{amp}} \frac{n(R_k)}{N(R_k)} \tag{3.32}$$

in which N_{amp} is the number of stress amplitudes considered, R_k is the k-th stress amplitude, $n(R_k)$ is the number of stress cycles obtained exploiting the rainflow algorithm for the k-th stress amplitude, $N(R_k)$ is the number of stress cycles with k-th amplitude needed to break the component and $T_{analysis}$ is the time of one analysis, which has to be chosen sufficiently large in order to obtain the stationarity of the estimation (3.32). Note that this time should also enable to satisfy the ergodicity (see section 1.1) thus avoiding a stochastic mean over

ξ. In [107] a procedure is proposed in order to evaluate the standard deviation associated to the fatigue damage estimation.

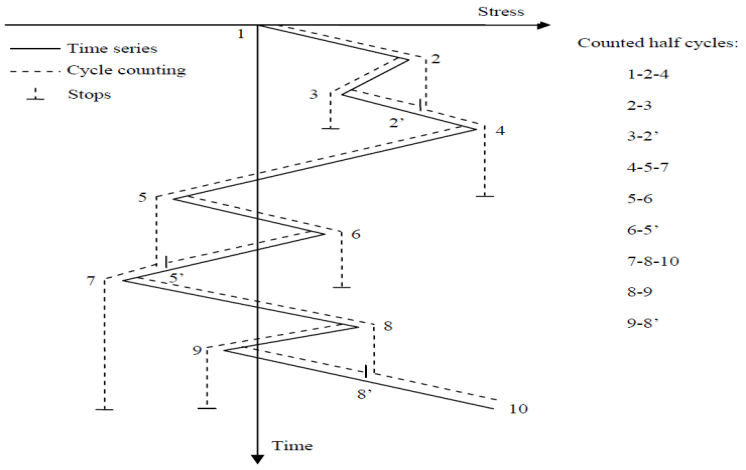

Figure 3.9: Illustration of the rainflow cycle counting method [47].

3.4.4 Specific criteria for wire ropes

An attempt to define a specific fatigue law for wire ropes which takes into account contact stresses occurring at the wires level has been made by Knapp and Chiu [80]. They considered only straight ropes subjected to tension fatigue. Diminished cable strength due to fatigue is assumed to be solely a consequence of stress concentrations at cross-wire contact points (interlayer contact). It is assumed that

- relative motion between wires in adjacent layers is negligible;
- the wire contact sites serve the same function in the process of crack development as a notch or other geometric stress-raisers;
- the stress concentration factor can be evaluated at the mean value of applied fluctuating tension;
- wire layers exert a uniform radial pressure on inner layers (i.e. there is a sufficiently large number of equally spaced wires in each layer);
- wires within a layer do not make circumferential contact.

Hobbs and Smith [61] proposed a fatigue criterion for multilayer spiral strands formulated from tension-bending test results, with the test configuration reported in Figure 3.10. The authors proposed a criterion with a parameter based

- on the quantities θ and T related to the tension-bending test,
- the relation between bending and curvature, given by the calculation of a bending stiffness $(EI)_{eq}$.

The dimensionless parameter comes from the bending analysis at the beam ends of a clamped

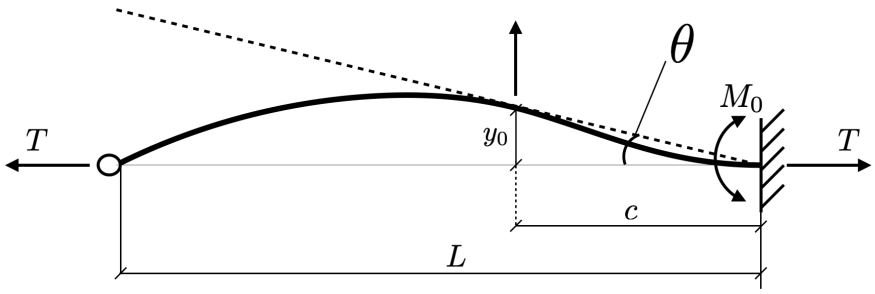

Figure 3.10: Tension-bending test configuration adopted in [61] for the determination of a tension-bending fatigue criterion.

beam under tension:

$$\frac{M_0}{\sqrt{T_u(EI)_{eq}}} = 1.1\tan(\theta)\sqrt{\frac{T}{T_u}} \tag{3.33}$$

with M_0 the bending moment at the clamped end and T_u the nominal breaking load. In Figure 3.11 it is represented the relationship observed between the dimensionless parameter and the number of bending cycles necessary to obtain the first wire break.

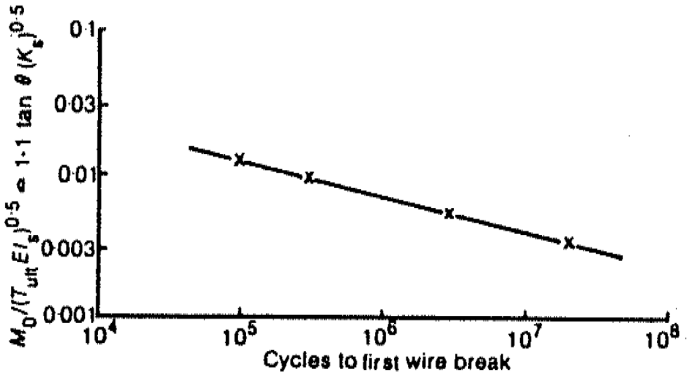

Figure 3.11: Experimental correlation between the dimensionless parameter and the number of bending cycles to first wire break [61].

In [120] Raoof elaborates a criterion somehow similar to the macroscopic fretting fatigue criteria proposed by Ruiz in [133]. It takes the effect of interwire fretting fully into account, by making use of a 'contact stress-slip' parameter. The parameter is expressed as

$$S = \frac{\sigma_x U(x)}{x} \tag{3.34}$$

where

- σ_x is the maximum tensile stress linked to the tension in the wire and the contact stresses, deduced from Hertz's contact theory, computed at the limit of the contact surface;

- U is the sliding amplitude
- x is the distance between two contact points in the external layer.

The application of this criterion is shown in [123], exploiting test results reported in [152], which were conducted for different rope diameters.

From the results obtained in [121] Raoof takes also into account the effect of the external hydrostatic pressure. Its influence by the way seems to be negligible for water depths up to 100 meters.

3.5 Conclusion

The key features related to fatigue have been detailed in this chapter.

The multiaxial and fretting fatigue criteria among the most used in the literature have been detailed in Section 3.3. It should be noted that the criteria in Sec. 3.3.1-3.3.2 are stress-based, while the criteria in Sec. 3.3.3-3.3.4 are energy-based. However, a lack of some understanding concerns the fretting fatigue mechanism, in which also the magnitude of the sliding between the bodies is important (Fig. 3.4).

Section 3.4 deals specifically with the fatigue of wire ropes. The currently used fatigue design rules and procedures concerning offshore mooring system have been detailed. They rely on tension-tension fatigue test, not taking into account the wire contact interactions. The fatigue criteria that have been formulated considering inter-wire fretting have been detailed in Section 3.4.4.

Chapter 4

Contact modeling

Contact is a strongly nonlinear kind of boundary condition. Within the finite element framework, different methods can be applied for an iterative solution of the nonlinear equation system associated with the weak form of the contact problem. A fast and reliable method is the Newton scheme, whose formulation relies on the linearization of the weak form.
In the present work, contact is involved both in the global model, where a part of the mooring lines is in contact with the seabed, and in the wire rope model. In particular, contact modeling represents the main issue for the simulation of wire rope mechanics. Because of the great number of contact interactions that are involved, the numerical simulations tend to be very time-consuming.

4.1 Basic concepts

In this section, the main features involving contact interactions are presented, by distinguishing between normal contact, which basically consists in forces that prevent the penetration of the bodies, and tangential (or frictional) contact, for which also forces resisting the relative tangential movements develop at the contact interface.

4.1.1 Normal contact

In statics, the contact constraint is expressed by the so-called *Hertz-Signorini-Moreau* condition. As done in [165], let us consider a point mass under gravitational load which is supported by a spring (Fig. 4.1). The motion of the mass is restricted by the presence of a rigid support, such that

$$g_N(u) = h - u \geq 0 \tag{4.1}$$

where g_N is the normal gap. Depending on the values of spring stiffness k and mass m, the point mass contacts or not the rigid surface. If contact occurs, a reaction force appears; in classical contact mechanics, we assume that the reaction force between rigid surface and

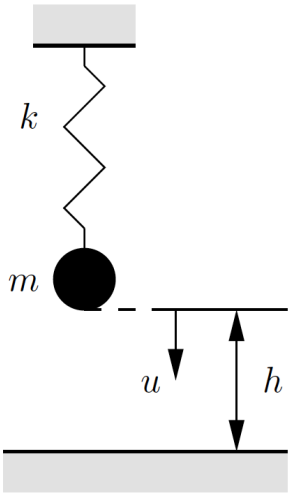

Figure 4.1: Mass-spring system [165].

point mass is negative, hence the contact pressure can only be compression (Fig. 4.2). Hence, the *Hertz-Signorini-Moreau* contact condition reads

$$g_N \geq 0, \quad t_N \leq 0, \quad t_N g_N = 0 \tag{4.2}$$

Such conditions coincide with Kuhn-Tucker complementary conditions in the theory of optimization. Therefore the normal contact force as function of the normal gap is shown in Figure 4.2.

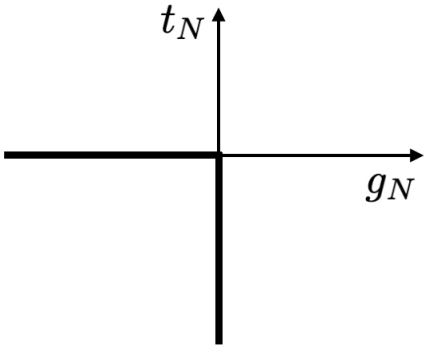

Figure 4.2: Normal contact law respecting the Hertz-Signorini-Moreau conditions.

When enforcing contact in a dynamic problem, the finite element space, time-stepping scheme and contact condition should be carefully chosen to ensure energy conservation and avoid spurious oscillations [34]. Multiple strategy have been proposed. A first one, like in Abaqus®, is to add damping in the system to avoid dynamic instability [1]. This could be done by using time-stepping dissipative scheme like the HHT (Hilber-Hughes-Taylor) one [34]. A second option is to use a time-stepping which respects an impact law. Finally, we can also mention a simplification which is to replace the *Hertz-Signorini-Moreau* condition by an approximation

involving the velocity instead of the displacement. Assume that $g_N = 0$ at a certain time t_c. Then, on a short time interval afterwards, $g_N \approx (t - t_c)\dot{g}_N$. This motivates the following contact condition in velocity [34]:

$$\dot{g}_N \geq 0, \quad t_N \leq 0, \quad t_N \dot{g}_N = 0 \tag{4.3}$$

This condition can be interpreted as a first-order approximation (with respect to the time variable) of the original contact condition (4.2). It is physically realistic for a short time interval and for a vanishing initial gap between the bodies in contact [38].

4.1.2 Tangential contact

Friction basically consists in the development of forces which resist relative tangential motion between two bodies in contact, mostly linked to the roughness of the body surfaces.
In general, in frictional contact one can distinguish between stick and slip states. In the first situation, there is no relative movement among the bodies in contact, while in slip state the magnitude of the frictional forces is not sufficient to prevent gross sliding. By denoting t_T the frictional force, a threshold function $f_s(t_T, t_N)$ can be defined such that

$$f_s < 0 \longrightarrow \text{stick}$$

$$f_s = 0 \longrightarrow \text{slip}$$

The simplest expression for f_s is given by the Coulomb's friction law, for which

$$f_s = t_T + \mu t_N$$

where μ is a parameter called friction coefficient, whose value depends on the surface properties. The stick-slip behavior can then be written in the form of Kuhn-Tucker conditions

$$\dot{g}_T \geq 0, \quad f_s \leq 0, \quad \dot{g}_T f_s = 0 \tag{4.4}$$

Considering a constant normal force t_N, in Figure 4.3 is reported the frictional force as function of the tangential sliding g_T.

4.2 Computational contact mechanics

Roughly, two steps can be distinguished in a contact algorithm: contact detection and resolution. The detection phase must determine which elements of the discretized solids are going to penetrate. Resolution implies that

- in normal direction, penetration has to be avoided by applying repulsive forces to the penetrating elements;
- in tangential direction, the frictional forces have to resist the sliding between the bodies.

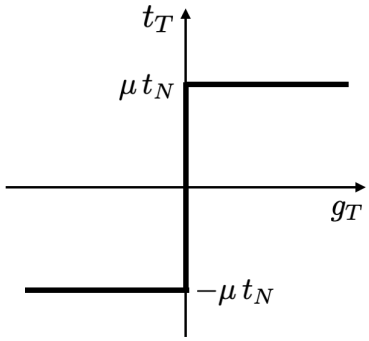

Figure 4.3: Friction force profile according to the Coulomb law.

Modeling contact in the Finite Element framework is usually a difficult task. Many different aspects have to be taken into account in order to properly represent the physical phenomenon to be modeled:

- geometrical discretization in the contact zone;
- contact detection;
- contact resolution;
- contact discretization;
- small or large sliding.

In the following, all the concepts will be presented considering quasi-static conditions, as usually done in the literature.

4.2.1 Discretization of the contact zone

In some contact problems, the discretization of the contact zone becomes a key aspect. In general, the finite element mesh it should be fine enough in order to correctly represent the contact geometry, but avoiding too oblong elements.

If a master-slave approach is used, the mesh should avoid sharp corners on the master surface, since this generates blind spots (Fig. 4.4) or use a smoothing procedure on the normal contact direction before the contact detection.

4.2.2 Contact detection

In Computational Contact Mechanics we need to detect contact when any penetration occurs. In many cases, the master-slave contact detection is used, which consists in checking if the slave node/surface is penetrating the master body. In the detection phase of implicit analyses contact elements are created (Fig. 4.5), including a slave node and several master nodes united by a master surface. In case of Lagrange multiplier or coupled augmented Lagrangian methods, contact elements contain also some additional degrees of freedom (Lagrange multipliers), one in case of frictionless contact and 2 or 3 in frictional case in 2D and 3D respectively. To keep track of stick-slip-stick behavior it is necessary to store also internal

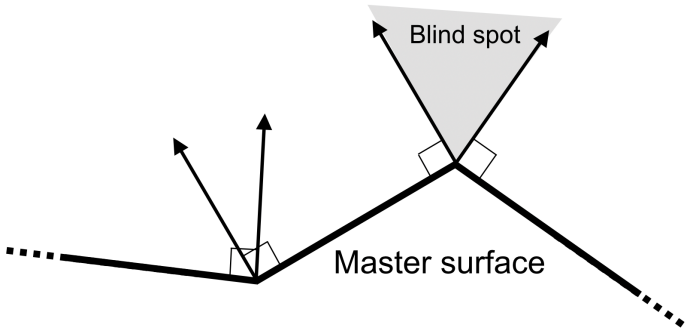

Figure 4.4: Blind spot generated by an edge on the master surface. In this case the closest point projection for contact detection fails.

history variables [168].

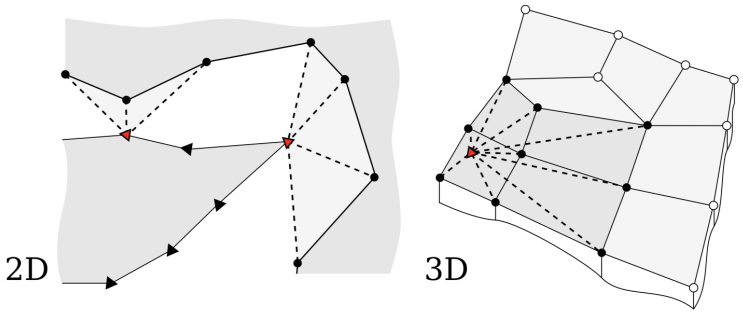

Figure 4.5: Examples of multi-face contact elements in 2D and 3D, dashed lines connect nodes of multi-face contact elements; triangles are slave nodes, while circles represent master nodes [168].

First of all, contact detection has to be established by fixing the distance d_{max}: if a slave node is closer than d_{max} to the master surface, this slave node is considered as possibly contacting at current load step and a contact element has to be created. Usually the parameter d_{max} is chosen accordingly to the master surface mesh and/or the maximal variation of displacement of contacting surface nodes during one iteration/increment.
The definition of the closest point $\underline{\rho}^*$ onto the master surface Γ_m for a given slave node $\underline{r}_s$ is the following:

$$\underline{\rho}^* \in \Gamma_m : \forall \underline{\rho} \in \Gamma_m, \mid \underline{r}_s - \underline{\rho}^* \mid \leq \mid \underline{r}_s - \underline{\rho} \mid \tag{4.5}$$

Expressing the master surface in a parametrized form $\underline{\rho} = \underline{\phi}(\xi)$, in order to detect the closest point one has to minimize the functional

$$F(\underline{r}_s, \xi) = \frac{1}{2}(\underline{r}_s - \underline{\phi}(\xi))^2 \tag{4.6}$$

$$\min_{\xi \in [0,1]} (\underline{r}_s - \underline{\phi}(\xi)) \Rightarrow \xi^* : \forall \xi \in [0,1], \mid \underline{r}_s - \underline{\phi}(\xi^*) \mid \leq \mid \underline{r}_s - \underline{\phi}(\xi) \mid \tag{4.7}$$

$$\min_{\xi\in[0,1]}(\underline{r}_s - \underline{\phi}(\xi)) \Leftrightarrow (\underline{r}_s - \underline{\phi}(\xi^*)) \cdot \frac{d\underline{\phi}}{d\xi} \mid_{\xi^*} = 0 \tag{4.8}$$

It is important to notice that the normal direction of the master surface could not be always defined. When the finite element method is used the master surface in many cases is not smooth, only continuous, i.e. $\underline{\phi}(\xi) \in C^0(\Gamma_m)$. This could lead to convergence problems and nonphysical oscillations, whose remedy could be the use of smoothing techniques (for instance, surface smoothing with Bezier surface) [165].

4.2.3 Contact resolution

Let us consider two bodies Ω_1 and Ω_2 in contact along a portion of their boundary.
Let $\mathbb{U}$ be the set of kinematically admissible displacements. The continuous formulation of the weak form of equilibrium equation with contact problems can be written as follows

$$\int_{\Omega_1\cup\Omega_2} \underline{\sigma} \cdot \delta\underline{\varepsilon} d\Omega - \int_{\Omega_1\cup\Omega_2} \underline{f}_v \cdot \delta\underline{u} d\Omega - \int_{\Gamma_1^N\cup\Gamma_2^N} \underline{f}_0 \cdot \delta\underline{u} d\Gamma - \int_{\Gamma^C} \underline{\sigma}_n^C \cdot \delta\underline{g}_n d\Gamma = 0 \quad \forall\delta\underline{u} \in \mathbb{U} \tag{4.9}$$

in which

- $\underline{\sigma}$ and $\underline{\varepsilon}$ are respectively the vector of internal stresses and strains;
- $\underline{u}$ is the displacement vector;
- $\underline{f}_v$ and $\underline{f}_0$ are respectively the volume forces and the applied surface forces applied on the Neumann boundary of the two bodies $\Gamma_1^N \cup \Gamma_2^N$;
- $\underline{\sigma}_n^C$ are the contact stresses on the contact boundary Γ^C;
- $\underline{g}_n$ collects the relative displacements at the contact boundary.

There exists many methods for contact resolution, i.e. to evaluate the contact term

$$\int_{\Gamma^C} \underline{\sigma}_n^C \cdot \underline{g}_n d\Gamma$$

Among them, the most used are the optimization methods, which are the following [165]:

- Penalty method,
- Lagrange multipliers method,
- Augmented Lagrangian method.

We just focus only on the Penalty method, which consists in defining a pressure-overclosure relationship of the kind

$$t_N = \epsilon_N(g_N) g_N \tag{4.10}$$

where ϵ_N is the normal penalty coefficient, which can be constant or can depend on g_N so as to smooth the nonlinearity in incipient contact situations. For instance, one can define a normal contact force defined as

$$t_N = \begin{cases} 0 & \text{if} \quad g_N > 0 \\ \dfrac{\epsilon_N}{-2p_{reg}} g_N^2 & \text{if} \quad -p_{reg} \le g_N \le 0 \\ \epsilon_N \left(g_N + \frac{p_{reg}}{2}\right) & \text{if} \quad g_N < -p_{reg} \end{cases} \tag{4.11}$$

so that the derivative of t_N is always continuous.
The drawback of the penalty method is that the achieved solution is not exact, i.e. it does not strictly respect the Signorini-Hertz-Moreau conditions, and depends on the penalty coefficient, which has to be properly defined in order to avoid too large penetration (penalty coefficient too small) or ill-conditioning of the global matrix (penalty coefficient too large). The other two methods allow to obtain an exact solution, but they introduce additional degrees of freedom, which increase the problem size or additional loops to solve the system.
In the tangential direction, the condition of no relative motion is approximated by a stiff elastic behavior, such that

$$t_T = \epsilon_T(g_T) g_T \tag{4.12}$$

The tangential penalty coefficient can be constant or it can be chosen such that the relative motion from the position of zero shear stress is bounded by a value g_T^{crit}, which represents the elastic slip value:

$$\epsilon_T = \frac{\mu\, t_N}{g_T^{crit}} \tag{4.13}$$

The same considerations drawn for the normal direction are valid for the tangential one as well: the obtained solution is approximated in the sense that it does not strictly respect the conditions (4.4). However, the elastic slip assumes a physical sense in tribology, since it corresponds to the micro-slip associated to the elastic deformation of the contact asperities.
The normal friction coefficient between steel and steel is between 0.3 and 0.4, but there is a lot of grease in the wire rope which acts as a lubricant. This reduces the friction coefficient, which is therefore adjusted down to 0.12, as done for instance in [125].

4.2.4 Contact discretization

Node-to-node

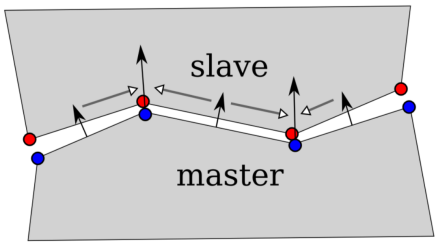

Figure 4.6: Node-to-node algorithm: in this case the definition of the normals at master nodes is defined as an average of the normals of adjacent segments [168].

This algorithm (Fig. 4.6) is the most simple one and passes the so-called Taylor's test, which is a patch test that requires that a uniform contact stress is correctly transmitted from one contacting surface to another. It can be used only in small deformation and small slip regime, and it requires conforming FE meshes. These conditions guarantee that contact pairs do not change during the analysis.

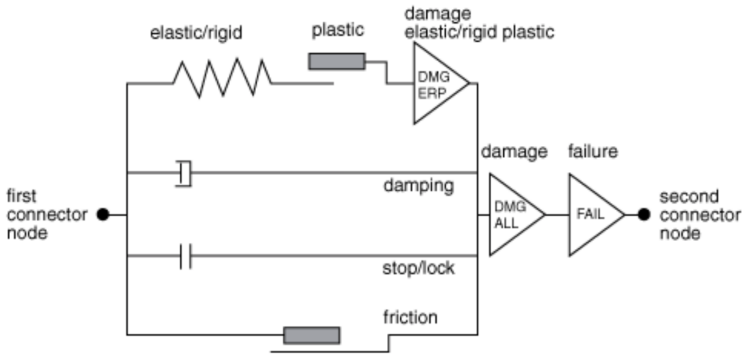

Figure 4.7: Schematic representation of a connector element in Abaqus® [1].

In Abaqus® this algorithm can be used by linking the contact pairs with connector elements (Fig. 4.7).

Node-to-surface

The node-to-surface approach represents the most traditional algorithm for contact detection. It adopts a so-called master/slave approach: contact conditions are established such that each node on the slave surface (slave nodes) effectively interacts with a point of projection on the master surface on the opposite side of the contact interface.

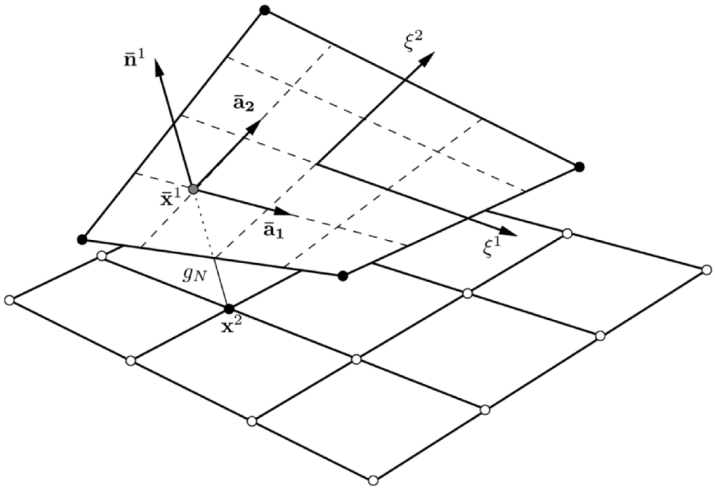

Figure 4.8: Node-to-surface contact element [165].

In 3D node-to-surface discretization the contact elements have $n_s + 1$ nodes, with n_s the number of nodes of a master surface element (Fig. 4.8). By using the same notation, the gap between the master surface and the slave node is given by

$$g_N = \left[\underline{x}^2 - \underline{x}^1(\overline{\xi}^1, \overline{\xi}^2)\right] \cdot \overline{n}^1 \tag{4.14}$$

in which $\underline{x}^2$ denotes the position of the slave node, $\underline{x}^1$ is the position of the closest point to the slave node belonging to the master surface, $\overline{\underline{n}}^1$ is the normal to the master surface at position $\underline{x}^1$ and $(\overline{\xi}^1, \overline{\xi}^2)$ are the convective coordinates of $\underline{x}^1$, i.e.

$$\underline{x}^1 = \sum_{i=1}^{4} N_i(\xi^1, \xi^2)\underline{x}_i^1 \tag{4.15}$$

with N_i the standard interpolation functions and $\underline{x}_i^1$ the nodal coordinates of the master surface nodes.

When the master surface is not flat, the coordinates $\overline{\underline{\xi}}(\overline{\xi}^1, \overline{\xi}^2)$ cannot be computed from a closed form expression, but an iterative process has to be applied. The following nonlinear system of equations for (ξ^1, ξ^2) has to be solved locally for each slave node $\underline{x}^2$:

$$\left[\underline{x}^2 - \underline{x}^1(\overline{\underline{\xi}})\right] \cdot \underline{x}^1_{,\alpha}(\overline{\underline{\xi}}) = \left[\underline{x}^2 - \sum_{i=1}^{4} N_i(\overline{\underline{\xi}})\underline{x}_i^1\right] \cdot \sum_{k=1}^{4} N_{k,\alpha}(\overline{\underline{\xi}})\underline{x}_k^1 = 0 \tag{4.16}$$

Using as a starting value the solution for a flat surface, one can apply the Newton-Raphson scheme to solve the system.

The only information needed for the slave surface is the location and surface area associated with each node. The direction of the slave surface normal and slave surface curvature are not relevant. Thus, the slave surface can be defined as a group of nodes (a node-based surface).

As a result, the slave nodes are not allowed to penetrate into the master surface. However, the nodes of the master surface can, in principle, penetrate into the slave surface. Namely this may happen if the slave surface is not refined enough with respect to the master one.

When a node-to-surface analysis with finite sliding is performed, in order to avoid convergence problems Abaqus®/Standard smooths automatically the master surface, since slave nodes tend to get stuck at points where the master surface normals are discontinuous [1].

Since node-to-surface discretization simply resists penetrations of slave nodes into the master surface, forces tend to concentrate at these slave nodes. This concentration could lead to spikes and valleys in the distribution of pressure across the surface.

Surface-to-surface

The surface-to-surface contact algorithm is generally seen as an improvement with respect to a node-to-surface approach. Namely, it improves numerical accuracy, produced by an integral form of the contact constraint, and considerable robustness in large sliding applications results from the non-local character of the formulation [86].

The so-called algorithm of Abaqus®/Standard is a master/slave formulation with a contact normal defined from the slave surface only. This property simplifies the linearization of contact and friction terms for the Newton-Raphson iteration scheme. To our knowledge, details on the integration scheme are not documented in [1], which limits the possibility to fully characterize this algorithm from literature references.

In the large sliding case, the contact occurs along incompatible mesh discretizations, which causes important difficulties concerning robustness and accuracy of the numerical results. Many strategies have been proposed to overcome these difficulties.

- In order to avoid a conflict in the contact and friction statuses, at the nodes and at the integration points, the normal and tangential gap estimations have to be substituted by averaged quantities interpolated from nodal values [95]. This point is a characteristic of the Mortar methods [118, 119, 43].
- A key point of these algorithms comes from the difficulty to integrate master contributions with polynomial terms which are not properly defined according to the slave integration surface. To solve this problem, a first approach is to increase the integration points [43]. Alternatively, an integration surface conforming to the two contacting surfaces can be determined at each iteration of the Newton scheme, which is very costly, particularly in 3D [118, 119].
- Another possibility to gain in robustness and accuracy has been proposed with unbiased algorithms [110, 136]. These algorithms sum up the contributions obtained by switching the slave and master role of the two surfaces, with particular selection of the forces and displacement to avoid the over-constrained locking.
- In any case, the classical finite element interpolations introduce a source of non-robustness because of the difference between the position of a point and the real geometry. In the contact framework, functions ensuring the continuity of the derivatives (e.g. NURBS) guarantee the continuity of the linearized momentum balance [28], which is fundamental for the Newton-Raphson iterative scheme.
- Another source of lack of robustness comes from the discontinuities on the edges of the solids in contact. This problem can be solved by dividing the integration domain in sub-domains, but this increases the computational cost. The approach in [35] suggests an alternative for the frictionless case, using the unbiased formulation of [136] in the isogeometric Mortar framework and adding extended finite elements to capture the discontinuity.

Beam-to-beam

Contact between beams has some specialties which are related to the description of the beam as a one-dimensional curve in space. Consequently, the formulation of the kinematical contact conditions is different [165]. The first algorithm for beam-to-beam contact have been developed by Wriggers and Zavarise in [166]. Lately, in order to extend this into the frictional case, in [169] the return-mapping algorithm is exploited. A generalization of this algorithm for the case of rectangular cross sections is given in [90] and [91]. In [82] the contact kinematics, the variational formulation and the constitutive relations for the contact forces are described in the Frenet-Serret basis. It allows to include not only normal and tangential interactions, but also rotational interaction between curves representing e.g. circular cross sections of beams. In [36] contact between beam elements is modeled by using an intermediate geometry to integrate contact contributions, as in a Mortar method which contributes to smooth the

functional for Newton algorithm. In [103, 104] the authors formulate the contact kinematics at the beam surfaces, whose points are identified by a set of convective coordinates. This approach allows to take into account rotational interactions and to deal with beam elements of arbitrary cross section.

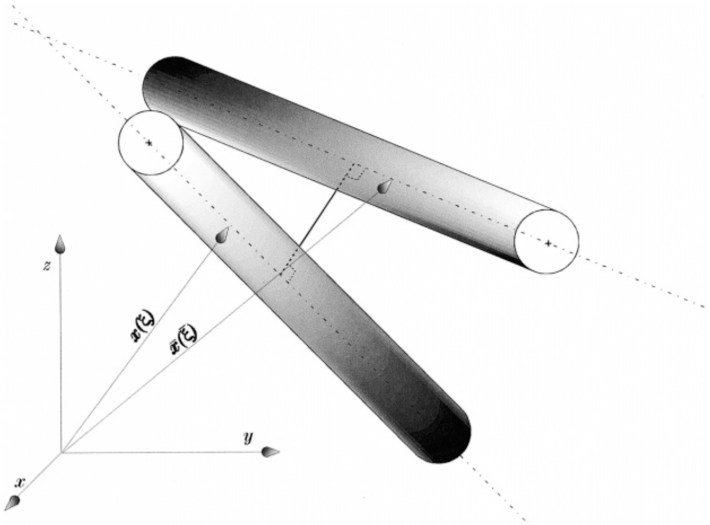

Figure 4.9: Beams in potential pointwise contact interaction [169].

As done in [166], let us consider a situation of pointwise contact of beams having circular cross sections (Fig. 4.9). The beam axes in the deformed configuration are described by the parametric curves $\underline{x}^{\xi}(\xi)$ and $\underline{x}^{\zeta}(\zeta)$. In order to determine whether the beams are in contact or not, one has to compute the minimum distance among them, regarding both parameters ξ and ζ as variables:

$$d(\xi,\zeta) = \min_{\xi,\zeta} \parallel \underline{x}^{\xi}(\xi) - \underline{x}^{\zeta}(\zeta) \parallel = \parallel \underline{x}^{\xi}(\overline{\xi}) - \underline{x}^{\zeta}(\overline{\zeta}) \parallel = \parallel \overline{x}^{\xi} - \overline{x}^{\zeta} \parallel \tag{4.17}$$

By denoting r_{ξ} and r_{ζ} the radii of the two contacting beams, we can introduce the gap function

$$g_N = d - (r_{\xi} + r_{\zeta}) \tag{4.18}$$

The minimum problem 4.17 is in general for arbitrary curves a nonlinear problem. The minimum distance is computed from [165]

$$\begin{cases} \dfrac{\underline{x}^{\xi}(\xi) - \underline{x}^{\zeta}(\zeta)}{\parallel \underline{x}^{\xi}(\xi) - \underline{x}^{\zeta}(\zeta) \parallel} \cdot \underline{x}^{\xi}_{,\xi}(\xi) = 0 \\ \dfrac{\underline{x}^{\xi}(\xi) - \underline{x}^{\zeta}(\zeta)}{\parallel \underline{x}^{\xi}(\xi) - \underline{x}^{\zeta}(\zeta) \parallel} \cdot \underline{x}^{\zeta}_{,\zeta}(\zeta) = 0 \end{cases} \tag{4.19}$$

The solution can be obtained via the Newton-Raphson method by solving the incremental system of equations

$$\begin{bmatrix} \underline{x}^{\xi}_{,\xi} \cdot \underline{x}^{\xi}_{,\xi} + (\underline{x}^{\xi} - \underline{x}^{\zeta}) \cdot \underline{x}^{\xi}_{,\xi\xi} & -\underline{x}^{\xi}_{,\xi} \cdot \underline{x}^{\zeta}_{,\zeta} \\ -\underline{x}^{\xi}_{,\xi} \cdot \underline{x}^{\zeta}_{,\zeta} & \underline{x}^{\zeta}_{,\zeta} \cdot \underline{x}^{\zeta}_{,\zeta} + (\underline{x}^{\zeta} - \underline{x}^{\xi}) \cdot \underline{x}^{\zeta}_{,\zeta\zeta} \end{bmatrix} \cdot \begin{bmatrix} \Delta\xi \\ \Delta\zeta \end{bmatrix} = - \begin{bmatrix} (\underline{x}^{\xi} - \underline{x}^{\zeta}) \cdot \underline{x}^{\xi}_{,\xi} \\ (\underline{x}^{\zeta} - \underline{x}^{\xi}) \cdot \underline{x}^{\zeta}_{,\zeta} \end{bmatrix} \tag{4.20}$$

In general, system (4.20) can have several or no solutions. In the case of straight beams, system (4.19) reduces to two linear equations and can be solved directly. Once the solution is known, the normal vector can be defined.
In tangential direction, an increment of slip in a time increment dt can be computed as [165]

$$\begin{aligned} dg_T^{\xi} &= \| \, d\xi \, \underline{x}_{,\xi}^{\xi} \, \| \\ dg_T^{\zeta} &= \| \, d\zeta \, \underline{x}_{,\zeta}^{\zeta} \, \| \end{aligned} \tag{4.21}$$

For straight beams, the tangent vectors are constant and the slip can be computed exactly as

$$\begin{aligned} g_T^{\xi} &= [\xi(t) - \xi(t_0)] l^{\xi} \\ g_T^{\zeta} &= [\zeta(t) - \zeta(t_0)] l^{\zeta} \end{aligned} \tag{4.22}$$

in which l^{ξ} and l^{ζ} are the beam lengths, while t_0 and t are the initial and final time respectively.
Note that the sliding is considered only along the beam directions, and not along circumferential directions. Therefore this simplified approach can be used only in the case of small beam cross sections.
In the case of parallel beams, the problem is completely different. A possibility is to verify if contact occurs by taking a radial direction of one of the beams as the contact direction [1].

4.2.5 Finite vs small sliding

There are two tracking approaches to account for the relative motion of the two surfaces forming a contact pair in mechanical contact simulations. Finite sliding is the most general and allows any arbitrary motion of the surfaces. Small sliding assumes that although two bodies may undergo large motions, there will be relatively little sliding of one surface along the other.
If large sliding occurs, the contact geometry changes significantly through computation and detection is required almost at each time step. As a consequence, in large deformation and large sliding problems the contact detection is one of the major computational costs [168]. More importantly, this change introduces strong non-linearity with the contact and the friction statuses which may result in failure of convergence of the Newton algorithm.
It is therefore fundamental to understand if the small sliding approach can be considered when modeling a contact phenomenon. The small sliding formulation would in fact allow to save computational time, since the contact detection would be performed just at the beginning of the analysis, with fixed contact pairs throughout the analysis.

4.3 Conclusion

Contact modeling is a key aspect for the proper modeling of the mechanical behavior of wire ropes. In this chapter, the main features and numerical techniques used to represent

this strongly nonlinear phenomenon have been presented, by subdividing a general contact algorithm in different stages.

In particular, we focused our attention on the contact modeling between beam elements and on the differences between a general finite-sliding contact algorithm and the ones exploiting a small-sliding assumption. It is clear that in the latter case the problem is simplified and the amount of computation can be strongly reduced. This aspect should be therefore carefully investigated, since it could be a way to speed-up the computation of the detailed mechanical response of a wire rope. Nevertheless, the validity of the small sliding assumption has to be assessed by comparison with a finite-sliding contact algorithm.

Part II

Obtained results

Chapter 5

Global Model

The global model of the FOWT allows to obtain the mechanical response of the mooring lines for each sea state to which the structure may be subjected during the structural lifespan. Initially, the chosen case study will be presented. Then, the computational steps performed by Deeplines^{TM} will be briefly described. Finally, the obtained results will be shown.

5.1 Presentation of the case study

The case study of this work is represented in Figure 5.1. It consists of a $3.6\,MW$ turbine, whose hub at $71.8\,m$ height, and which has been downsized from the NREL 5 MW [73]. The floater is an evolution of the hybrid spar-barge from the design presented in [116]. The sea depth is uniform and equal to $100\,m$.

5.1.1 Design of the mooring system

The mooring system has been designed with respect to the ultimate limit state, i.e. with a sea state having a return period of 50 years. The following requirements have to be fulfilled:

- no compression in any part of the mooring lines;
- the angle described by the vertical direction and the head of the mooring lines is never lower than 10°;
- the wire rope parts must not touch the seabed at any time (only chains can effectively resist abrasion).

The wire rope profile that has been chosen (Fig. 5.2) enables the structure to respect these three criteria and resists the highest tension obtained in the extreme loading simulation. It is a six-layer steel wire rope, whose diameter is $60.4\,mm$. The layers have alternate lay angle directions and are composed of 5, 11, 17, 23, 29 and 35 wires from the inner to the outer.

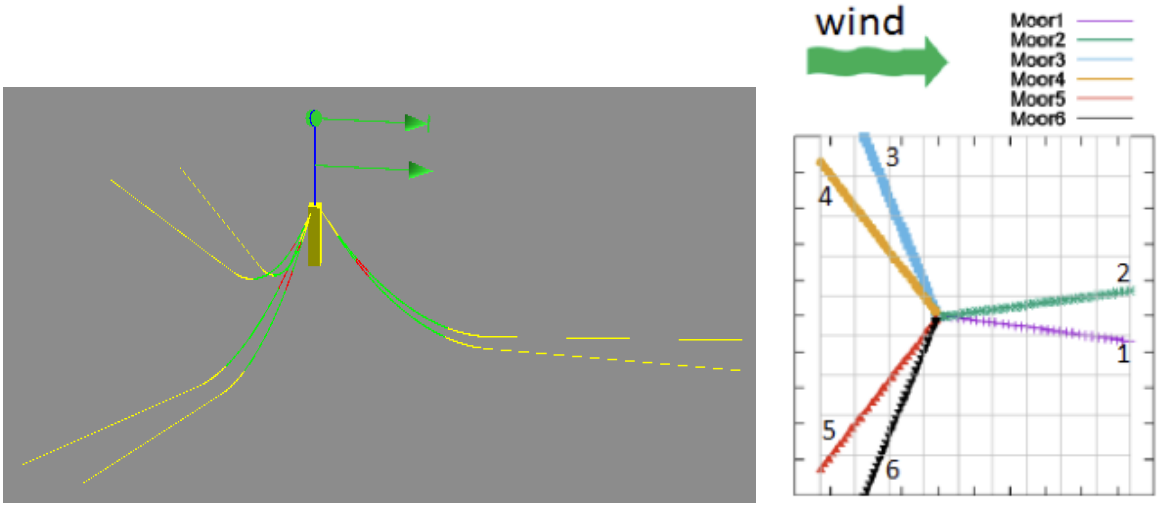

(a) *Side view* (b) *Top view*

Figure 5.1: a) Global scale model representation in Deeplines^{TM}; b) top view of the global model, representing the mooring line numbering and their with respect to the wind direction (which is collinear to the direction of propagation of the waves).

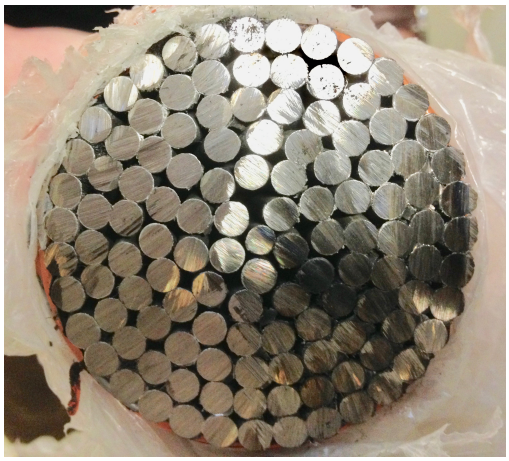

Figure 5.2: The cross section of the chosen wire rope profile.

5.1.2 Mooring system

The mooring lines are catenary-shaped and attached to the floater in three pairs. The bisector of the horizontal projection of each pair is equally spaced with respect to the others, so that the angle between two of them is of 120°. The lines are composed by three segments, whose lengths are reported in Table 5.1.
On each mooring line are positioned six additional masses of $2\,tons$, starting at a distance of $60\,m$ from the floater with a spacing of $4\,m$. Their presence limit the floater movements

Segment	Length (m)
Chain	30.0
Wire rope	20.0
Wire rope with add. mass	40.0
Wire rope	100.0
Chain	382.0

Table 5.1: Mooring line composition.

and keep the lines in tension. The additional masses are modeled by using beam elements with an increased linear mass, since lumped masses would artificially increase the curvature in that zone.

Mooring lines modeling

The shape of the lines is catenary. An advantage of this configuration with respect to tension legs (see Fig. 1.4c) consists in the possibility to use cheaper anchors, because they are subjected to lower tension, thanks to the heavy chains resting on the seafloor. Its initial shape is given by:

$$z(u) = a \cosh\left(\frac{u - u_c}{a}\right) - a - w_d \tag{5.1}$$

in which

- (u, z) are respectively the horizontal and vertical coordinates, with $u = 0$ corresponding to the center of the floater while $z = 0$ is the position of the sea level;
- u_c is the horizontal distance between the center of the floater and the point in which the rope touches the seabed;
- w_d is the water depth;
- a is a parameter which depends on u_c, w_d and the position of the fairlead, that gives the starting position of the catenary (u_h, z_h).

The parameter a can be obtained by exploiting the boundary condition $z(u_h) = z_h$ and by using the Newton-Raphson procedure. It is then possible to compute the length of the catenary, according to the expression

$$l(u) \approx \int_{u_h}^{u} \sqrt{1 + [z'(u)]^2} du = a \left[\sinh\left(\frac{u - u_c}{a}\right) - \sinh\left(\frac{u_h - u_c}{a}\right)\right] \tag{5.2}$$

By replacing $u = u_c$ in (5.2), one obtains

$$l(u_c) = -a \sinh\left(\frac{u_h - u_c}{a}\right) \tag{5.3}$$

As one can see, the initial shape of the catenary is independent from the total radius, i.e. the horizontal distance between the center of the floater and the anchor.

Wire ropes are modeled by beam elements, whose formulation takes large rotations and displacements into account [68]. Besides the axial and bending stiffness, these elements take into account also the torsional stiffness and the shear deformability. However, axial, bending and torsional behavior are fully uncoupled, which is not the case for wire ropes. Chains have no bending stiffness and are therefore modeled by bar elements. In Table 5.2 are reported the chracteristics of the mooring components. The bending stiffness of the wire orpe will be detailed in Sec. 5.1.4.
Both ends of each line are restrained by connections of type *pin*.
In order to compute the Morison drag forces, Deeplines^{TM} requires in the input phase the diameter of the line portions and other four parameters, namely the drag coefficients and the inertia coefficients, both in axial and normal directions. Their values for wire ropes and chains is reported in Table 5.3.

Component	$EA\ (MN)$	$GJ\ (Nm^2/rad)$	Lin. mass (kg/m)
Chain	5.59	/	131.0
Wire rope	3.35	$1.e+6$	16.95

Table 5.2: Axial and torsional stiffness associated to the mooring line components.

Component	$C_{d//}$	$C_{d\perp}$	$C_{m//}$	$C_{m\perp}$
Chain	1.15	2.4	1.5	2.
Wire rope	0.4	1.4	1.2	2.

Table 5.3: Hydrodynamic coefficients chosen for the line components. C_d represents the drag coefficients, while C_m denotes the inertia coefficients. The symbols // and $\perp$ denote respectively the directions parallel and normal to the axial direction of the line.

The modeling of contact between mooring line and seabed is based on a penalty method detailed in [44] and no friction is assumed.

5.1.3 Environmental loading

The aerodynamic modeling of the wind turbine, which can be for instance performed in DeeplinesWind^{TM}, is out of the scope of the thesis. Therefore, for the sake of simplification a steady-state wind assumed collinear to the swell will be considered in the analyses, with constant velocity V_{wind}. It acts on the out-of-sea part of the structure and its action is modeled by the introduction of a couple of forces, on the tower and on the nacelle. In the operational regime, i.e. when the turbine rotates, a moment on the nacelle is added.
The turbine operates differently according to the value of wind speed. In particular, one can consider three different intervals.

1. $V_{wind} \leq v_{in}\, m/s$: it is a shutdown case, since the wind speed is not sufficient to produce an effective rotation of the blades. Furthermore, at low wind speeds turbulence is

usually not negligible and can generate stress fluctuations in the blades, affecting their fatigue life. v_{in} is called *cut-in speed*, and it is usually equal to $3\,m/s$.

2. $v_{in} \leq V_{wind} \leq v_{out}$: it is the operational regime, in which the turbine rotates and the generator produces electricity.
3. $V_{wind} \geq v_{out}$: the rotation of the blades is mechanically stopped by a brake system to prevent damaging. v_{out} is called *cut-out speed*, and it is usually set to $25\,m/s$.

In shutdown cases, the thrusts are computed according to Morison's equation, considering the body as fixed. In the operational case the values of these solicitations are determined according to aerodynamic computations, whose results are reported in Figure 5.3.

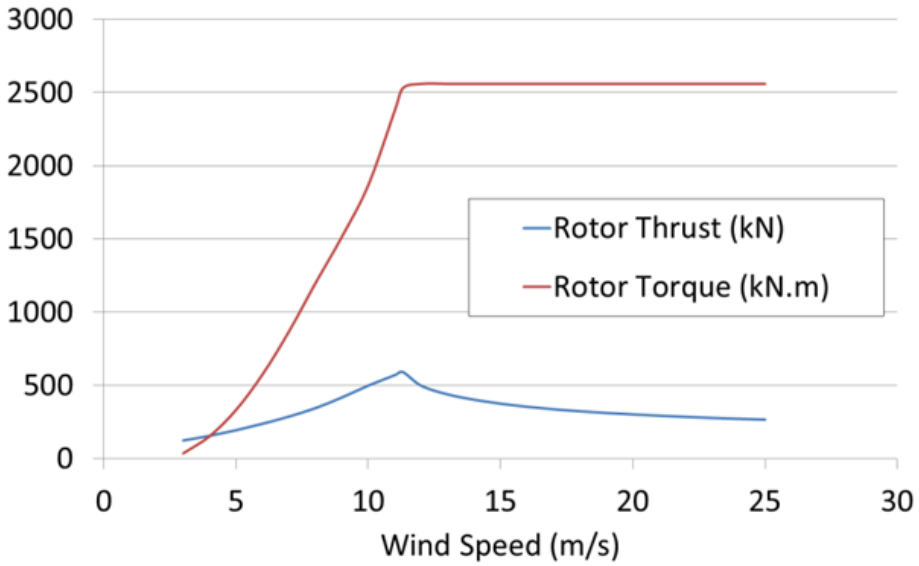

Figure 5.3: Thrust and torque on the rotor as function of the wind speed. These results have been obtained by means of the software DeeplinesWind^{TM}.

In the range from 3 to $12\,m/s$, the rotor speed increases. At $12\,m/s$ the power output reaches the limit that the electrical generator is capable of produce. This limit is called *rated power output* and the wind speed at which it is reached is called the *rated wind speed*. At higher wind speeds, the design of the turbine is arranged to limit the power to this maximum level and there is no further rise in the rotor speed. For large turbines, as the one installed offshore, this is achieved by adjusting the blade angles (pitching) so as to keep the rotor speed constant. Consequently, in Figure 5.3 one can see that at the rated wind speed the rotor torque reaches its plateau and the thrust is the maximum one.

For what concerns the sea waves, they are modeled as superposition of harmonic components, whose amplitude is defined according to a JONSWAP spectrum (Fig. 1.1) which is different for each sea state reported in the Wave Scatter Diagram (Fig. 1.2). The computation of the wave forces on the floater is associated to linear hydrodynamics (Fig. 1.7) and is computed thanks to transfer functions. These functions are already available since they have been computed for the chosen floater design by means of the software Diodore^{TM}.

5.1.4 Bending behavior

While the axial stiffness is a parameter defined in wire rope catalogs for each profile, the bending stiffness, being strongly nonlinear and dependent on tension, is conversely never defined.

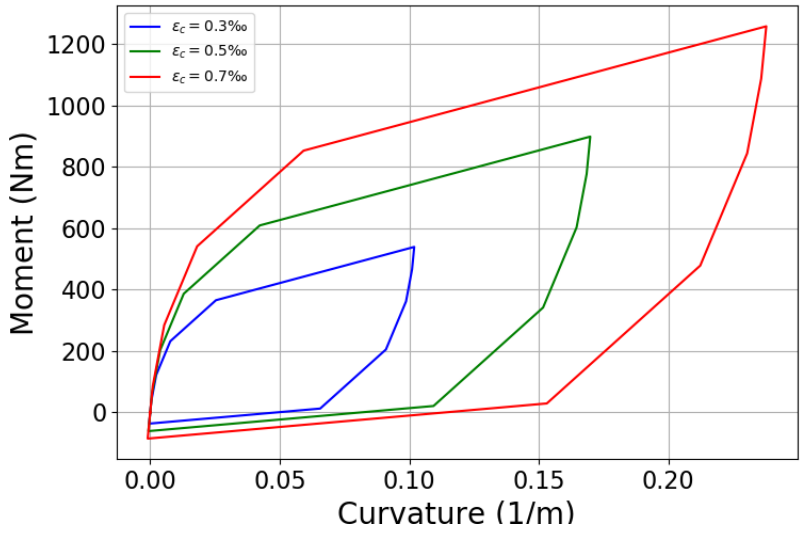

Figure 5.4: Simplified analytical bending diagram of a 60.4 mm spiral strand wire rope for different values of rope axial strain.

The bending behavior of wire rope has been explained in section 2.3.2. Following the analytical developments in [111], a simplified multilinear moment-curvature diagram can be defined for a certain value of applied tension (Fig. 5.4). However, in Deeplines^{TM} it is not possible to implement exactly this kind of bending behavior. Therefore the nonlinear bending behavior is implemented by fitting a bending curve with constant tension (Fig. 5.5).

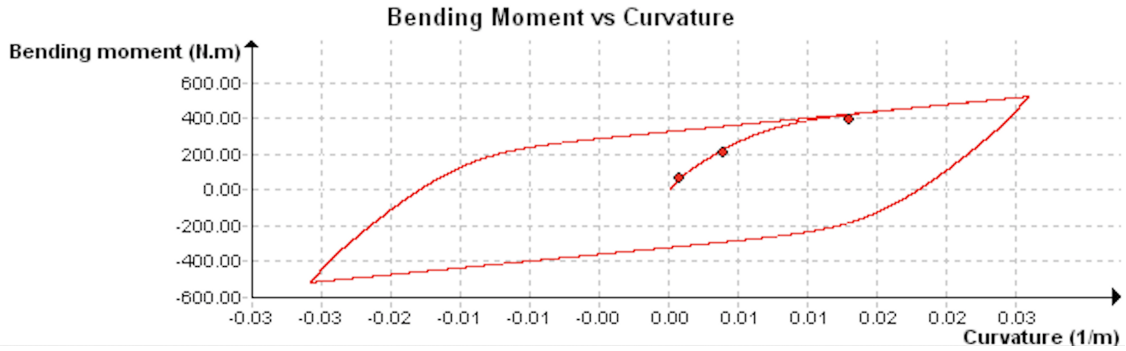

Figure 5.5: Hysteretic bending behavior implemented in Deeplines^{TM}, which has been obtained by fitting the bending behavior for $\varepsilon = 0.5‰$.

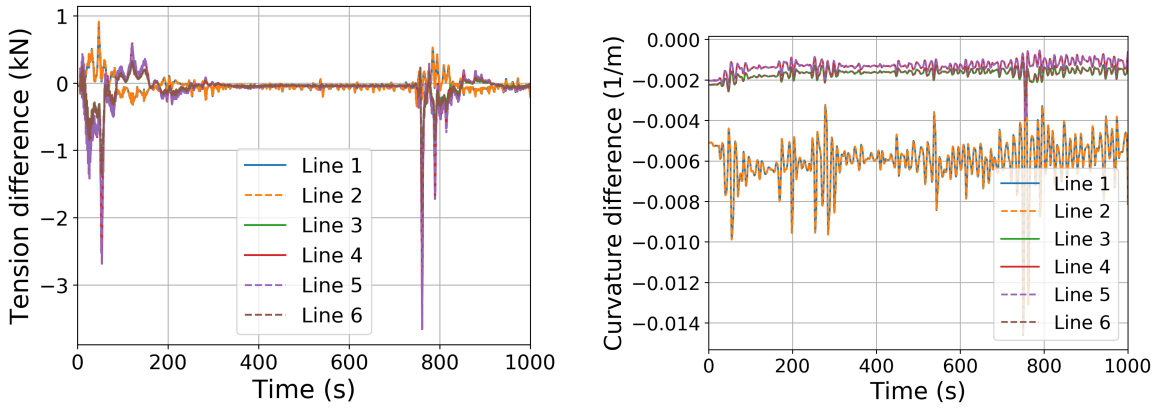

(a) *Tension* (b) *Curvature*

Figure 5.6: Difference of time domain evolution of tension and curvature obtained with $EI = EI_{max}$ and the nonlinear bending behavior of Fig. 5.5, for an extreme sea state (Fig. 5.7). These plots are referred to the section most subjected to bending of the lines, which is at $s = 79\,m$.

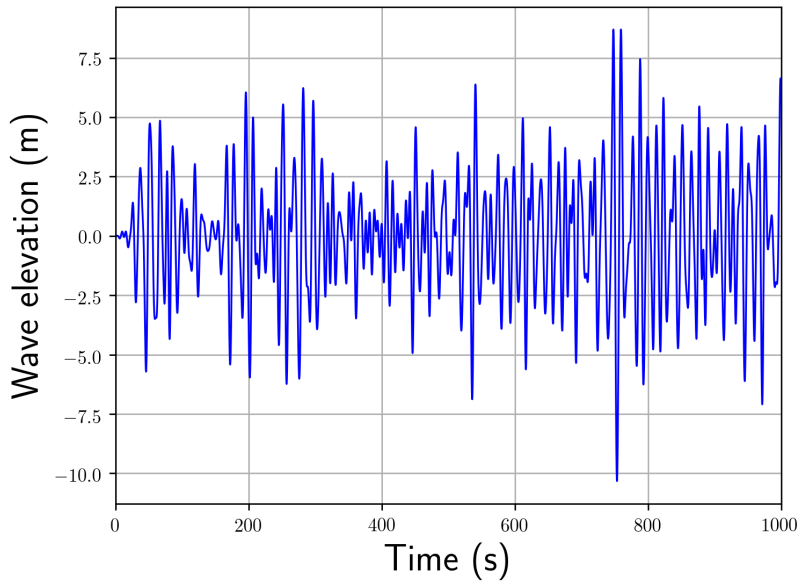

Figure 5.7: Wave elevation of the extreme sea state, with the highest wave hitting the floating system at $t = 750\,s$.

Analyses with an extreme sea state (representative of the Ultimate Limit State condition) have been conducted by choosing either a constant bending stiffness $EI = EI_{max}$, i.e. considering the wires completely adherent on each other, or the nonlinear bending stiffness of Fig. 5.5. EI_{max} is the initial slope of the bending diagrams in Fig. 5.4.
Figure 5.6 reports the obtained differences in tension and curvature time series for all the lines, for the portion at the bottom of the zone with the additional masses (i.e. where the

amplitude of curvature variation is the highest). It can been seen that the bending behavior does not have a considerable influence on the mooring tension and curvature. The value of the tensile force are almost identical. For the curvature, one can see the distributions are affected by an offset, indeed very low, but which is actually not important in fatigue estimations, in which what matters is the amplitude of the oscillations. The largest difference of curvature is found for the mooring lines 1 and 2, i.e. the leeward lines (see Fig. 1.9-5.1b). In particular, this difference is associated to the moment when the biggest waves hit the floater (Fig. 5.7). However, a fatigue analysis is conducted on the whole set of possible sea states occurring during the structural lifespan (see Sec. 3.4.3). Since such extreme wave conditions are very rare, they have a negligible influence on the final fatigue damage estimation (i.e. p_{sea} in (3.31) is extremely low). We can therefore assess that the bending stiffness plays a minor role in a fatigue analysis. This results justifies the use of a top-down approach, since the results of the global model do not depend on the local wire rope model.
In order to limit the nonlinearity of the global model, and consequently enhance the convergence, it has been chosen to perform the analysis of the wave scatter diagram of Figure 1.2 with a constant bending stiffness.

5.1.5 Analysis steps

The analyses in Deeplines^{TM} are basically subdivided in two parts.
Firstly, a static analysis computes the system response when subjected to wind load, hydrostatic forces and drift from the sea, which is computed as

$$f_{drift} = 2\int_0^{+\infty} S_J(\omega) H_2^-(\omega,\omega) d\omega \tag{5.4}$$

where S_J is the JONSWAP spectrum (section 1.1.1) and H_2^- is the Quadratic Transfer Function of the second order wave forces in mode difference [99]. Because of the non-linear behavior of the system, these forces are incremented linearly over a user-defined number of steps.
The action of the sea waves is added in the second analysis step, which is a dynamic calculation that can be tackled by time domain or frequency domain computation. Frequency domain computations have the advantage to be much faster, but it has been observed that they may be used only for low-intensity sea states. For severe sea states they yield completely different results with respect to time domain ones, mostly for what concerns the wire rope curvature. This limitation is mainly due to contact changes between lines and seabed in time domain, whereas in frequency domain, since all the nonlinearities are eliminated, the line is stuck on the seabed at the initial contact zones.
The time integration is performed with the Newmark scheme [105], using $\gamma = 0.6$ and $\beta = 0.3$. These coefficients have been recommended by Principia after studies fitting them to the damping observed in wave-basin tests.
At the beginning of the dynamic analysis, the dynamic loading (i.e. the sea waves in this case study) is increased smoothly until reaching the specified amplitude in a user-defined

time interval, of 50 s in our case. Since the total analysis time is 1000 s, the time series of line curvature and tension are 950 s long.

5.2 WSD analysis

An industrial design should consider thousands of simulations to sample the joint probability of swell and wind, and possible non alignment of these with the turbine. This task is out of the scope of this thesis. We simplify the loading cases by considering only collinear swell and waves with an aligned turbine, and reduce the sea states to the 153 ones of the Wave Scatter Diagram of Figure 1.2. Also, the results presented are computed with the wind thrusts corresponding to a non operating turbine with a reference wind speed of 42.5 m/s.

Segment	N_{ele}	L_{ele} (m)
Chain-1	4	7.5
Wire rope-1	2	10.0
Wire rope-2	20	2.0
Wire rope-3	8	12.5
Chain-2	30	5.33
Chain-3	20	11.1

Table 5.4: Global model discretization.

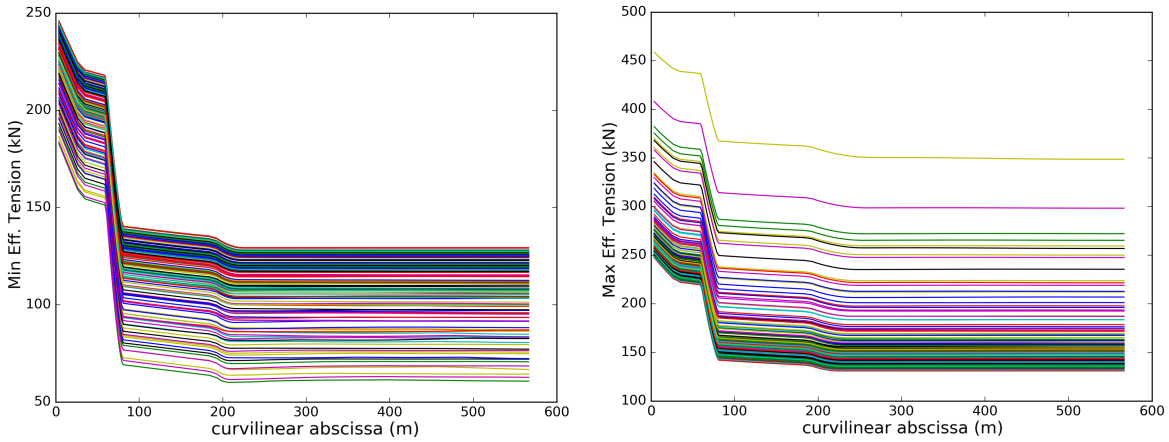

(a) *Minimum value* (b) *Maximum value*

Figure 5.8: Envelops of tension for the mooring line '1' (see Fig. 5.1b) of the converged analyses. The high gradient is caused by the presence of the additional masses. When the line rests on the seabed, the tension is constant since the contact is modeled as frictionless.

The chosen mooring line discretization is reported in table 5.4. The calculation time have been of about 50 hours, using a Intel® Xeon® CPU E5-1620 v3 @ 3.50GHz, with 8 logical processors.

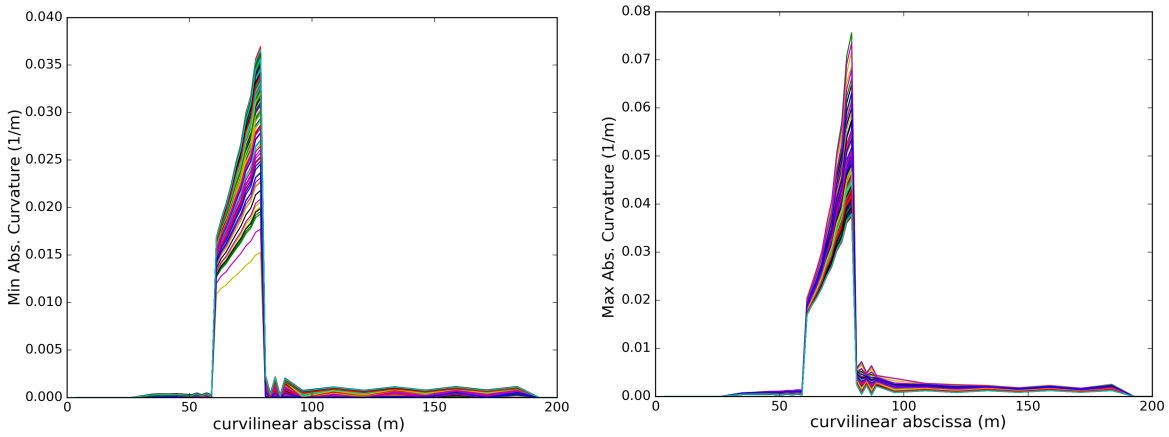

(a) *Minimum value* (b) *Maximum value*

Figure 5.9: Envelops of curvature for the mooring line '1' (see Fig. 5.1b) of the converged analyses. The higher values of curvature are located in correspondence of the additional masses.

The results in terms of tension and curvature envelops are reported in Figures 5.8-5.9. The envelops gather the minimum and maximum values of the correspondent quantity at each position along the line. Note that the curvature in the chain zone is null because they are modeled with bar elements, which do not consider curvature for the determination of the mechanical response.

Since the fatigue is determined by stress fluctuations and mean values, from these results we identify two critical zones:

I) the top part of the wire rope, which is subjected to the highest mean tension;

II) the zone in correspondence of the additional masses, which is subjected to a high tension range and the higher range of curvature variation (this is the zone which may suffer free-bending fatigue).

5.3 Conclusion

From the results of this chapter, the wire rope profile which will be analyzed by the local model has been chosen. From the analysis of the wave scatter diagram, critical zones for fatigue have been identified. They are located at the top of the line, where the mean tension is the highest, and the limit with the bottom part of the zone with the additional masses, which is characterized by the largest variations of curvature.

It has been proved that a nonlinear bending behavior, representative of the one of the real rope for a given tension, does not have much influence on the tension and curvature time series, at a given critical location. This will justify the use of a top-down scheme, i.e. the results of the global model do not depend on what happens locally on the wire rope.

Chapter 6

Towards a simplified wire rope model

As discussed in Section 2.3.5, wire rope models with beam elements for each wire reduce significantly the CPU cost when compared to 3D models, while they provide a correct estimate of the wire kinematics. We consider this simplification in the following. The subsequent step concerned the choice of the contact and friction modeling.

6.1 Tested models

A large panel of possibilities available within Abaqus®/Standard (implicit scheme) for modeling contact between beam elements has been tested. Initially, the edge-to-edge contact algorithm has been used (Sec. 6.1.1). Then, another model has been created, in which surface elements are introduced in order to track the wire surfaces (Sec. 6.1.2). Finally, a new mesh generation strategy has been developed, allowing for the use of a node-to-node contact discretization (Sec. 6.1.3).
Two benchmark tests, detailed in Section 6.2.1, have been conceived in order to assess the capability of three models in the simulation of the frictional contact interactions between wires.

6.1.1 Edge-to-edge model

The edge-to-edge contact algorithm implemented in Abaqus® models contact between beam elements having a circular cross-section. According to the beam configuration, it employs one of the following formulations.

- The formulation named *cross* is used in the case of non-parallel beams, where the contact normal is defined as the normalized cross product between the beam tangents. This occurs for the contact between wires in different layers.
- The formulation named *radial* deals with parallel beams, with the contact normal defined as the radial direction of one of the beams. This type of contact occurs between adjacent wires in a same layer.

The two formulations allow therefore to deal with all the contacts involved within a wire rope, but some issues in the use of this approach have been observed:

- the results in benchmark tests that will be detailed in Sec. 6.2 are not in agreement with the analytical ones,
- we have not found the way to retrieve separately different contact contributions when a beam element is simultaneously in contact with several beam elements (post-processing problem),
- the computational cost in modeling a multilayer wire rope is too high,
- it neglects the rotational interactions between the beams.

The latter point means that only the translations are taken into account for the determination of the sliding between the beams. As a consequence, rolling interactions are not considered. Moreover, the tangential forces which actually act in correspondence of the beam surfaces are directly applied to the beam nodes without any additional moment (see Fig. 8.39). Accounting for these moments is actually crucial for the analysis of spiral stands.

6.1.2 Model with surface elements

Because of the problems encountered with the edge-to-edge algorithm, another numerical model has been developed. It is based on the introduction of surface elements in correspondence of the wire surfaces. In each beam section, the nodes of these elements are linked to the beam nodes via MPC (multi-point constraints) of type *beam* [1]. From a kinematical point view, this means to link the surface nodes to the beam nodes by rigid rods, that follow the rotation of the master (beam) node (Fig. 6.1). The degrees of freedom of the slave (surface) nodes are therefore expressed as function of the correspondent master node and disappear from the equilibrium system. The kinematics of the resulting model is thus very similar to the rigid section kinematics of the classical Euler-Bernoulli beam theory.

The contact elements are associated to the surface elements. Therefore it is possible to use a node-to-surface or a surface-to-surface contact discretization. However, the use of latter one is suggested in [1].

The results obtained with this type of model are in agreement with the analytical ones. This model takes also into account the rotational interactions between the beams, i.e. twisting and rolling. However, it cannot be considered the proper model for wire rope analysis, since

- it is computationally very expensive,
- the geometry of the curved wire surfaces cannot be properly modeled by linear surface elements,
- convergence is generally obtained with lower penalty coefficients with respect to the other algorithms.

6.1.3 Model with connector elements

From the conclusions drawn for the previous model, it has been clear that another type of contact modeling needed to be investigated.

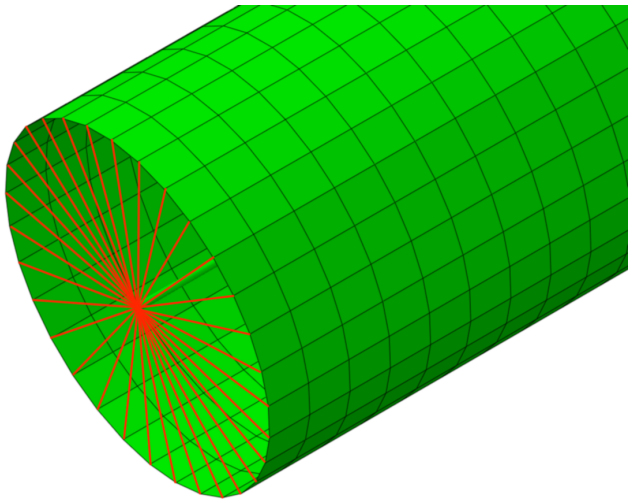

Figure 6.1: Each node of the surface element is linked to the beam nodes by rigid rods, here represented in red, which follow the degrees of freedom of the beam node.

Within Abaqus®, another type of contact modeling is offered, with the use of connector elements (Fig. 4.7), i.e. of a node-to-node contact discretization. Hence a new model has been developed, employing connector elements placed at nodes which are in contact in the initial configuration. This approach can be used only in the case of small sliding, since the contact pairing is determined once for all from the undeformed model configuration, avoiding the need to determine potential contacting nodes during the course of the analysis.

A python script is used for the generation of the model input file. The nodes of the finite element mesh are placed in correspondence of the initial contact points at each wire, which can be determined by straightforward geometric operations. In particular, (2.46) is used determining the uniform contact spacing along the helical wires at the interface between the adjacent layer. Then other nodes are placed, according to the maximum element length chosen by the user.

For the modeling of line contact between the central wire and the first layer, the node distribution along the wires should be uniform, since in this way a uniform nodal penetration generates a uniform line pressure in the penalty method framework.

In normal direction, defined as the direction connecting the two nodes, an asymmetric elastic law is assigned to the connector elements. A constant non-zero penalty stiffness is defined for negative relative normal displacement to resist penetration, while for relative opening the stiffness is set to zero (i.e. no adhesion). For the tangential behavior, the user can define basically any type of frictional interaction.

There exists different types of contact elements, according to the forces and moments that can be transferred between the nodes and to the update of the directions in which its behavior is specified (in our case, these are the contact directions). After some numerical tests, the best connector type for our application was the so-called *cartesian*: it can transfer just contact forces (no moments) and it updates the contact directions by following the rotational degrees

of freedom of one node (i.e. it employs a master-slave approach).
The forces transmitted by the connector depend on the relative motion of the two nodes. By denoting a the master node and b the slave node, the components of relative motion are defined as

$$u^x = \underline{e}_1^a \cdot (\underline{x}_b - \underline{x}_a) - x_0, \quad u^y = \underline{e}_2^a \cdot (\underline{x}_b - \underline{x}_a) - y_0, \quad u^z = \underline{e}_3^a \cdot (\underline{x}_b - \underline{x}_a) - z_0$$

in which

- x_0, y_0 and z_0 the initial coordinates of node b relative to the local coordinate system at node a,
- $\underline{x}_a$ and $\underline{x}_b$ are the position vectors respectively of node a and b,
- $\underline{e}_1^a$, $\underline{e}_2^a$, $\underline{e}_3^a$ are the three directions in which the connector behavior is specified.

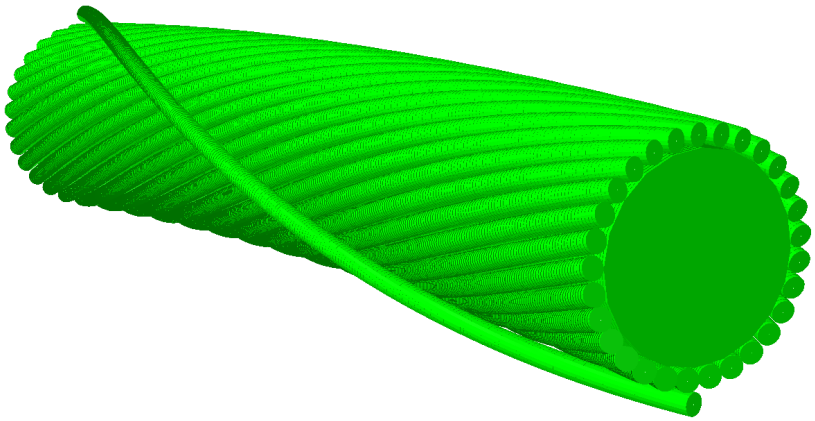

Figure 6.2: Simplified model for the sliding estimation in the mooring line.

It should be mentioned that in other connector types moments can also be transferred. However, their magnitude would be wrong, since they would be determined by considering as moment arm the distance between the nodes (i.e. between the beam axes) and not between the beam surface and the respective beam axis.
In order to investigate if the small sliding hypothesis was feasible for the case study described in Chapter 5, a simplified model of the wire rope has been considered (Fig. 6.2). It consists of applying constant tension and curvature to the central wire, within a range relevant to mooring line application to a rope portion, in which:

- the first four wire layers are substituted by a single wire, whose radius is

$$\overline{r} = r_c + 2\sum_{i=1}^{4} r_i$$

  with r_c the radius of the central wire and r_i the radius of the wires in the i-th layer;
- all the wires in the fifth layer, which is the penultimate of the real rope, are modeled and are in line contact with the central wire;

- only one wire is introduced for the last layer, whose end positions are at outer and inner arc;
- the end nodes of the helical wires are kinematically coupled to the respective end node of the central wire in order to have a plane section kinematics, hence representing correctly the kinematics of the outer wire (see Sec. 9.1.1).

This simplified model has been used to estimate the interlayer sliding in the tension-curvature range of interest for our case study. The small sliding approach has been validated (Fig. 6.3).

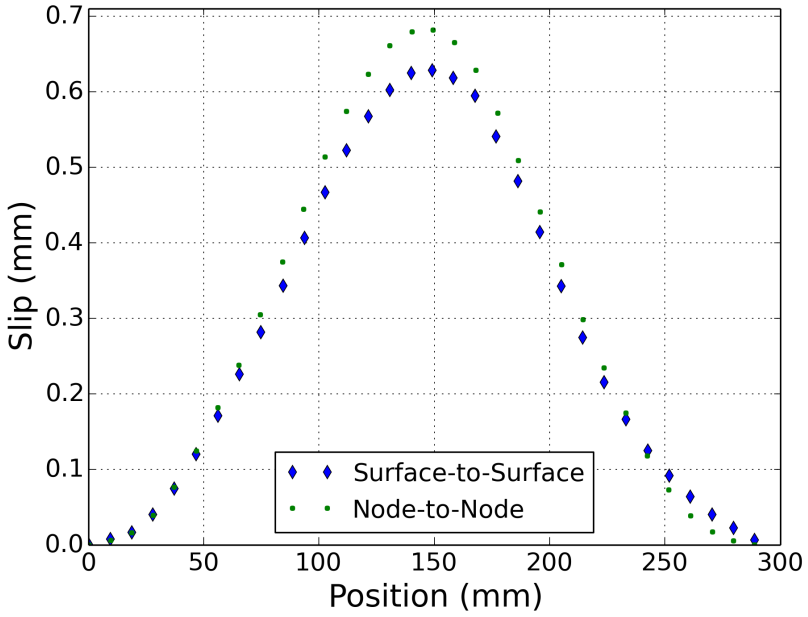

Figure 6.3: Interwire slip evaluated for the external helix in Figure 6.2, with $\varepsilon = 1.e-3$ and $\kappa = 1.3e-1\,m^{-1}$.

The results obtained with this model are in good agreement with the analytical ones (see Sec. 6.2.2), pointing out the validity of the node-to-node contact strategy. The computational cost is considerably lower with respect to any other model: this is linked to the fixed contact pairing, which basically reduces to just few operations the contact detection phase (which for curved beams is time-consuming, see Sec. 4.2.4).

Nevertheless, convergence issues have been observed when dealing with more complex problems, namely in the modeling of a multilayer wire rope in a tension-bending tests (see Sec. 8.4). The convergence is lost after some increment during the pure tension phase.

This problem is linked to the wrong update of the contact directions: since they are linked to the rotations of the master node, the wire rotations can cause irrelevant rotations of the contact normal (Fig. 6.4). This rotation may be also the reason of the sliding overestimation shown in Figure 6.3.

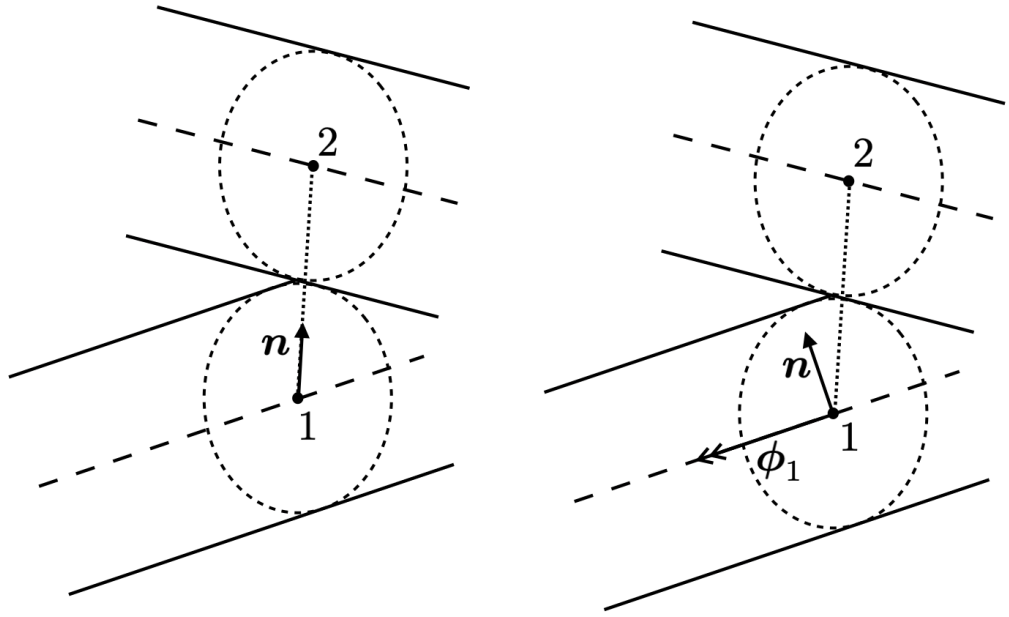

Figure 6.4: A rotation $\underline{\phi}_1$ of the master node 1 around the beam tangent causes an irrelevant rotation of the normal contact vector.

6.2 Rope benchmark tests

These benchmarks have been conceived in order to analyze the model capabilities to deal with line and trellis contacts occurring in a wire rope.

6.2.1 Description

The two benchmarks are represented in Figure 6.5. The benchmark 1 consists of a helical wire wrapped around the central wire. With this test one can analyze the capability of the different models in dealing with line contact. The benchmark 2 is composed of a layer of six helical wires and a single helical wire in contact with the layer underneath. The aim of this benchmark is to compare the results when localized contacts are involved.

All the wires have the same properties, which are reported in Table 6.1, and the friction coefficient is set to 0.5. The length of the models corresponds to two times the lay length of the respective external helix, i.e. about 127.1 mm for benchmark 1 and 254.2 mm for benchmark 2.

The ends of the helical wires are linked via a kinematic coupling to the degrees of freedom of the end nodes of the central wire. In particular, a plane end section kinematics is imposed, but the displacement and the rotation respectively in and around the radial direction are left free. Since the ends of the most external wires are in outer-arc position, it should be pointed out that these boundary conditions do not generate significant edge effects on these wires (see Sec.9.1.1).

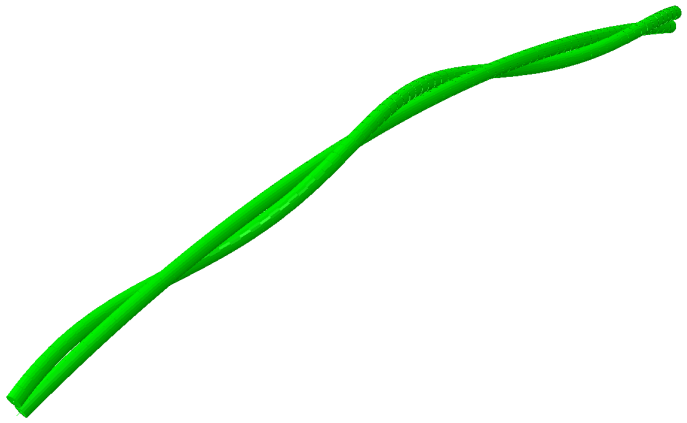

(a) *Benchmark 1*

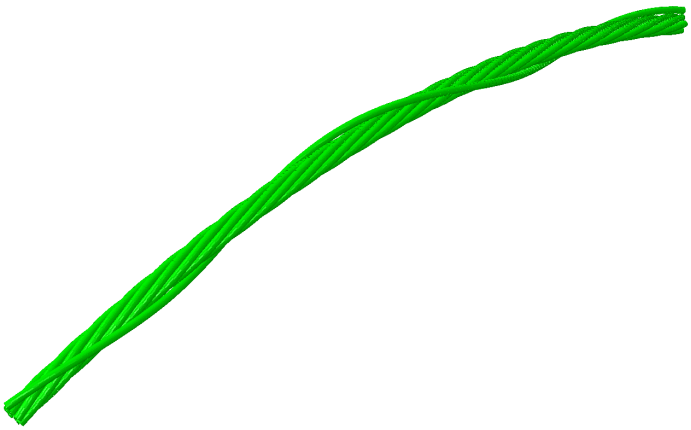

(b) *Benchmark 2*

Figure 6.5: Rope benchmarks: deformed configuration at load step 4.

Wire radius	$2.15\,mm$
Lay angle	$12°$
Young Modulus	$70\,GPa$
Poisson Coefficient	0.3

Table 6.1: Properties of the wires in benchmark 1 and 2.

The kinematics of the central wire is completely controlled in order to obtain uniform axial strain and curvature along the wire. The results in three different regimes will be analyzed:

1. pure tension ($\varepsilon = 1.e-3$, kept constant during the subsequent steps),
2. bending with small curvature (stick state), in particular $\kappa = 1.e-6\,mm^{-1}$ for benchmark 1 and $\kappa = 1.e-5\,mm^{-1}$ for benchmark 2,
3. bending with high curvature (slip state), with $\kappa = 1.e-3\,mm^{-1}$ for both benchmarks.

In order to obtain results as close as possible to the analytical ones, the contact penalty

stiffness in normal and tangential direction has to be as high as possible.

6.2.2 Results - benchmark 1

For this benchmark, the penalty parameters are the ones reported in Table 6.2.

	ϵ_N	Elastic slip
Connectors	$1.e+5\,N/mm$	$5.e-4\,mm$
Edge-to-Edge	$1.e+5\,N/mm$	$1.e-4\,mm$
Surface-to-Surface	$1.e+5\,N/mm^2$	$1.e-3\,mm$

Table 6.2: Penalty coefficients, benchmark 1.

The axial strain comparisons are shown in Fig. 6.6. Concerning the surface-to-surface model, the axial strain distributions are qualitatively in agreement with the analytical results, but shifted downwards. This is linked to the reduction of the helical radius (see eq. (2.27)), which is more important than in the other models. In particular, in the surface-to-surface case one has approximately $\Delta R = -7.5e-3\,mm$, hence by using (2.27) one gets $\varepsilon_i \approx 8.81e-4$, in accordance to what is shown in Figure 6.6a. With this simple calculation, it can be appreciated the influence that ΔR may have on the numerical results, even if its magnitude is relatively small.

The higher radius reduction in the surface-to-surface model is also a consequence of approximating the cylindrical wire surface with planar surface elements. Moreover, this generates the oscillations in the axial strain distributions in Fig. 6.6a-b.

The edge-to-edge model is not in agreement with the analytical results when bending is involved (see Fig. 6.6b-c). The extreme values appear to be shifted. In particular, both in stick and slip states the lowest values are located on the neutral plane, which is counter-intuitive. Moreover, the amplitude of the axial strain oscillations is higher than the one in the analytical solutions.

Conversely, the results obtained with the connectors are in very good agreement with the analytical predictions.

6.2.3 Results - benchmark 2

The penalty parameters used for this benchmark are reported in Table 6.3. One may see that the chosen contact stiffness is generally lower with respect to the previous benchmark (see Tab. 6.2). In fact, the localized contact positions tend to give rise to numerical instabilities and covergence difficulties at lower contact stiffness than in the line contact case.

In Fig. 6.7 the results obtained with three models are compared with the analytical ones. As for the previous benchmark, the surface-to-surface model is qualitatively in agreement with the analytical results, but its results are shifted downwards. Nevertheless, the axial strain oscillations are lower because of the helical radius contraction.

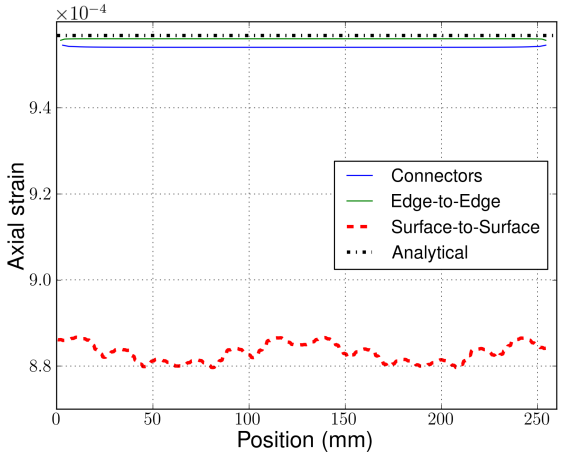

(a) *Tension*

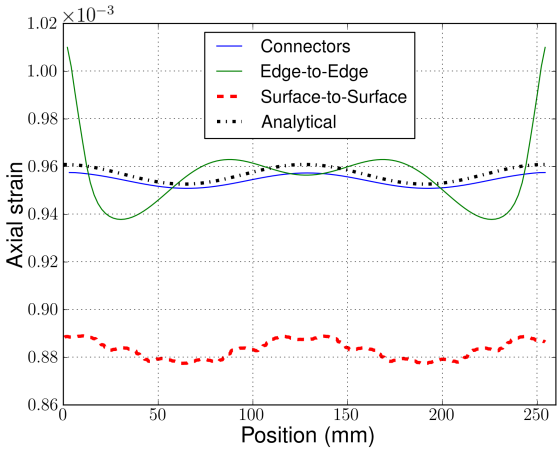

(b) *Bending - stick*

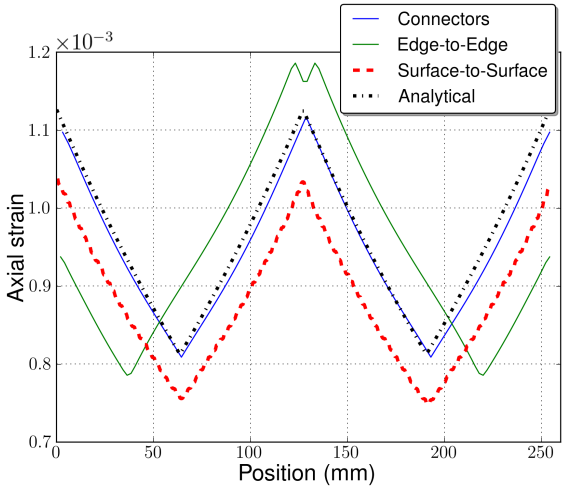

(c) *Bending - slip*

Figure 6.6: Benchmark 1: comparison between numerical and analytical results in different regimes.

	ϵ_N	Elastic slip
Connectors	$1.e+5\,N/mm$	$5.e-3\,mm$
Edge-to-Edge	$1.e+5\,N/mm$	$1.e-4\,mm$
Surface-to-Surface	$1.e+4\,N/mm^2$	$1.e-2\,mm$

Table 6.3: Penalty coefficients, benchmark 2.

- In stick state, one has to consider that the amplitude of these oscillations depends on the distance from the central axis (see (2.41)).
- In slip state, one has to consider that at lower axial force correspond lower normal contact force (eq. (2.44)),which reduces the friction forces, generating a lower gradient

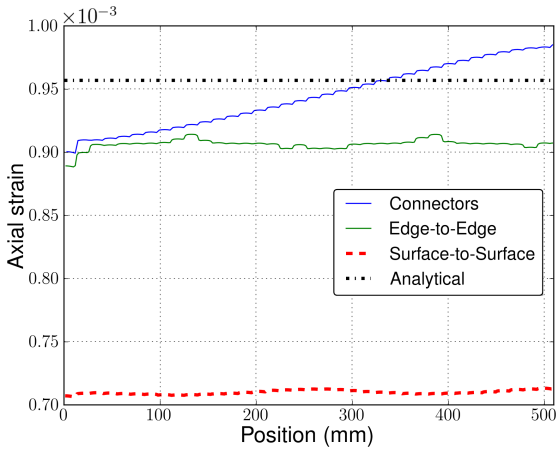

(a) *Tension*

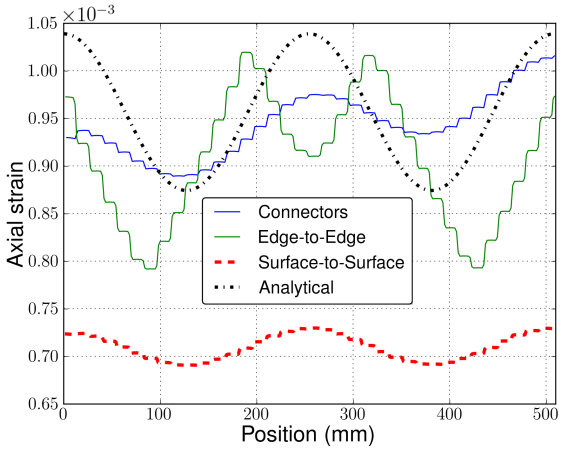

(b) *Bending - stick*

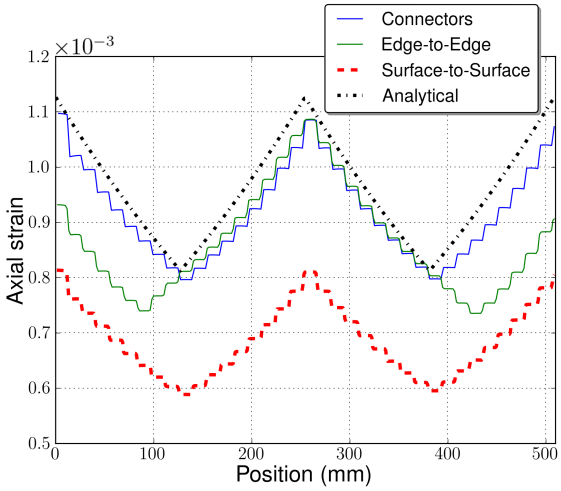

(c) *Bending - slip*

Figure 6.7: Benchmark 2: comparison between numerical and analytical results in different regimes.

in the axial strain profile.

As it happened for the benchmark 1, the edge-to-edge model is not in accordance with the analytical results when bending is involved.

Concerning the model with connector elements, one can notice that in tension and for small curvatures the axial strain is affected by a non-zero mean gradient. The cause of this behavior can be linked to an approximation of the normal contact direction.

6.3 Conclusion

We faced several limitations when using the tools in Abaqus®/Standard to model beam-to-beam contact and friction. We did not find any way to overcome these difficulties. Maybe this is possible, but our experience demonstrates the complexity of dealing properly with contact when complex geometries are considered. This is particularly true within a legacy code. The number of options does not help but their existence testifies in favor of the need to develop specific procedures depending of the test case, which could explain the difficulty one has if the treated case does not belong to a certain category.

Chapter 7

Development of a new contact element

From the results obtained employing the connector elements, one could state that the use of a node-to-node contact discretization is very attractive from a computational point of view. However the lack of convergence linked to a non-optimal update of the contact directions limits the use of the connector elements already available in Abaqus® to just simple cases.

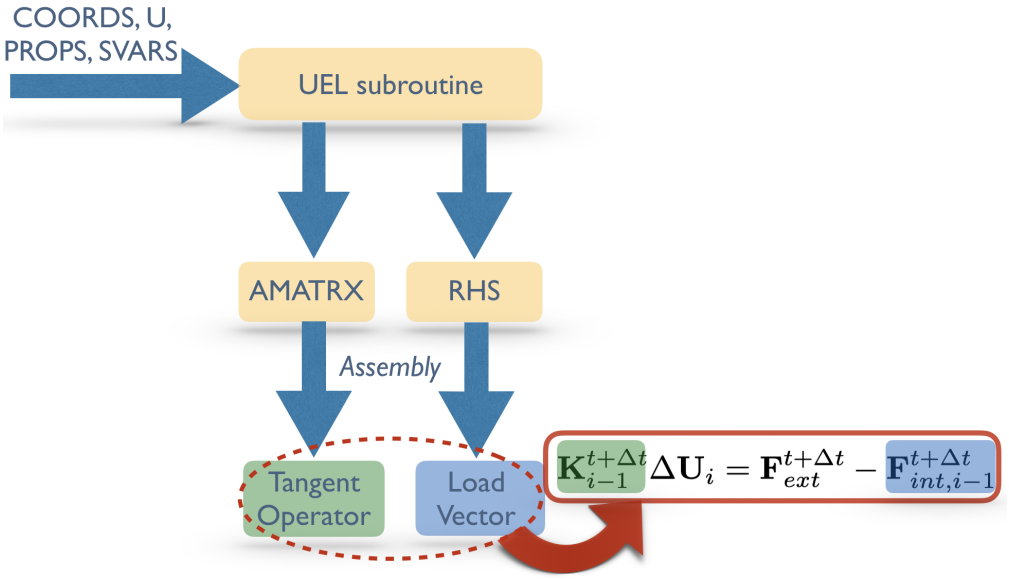

Figure 7.1: User-element scheme. The name of the variables are chosen as reported in [1].

This observation motivated the development of a new node-to-node contact element, with a correct update of the contact directions. Once formulated, the element has been coded in a user-subroutine UEL (User ELement).

The user-element subroutine is called by the solver at each iteration and for each user-element in the model. The subroutine receives in input the nodal kinematics (initial coordinates, displacements, rotations, last converged increment of displacements and rotations) and the values of the element state variables. As output, the subroutine yields the updated state

variables, the element stiffness matrix and load vector. From the latter two, the solver builds up the global tangent operator and the global load vector respectively, in the assembly phase (Fig. 7.1).

7.1 Contact kinematics

The element is formulated for the contact of non-parallel beams, assuming a pointwise contact interaction. It is a two-node contact element and the contact pairing is determined once for all from the undeformed (reference) configuration. Therefore, for the contact kinematics small sliding is considered, but large rotations may occur.

The use of this contact element can be extended to the modeling of line contact, provided that the beam nodes are evenly distributed and that the beams are non-parallel. Hence, considering wire rope modeling, it can be used for the interlayer contacts (including first layer with central wire) but it cannot be used for the simulation of contact between wires in the same layer.

7.1.1 Definition of normal and "apparent" tangential gap

Being a node-to-node contact formulation, the mesh generation procedure is the one already employed for the model with the connector elements (see Sec. 6.1.3). Beam meshes are therefore defined in order to locate mesh nodes at the locations which minimize the distance between the two beams, that we denote $\underline{X}_1$ and $\underline{X}_2$.

Regarding the modeling of line contact between non parallel beams, the nodes have to be equally spaced along the beam axes, in order to obtain a uniform line pressure in case of a uniform penetration (in the penalty method framework).

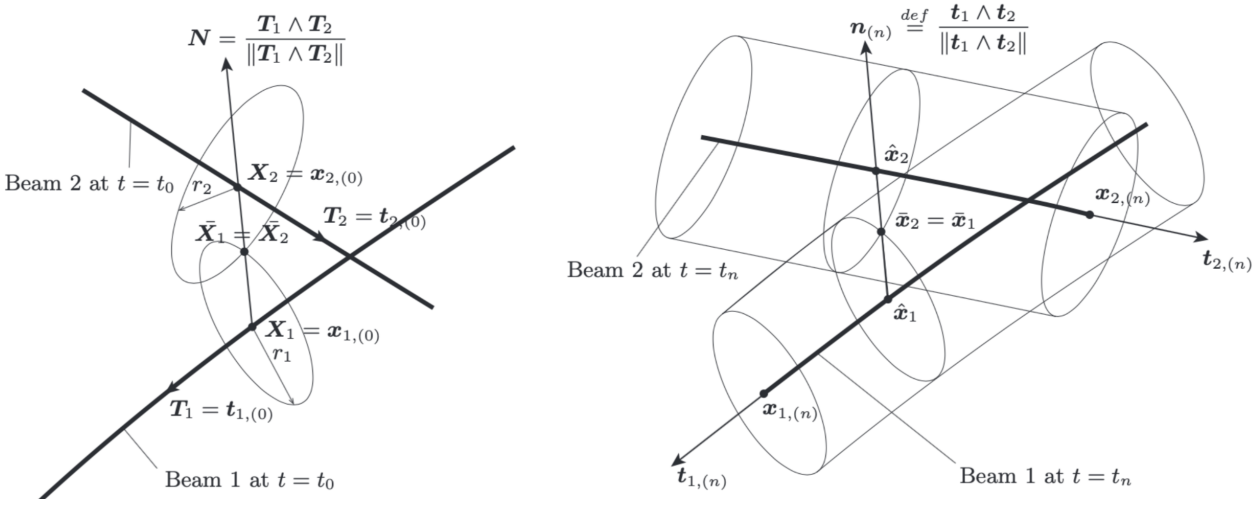

Figure 7.2: Beam-to-beam contact in the initial configuration (increment $t = 0$) on the left and in a generic deformed configuration (increment $t = n + 1$) on the right.

The contact normal in the reference (initial) configuration (Fig. 7.2) is defined as follows:

$$\underline{N} = \frac{\underline{T}_1 \wedge \underline{T}_2}{\|\underline{T}_1 \wedge \underline{T}_2\|} = \frac{\underline{X}_2 - \underline{X}_1}{\|\underline{X}_2 - \underline{X}_1\|} \tag{7.1}$$

where $\underline{T}_1$ (resp. $\underline{T}_2$) is the tangent director of beam 1 (resp. beam 2) at node $\underline{X}_1$ (resp. $\underline{X}_2$). For beams initially in contact and having circular cross-section, the "virtual" contact point is the point $\bar{\underline{X}}_1 = \bar{\underline{X}}_2$ such that:

$$\bar{\underline{X}}_1 - \underline{X}_1 = r_1\,\underline{N} \quad \text{and} \quad \bar{\underline{X}}_2 - \underline{X}_2 = -r_2\,\underline{N}$$

where r_1 and r_2 are the beam radii.
In the current configuration (Fig. 7.2), $\underline{x}_1$ (resp. $\underline{x}_2$) is determined by adding the displacement $\underline{u}_1$ (resp. $\underline{u}_2$) to the reference configuration:

$$\underline{x}_1 = \underline{X}_1 + \underline{u}_1 \quad \text{and} \quad \underline{x}_2 = \underline{X}_2 + \underline{u}_2$$

Points $\hat{\underline{x}}_1$ and $\hat{\underline{x}}_2$ are the two beam points that minimize the distance between beam 1 and beam 2 such that:

$$\begin{cases} (\hat{\underline{x}}_2 - \hat{\underline{x}}_1) \cdot \underline{t}_1(\hat{\underline{x}}_1) &= 0 \\ (\hat{\underline{x}}_2 - \hat{\underline{x}}_1) \cdot \underline{t}_2(\hat{\underline{x}}_2) &= 0 \end{cases} \tag{7.2}$$

If contact occurs and assuming constant beam radii (i.e. the Poisson effect and any degradation of the surfaces are neglected), the contact point $\bar{\underline{x}}_2 = \bar{\underline{x}}_1$ is such that:

$$\bar{\underline{x}}_1 - \hat{\underline{x}}_1 = r_1\,\underline{n} \quad \text{and} \quad \bar{\underline{x}}_2 - \hat{\underline{x}}_2 = -r_2\,\underline{n}$$

where the contact normal is defined by:

$$\underline{n} = \frac{\underline{t}_1(\hat{\underline{x}}_1) \wedge \underline{t}_2(\hat{\underline{x}}_2)}{\|\underline{t}_1(\hat{\underline{x}}_1) \wedge \underline{t}_2(\hat{\underline{x}}_2)\|} = \frac{\hat{\underline{x}}_2 - \hat{\underline{x}}_1}{\|\hat{\underline{x}}_2 - \hat{\underline{x}}_1\|}$$

In this work, under the small-sliding assumption, the beam tangent at point $\hat{\underline{x}}_1$ (resp. $\hat{\underline{x}}_2$) is assumed to be very closed to the tangent at point $\underline{x}_1$ (resp. $\underline{x}_2$). In other words, one assumes that beams remain locally straight in the proximity of the initial contact position. Therefore, the contact normal is here defined by:

$$\underline{n} \overset{def}{=} \frac{\underline{t}_1(\underline{x}_1) \wedge \underline{t}_2(\underline{x}_2)}{\|\underline{t}_1(\underline{x}_1) \wedge \underline{t}_2(\underline{x}_2)\|} \tag{7.3}$$

Subsequently, the definition (7.2) of points $\hat{\underline{x}}_1$ and $\hat{\underline{x}}_2$ is changed into:

$$\begin{cases} \hat{\underline{x}}_1 \overset{def}{=} \underline{x}_1 + \xi^1 \underline{t}_1(\underline{x}_1) \\ \hat{\underline{x}}_2 \overset{def}{=} \underline{x}_2 - \xi^2 \underline{t}_2(\underline{x}_2) \end{cases}$$

where ξ^1 and ξ^2 are the contravariant components of the "apparent" tangential gap between nodes $\underline{x}_1$ and $\underline{x}_2$ defined by (Fig. 7.3):

$$\hat{\underline{g}}_T = \Pi\,(\underline{x}_2 - \underline{x}_1) = \xi^1 \underline{t}_1(\underline{x}_1) + \xi^2 \underline{t}_2(\underline{x}_2) \tag{7.4}$$

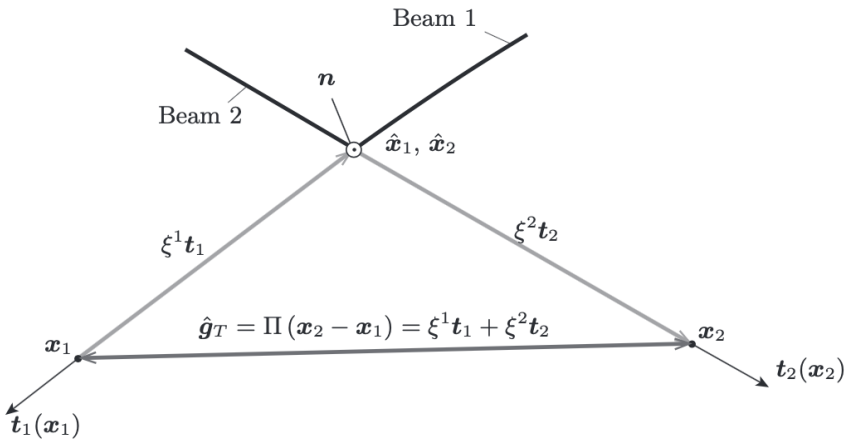

Figure 7.3: Projected view of the apparent tangential gap $\underline{\hat{g}}_T$ on the contact tangent plane.

and where $\Pi(\cdot) = (\underline{\underline{I}}_d - \underline{n} \otimes \underline{n})(\cdot)$ is the projection operator on the local tangent plane defined by normal $\underline{n}$. The "apparent" tangential gap $\underline{\hat{g}}_T$ and the "accumulated" tangential gap function $\underline{g}_T$ that will be defined in (7.31) must not be confused.
The current gap can then be decomposed into a normal and a tangential parts as follows:

$$\underline{g} = \underline{x}_2 - \underline{x}_1 - (r_1 + r_2)\,\underline{n} = g_N\,\underline{n} + \underline{\hat{g}}_T \tag{7.5}$$

with:

$$\left\{ \begin{array}{rcl} g_N & = & (\underline{x}_2 - \underline{x}_1) \cdot \underline{n} - (r_1 + r_2) \\ \underline{\hat{g}}_T & = & \Pi\,(\underline{x}_2 - \underline{x}_1) = \xi^1 \underline{t}_1(\underline{x}_1) + \xi^2 \underline{t}_2(\underline{x}_2) \end{array} \right.$$

The inequality constraint of the non-penetration condition reads:

$$g_N = (\underline{x}_2 - \underline{x}_1) \cdot \underline{n} - (r_1 + r_2) \geqslant 0$$

A penetration function (for penalty method) can also be defined:

$$\bar{g}_N = \left\{ \begin{array}{cc} (\underline{x}_2 - \underline{x}_1) \cdot \underline{n} - (r_1 + r_2) & \text{if } (\underline{x}_2 - \underline{x}_1) \cdot \underline{n} - (r_1 + r_2) < 0 \\ 0 & \text{otherwise} \end{array} \right. \tag{7.6}$$

It should be noticed that since the normal $\underline{n}$ is defined from beam directors $\underline{t}_1$ and $\underline{t}_2$, the choice of the orientations of beam directors $\underline{t}_1$ and $\underline{t}_2$ has to be done so that the normal is oriented from beam 1 to beam 2. This orientation convention can be done accordingly and explicitly from the initial contact configuration.

7.1.2 Definition of beam tangent directors

A beam tangent director $\underline{t}_i$ in the current configuration is defined as the initial tangent $\underline{T}_i$ rotated according to the rotation vector of the correspondent node $\underline{\Phi}_i$ (represented by rotation degrees of freedom):

$$\underline{t}_i = \underline{\underline{R}}(\underline{\Phi}_i)\underline{\Phi}_i \tag{7.7}$$

Let us define the skew-symmetric matrix $\hat{\underline{\underline{\Phi}}}_i$ associated with $\underline{\Phi}_i$ by the relationships:

$$\hat{\underline{\underline{\Phi}}}_i \, \underline{\Phi}_i = \underline{0} \quad \text{and} \quad \hat{\underline{\underline{\Phi}}}_i \, \underline{v} = \underline{\Phi}_i \wedge \underline{v}$$

for all vectors $\underline{v}$. The rotation matrix $\underline{\underline{R}}(\underline{\Phi}_i)$ in (7.7) is expressed as

$$\underline{\underline{R}}(\underline{\Phi}_i) = \underline{\underline{R}}_i = \exp \hat{\underline{\underline{\Phi}}}_i = \underline{\underline{I}}_d + \hat{\underline{\underline{\Phi}}}_i + \frac{1}{2!}\hat{\underline{\underline{\Phi}}}_i^{\,2} + \dots$$

However, the above infinite series has the following closed-form expression:

$$\underline{\underline{R}}_i = \exp \hat{\underline{\underline{\Phi}}}_i = \cos\|\underline{\Phi}_i\| \underline{\underline{I}}_d + \frac{\sin\|\underline{\Phi}_i\|}{\|\underline{\Phi}_i\|}\hat{\underline{\underline{\Phi}}}_i + \frac{1-\cos\|\underline{\Phi}_i\|}{\|\underline{\Phi}_i\|^2}\underline{\Phi}_i\underline{\Phi}_i^T \tag{7.8}$$

$$= \underline{\underline{I}}_d + \frac{\sin\|\underline{\Phi}_i\|}{\|\underline{\Phi}_i\|}\hat{\underline{\underline{\Phi}}}_i + \frac{1-\cos\|\underline{\Phi}_i\|}{\|\underline{\Phi}_i\|^2}\hat{\underline{\underline{\Phi}}}_i^{\,2} \tag{7.9}$$

where the second expression is obtained by noting that $\underline{\Phi}_i\underline{\Phi}_i^T = \|\underline{\Phi}_i\|^2\underline{\underline{I}}_d + \hat{\underline{\underline{\Phi}}}_i^{\,2}$.
In the following, $\underline{t}_1$ and $\underline{t}_2$ denote respectively the beam tangent directors $\underline{t}_1\left(\underline{\Phi}(\underline{x}_1)\right)$ and $\underline{t}_2\left(\underline{\Phi}(\underline{x}_2)\right)$ in order to alleviate the notations. Note that tangent director $\underline{t}$ is not necessarily tangent to the beam axis in the deformed configuration due to the shear deformation contribution. In our case, wires are very slender and shear deformation contribution can reasonably neglected.

7.1.3 Covariant and contravariant components for the tangential gap

From (7.4) one can see that the projection of the nodes on the tangential plane $\hat{\underline{g}}_T$ is defined by the components ξ^i along the beam tangents, which in general are not orthogonal. For this reason, we have to introduce the (covariant) basis $(\underline{t}_1, \underline{t}_2, \underline{n})$ and its dual (contravariant) basis $(\underline{t}^1, \underline{t}^2, \underline{n})$ such that $\underline{t}^j \cdot \underline{t}_i = \delta_i^j$. Then one can define the covariant and contravariant components with respect to the covariant and contravariant basis for a vector which lies in the tangent plane.
By introducing the (symmetric second order) metric tensor $\underline{\underline{M}}$ such that $M_{ij} = \underline{t}_i \cdot \underline{t}_j$ such that:

$$\underline{t}^i = M^{ij}\underline{t}_j \quad \text{with} \quad M^{ij}M_{jk} = \delta_k^i = \delta_i^k$$

one easily deduces the following relation between the covariant and contravariant components:

$$\xi_i M^{ij} = \xi^j \quad \text{and} \quad \xi_i = M_{ij}\xi^j$$

Covariant and contravariant components have to be clearly distinguished. Note that M^{ij} denotes a given component of the inverse of metric tensor $\underline{\underline{M}}$.
Starting from (7.4), one gets (Fig. 7.3):

$$\hat{\underline{g}}_T = \Pi\left(\underline{x}_2 - \underline{x}_1\right) = \bar{\underline{x}}_2(\xi^1, \xi^2) - \underline{x}_1 = \xi^1\underline{t}_1(\underline{x}_1) + \xi^2\underline{t}_2(\underline{x}_2)$$

where is it has been chosen to consider a tangential plane passing from $\underline{x}_1$. It can be noticed that this choice is completely arbitrary and does not affect the results in the following. Thus,

$$\xi^i = \left(\bar{\underline{x}}_2(\xi^1,\xi^2) - \underline{x}_1\right)\cdot\underline{t}^i = (\underline{x}_2 - \underline{x}_1)\cdot\left(M^{ij}\underline{t}_j\right)$$

Therefore we get

$$\begin{pmatrix}\xi^1\\ \xi^2\end{pmatrix} = \underline{\underline{M}}^{-1}\begin{pmatrix}(\underline{x}_2-\underline{x}_1)^T & \underline{0}\\ \underline{0} & (\underline{x}_2-\underline{x}_1)^T\end{pmatrix}\begin{pmatrix}\underline{t}_1\\ \underline{t}_2\end{pmatrix} = \underline{\underline{M}}^{-1}\underline{\underline{A}}\begin{pmatrix}\underline{t}_1\\ \underline{t}_2\end{pmatrix} \tag{7.10}$$

$$\begin{pmatrix}\xi_1\\ \xi_2\end{pmatrix} = \underline{\underline{M}}\begin{pmatrix}\xi^1\\ \xi^2\end{pmatrix} = \begin{pmatrix}(\underline{x}_2-\underline{x}_1)^T & \underline{0}\\ \underline{0} & (\underline{x}_2-\underline{x}_1)^T\end{pmatrix}\begin{pmatrix}\underline{t}_1\\ \underline{t}_2\end{pmatrix} \tag{7.11}$$

Note that the "apparent tangential gap $\hat{\underline{g}}_T$ must not be confused with the tangential gap function $\underline{g}_T^{e,tr}$ defined in Sec. 7.3.2, which will be used for the integration of the tangential contact interaction, and with the total tangential gap $\underline{g}_T$ defined in Sec. 7.1.6.

7.1.4 Variation of normal and apparent tangential gap

Since $\bar{\underline{x}}_2(\xi^1,\xi^2) - \underline{x}_1 = \hat{\underline{g}}_T$, one deduces that:

$$g_N\,\underline{n} = (\underline{x}_2 - \underline{x}_1) - \hat{\underline{g}}_T - (r_1+r_2)\underline{n}$$

Taking the variation of this equation leads to:

$$\begin{aligned}\delta g_N\,\underline{n} + g_N\,\delta\underline{n} &= \delta\underline{x}_2 - \delta\underline{x}_1 - \delta\hat{\underline{g}}_T - (r_1+r_2)\delta\underline{n} &(7.12)\\ &= \delta\underline{x}_2 - \delta\underline{x}_1 - \delta\left(\xi^i\,\underline{t}_i\right) - (r_1+r_2)\delta\underline{n} &(7.13)\\ &= \delta\underline{x}_2 - \delta\underline{x}_1 - \delta\xi^i\,\underline{t}_i - \xi^i\,\delta\underline{t}_i - (r_1+r_2)\delta\underline{n} &(7.14)\end{aligned}$$

Note that, since $\underline{t}_i$ depends on the rotation vector $\underline{\Phi}(\underline{x}_i)$, variations $\delta\underline{t}_i$ (as well as $\delta\underline{n}$) has to be accounted for. Taking the dot product of this equation with $\underline{n}$ results in the following expression for δg_N:

$$\delta g_N = \left(\delta\underline{x}_2 - \delta\underline{x}_1 - \xi^i\,\delta\underline{t}_i\right)\cdot\underline{n} = (\delta\hat{\underline{x}}_2 - \delta\hat{\underline{x}}_1)\cdot\underline{n} = (\delta\bar{\underline{x}}_2 - \delta\bar{\underline{x}}_1)\cdot\underline{n} \tag{7.15}$$

since $\underline{t}_i\cdot\underline{n} = 0$ and $\underline{n}\cdot\delta\underline{n} = 0$ due to the fact that $\|\underline{n}\| = \underline{n}\cdot\underline{n} = 1$ that implies $\delta(\underline{n}\cdot\underline{n}) = \underline{n}\cdot\delta\underline{n} = 0$.
Likewise, taking the dot product of (7.12) with $\underline{t}_j$ results in the following expression:

$$g_N\,\delta\underline{n}\cdot\underline{t}_j = (\delta\underline{x}_2 - \delta\underline{x}_1)\cdot\underline{t}_j - \delta\xi^i\,\underline{t}_i\cdot\underline{t}_j - \xi^i\,\delta\underline{t}_i\cdot\underline{t}_j - (r_1+r_2)\delta\underline{n}\cdot\underline{t}_j \tag{7.16}$$

Since one has the following conditions:

$$\left\{\begin{array}{lll}\underline{n}\cdot\underline{t}_i = 0 & \Rightarrow & \delta(\underline{n}\cdot\underline{t}_i) = \delta\underline{n}\cdot\underline{t}_i + \underline{n}\cdot\delta\underline{t}_i = 0 \Rightarrow \delta\underline{n}\cdot\underline{t}_i = -\underline{n}\cdot\delta\underline{t}_i\\ \underline{n}\cdot\underline{n} = 1 & \Rightarrow & \delta(\underline{n}\cdot\underline{n}) = \underline{n}\cdot\delta\underline{n} = 0\\ \underline{t}_i\cdot\underline{t}^j = 0 & \Rightarrow & \delta(\underline{t}_i\cdot\underline{t}^j) = \underline{t}_i\cdot\delta\underline{t}^j + \delta\underline{t}_i\cdot\underline{t}^j = 0 \Rightarrow \underline{t}_i\cdot\delta\underline{t}^j = -\delta\underline{t}_i\cdot\underline{t}^j\end{array}\right. \tag{7.17}$$

one deduces the variation of the contravariant component ξ^i or contravariant ξ_j:

$$\begin{array}{rrcl} & -g_N\,\underline{n}\cdot\delta\underline{t}_j &=& (\delta\underline{x}_2-\delta\underline{x}_1)\cdot\underline{t}_j-\delta\xi^i\,M_{ij}-\xi^i\,\delta\underline{t}_i\cdot\underline{t}_j+(r_1+r_2)\,\underline{n}\cdot\delta\underline{t}_j \\ \Leftrightarrow & \delta\xi^i\,M_{ij} &=& (\delta\underline{x}_2-\delta\underline{x}_1)\cdot\underline{t}_j-\xi^i\,\delta\underline{t}_i\cdot\underline{t}_j+(g_N+r_1+r_2)\,\underline{n}\cdot\delta\underline{t}_j \\ \Leftrightarrow & \delta\xi^i\,M_{ij}=\delta\xi_j &=& (\delta\underline{x}_2-\delta\underline{x}_1-\xi^i\,\delta\underline{t}_i)\cdot\underline{t}_j+(g_N+r_1+r_2)\,\underline{n}\cdot\delta\underline{t}_j \end{array} \tag{7.18}$$

Note that the variation depends on ξ^i, the normal gap g_N and the beam radii r_1 and r_2. It can also been shown that:

$$\delta\xi_j=\delta(\hat{\underline{g}}_T\cdot\underline{t}_j)=(\delta\underline{x}_2-\delta\underline{x}_1)\cdot\underline{t}_j+(\underline{x}_2-\underline{x}_1)\,\delta\underline{t}_j$$

7.1.5 Increment of tangential gap

Considering the kinematics described so far, we have now to define the tangential gap increment $\underline{g}_T^{\Delta}$, defined by the relative displacement experienced by the material points $\bar{\underline{x}}_1$ and $\bar{\underline{x}}_2$ that were in contact in configuration at t_n, projected on the new tangential plane in configuration t_{n+1}.

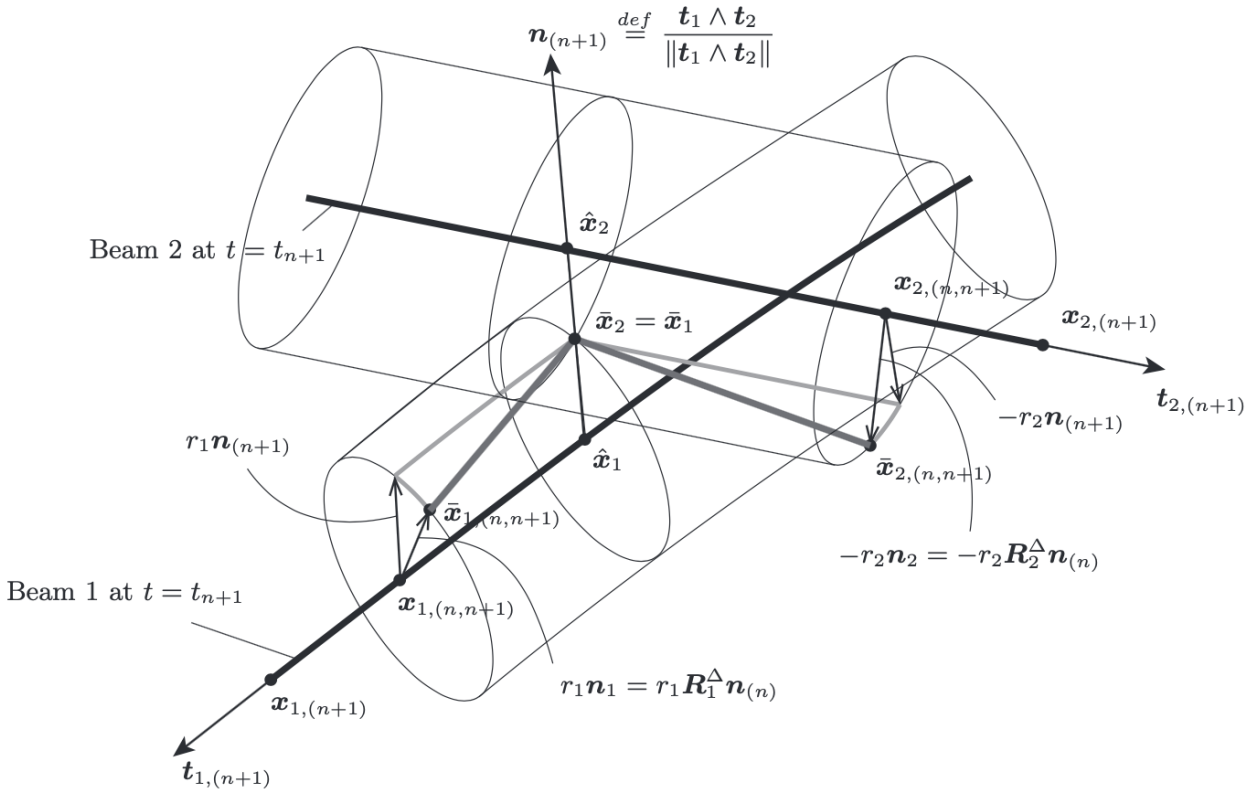

Figure 7.4: Projected view of the apparent tangential gap $\hat{\underline{g}}_T$ on the contact tangent plane.

Firstly, $\bar{\underline{x}}_1$ and $\bar{\underline{x}}_2$ are mapped in the new configuration at t_{n+1} (Fig. 7.4). These new positions are denoted respectively $\bar{\underline{x}}_{1,(n,n+1)}$ and $\bar{\underline{x}}_{2,(n,n+1)}$, where first index n refers to the fact that

they were the material points in contact at configuration n and second index $n+1$ refers to the configuration where the material points are mapped. The new material points in contact are simply denoted by $\bar{\underline{x}}_{1,(n+1)}$ and $\bar{\underline{x}}_{2,(n+1)}$.
For each beam, on time increment $\Delta t_{n+1} = t_{n+1} - t_n$, the distance between the previous material point in contact in configuration n and the current material point in contact at configuration $n+1$ can be defined for each beam as

$$\left\{ \begin{array}{rcl} \underline{d}_1^{\Delta} & = & \bar{\underline{x}}_{1,(n,n+1)} - \bar{\underline{x}}_{1,(n+1)} \\ \underline{d}_2^{\Delta} & = & \bar{\underline{x}}_{2,(n,n+1)} - \bar{\underline{x}}_{2,(n+1)} \end{array} \right. \tag{7.19}$$

The normal direction changes in the new configuration (Fig. 7.2) and is defined by:

$$\underline{n}_{(n+1)} \overset{def}{=} \frac{\underline{t}_{1,(n+1)} \wedge \underline{t}_{1,(n+1)}}{\|\underline{t}_{1,(n+1)} \wedge \underline{t}_{2,(n+1)}\|}$$

where $\underline{t}_{i,(n+1)} = \underline{t}_i(\underline{x}_{i,(n+1)})$ denotes the current director of beam i at material point $\underline{x}_{i,(n+1)}$.

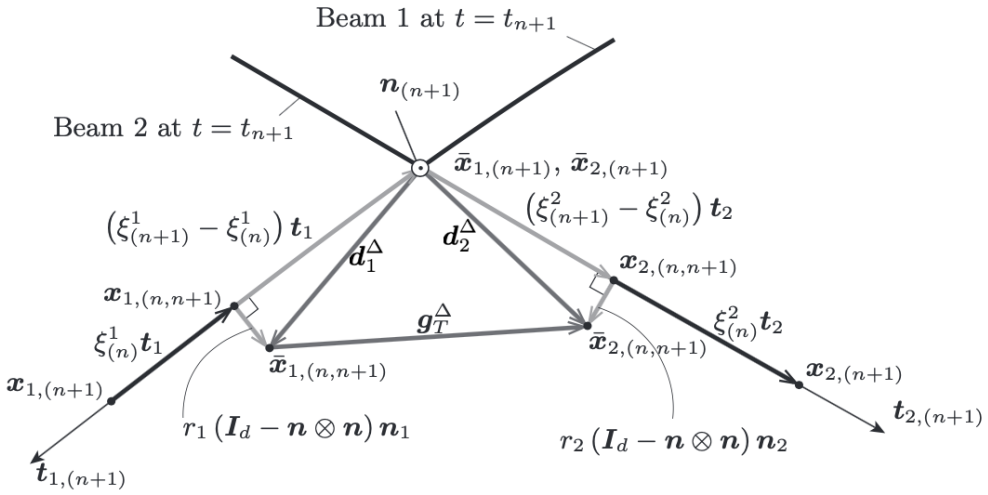

Figure 7.5: Tangential sliding components projected on the tangential plane at increment $n+1$.

The increment of tangential gap $\underline{g}_T^{\Delta}$ is defined as the projection of the difference between $\underline{d}_2^{\Delta}$ and $\underline{d}_1^{\Delta}$ in the current tangent contact plane at configuration $n+1$. To alleviate the notation, the subscript $(n+1)$ to indicate a quantity referred to the current time increment will be discarded from now on. One has (Fig. 7.5):

$$\underline{g}_T^{\Delta} = (\underline{\underline{I}}_d - \underline{n} \otimes \underline{n})(\underline{d}_2^{\Delta} - \underline{d}_1^{\Delta}) \tag{7.20}$$

with

$$\begin{array}{rcl} \underline{d}_1^{\Delta} & = & \underline{x}_1 + \xi^1_{(n)} \underline{t}_1 + r_1 \underline{n}_1 - (\underline{x}_1 + \xi^1 \underline{t}_1 + r_1 \underline{n}) \\ & = & -(\xi^1 - \xi^1_{(n)}) \underline{t}_1 + r_1 (\underline{n}_1 - \underline{n}) \\ \underline{d}_2^{\Delta} & = & \underline{x}_2 - \xi^2_{(n)} \underline{t}_2 - r_2 \underline{n}_2 - (\underline{x}_2 - \xi^2 \underline{t}_1 - r_2 \underline{n}) \\ & = & (\xi^2 - \xi^2_{(n)}) \underline{t}_2 - r_2 (\underline{n}_2 - \underline{n}) \end{array} \tag{7.21}$$

$$\underline{n}_1 = \underline{\underline{R}}_1^{\Delta}\underline{n}_{(n)}; \quad \underline{\underline{R}}_1^{\Delta} = \underline{\underline{R}}(\underline{\Phi}_1^{\Delta}) \tag{7.22}$$

$$\underline{n}_2 = \underline{\underline{R}}_2^{\Delta}\underline{n}_{(n)}; \quad \underline{\underline{R}}_2^{\Delta} = \underline{\underline{R}}(\underline{\Phi}_2^{\Delta}) \tag{7.23}$$

and in which $\underline{\Phi}_i^{\Delta}$ is the rotation in the current increment of beam i. Therefore one gets

$$\begin{array}{rl} \underline{g}_T^{\Delta} & = (\underline{\underline{I}}_d - \underline{n}\otimes\underline{n})[(\xi^i - \xi^i_{(n)})\underline{t}_i - r_i\underline{n}_i] \\ & = (\xi^i - \xi^i_{(n)})\underline{t}_i - (\underline{\underline{I}}_d - \underline{n}\otimes\underline{n})r_i\underline{n}_i \end{array} \tag{7.24}$$

This definition of $\underline{g}_T^{\Delta}$ is equivalent to quantifying the amount of relative sliding by approximating the actual movement histories by straight lines projected on the contact tangent plane at configuration $n+1$. It is clear that the more the time step decreases, the better the approximation of the theoretical path of the contact material point on each beam is. It can be noted that with this definition of $\underline{g}_T^{\Delta}$ also relative movements generated by rolling are taken into account.

First terms $\left(\xi^i - \xi^i_{(n)}\right)\underline{t}_i$ reflects the relative sliding in the beam axes direction and the term $\left(\underline{\underline{I}}_d - \underline{n}\otimes\underline{n}\right)(r_1\underline{n}_1 + r_2\underline{n}_2)$ is associated with sliding along the circumferential directions of each beam. This second term is not considered when the contact problem between beams is treated as contact between curves, as occurs in [169]. In other words, the sliding between curves can be described by the evolution of the parameters ξ^i, while the characterization of the sliding between the beam surfaces, being two-dimensional, requires two components. This has been done for instance in [104], where the beam surfaces are described by couples of convective coordinates.

Since $\underline{\underline{I}}_d - \underline{n}\otimes\underline{n} = \underline{t}^i\otimes\underline{t}_i = \underline{t}_i\otimes\underline{t}^i$ and $\underline{n}_i\cdot\underline{t}_i = 0$, the tangential gap increment can be expressed as

$$\begin{array}{rcl} \underline{g}_T^{\Delta} = & (\underline{t}^j\otimes\underline{t}_j)[(\xi^i - \xi^i_{(n)})\underline{t}_i - r_i\underline{n}_i] \\ = & [(\xi^i - \xi^i_{(n)})\underline{t}_i\cdot\underline{t}_j - r_i\underline{n}_i\cdot\underline{t}_j]\underline{t}^j \\ = & (\xi_j - \xi^i_{(n)}M_{ij} - r_i\underline{n}_i\cdot\underline{t}_j)\underline{t}^j \\ = & [\xi_1 - \xi^i_{(n)}M_{i1} - r_2\underline{n}_2\cdot\underline{t}_1]\underline{t}^1 + [\xi_2 - \xi^i_{(n)}M_{i2} - r_1\underline{n}_1\cdot\underline{t}_2]\underline{t}^2 \\ = & g_{T1}^{\Delta}\underline{t}^1 + g_{T2}^{\Delta}\underline{t}^2 \end{array} \tag{7.25}$$

or equivalently

$$\begin{array}{rcl} \underline{g}_T^{\Delta} & = & (\underline{t}_j\otimes\underline{t}^j)[(\xi^i - \xi^i_{(n)})\underline{t}_i - r_i\underline{n}_i] \\ & = & [(\xi^i - \xi^i_{(n)})\underline{t}_i\cdot\underline{t}^j - r_i\underline{n}_i\cdot\underline{t}^j]\underline{t}_j \\ & = & [(\xi^1 - \xi^1_{(n)}) - (r_1\underline{n}_1 + r_2\underline{n}_2)\cdot\underline{t}^1]\underline{t}_1 + [(\xi^2 - \xi^2_{(n)}) - (r_1\underline{n}_1 + r_2\underline{n}_2)\cdot\underline{t}^2]\underline{t}_2 \end{array} \tag{7.26}$$

Considering (7.25), the variation can be expressed as

$$\begin{array}{l} \delta\underline{g}_T^{\Delta} = \delta\xi_i\underline{t}^i - (\xi^2_{(n)}\underline{t}^1 + \xi^1_{(n)}\underline{t}^2)\delta M_{12} + g_{Ti}^{\Delta}(M^{ij}\delta\underline{t}_j) + g_{Ti}^{\Delta}(\delta M^{ij}\underline{t}_j) - \ldots \\ \ldots r_2\left[\delta\underline{n}_2\cdot\underline{t}_1 + \underline{n}_2\cdot\delta\underline{t}_1)\right]\underline{t}^1 - r_1\left[\delta\underline{n}_1\cdot\underline{t}_2 + \underline{n}_1\cdot\delta\underline{t}_2\right]\underline{t}^2 \end{array} \tag{7.27}$$

while considering (7.26) one gets

$$\begin{array}{rl} \delta\underline{g}_T^{\Delta} = & \delta\xi^i\underline{t}_i - (r_1\delta\underline{n}_1 + r_2\delta\underline{n}_2)\underline{t}^i\cdot\underline{t}_i + (\xi^i - \xi^i_{(n)})\delta\underline{t}_i - \ldots \\ & \ldots(r_1\underline{n}_1 + r_2\underline{n}_2)(\delta M^{ij}\underline{t}_j + M^{ij}\delta\underline{t}_j)\cdot\underline{t}_i - (r_1\underline{n}_1 + r_2\underline{n}_2)\underline{t}^i\cdot\delta\underline{t}_i \end{array} \tag{7.28}$$

7.1.6 Tangential gap function

Once determined the tangential gap increment form (7.24), the total tangential gap is computed by summing the tangential gap that has been previously accumulated, that we denote $\underline{g}_{T,(n)}$.
It is worth recalling now that in the described contact kinematics arbitrary large rotations can occur. Therefore, the accumulated tangential sliding $\underline{g}_{T,(n)}$ has to be rotated in the current configuration $n+1$ before the increment (7.24) is added.
The strategy used here to perform the rotation of the tangential sliding is different with respect to the one proposed in [104], where just the rotation of one of the two contacting beams is used. We express the accumulated tangential sliding as

$$\underline{g}_{T,(n)} = \xi^{i,tot}_{(n)} \underline{t}_{i,(n)} \tag{7.29}$$

in which the coefficients $\xi^{i,tot}_{(n)}$ are determined by exploiting the relations between covariant and contravariant components detailed in Sec. 7.1.3, i.e.

$$\xi^{i,tot}_{(n)} = \underline{g}_{T,(n)} \underline{t}^{i}_{(n)}$$

It should be noticed that the components $\xi^{i,tot}_{(n)}$ has no physical meaning. However, any vector on the tangential plane can be expressed in the basis of the beam tangents. The accumulated tangential sliding can be now rotated as

$$\underline{g}_{T,(n,n+1)} = \xi^{i,tot}_{(n)} \underline{t}_{i} \tag{7.30}$$

where $\underline{t}_i$ are the beam tangents in the current configuration.
The transformation from (7.29) to (7.30) is equivalent as the one employed in [104] in the case in which the dot product of the beam tangents remains unchanged. Conversely, if $\underline{t}_1 \cdot \underline{t}_2$ varies, the accumulated sliding is rotated differently with the two approaches. However, an optimal way to perform this rotation does not exist. This is linked to the approximation that is done by considering the contact condensed in one point rather than distributed on the actual contact patch (which is elliptical, see Sec. 2.4.2).
The total tangential gap can be finally evaluated as

$$\underline{g}_{T} = \underline{g}^{\Delta}_{T} + \underline{g}_{T,(n,n+1)} \tag{7.31}$$

7.2 Constitutive equations for tangential contact

Coulomb's law and other constitutive equations for friction can be formulated in the framework of elasto-plasticity. This has been investigated by several authors who developed different constitutive equations for frictional problems (see Chapter 5 in [165]).

7.2.1 Elasto-plastic analogy for friction

The key idea of the elasto-plastic approach is a split of the tangential slip $\underline{g}_T$ into an elastic (stick or adhesive) part $\underline{g}_T^e$ and a plastic (slip) part $\underline{g}_T^s$:

$$\underline{g}_T = \underline{g}_T^e + \underline{g}_T^s \tag{7.32}$$

This split can be viewed as a regularization step of the frictional law. However, one also can find a physical interpretation, in the sense that elastic tangential micro displacements $\underline{g}_T^e$ occur at the contact interface because of the elastic behavior of the asperities in the real contact area. Hence, they model an elastic stick behavior since the associated deformations vanish once the loading is removed from the system.

The simplest possible model for the elastic part of the tangential contact is an isotropic linear elastic relation, which yields:

$$\underline{t}_T = \varepsilon_T \, \underline{g}_T^e \tag{7.33}$$

where ε_T is the tangential elastic constant.

The plastic frictional tangential slip $\underline{g}_T^s$ is governed by a constitutive evolution equation which can be formally derived by using standard concepts of elasto-plasticity theory [87]. Let us introduce for the derivation of a slip rule, in analogy to the derivation of a plastic flow rule, the dissipation:

$$\mathcal{D}^s = \underline{t}_T \cdot \dot{\underline{g}}_T^s \geqslant 0$$

due to the plastic slip increment. Now consider an elastic domain:

$$\mathbb{E}_T = \left\{ \underline{t}_T \in \mathbb{R}^3 \,|\, f_s(\underline{t}_T) \leqslant 0 \right\}$$

in the space of the contact tangential stress. A simple expression for f_s is given by:

$$f_s(\underline{t}_T) = \|\underline{t}_T\| - \mu \, p_N \leqslant 0 \tag{7.34}$$

which is the plastic slip criterion for a given (positive) contact pressure p_N, and is equivalent to classical Coulomb's law. The frictional coefficient μ is a parameter depending on the properties of the contacting surfaces.

The evolution equation for the plastic slip can now be computed from the maximum dissipation principle, well known from the theory of plasticity. The derivation is done here assuming the simple slip criterion (7.34), however the methods also hold for more advanced slip criteria. Additionally, one has the loading-unloading conditions in Kuhn-Tucker form:

$$\dot{\gamma} \geqslant 0, \quad f_s(\underline{t}_T) \leqslant 0, \quad \dot{\gamma} f_s(\underline{t}_T) = 0$$

which determine the plastic parameter $\dot{\gamma}$.

To sum up, the constitutive evolution equation for the plastic or frictional slip can be stated in a general form of a slip rule for large deformations in the contact zone as

$$\dot{\underline{g}}_T^s = \dot{\gamma} \, \frac{\partial f_s(\underline{t}_T)}{\partial \underline{t}_T} = \dot{\gamma} \, \underline{n}_T \quad \text{with} \quad \underline{n}_T = \frac{\underline{t}_T}{\|\underline{t}_T\|} \tag{7.35}$$

$\dot{\gamma}$ is a parameter which describes the magnitude of the plastic slip.

Anisotropic behavior

One can also think of anisotropic elastic constitutive behavior leading to:

$$\underline{t}_T = \underline{\underline{C}}_T \, \underline{g}^e_T \tag{7.36}$$

with the constitutive tensor $\underline{\underline{C}}_T$. The non-isotropic behavior is sometimes necessary. Models for anisotropic friction can be found in [100, 55, 101, 57] The model introduced in [100] is expressed in an orthogonal cartesian reference frame in the tangent plane of the contact interface. With respect to that, the slip function is described by a super ellipse:

$$f_s(p_N, t_{Tx}, t_{Ty}) = \left[\left(\frac{t_{Tx}}{\mu_x} \right)^n + \left(\frac{t_{Ty}}{\mu_y} \right)^n \right]^{1/n} - p_N \tag{7.37}$$

where t_{Tx} and t_{Ty} denote the tangential stresses in x and y directions, while n is a parameter which determines the form of the ellipse. This model assumes a special case of anisotropic behavior which has different friction parameters with respect to the cartesian coordinate axes. The evolution equation is now given by two equations for the x and y directions

$$\dot{g}^s_{Tx} = \dot{\gamma} \frac{\partial f_s}{\partial \delta t_{Tx}} \quad \dot{g}^s_{Ty} = \dot{\gamma} \frac{\partial f_s}{\partial \delta t_{Ty}} \tag{7.38}$$

Again, the Kuhn-Tucker conditions can be set up to complete the formulation:

$$\dot{\gamma} \geqslant 0, \quad f_s(t_{Tx}, t_{Ty}) \leqslant 0, \quad \dot{\gamma} f_s(t_{Tx}, t_{Ty}) = 0$$

The dissipation function, which is needed for instance in thermo-mechanical applications or problems where wear has to be computed, can also be stated; it yields

$$\mathcal{D}^s = \underline{t}_T \cdot \dot{\underline{g}}^s_T = t_{Tx} \dot{g}^s_{Tx} + t_{Ty} \dot{g}^s_{Ty}$$

This modeling approach may be used in the case of beam to beam pointwise contact to account for indentation phenomena. In this case, the orthotropic directions can be defined as the (orthogonal) axes of the elliptic contact zone predicted by Hertz theory (see Sec. 2.4.2). Concerning overhead electrical wire ropes, from the results obtained in [84] an anisotropic behavior seems to better represent the contact interactions between aluminum wires than the isotropic one, in order to represent the effects of surface indentation (see Fig. 2.15). For steel wire ropes, it should be mentioned that with the onset of surface degradation mechanisms, the frictional properties of the surfaces may vary, in particular with cyclic loading [139]. However, in this work, for the sake of simplicity, only the isotropic frictional behavior with a constant friction coefficient will be considered.

7.2.2 Local integration of the friction law

In the following section the integration of the local constitutive equations at the contact interface for friction is discussed. One has to solve an evolution equation for the frictional slip, which is coupled with the slip condition f_s, and hence coupled with an inequality.

The algorithmic update of the tangential stress $\underline{t}_T$ and dissipation $\mathcal{D}^s$ is performed by the return algorithm based on an objective (backward Euler) integration of the evolution equation for the plastic slip (see [165] for further details and additional references).
The results can be summarized as follows:

1. **Calculation of the slip increment** within the time step Δt_{n+1} from (7.24).
2. **Computation of the elastic trial state** from (7.33) and evaluation of the slip criterion (7.34) at time t_{n+1}. As shown in (7.33), one needs to compute the elastic part of the tangential gap function (7.32) in order to capture the previously converged sliding tendency. Thus, the trial slip $\underline{g}_T^{e,tr}$ is obtained by adding the previously accumulated elastic slip $\underline{g}_{T,(n)}^{e} = \xi_{e,(n)}^{i}\underline{t}_{i,(n)}$ mapped according to the rotations of the beam axes, which is simply
$$\underline{g}_{T,(n,n+1)}^{e} = \xi_{e,(n)}^{i}\underline{t}_i \tag{7.39}$$
where the coefficients $\xi_{e,(n)}^{i}$ are obtained as $\xi_{e,(n)}^{i} = \underline{g}_{T,(n)}^{e} \cdot \underline{t}_{(n)}^{i}$. One can notice that is the same mapping that has already been described for the total slip in Sec. 7.1.6. Therefore, one defines the trial "elastic" part of the accumulated relative sliding gap as follows.
$$\underline{g}_T^{e,tr} = \underline{g}_T^{\Delta} + \underline{g}_{T,(n,n+1)}^{e} \tag{7.40}$$
The notation $\underline{g}_T^{e,tr}$ has been chosen instead of $\underline{g}_T$ since it does not contain information about the previous accumulated sliding of the contact history, but only the last-step "elastic" tendency of sliding assuming a penalty approach for the trial tangential direction. The elastic trial state can be now computed as
$$\underline{t}_T^{tr} = c_T\,\underline{g}_T^{e,tr} \tag{7.41}$$
$$f_s^{tr} = \|\underline{t}_T^{tr}\| - \mu\, p_N \tag{7.42}$$
where $p_N = c_N|g_N| = c_N \operatorname{sign}(g_N)\, g_N \geqslant 0$ (since $g_N < 0$ when contact occurs) and where c_N is the normal elastic constant (or $c_N = \varepsilon_N$ from a "regularization" point of view). A value of the slip criterion which fulfills $f_s^{tr} \leqslant 0$ indicates stick. Hence no sliding takes place. For $f_s^{tr} > 0$ sliding occurs in the tangential direction, and a return mapping of the trial tangential force to the slip surface has to be performed.
3. **Return mapping procedure** is derived from the time integration algorithm. In case the implicit Euler scheme is applied to approximate the evolution equation (7.35), one can compute the increment of plastic slip at time $n+1$:
$$\underline{g}_T^{s,\Delta} = \lambda_{n+1}\Delta t_{n+1}\,\underline{n}_T = \Delta\lambda\,\underline{n}_T \quad \text{with} \quad \underline{n}_T = \frac{\underline{t}_T}{\|\underline{t}_T\|} \tag{7.43}$$
where classical notation $\Delta\lambda = \lambda_{n+1}\Delta t_{n+1}$ has been used. With the standard arguments regarding the projection schemes [142], one obtains:
$$\begin{cases} \underline{t}_T = \underline{t}_T^{tr} - c_T\Delta\lambda\,\underline{n}_T \\ \underline{n}_T = \underline{n}_T^{tr} \quad \text{with} \quad \underline{n}_T^{tr} \overset{def}{=} \dfrac{\underline{t}_T^{tr}}{\|\underline{t}_T^{tr}\|} \end{cases}$$

□ Proof: From $\underline{t}_T^{tr} = \underline{t}_T + c_T\,\Delta\lambda\,\underline{n}_T$ and since $\underline{t}_T = \underline{n}_T\|\underline{t}_T\|$, one gets:

$$\underline{n}_T\|\underline{t}_T\| = \underline{t}_T^{tr} - c_T\,\Delta\lambda\,\underline{n}_T \tag{7.44}$$

which leads to $\underline{n}_T = \dfrac{\underline{t}_T^{tr}}{\|\underline{t}_T\| + c_T\,\Delta\lambda}$. As $\|\underline{t}_T\| + c_T\,\Delta\lambda \geq 0$, one deduces that $\underline{n}_T$ and $\underline{t}_T^{tr}$ are collinear. Thus, $\underline{n}_T = \dfrac{\underline{t}_T^{tr}}{\|\underline{t}_T^{tr}\|}$ which ends the proof. □

If sliding occurs when $f_s^{tr} > 0$, the return mapping procedure aims at setting $f_s = \|\underline{t}_T\| - \mu\,p_N = 0$, that is to say $\|\underline{t}_T\| = \mu\,p_N$. From (7.44) and since $\underline{n}_T = \underline{n}_T^{tr}$, one gets:

$$\|\underline{t}_T\| = \|\underline{t}_T^{tr}\| - c_T\,\Delta\lambda = \mu\,p_N$$

which leads to:

$$\Delta\lambda = \frac{1}{c_T}\left(\|\underline{t}_T^{tr}\| - \mu\,p_N\right) = \frac{f_s^{tr}}{c_T}$$

Thus, the total frictional slip is given by:

$$\underline{t}_T = \underline{t}_T^{tr} - c_T\Delta\lambda\,\underline{n}_T = \mu\,p_N\,\underline{n}_T^{tr} = \mu\,p_N\,\frac{\underline{t}_T^{tr}}{\|\underline{t}_T^{tr}\|}$$

The accumulated elastic gap and accumulated relative sliding can be deduced subsequently:

$$\left\{\begin{array}{lcl} \underline{g}_T^e &=& \underline{g}_T^{e,tr} - \underline{g}_T^{s,\Delta} = \underline{g}_T^{e,tr} - \Delta\lambda\,\underline{n}_T^{tr} = \xi_e^i\underline{t}_i \\ \underline{g}_T^s &=& \underline{g}_{T,(n,n+1)}^s + \underline{g}_T^{s,\Delta} \end{array}\right.$$

One obviously has: $\underline{t}_{T,(n+1)} = c_T\left(\underline{g}_{T,(n+1)}^{e,tr} - \Delta\underline{g}_{T,(n+1)}^s\right) = c_T\,\underline{g}_{T,(n+1)}^e$. Note that one always has : $\underline{t}_{T,(n+1)} = \|\underline{t}_{T,(n+1)}\|\underline{n}_{T,(n+1)}$ with $\underline{n}_{T,(n+1)} = \dfrac{\underline{g}_{T,(n+1)}^{e,tr}}{\|\underline{g}_{T,(n+1)}^{e,tr}\|}$. Then total tangential slip can be then computed from (7.31).
This update completes the local integration algorithm for the frictional interface law.

7.3 Linearization of contact conditions

The solution of the nonlinear equation system associated with the weak form of the beam-to-beam contact problem is obtained via the Newton-Raphson scheme. This method relies on the linearization of the weak form. In our case, the total virtual work expression is the sum of the virtual deformation of beam elements and the contribution of the contact elements.
The contribution of a contact element to the weak form can be expressed by treating separately normal and tangential contributions:

$$\delta W_C = \delta W_C^N + \delta W_C^T \tag{7.45}$$

7.3.1 Normal contact

Considering a penalty method approach with constant penalty parameter ϵ_N, the variation of virtual work associated to normal contact is

$$\delta W_C^N = t_N \delta g_N = \epsilon_N g_N \delta g_N \tag{7.46}$$

where $t_N = \epsilon_N g_N$ is the normal contact force and δg_N given by (7.15). Thus, the linearization of δW_C^N is

$$\Delta\delta W_C^N = \Delta(t_N \delta g_N) = \epsilon_N \Delta g_N \delta g_N + \epsilon_N g_N \Delta\delta g_N \tag{7.47}$$

The linearization of g_N (Δg_N) has the same structure than the variation of g_N (δg_N). Hence with (7.15), by exchanging δ by Δ, one obtains:

$$\Delta g_N = \left(\Delta \underline{x}_2 - \Delta \underline{x}_1 - \xi^i \, \Delta \underline{t}_i\right) \cdot \underline{n} \tag{7.48}$$

The linearization of the gap in the normal direction $\Delta\delta g_N$ is more involved and has to be computed from the full variation of $g_N = (\underline{x}_2 - \bar{\underline{x}}_2) \cdot \underline{n}$, since terms which are zero in (7.15) can also contribute to the tangent (a function can have a non-zero tangent at positions where it is zero). Starting from (7.12), one gets:

$$\delta g_N \, \underline{n} + g_N \, \delta \underline{n} = \delta \underline{x}_2 - \delta \underline{x}_1 - \delta\xi^i \, \underline{t}_i - \xi^i \, \delta \underline{t}_i - (r_1 + r_2)\delta \underline{n} \tag{7.49}$$

Note that since $\underline{t}_i$ as well as $\delta \underline{t}_i$ and $\delta \underline{n}$ depend on the rotation vector $\underline{\Phi}(\underline{x}_i)$, they have to be linearized. Linearization of variation $\delta \underline{x}_1$ and $\delta \underline{x}_2$ are zero.

$$\begin{aligned} &\Delta\delta g_N \, \underline{n} + \delta g_N \, \Delta \underline{n} + \Delta g_N \, \delta \underline{n} + g_N \, \Delta\delta \underline{n} = \\ &= -\Delta\delta\xi^i \, \underline{t}_i - \delta\xi^i \, \Delta \underline{t}_i - \Delta\xi^i \, \delta \underline{t}_i - \xi^i \, \Delta\delta \underline{t}_i - (r_1 + r_2)\Delta\delta \underline{n} \end{aligned} \tag{7.50}$$

By multiplication with $\underline{n}$, this equation leads to:

$$\Delta\delta g_N + g_N \, (\Delta\delta \underline{n} \cdot \underline{n}) = -\delta\xi^i \, (\Delta \underline{t}_i \cdot \underline{n}) - \Delta\xi^i \, (\delta \underline{t}_i \cdot \underline{n}) - \xi^i \, (\Delta\delta \underline{t}_i \cdot \underline{n}) - (r_1 + r_2)(\Delta\delta \underline{n} \cdot \underline{n}) \tag{7.51}$$

since $\Delta \underline{n} \cdot \underline{n} = 0$, $\delta \underline{n} \cdot \underline{n} = 0$ and $\underline{t}_i \cdot \underline{n} = 0$. The term $\Delta\delta \underline{n} \cdot \underline{n}$ can be rewritten as $\Delta(\delta \underline{n} \cdot \underline{n}) = \Delta\delta \underline{n} \cdot \underline{n} + \Delta \underline{n} \cdot \delta \underline{n} = 0$. From this identity, one deduces that $\Delta\delta \underline{n} \cdot \underline{n} = -\Delta \underline{n} \cdot \delta \underline{n}$. Finally, it comes that:

$$\Delta\delta g_N = -(\delta\xi^i \, \Delta \underline{t}_i + \Delta\xi^i \, \delta \underline{t}_i + \xi^i \, \Delta\delta \underline{t}_i) \cdot \underline{n} + (g_N + r_1 + r_2)(\Delta \underline{n} \cdot \delta \underline{n}) \tag{7.52}$$

7.3.2 Tangential contact

The tangential contact contribution to the weak form is

$$\delta W_C^T = \underline{t}_T \cdot \delta \underline{g}_T \tag{7.53}$$

with $\underline{t}_T$ the tangential contact force, whose expression is different in stick and slip regimes. For the term $\delta \underline{g}_T$ as done in [104] we consider

$$\delta \underline{g}_T = \delta \underline{g}_T^{\Delta} + \delta \underline{g}_{T,(n,n+1)} \tag{7.54}$$

with $\delta \underline{g}_T^{\Delta}$ defined in (7.27) and

$$\delta \underline{g}_{T,(n,n+1)} = \xi^i_{e,(n)} \delta \underline{t}_i \tag{7.55}$$

The general expression of the linearization of δW_C^T is

$$\Delta\delta W_C^T = \Delta(\underline{t}_T \cdot \delta \underline{g}_T) = \Delta \underline{t}_T \cdot \delta \underline{g}_T + \underline{t}_T \cdot \Delta\delta \underline{g}_T \tag{7.56}$$

From (7.27) one can write the linearization of $\delta \underline{g}_T$ as

$$\begin{aligned}
\Delta\delta \underline{g}_T^{\Delta} = \quad & \Delta\delta\xi_i \underline{t}^i - [\xi^2_{(n)} \Delta(M^{1j} \underline{t}_j) + \xi^1_{(n)} \Delta(M^{2j} \underline{t}_j)] \delta M_{12} - \dots \\
& \dots (\xi^2_{(n)} \underline{t}^1 + \xi^1_{(n)} \underline{t}^2) \Delta\delta M_{12} + \Delta g^{\Delta}_{Ti} (M^{ij} \delta \underline{t}_j) + \Delta g^{\Delta}_{Ti} (\delta M^{ij} \underline{t}_j) - \dots \\
& \dots r_2 \left(\delta \underline{n}_2 \cdot \underline{t}_1 + \underline{n}_2 \cdot \delta \underline{t}_1\right) (M^{i1} \Delta \underline{t}_1) - \dots \\
& \dots r_1 \left(\delta \underline{n}_1 \cdot \underline{t}_2 + \underline{n}_1 \cdot \delta \underline{t}_2\right) (M^{i2} \Delta \underline{t}_2) - \dots \\
& \dots r_2 \left(\Delta\delta \underline{n}_2 \cdot \underline{t}_1 + \delta \underline{n}_2 \cdot \Delta \underline{t}_1 + \dots \right. \\
& \dots \left. \Delta \underline{n}_2 \cdot \delta \underline{t}_1 + \underline{n}_2 \cdot \Delta\delta \underline{t}_1\right) \underline{t}^1 - \dots \\
& \dots r_1 \left(\Delta\delta \underline{n}_1 \cdot \underline{t}_2 + \delta \underline{n}_1 \cdot \Delta \underline{t}_2 + \dots \right. \\
& \dots \left. \Delta \underline{n}_1 \cdot \delta \underline{t}_2 + \underline{n}_1 \cdot \Delta\delta \underline{t}_2\right) \underline{t}^2 + \dots \\
& \dots g^{\Delta}_{Ti} (M^{ij} \Delta\delta \underline{t}_j) + g^{\Delta}_{Ti} (\Delta M^{ij} \delta \underline{t}_j) + \dots \\
& \dots g^{\Delta}_{Ti} (\delta M^{ij} \Delta \underline{t}_j) + g^{\Delta}_{Ti} (\Delta\delta M^{ij} \underline{t}_j)
\end{aligned} \tag{7.57}$$

with

$$\begin{aligned}
\Delta g^{\Delta}_{T1} &= \Delta\xi_1 - \xi^2_{(n)} (\underline{t}_2 \cdot \Delta \underline{t}_1 + \underline{t}_1 \cdot \Delta \underline{t}_2) - r_2 \left(\Delta \underline{n}_2 \cdot \delta \underline{t}_1 + \delta \underline{n}_2 \cdot \Delta \underline{t}_1\right) \\
\Delta g^{\Delta}_{T2} &= \Delta\xi_2 - \xi^1_{(n)} (\Delta \underline{t}_2 \cdot \delta \underline{t}_1 + \Delta \underline{t}_1 \cdot \delta \underline{t}_2) - r_1 \left(\Delta \underline{n}_1 \cdot \delta \underline{t}_2 + \delta \underline{n}_1 \cdot \Delta \underline{t}_2\right)
\end{aligned} \tag{7.58}$$

Actually, this term has not been implemented in the user-element subroutine. In fact, a satisfying convergence rate is attained for high tangential penalty stiffness with the first term of (7.56) only.

Elasto-plastic tangent modulus

In the sticking case, there is no sliding and $\lambda = \dot{\gamma} = 0$, the tangential behavior is elastic and, according to (7.35), $\dot{\underline{g}}_T^s = \dot{\gamma} \dfrac{\partial f_s(\underline{t}_T)}{\partial \underline{t}_T} = \mathbf{0}$. Thus:

$$\Delta \underline{t}_T = c_T \left(\Delta \underline{g}_T^{\Delta} + \Delta \underline{g}_{T,(n,n+1)}\right) = c_T \, \Delta \underline{g}_T^{e,tr} \tag{7.59}$$

The tangent modulus is the tangential elastic constant c_T (or $c_T = \varepsilon_T$ from a "regularization" point of view).

In the sliding case, one remains in the elastic domain: $f_s(\underline{t}_T) = 0$ and $\lambda = \dot{\gamma} > 0$. The loading point remains on the slip criterion: $\dot{f}_s(\underline{t}_T) = 0$. The consistency condition states that : $\lambda \dot{f}_s(\underline{t}_T) = 0$ if $f_s(\underline{t}_T) = 0$. One can express the "consistent" tangent modulus according to $\underline{g}_T^{e,tr}$ as follows:

$$\begin{aligned}
\underline{t}_T &= c_T \, \underline{g}_T^e \\
&= c_T \left(\underline{g}_T^{e,tr} - \lambda \underline{n}_T\right) \\
&= c_T \, \underline{g}_T^{e,tr} - c_T \left[\frac{1}{c_T} \left(\|\underline{t}_T^{tr}\| - \mu \, p_N\right)\right] \underline{n}_T \\
&= \mu \, p_N \, \underline{n}_T
\end{aligned}$$

One deduces that:

$$\Delta \underline{t}_T = \mu \, \Delta p_N \, \underline{n}_T + \mu \, p_N \, \Delta \underline{n}_T$$

One can easily show that:

$$\Delta \underline{n}_T = \Delta \left(\frac{\underline{g}_T^{e,tr}}{\|\underline{g}_T^{e,tr}\|} \right) = \frac{1}{\|\underline{g}_T^{e,tr}\|} \left(\underline{\underline{I}} - \underline{n}_T \otimes \underline{n}_T \right) \Delta \underline{g}_T^{e,tr}$$

One finally obtains as shown in [104]:

$$\Delta \underline{t}_T = \frac{\mu \, p_N}{\|\underline{g}_T^{e,tr}\|} \left(\underline{\underline{I}} - \underline{n}_T \otimes \underline{n}_T \right) \Delta \underline{g}_T^{e,tr} + \mu \, \Delta p_N \, \underline{n}_T \tag{7.60}$$

7.3.3 Calculation of tangent operator and load vector

In order to formulate the contact element, the virtual work associated to normal and tangential contact, expressed by (7.46) and (7.53) respectively, and their linearization (7.47) and (7.56) have to be expressed as function of the nodal degrees of freedom, that we gather in the vector

$$\underline{d} = \begin{pmatrix} \underline{u}_1 \\ \underline{\Phi}_1 \\ \underline{u}_2 \\ \underline{\Phi}_2 \end{pmatrix} \tag{7.61}$$

where $\underline{u}_i$ and $\underline{\Phi}_i$ are respectively the displacements and rotations of node i. In the Appendices B and C, the interested reader can find the terms associated to the linearization and to the contribution to the weak form of the contact conditions.

7.4 Conclusion

In the development of this new frictional contact element, we chose to prioritize the robustness of the formulation, with the contact normal that varies smoothly at each iteration of the Newton-Raphson algorithm. Namely we avoided the use of finite sliding techniques (see Sec. 4.2.4), such as normal smoothing, isogeometric elements or Mortar method.

Another important aspect is the contact detection phase, which can be time-consuming concerning contact between beams. Conversely, with this formulation it is very fast, since it consists of just few operations thanks to the fixed contact pairing.

Chapter 8

Model validation

Once implemented in Abaqus®/Standard as a user element, the new contact element described in Chapter 7 has been employed in some numerical tests for its validation. When possible, the obtained results are compared with the edge-to-edge and surface-to-surface models, which have been described in Sections 6.1.1 and 6.1.2 respectively.
Three types of benchmark have been considered.

- The first benchmark consists of a pointwise contact interaction among slender beams. Beside the contact forces, the convergence rate has been evaluated with respect to the beam contact modeling formulated in [169].
- The second group of benchmarks has already been described in Sec. 6.2.1. Its aim is to verify the user element behavior in the modeling of helical-shaped structures. The helix kinematics is compared with the one obtained by the other models. Moreover, the capability of the model to fit the analytical results is investigated.
- The last benchmark concerns a tension-bending test of a four-layer wire rope. The results are compared with experimental [111] and numerical [84] ones.

Firstly, a frame invariance test with respect to rigid rotations has been conducted.

8.1 Frame invariance test

In this simple test, the degrees of freedom of the two nodes belonging to a single user element are completely controlled. It involves the three following steps.

1. Contact is imposed in the first step, with a relative movement in the normal direction.
2. In the second step, a tangential relative displacement is applied, in order to develop frictional forces.
3. In the last step, a rigid rotation is applied to the system.

The results with one increment (Tab. 8.1) show that the moments which originate from the definition of the weak form contributions (Eq. (B.33)-(C.68)) change their magnitude after the rigid rotation. This nonphysical result is generated by the use of the matrix $\underline{\underline{H}}(\underline{\Phi})$ (Eq.

N. of increments	% diff. M_1	% diff. M_2
1	-2.55	-0.15
10	-0.12	-0.03
100	$-1.e-3$	$1.e-3$
1000	≈ 0	≈ 0

Table 8.1: Results of the frame invariance test with $\underline{\underline{H}}(\underline{\Phi}^{\Delta})$. The first column indicates the number of increments to apply a rigid rotation of $\pi/4$. The other columns report the percentage differences of the moments at the nodes after the rigid rotation with respect to their value at the second step.

(A.16)), i.e. the matrix linking a variation of the linearized rotation field $\delta\underline{\theta}$ to a variation of the nodal rotation vector $\delta\underline{\Phi}$ through, the relation [1]

$$\delta\underline{\theta} = \underline{\underline{H}}(\underline{\Phi}) \cdot \delta\underline{\Phi}$$

The invariance can be recovered by computing the matrix $\underline{\underline{H}}$ with respect to the rotation occurring at the current increment $\underline{\Phi}^{\Delta}$ [13, 48]. Table 8.1 shows that, with this modification, a small error is recovered is the rotation if performed with a sufficient number of increments. Nevertheless, we observed that the use of $\underline{\underline{H}}(\underline{\Phi}^{\Delta})$ involves convergence problems in the tension-bending test reported in Section 8.4. Namely, the convergence criterion which is not satisfied is the one concerning the largest correction to rotation compared to the largest increment of rotation, whose maximum allowed ratio is by default set to $1.e-2$. However, it has been ascertained that up to the last converged increment the solution given by using $\underline{\underline{H}}(\underline{\Phi})$ or $\underline{\underline{H}}(\underline{\Phi}^{\Delta})$ are practically the same.
As a consequence, in the following the formulation with $\underline{\underline{H}}(\underline{\Phi})$ is employed for the sake of robustness. In future works, this frame variance issue should be however investigated.

8.2 Pointwise contact benchmark

This benchmark has been taken from [169]. It consists of two beams being orthogonal to each other (Fig. 8.1). The horizontal beam length is equal to 14 units, and the vertical one is equal to 10 units. The initial distance between the beams axes in the out-of-plane direction is equal to 1 unit. The horizontal beam is clamped at both ends. The vertical one is clamped at the bottom-end, where also an out-of-plane displacement toward the other beam, equal to 0.3 units, and a horizontal displacement equal to 0.03 units are applied at each of the subsequent load steps. The other beam end is free.
The geometrical and material parameters are gathered in Table 8.2.
The beams come at incipient contact at the second load step. It can be noticed that, since the nodes are evenly distributed at a distance of 1 unit (Fig. 8.1a), the initial contact points do not correspond to the user element node, since for the horizontal beam one has

$$\hat{\underline{x}}_h = \underline{x}_h + 0.06\,\underline{e}_1$$

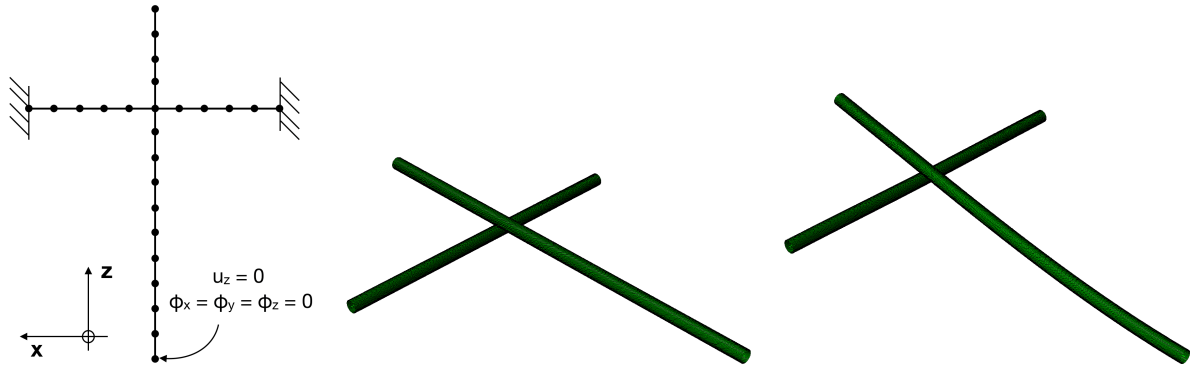

(a) (b) (c)

Figure 8.1: (a) Top view with beam discretization. (b) Initial configuration. (c) Deformed configuration.

Area	$4.0e-2$
Beam radius	0.2
Moment of Inertia	$2.0e-4$
Young Modulus	$1.0e+8$
Poisson Coeff.	0.0

Table 8.2: Beam properties.

where $\underline{x}_h$ is the position vector of the user-element node and $\underline{e}_1$ is the unit vector in x direction (Fig. 8.1a).
For the sake of comparison, the contact penalty coefficient are set as in [169] to $\epsilon_N = \epsilon_T = 1.e+4$ units. The convergence rate of the two models for different value of friction coefficient, reported in Table 8.3, is comparable. In Table 8.4 are reported the values of the contact forces, from which one can notice that the stick-slip transition is not equally predicted by the two models. Actually, it is worth mentioning that the models evaluate the tangential sliding differently, since in [169] the dimensions of the beam cross-sections are neglected, i.e. only the sliding components along the beam axes are considered.

Load step	$\mu = 0.$		$\mu = 0.1$		$\mu = 0.8$		$\mu = 1.5$	
	[169]	User-Element	[169]	User-Element	[169]	User-Element	[169]	User-Element
3				3.82e+3	1.44e+5	3.81e+3		
	1.44e+5		1.44e+5	3.12e+0	4.81e+0	2.13e+1	1.44e+5	3.812e+3
	1.02e+1	3.88e+3	1.18e+1	1.01e+0	1.49e+1	3.46e-1	5.15e+0	1.80e+0
	2.41e-3	1.89e+0	6.60e-2	6.70e-2	1.16e-2	2.81e-4	1.03e-3	3.16e-1
	1.73e-8	1.36e-3	2.77e-6	4.64e-3	8.96e-6	5.17e-7	7.12e-7	4.91e-6
	2.33e-10	6.34e-9	2.70e-10	8.18e-6	6.99e-9	8.88e-9	5.65e-10	1.86e-8
				8.71e-9	1.48e-10			
4	1.44e+5	3.87e+3	1.44e+5	3.92e+3	1.44e+5	3.94e+3	1.44e+5	3.94e+3
	1.09e+1	1.88e+0	1.02e+1	4.57e+0	5.36e+0	1.93e+0	5.15e+0	1.93e+0
	2.41e-3	7.06e-5	2.32e-3	4.21e+0	2.81e-2	8.96e-2	7.21e-3	8.96e-2
	1.73e-8	5.56e-8	1.35e-6	5.31e-2	4.92e-5	6.98e-6	1.77e-5	6.98e-6
	2.33e-10	1.49e-8	3.95e-10	5.16e-4	1.22e-7	3.25e-8	4.38e-8	3.25e-8
				8.59e-8	3.44e-10		2.55e-10	
5				3.99e+3				
	1.44e+5	3.84e+3	1.44e+5	7.80e+0	1.44e+5	3.99e+3	1.44e+5	3.99e+3
	1.17e+1	1.86e+0	1.09e+1	7.95e+0	8.34e+0	2.02e+0	6.11e+0	1.99e+0
	3.03e-3	2.40e-3	2.69e-3	3.32e-1	2.91e-2	1.43e-1	1.90e-2	2.99e-3
	2.90e-8	2.33e-7	2.41e-6	2.91e-3	2.00e-5	5.55e-5	7.81e-5	1.10e-5
	2.08e-10	7.58e-9	1.32e-9	2.11e-6	1.76e-7	2.97e-7	3.22e-7	2.60e-8
				5.98e-9	2.97e-10	7.70e-9	1.32e-9	
6				3.80e+3	1.44e+5	3.83e+3	1.44e+5	3.95e+3
	1.44e+5	3.79e+3	1.44e+5	1.83e+0	1.06e+1	1.86e+0	7.21e+0	7.91e+0
	1.23e+1	1.83e+0	1.55e+1	4.46e-2	6.66e-2	3.03e-2	3.55e-2	6.27e-1
	3.35e-3	8.33e-3	3.12e-3	3.08e-5	8.33e-5	4.49e-5	2.02e-4	1.56e-4
	3.57e-8	7.46e-7	3.83e-6	3.71e-7	9.33e-7	1.67e-7	1.15e-6	1.54e-5
	3.39e-10	4.65e-9	3.43e-9	4.82e-9	7.70e-10	8.51e-9	6.56e-9	1.35e-7
							3.26e-10	4.45e-9

Table 8.3: Comparison of the convergence rate for the model in [169] and the proposed model, for which the absolute value of the largest residual force is plotted.

	User-Element		[169]	
Friction coeff.	F_N	F_T	F_N	F_T
$\mu = 0.$	17.69	0.	17.2	0.
	35.37	0.	34.3	0.
	52.93	0.	51.3	0.
	70.21	0.	68.4	0.
$\mu = 0.1$	17.72	1.77 (slip)	17.0	1.7 (slip)
	35.27	3.53 (slip)	33.8	3.28 (slip)
	52.72	5.27 (slip)	50.4	5.04 (slip)
	69.87	6.99 (slip)	67.0	6.70 (slip)
$\mu = 0.8$	18.02	9.20 (stick)	16.0	11.5 (stick)
	34.84	12.39 (stick)	30.8	24.5 (slip)
	50.77	40.62 (slip)	45.0	36.0 (slip)
	66.96	53.57 (slip)	58.4	46.7 (slip)
$\mu = 1.5$	18.02	9.20 (stick)	14.44	11.5 (stick)
	34.84	12.39 (stick)	31.52	24.7 (stick)
	48.98	63.06 (stick)	48.16	39.4 (stick)
	64.28	96.42 (slip)	64.19	55.8 (stick)

Table 8.4: Comparison of contact forces, obtained with $\epsilon_N = \epsilon_T = 1.e + 4$.

	User-Element		Edge-to-Edge		Surface-to-Surface	
Friction coeff.	F_N	F_T	F_N	F_T	F_N	F_T
$\mu = 0.$	17.69	0.	14.52	0.	17.67	0.
	35.37	0.	32.20	0.	35.44	0.
	52.93	0.	49.75	0.	53.11	0.
	70.21	0.	67.05	0.	69.87	0.
$\mu = 0.1$	17.72	1.77 (slip)	14.51	1.45 (slip)	17.70	1.68 (slip)
	35.28	3.53 (slip)	32.16	3.22 (slip)	35.34	3.54 (slip)
	52.72	5.27 (slip)	49.66	4.97 (slip)	52.90	5.30 (slip)
	69.87	6.99 (slip)	66.87	6.69 (slip)	70.16	7.03 (slip)
$\mu = 0.8$	18.04	9.68 (stick)	14.44	11.56 (slip)	17.19	8.43 (stick)
	34.70	15.16 (stick)	31.52	25.47 (slip)	34.04	17.11 (stick)
	50.77	40.62 (slip)	48.88	39.11 (slip)	50.88	40.68 (slip)
	66.96	53.57 (slip)	65.47	52.38 (slip)	67.19	53.72 (slip)
$\mu = 1.5$	18.09	11.04 (stick)	14.44	13.07 (stick)	17.60	10.47 (stick)
	34.68	15.63 (stick)	31.52	47.28 (slip)	33.51	21.11 (stick)
	48.98	73.47 (slip)	48.16	72.24 (slip)	48.97	73.41 (slip)
	64.28	96.42 (slip)	64.19	96.29 (slip)	64.44	96.60 (slip)

Table 8.5: Comparison of contact forces obtained for different values of friction coefficient, with an elastic slip of $1.e - 3$.

In order to further investigate the validity of these results, it has been decided to run the benchmark employing the edge-to-edge (Sec. 6.1.1) and surface-to-surface (Sec. 6.1.2) con-

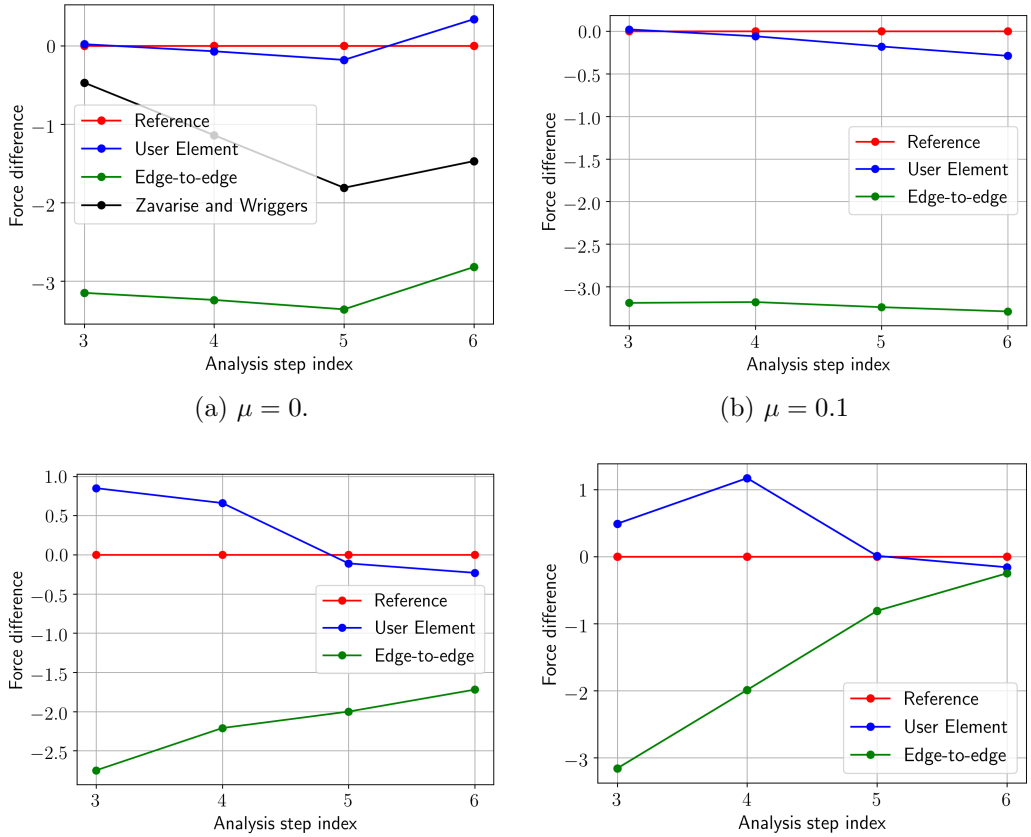

(a) $\mu = 0.$ (b) $\mu = 0.1$

(c) $\mu = 0.8$ (d) $\mu = 1.5$

Figure 8.2: Normal force difference with respect to the reference model, for different values of the friction coefficient.

tact discretizations. The latter is considered to be the reference model, in which the circular cross sections are interpolated by 90 surface elements places along the circumference, while 500 elements are placed along the beam axes. The discretization of the edge-to-edge model is the same employed for the user elements (see Fig. 8.1a).

For ease of implementation of the contact law, the tangential contact behavior is not defined by a constant penalty stiffness, but by the elastic slip, see (4.13), of $1.e-3$ units. Consequently, the results in [169] are not valid anymore for $\mu \neq 0$. In normal direction, penalty coefficients of $1.e+4$ and $1.e+6$ units are chosen for the edge-to-edge and surface-to-surface model respectively. The higher penalty coefficient for the surface-to-surface model is used in order to limit the penetration between the surfaces.

The contact force comparison is reported in Table 8.5 and in Figures 8.2-8.3. One can see that the results obtained with the proposed model are in closer agreement with the reference model. The biggest difference in the shear force is obtained at step 4 for $\mu = 1.5$. However, this difference is linked to a difference in the slip estimation in the order of $1.e-4$ units.

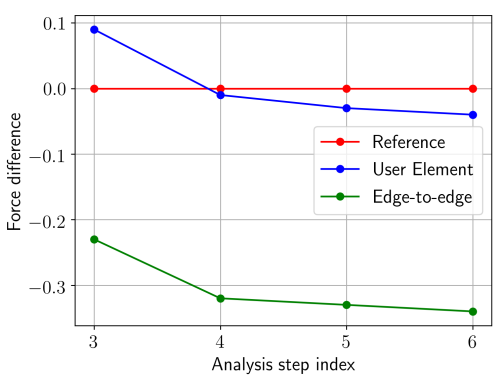

(a) $\mu = 0.1$

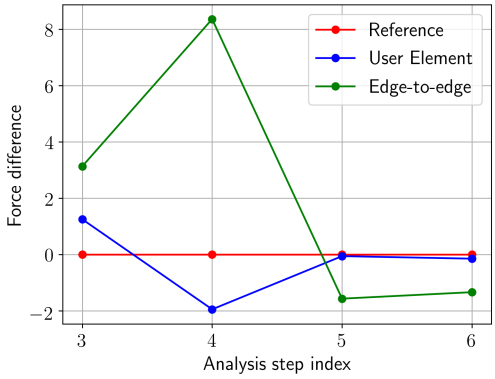

(b) $\mu = 0.8$

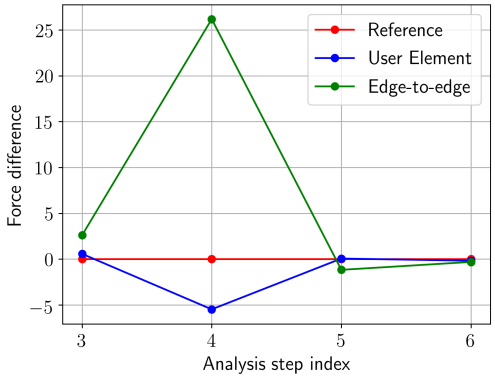

(c) $\mu = 1.5$

Figure 8.3: Tangential force difference with respect to the reference model, for different values of the friction coefficient.

8.3 Rope benchmark tests

The two benchmarks, represented in Figure 6.5, have already been described in Section 6.2.1. The load steps that will be considered are reported in Table 8.6. The load step 1 consists of a pure tensile loading. From step 2 to 4 the rope curvature is increased. Finally at load step 5 the central wire is straighten again.

Load step	$\boldsymbol{\varepsilon}$	$\boldsymbol{\kappa}$ (mm^{-1})
1	$1.e-3$	$0.$
2	$1.e-3$	$1.e-6$
3	$1.e-3$	$5.e-5$
4	$1.e-3$	$1e-3$
5	$1.e-3$	$0.$

Table 8.6: Load steps for benchmarks 1 and 2. ε and κ are respectively the axial strain and the curvature of the central wire.

The results obtained with the user-element are compared with the ones obtained by edge-to-edge and surface-to-surface models, considering the displacements of the external helical wire expressed in terms of relative displacements with respect to the reference cylinder (see Fig. 8.4 and Sec. 2.2.2). As in the pointwise contact benchmark, the surface-to-surface model is taken as the reference.

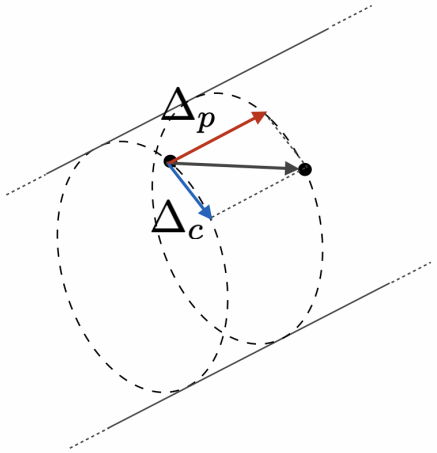

Figure 8.4: Relative displacement with respect to the reference cylinder, whose radius is the one of the helix.

In comparing the helix kinematics, the normal penalty coefficients (Tab. 8.7) are set in order to obtain approximately the same helix radius contraction after the first pure tensile load step. This is important since this contraction affects the axial force on the helical wire, see (2.27), which modifies the normal contact force, see (2.34), and therefore the sliding behavior. Concerning the tangential contact stiffness, the same elastic slip is chosen for all the models.

For the comparison with the analytical results, the normal penalty stiffness is $\epsilon_N = 2.e+5\,N/mm$ and the elastic slip is set to $1.e-4\,mm$.

	ϵ_N	Elastic slip
User Elements	$4.e+3\,N/mm$	$1.e-3\,mm$
Edge-to-Edge	$8.e+2\,N/mm$	$1.e-3\,mm$
Surface-to-Surface	$1.e+5\,N/mm^2$	$1.e-3\,mm$
	ϵ_N	Elastic slip
User Elements	$2.e+3\,N/mm$	$1.e-2\,mm$
Edge-to-Edge	$1.e+3\,N/mm$	$1.e-2\,mm$
Surface-to-Surface	$1.e+4\,N/mm^2$	$1.e-2\,mm$

Table 8.7: Penalty coefficients used for the helix kinematics comparison, for benchmark 1 (on the top) and benchmark 2 (on the bottom).

8.3.1 Results - Benchmark 1

Helix kinematics - Tension

In pure tensile regime, the helical wire should remain as close as possible to the perfectly stick configuration, for which $\Delta_p = \Delta_c = 0$ along the whole length. The results are reported in Fig. 8.5.

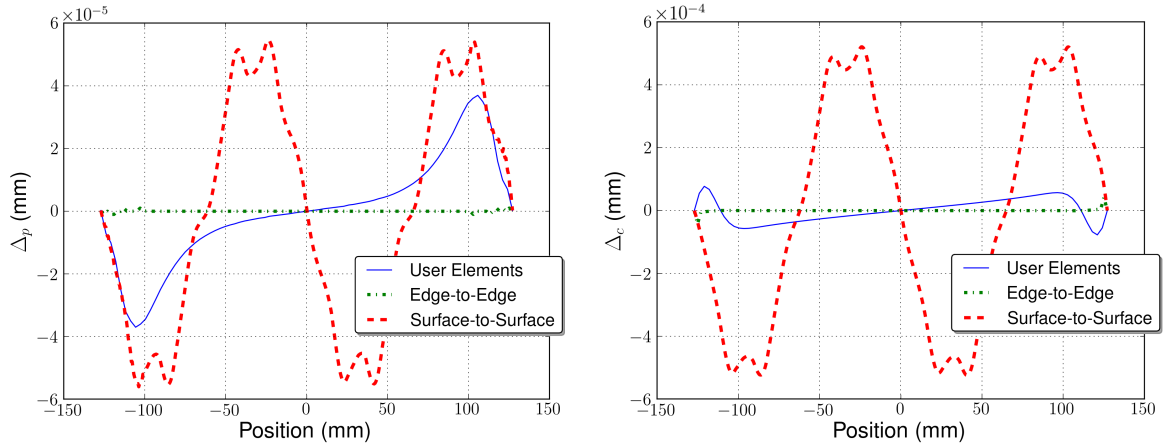

(a) Δ_p (b) Δ_c

Figure 8.5: Benchmark 1, relative displacements with respect to the reference cylinder at load step 1 (pure tension).

It can be noticed that the results of the surface-to-surface model are affected by some oscillations (indeed, very small, almost two orders of magnitude lower than the admissible elastic

slip). This is linked to the approximation of the discretization of a curved cylindrical surface with planar surface elements.
The kinematics obtained with the user-element model is not exactly the one of a adherent helix, even if the values of Δ_p and Δ_c are very small. The reason of this deviation is linked to the approximation in the calculation of the contact normal, which is evaluated from (7.3). Conversely, the relative displacements obtained with the edge-to-edge model are almost null everywhere.

Helix kinematics - Bending

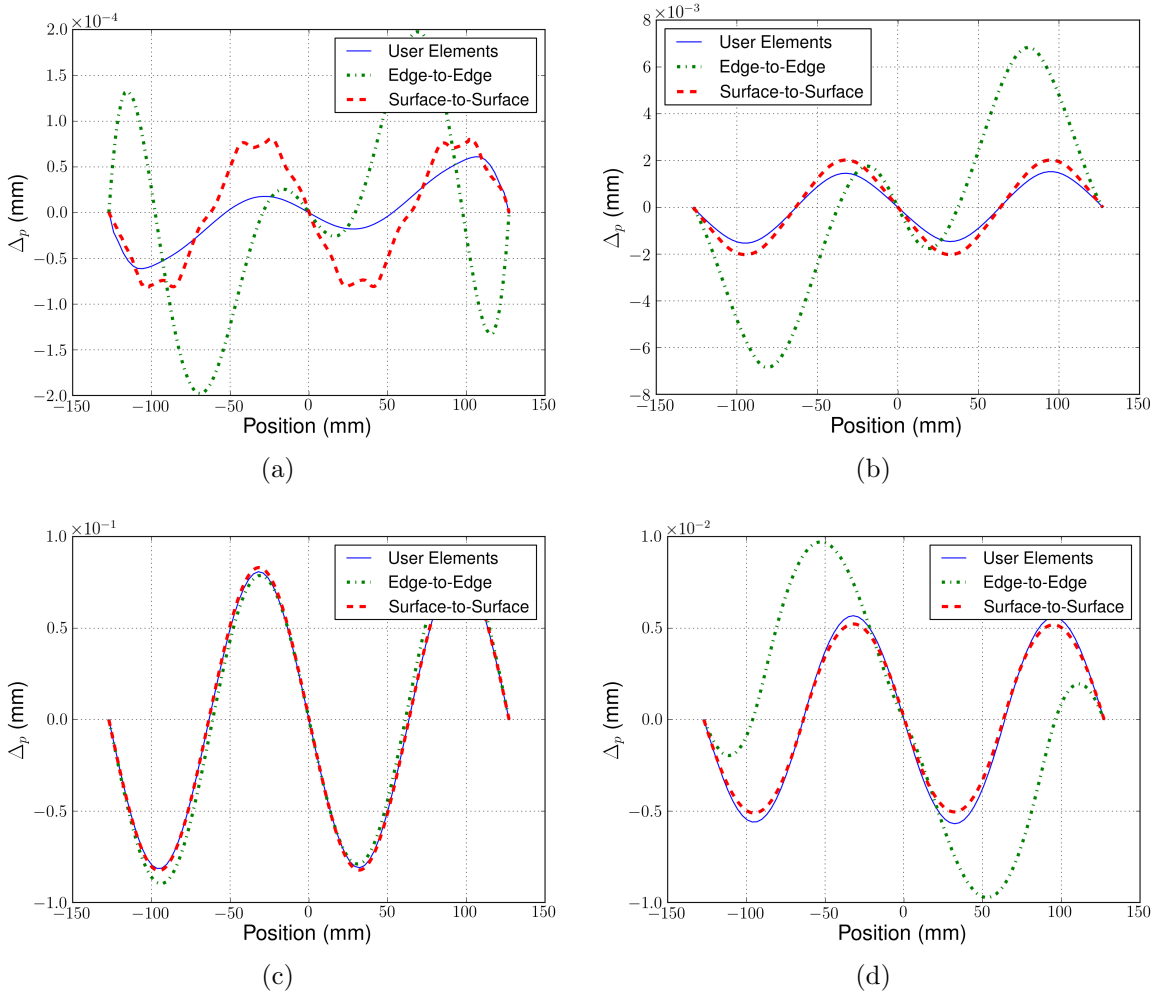

Figure 8.6: Benchmark 1, Δ_p comparison: (a) Load step 2 (b) Load step 3 (c) Load step 4 (d) Load step 5.

Concerning the bending behavior, the results are reported in Figures 8.6-8.7. One can see that the user-element model is in close agreement to the surface-to-surface (i.e. reference) model.

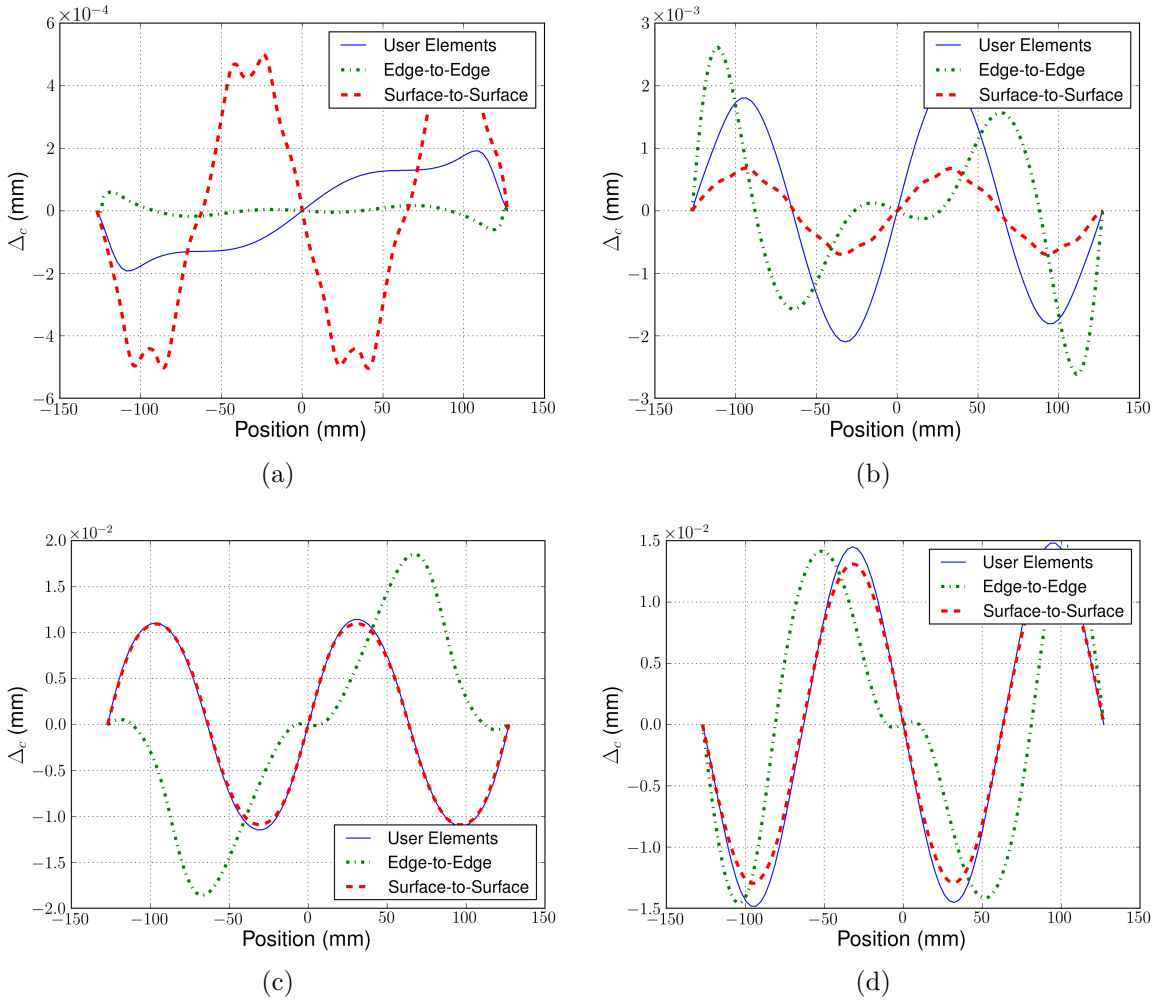

Figure 8.7: Benchmark 1, Δ_c comparison: (a) Load step 2 (b) Load step 3 (c) Load step 4 (d) Load step 5.

Qualitatively, The biggest difference is obtained for the load step 2, where the oscillations affecting the surface-to-surface results originates from the approximate discretization of the cylindrical wire surfaces by the surface elements, as was already shown in Figure 8.5.

One can observe that the kinematics obtained with the edge-to-edge model is not in accordance with the surface-to-surface (i.e. reference) model, both concerning the qualitative distribution and the amplitude of the relative displacements, higher with respect to the ones given by the other models. This actually explains the results shown in Figure 6.6.

In Figure 8.8 one can see the influence of taking into account the sliding along the beam circumference. In fact, by only evaluating the sliding component along the beam axis (i.e. considering contact between curves), the relative displacements (Fig. 8.8a) are closer to the ones of the geodesic curve (see Sec. 2.2.2), reducing the axial strain variation (Fig. 8.8b). Considering also the friction work due to sliding along the circumference, the wire kinematics

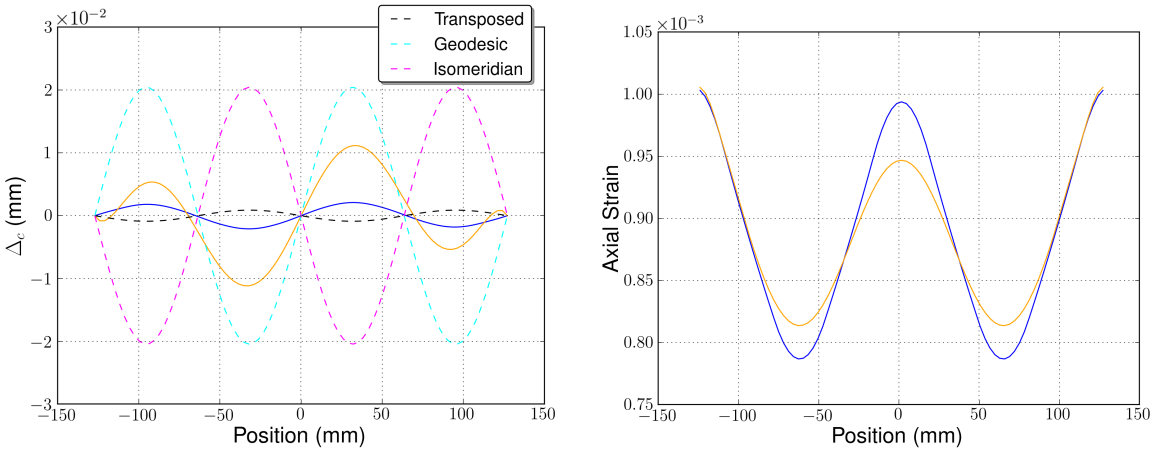

(a) (b)

Figure 8.8: Comparison at load step 3 considering just the sliding along the beam axes, in orange, and considering also the sliding component along the circumferential direction at the beam surfaces (i.e. the second term in Eq. (7.24)), in blue. (a) Relative displacement Δ_c. (b) Axial strain.

is closer to the one described by the transposed curve.

Axial strain distribution

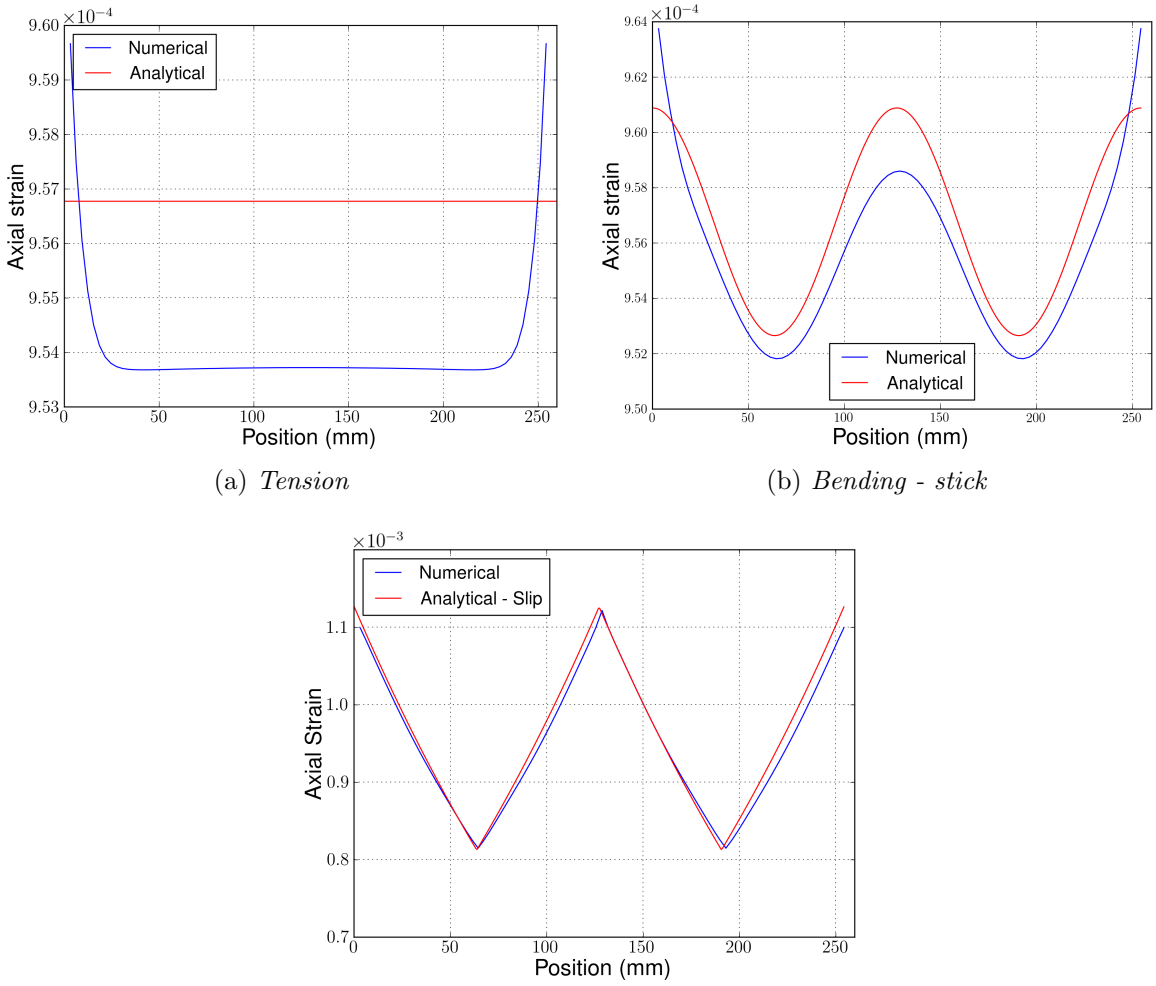

(a) *Tension*

(b) *Bending - stick*

(c) *Slip state*

Figure 8.9: Comparison of the axial strain obtained with the user element with the analytical solutions (from Eq. (2.41)-(2.43)).

The user-element model is also able to fit the analytical curves of the axial strain distribution, in tension and in the different bending regimes (Fig. 8.9). It is worth mentioning that the tangential contact stiffness has an important effect on the axial strain variation in stick state, as shown in Figure 8.10. In particular, an elastic slip of $1.e-4\,mm$ allows to obtain axial strain oscillations comparable with the analytical ones (Fig. 8.9b). The edge effects are probably linked to the boundary conditions on the rotational degrees of freedom at the two end sections.

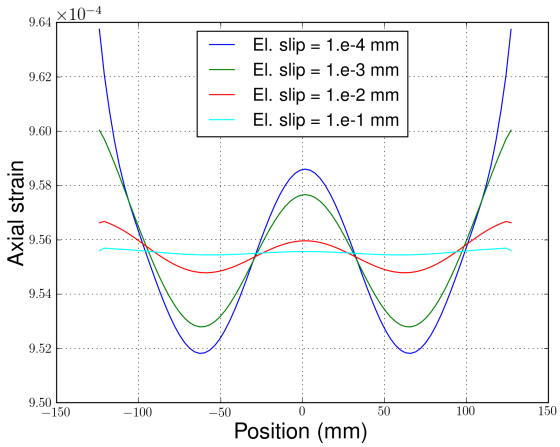

Figure 8.10: Influence of the elastic slip value on the amplitude of the axial strain oscillations in stick state.

8.3.2 Results - Benchmark 2

Helix kinematics - Tension

In pure tension, the helix kinematics obtained with the different models is shown in Fig. 8.11.

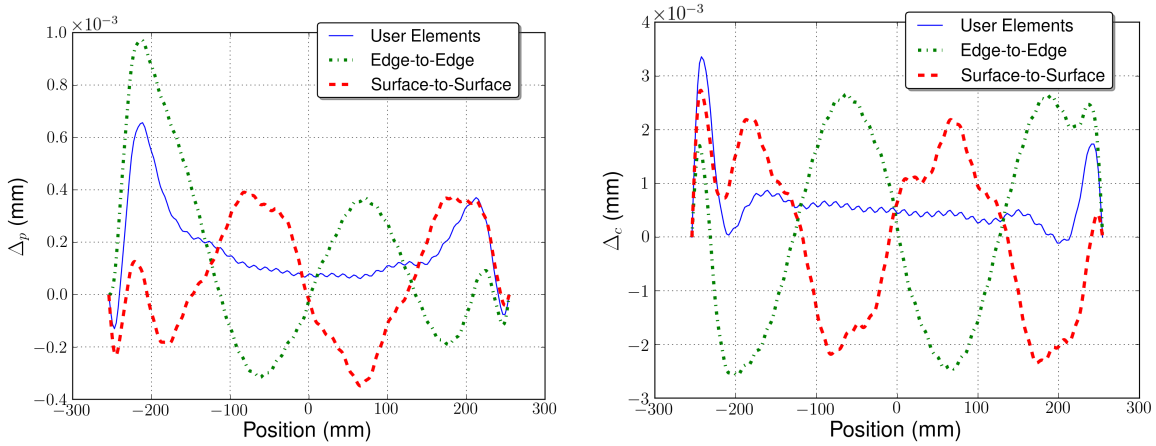

(a) Δ_p (b) Δ_c

Figure 8.11: Benchmark 2, relative displacements with respect to the reference cylinder at load step 1 (pure tension).

One can notice that in all the numerical models the wire kinematics somehow deviates from the one of a perfectly adherent helix. This is primarily due to the influence of the edge effects, since at the model ends the trellis contact is such that the external helical wire is not in contact with the layer underneath. However, concerning the Δ_c distribution (Fig. 8.11)

obtained with the user-element model, one observes that it does not change sign, while in the other models the distributions oscillate around zero.

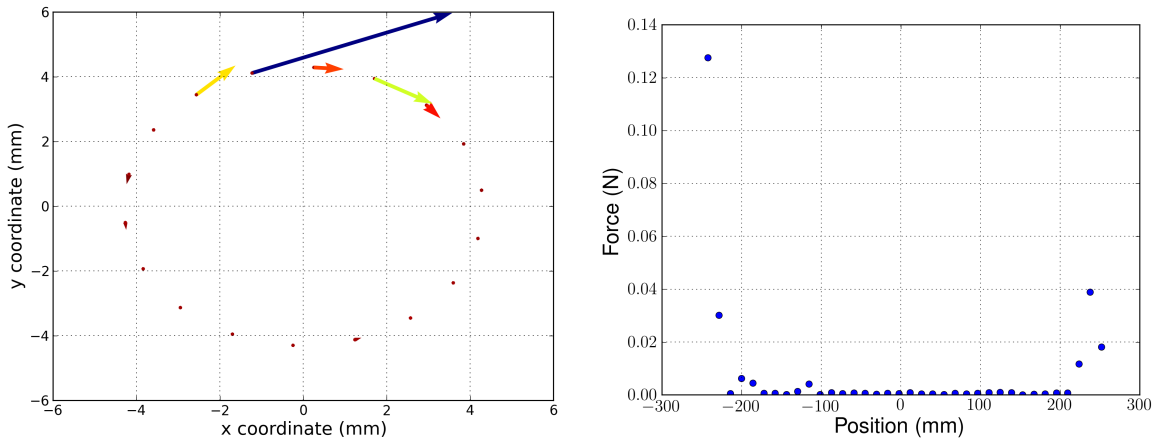

(a) (b)

Figure 8.12: Benchmark 2, load step 1 (pure tension): a) direction of the vectors $\underline{F}_N^{diff}$ at all the contact points projected on the $x-y$ plane; b) norm of $\underline{F}_N^{diff}$.

The Δ_c distribution of the user-element model actually originates from a lack of equilibrium involving the normal contact forces. Let us consider a beam node belonging to a wire in the first layer, which is in contact both with the central wire and with the external helix. The node is at position θ, defined on the $x-y$ plane, with the third cartesian axis z collinear with the central wire axis. The normal vector associated to the node is hence

$$\underline{n} = \begin{pmatrix} \cos(\theta) \\ \sin(\theta) \\ 0 \end{pmatrix}$$

On this nodes two contact forces are acting, from the internal user-element (contact with the central wire) and from the external user element (contact with the external helix). Thus, by separating normal and tangential components one has

$$\underline{F}_1 = F_{N1}\underline{n}_1 + F_{T1}\underline{t}_1, \qquad \underline{F}_2 = F_{N2}\underline{n}_2 + F_{T2}\underline{t}_1$$

We now take the difference of the normal contact forces and we project it on the tangential plane defined by the vector n, i.e.

$$\underline{F}_N^{diff} = (\underline{\underline{I}} - \underline{n} \otimes \underline{n})(F_{N2}\underline{n}_2 - F_{N1}\underline{n}_1)$$

The results are shown in Figure 8.12. One can see that the vectors $\underline{F}_N^{diff}$ point mainly in clockwise sense by looking at Figure 8.12a. These forces basically measure a lack in precision for the determination of the contact normal and are higher at the model ends. This arises therefore from edge effects.

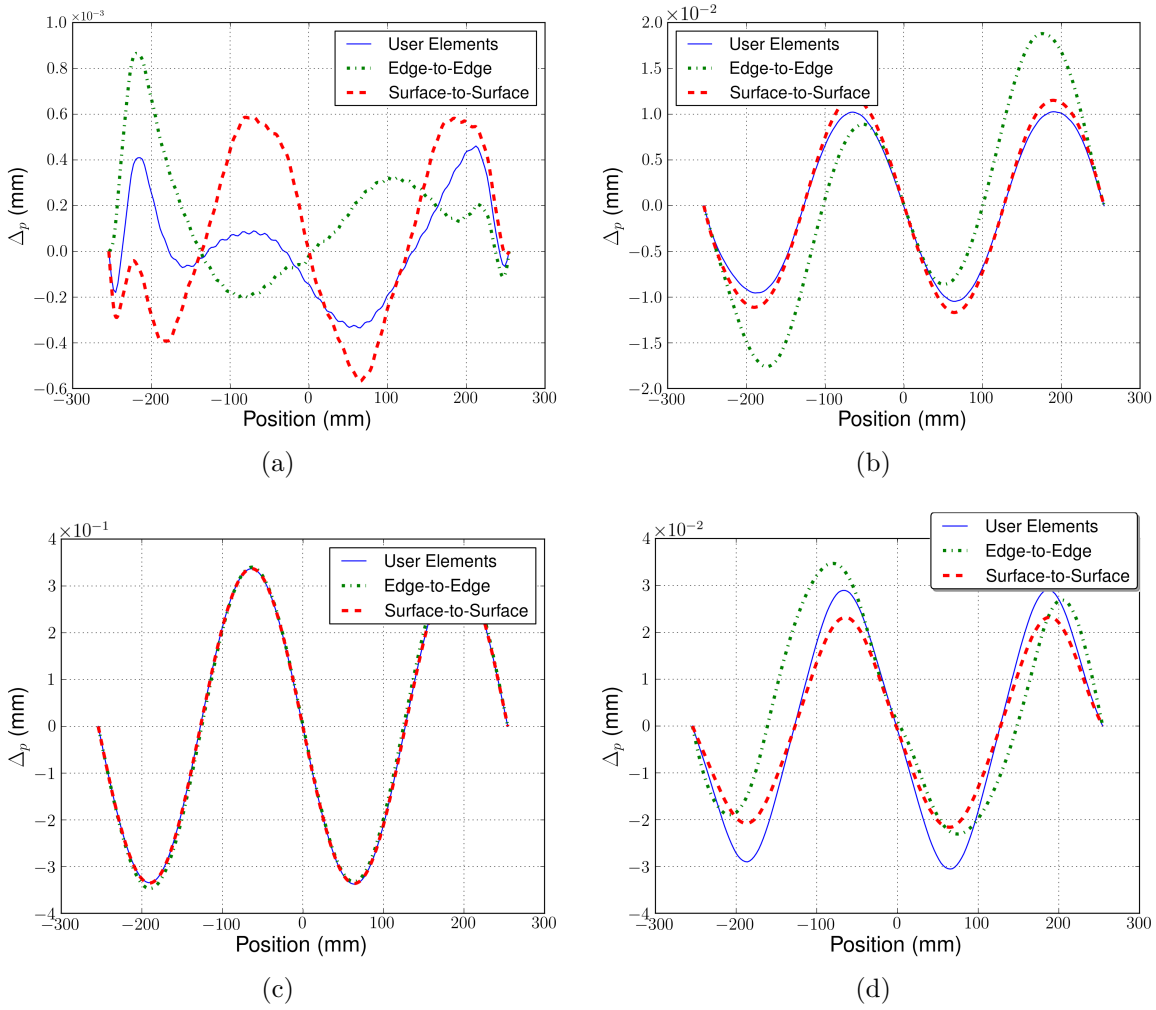

Figure 8.13: Benchmark 2, Δ_p comparison: (a) Load step 2 (b) Load step 3 (c) Load step 4 (d) Load step 5.

Helix kinematics - Bending

The results concerning the helix kinematics are reported in Fig. 8.13-8.14. One can notice that the model employing the user-elements is in good agreement with reference model, even if the results are not that close as it was for benchmark 1.

It can be noticed that the distribution of Δ_c at load step 2 (Fig. 8.14) is nearly the same as the one reported in Figure 8.11, which is referred to tension.

By taking the norm of the two sliding components, one can see that, except for very small curvature, the results are in a pretty good agreement during the bending phase, while at the end of the unbending phase with our model we obtain a residual sliding which is higher with respect to the one obtained with the reference (i.e. surface-to-surface) model (Fig. 8.15).

A possible explanation for this difference can be linked to the fact that the user-element does

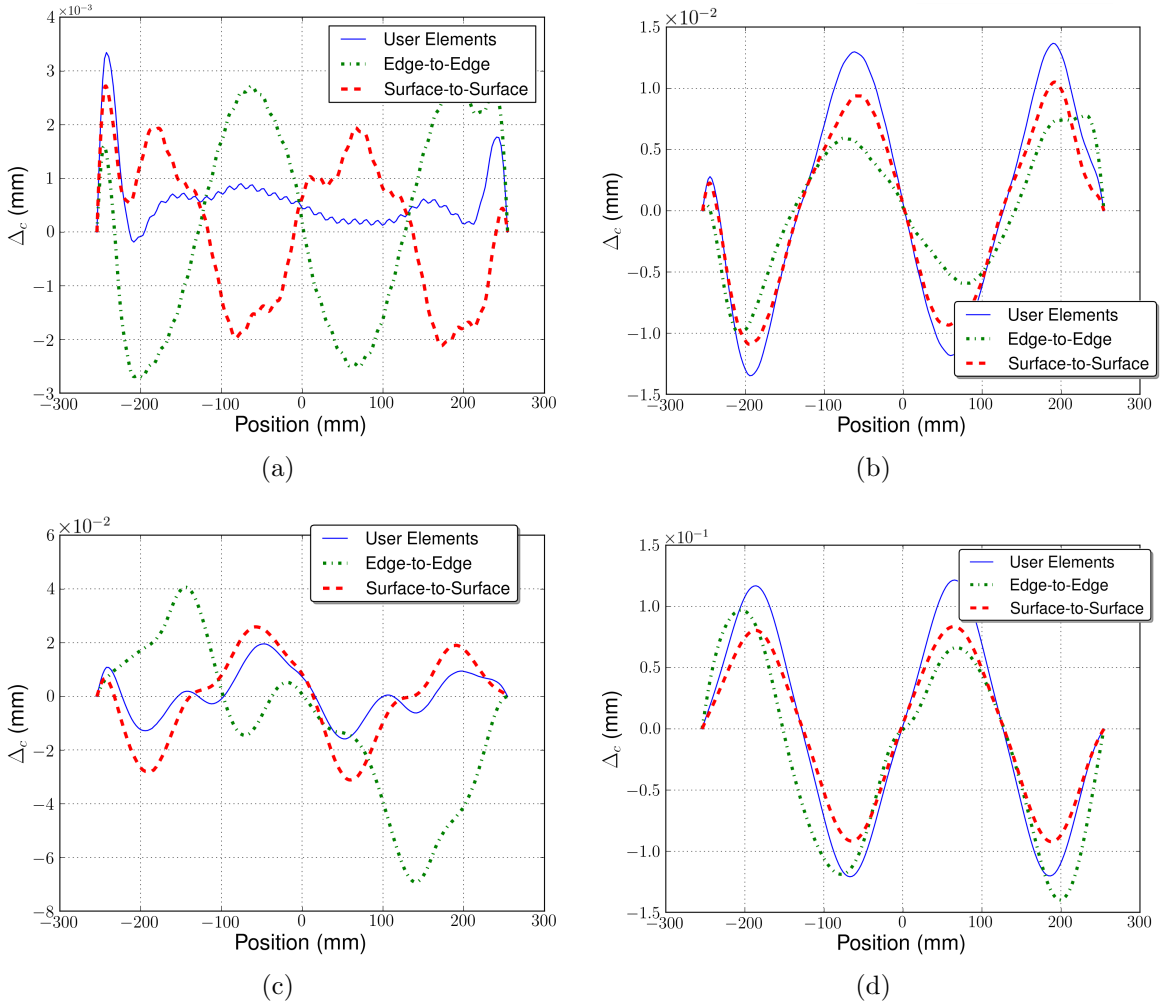

Figure 8.14: Benchmark 2, Δ_c comparison: (a) Load step 2 (b) Load step 3 (c) Load step 4 (d) Load step 5.

not offer any rigidity with respect to a relative rotation of the beams around the contact normal. Conversely, in the surface-to-surface model the contact "points" have a finite dimension (Fig. 8.16) and therefore this relative movement is opposed by friction. In the real world, the contact patches have an elliptical shape (see Sec. 2.4.2) and therefore this rigidity is physically present.

The effect of this "extra-stiffness", which is offered only by the surface-to-surface model, can be observed by looking at the charts in Fig. 8.17, representing the lay angle variation with respect to the initial one, which is $\alpha = 12°$. In particular, one can notice that the lay angle variations are generally higher for the user-element model and the edge-to-edge model.

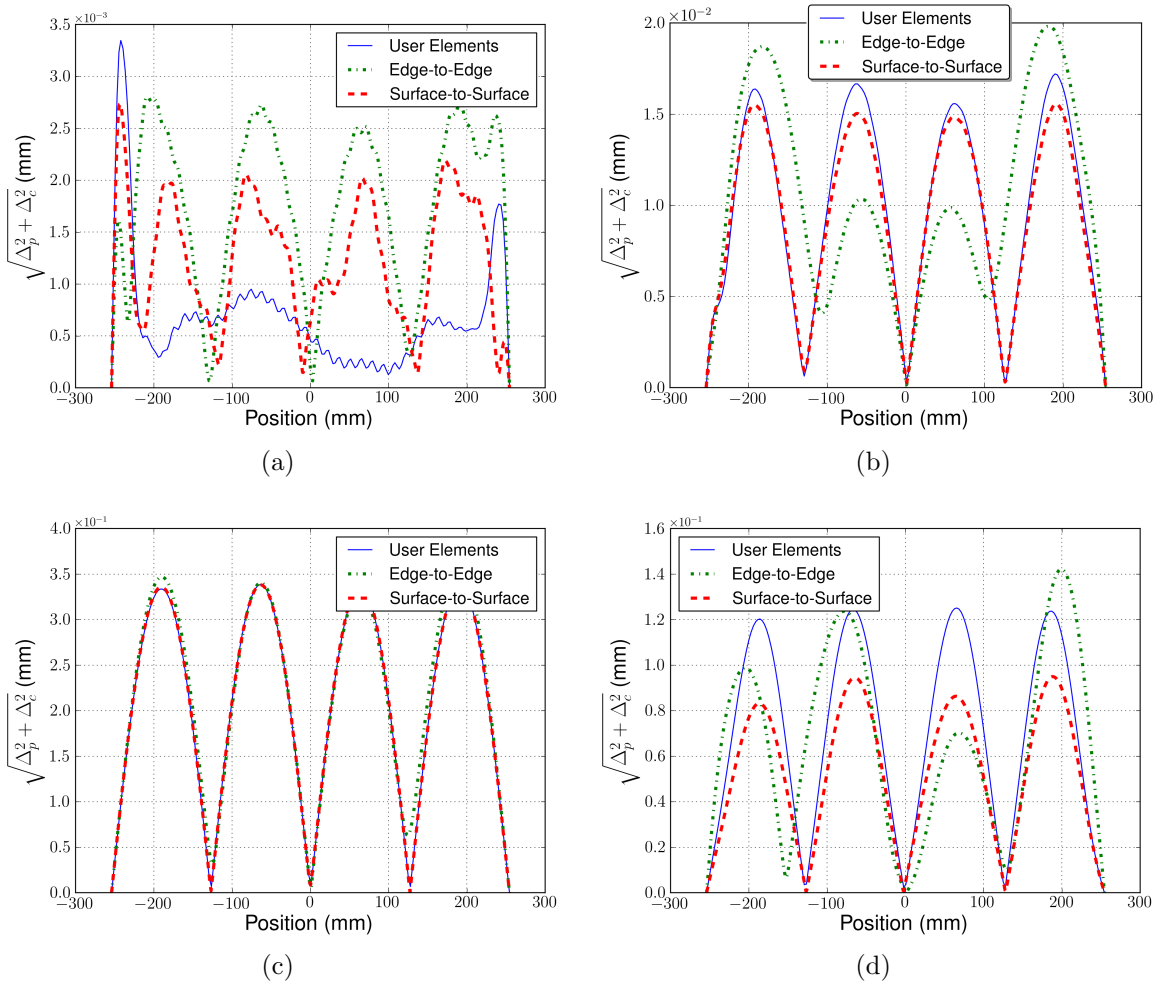

Figure 8.15: Benchmark 2, total slip comparison: (a) Load step 2 (b) Load step 3 (c) Load step 4 (d) Load step 5.

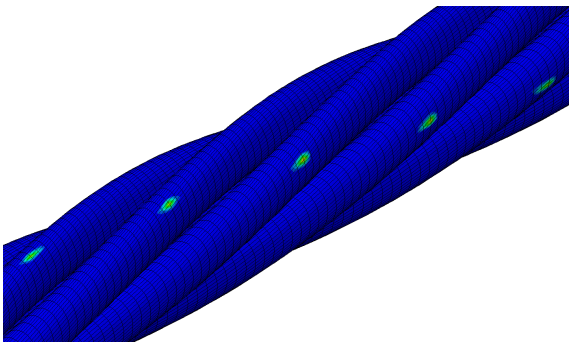

Figure 8.16: Contact areas displayed for the benchmark 2 in the surface-to-surface model.

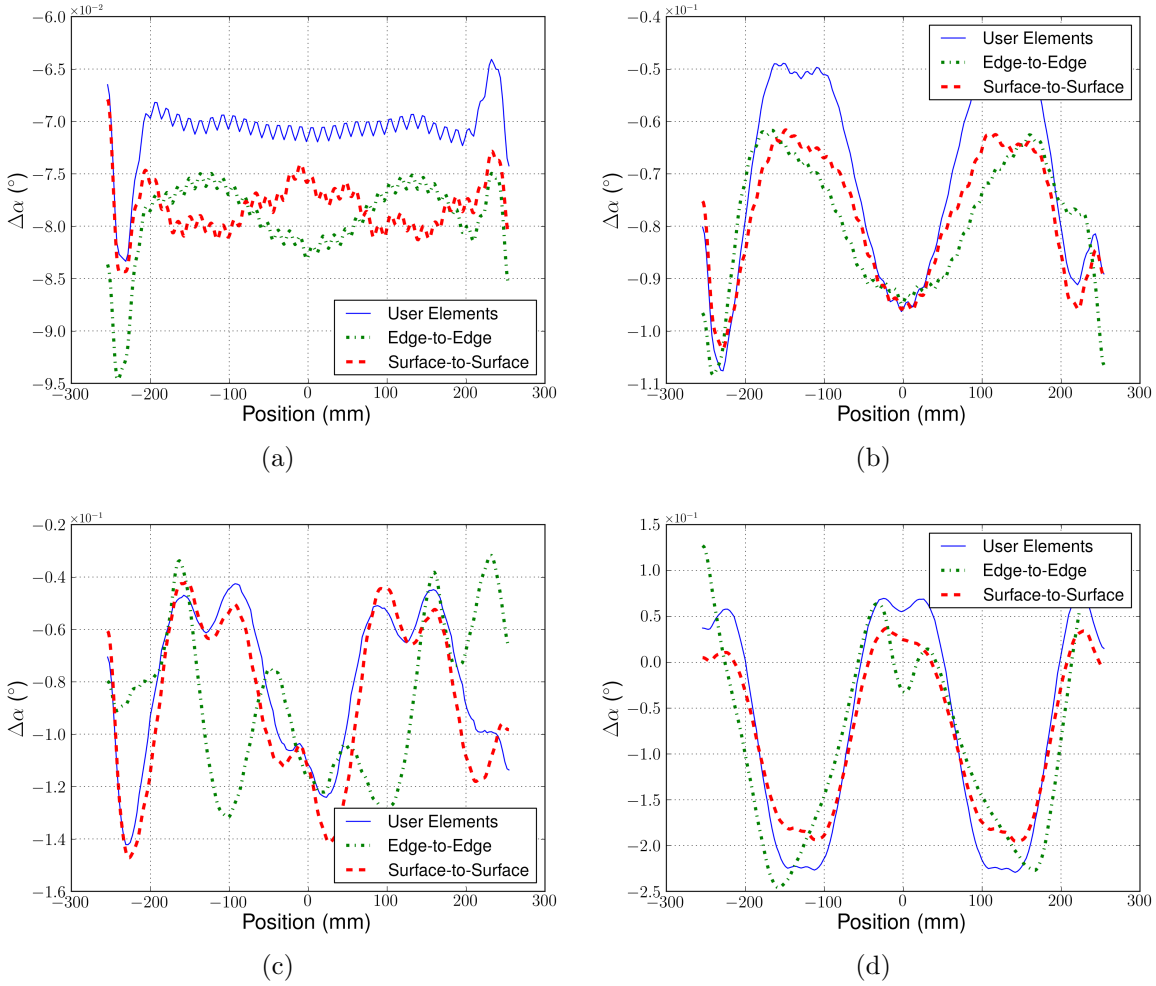

Figure 8.17: Benchmark 2, comparison of the lay angle variation: (a) Load step 2 (b) Load step 3 (c) Load step 4 (d) Load step 5.

Axial strain distribution

The comparison with the analytical results is shown in Fig. 8.18, where the analytical formulae consider line contact.

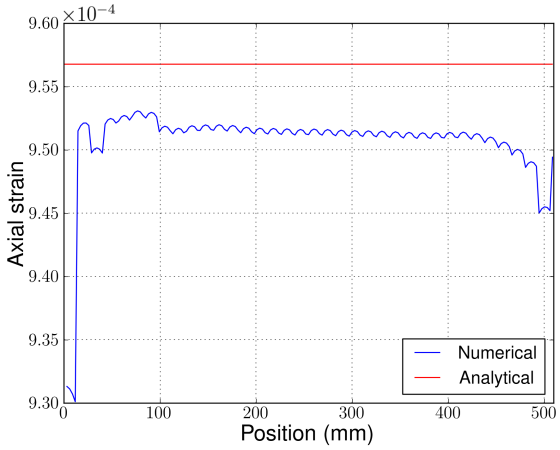

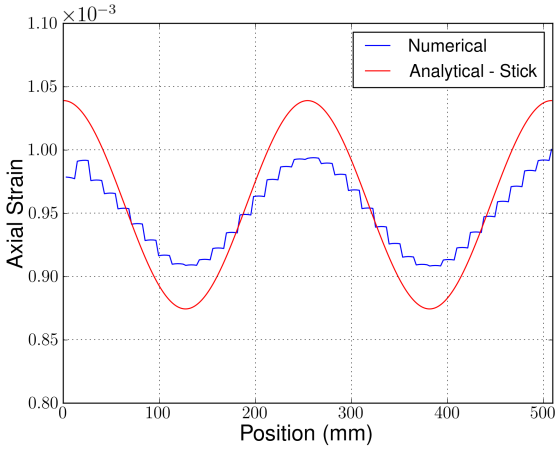

(a) *Tension*

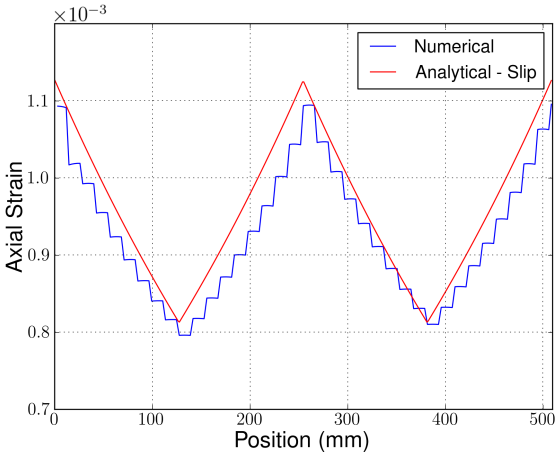

(b) *Slip state*

Figure 8.18: Comparison of the axial strain obtained with the user element with the analytical ones (from Eq. (2.41)-(2.43)).

One may observe that the axial strain amplitude in stick state is lower with respect to the one predicted analytically. There are actually a couple of reasons explaining this fact.

1. Since the spacing of the contact patch is about $14.5\,mm$ along the helical wire, the points in between can actually displace in order to minimize the elastic energy. This causes also the scattering in Fig. 8.13a-8.14a.
2. Because of the penalty formulation, the wires in the first layer are not perfectly stuck to the central wire. Hence, the analytical formula which assumes that the wire is glued to its reference cylinder (see Sec. 2.2.2) is less valid.

8.4 Tension-Bending test

The capabilities of the contact element to deal with the modeling of a multilayer spiral strand has been tested, with the simulation of a tension-bending test, represented in Fig. 8.19. It is actually a test from [111] for studying the resistance to wind vibration of a overhead conductor (Aluminum Conductor Steel Reinfroced, ACSR). The wire rope is subjected to a tensile force $T = 40\,kN$ and to a cyclic transversal force, ranging from $V_{min} = 0\,kN$ to $V_{max} = 4.3\,kN$, applied at midspan. The wire rope ends are clamped, i.e. any rotation and relative sliding movement between the wires is prevented. It is actually allowed for the wires to move relatively in radial direction.

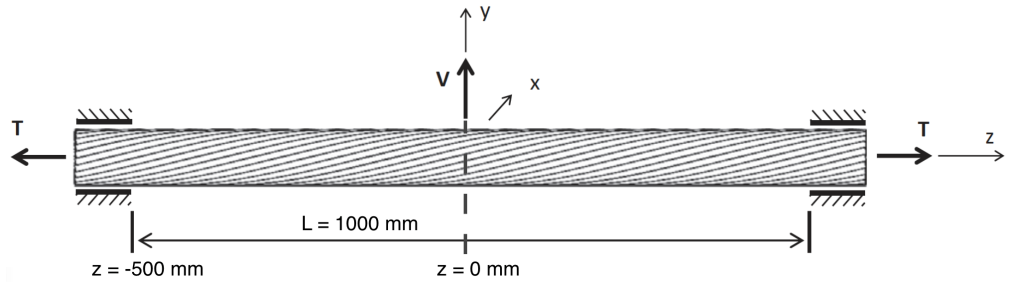

Figure 8.19: Tension bending test scheme [84].

Layer Nb.	**Nb. of wires**	**Wire diam.** (mm)	**E** (GPa)	ν	**Lay Angle** (deg.)
Core	1	3.34	210	0.3	-
1	6	3.34	180	0.3	6.06
2	12	3.32	65	0.33	11.99
3	18	3.32	65	0.33	11.80
4	24	3.32	65	0.33	13.10

Table 8.8: Wire rope characteristics [84]. It is constituted by steel wires (central wire and first layer) and aluminum wires (second, third and fourth layer).

The characteristics of the ACSR Cardinal wire rope are reported in Table 8.8. The friction coefficient at the steel-steel and steel-aluminum interfaces is set to 0.3, while for the aluminum-aluminum interface is set to 0.5.

In the user-element model, lateral contact between the wires at the same layer is introduced via the use of tube-to-tube contact elements. These contact elements aim to model finite-sliding interactions between tubular structures in which the bodies are roughly parallel along their surface. Namely, they are slide line contact elements, for which it is assumed that the relative motion of the two beams is predominantly along the line defined by the axis of one of the beams [1].

This test was performed in [111] and has been simulated numerically in [84], where the authors model the wires with quadratic beam elements and use the beam-to-beam contact algorithm of the commercial software ANSYS. The obtained results will be therefore compared to the experimental ones, regarding the rope deflection, and the numerical ones that involves axial

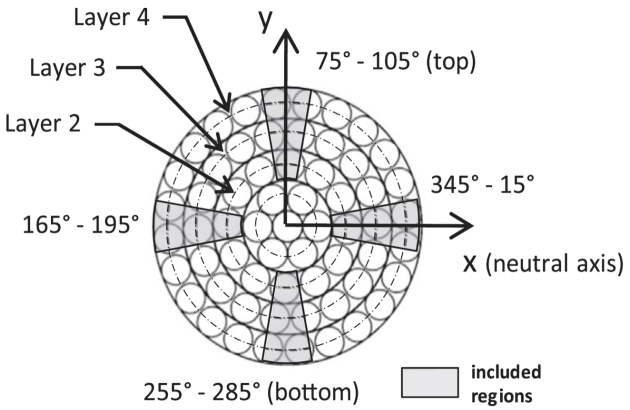

Figure 8.20: Sectors of the ACSR Cardinal wire rope cross-section [84].

force, contact forces and interwire slip, which will be compared in the portion $-500\,mm \leq z \leq 0\,mm$ and for different sectors and layers (Fig. 8.20). Moreover, the test has been simulated by using the edge-to-edge contact algorithm of Abaqus®, but for which only the axial force distribution along the wires and the rope deflection are available results, since post-processing contact quantities in case of multiple interactions on a single beam node are not directly accessible.

In particular, the quantities obtained at $V = V_{max}$ and their variation between configurations $V = V_{max}$ and $V = 0$ will be compared. Because of the hysteretic bending behavior of the wire rope, two bending cycles are simulated. The quantities reported in the following are referred to the second bending cycle.

Regarding the axial force, the results are shown in Fig. 8.21 to 8.26. One can observe that the results given by the three models are generally in good agreement. The highest differences concern the results for layer 2 (Fig. 8.21-8.22), for which one can see that

- at $V = V_{max}$ the user element model predicts a higher gradient of axial force along the sectors;
- for the axial force variation on the neutral plane, it is lower for the user-element model in the zone in between the clamped end and the midspan.

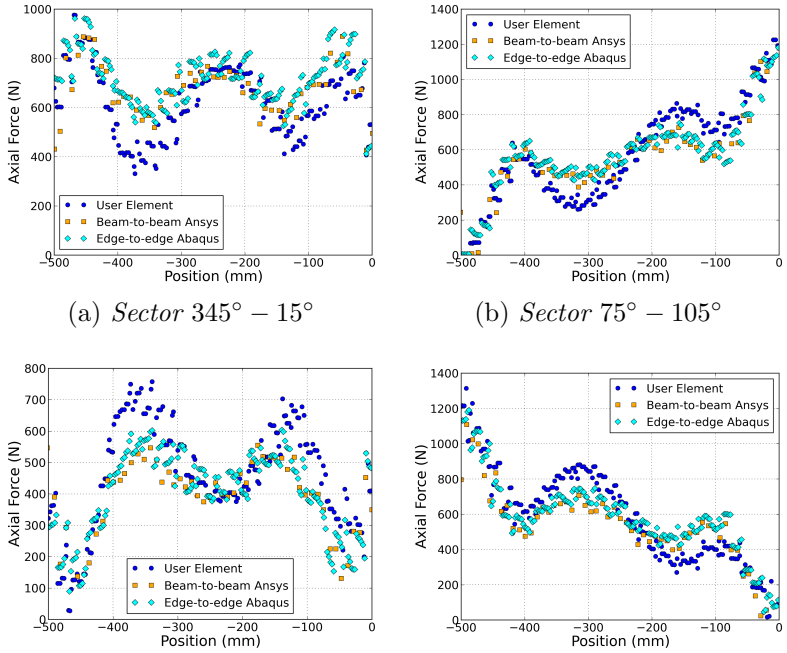

(a) *Sector* 345° − 15° (b) *Sector* 75° − 105°

(c) *Sector* 165° − 195° (d) *Sector* 255° − 285°

Figure 8.21: Axial force comparison at $V = V_{max}$, layer 2.

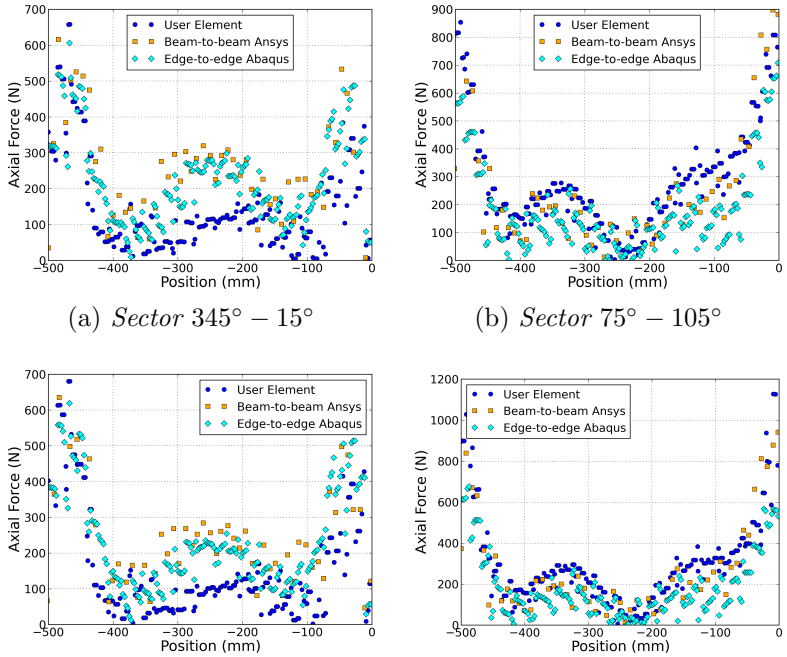

(a) *Sector* 345° − 15° (b) *Sector* 75° − 105°

(c) *Sector* 165° − 195° (d) *Sector* 255° − 285°

Figure 8.22: Axial force variation comparison, layer 2.

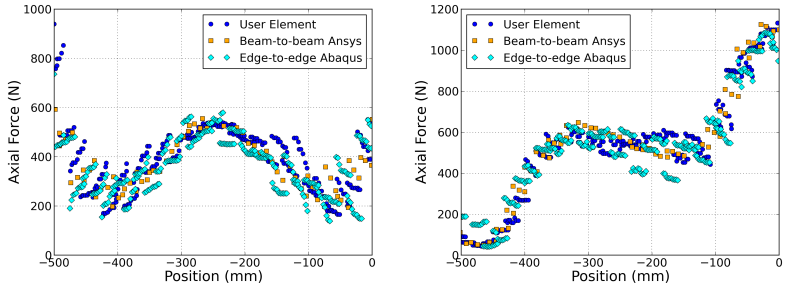

(a) *Sector* 345° − 15° (b) *Sector* 75° − 105°

(c) *Sector* 165° − 195° (d) *Sector* 255° − 285°

Figure 8.23: Axial force comparison at $V = V_{max}$, layer 3.

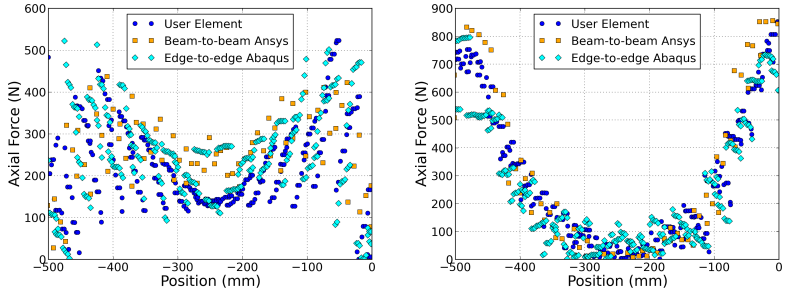

(a) *Sector* 345° − 15° (b) *Sector* 75° − 105°

(c) *Sector* 165° − 195° (d) *Sector* 255° − 285°

Figure 8.24: Axial force variation comparison, layer 3.

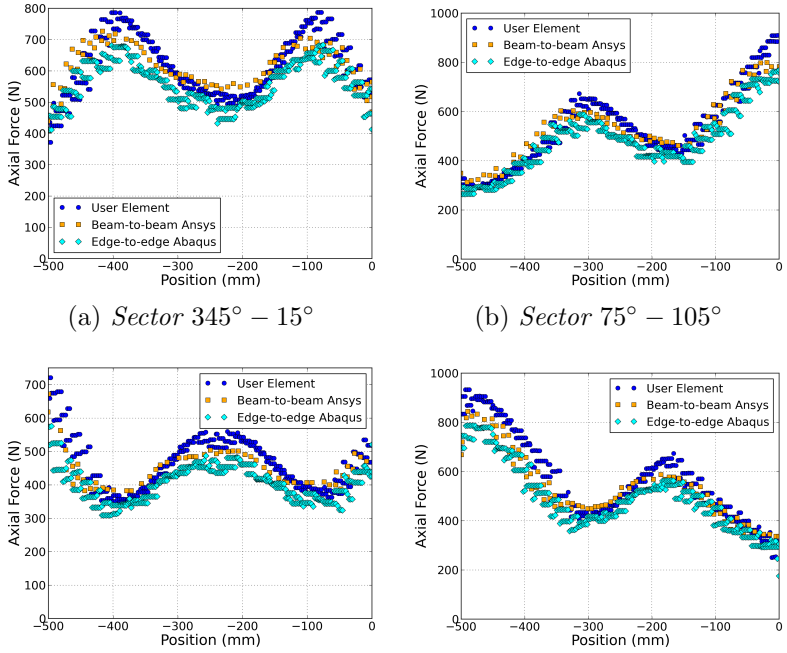

(a) *Sector* 345° − 15° (b) *Sector* 75° − 105°

(c) *Sector* 165° − 195° (d) *Sector* 255° − 285°

Figure 8.25: Axial force comparison at $V = V_{max}$, layer 4.

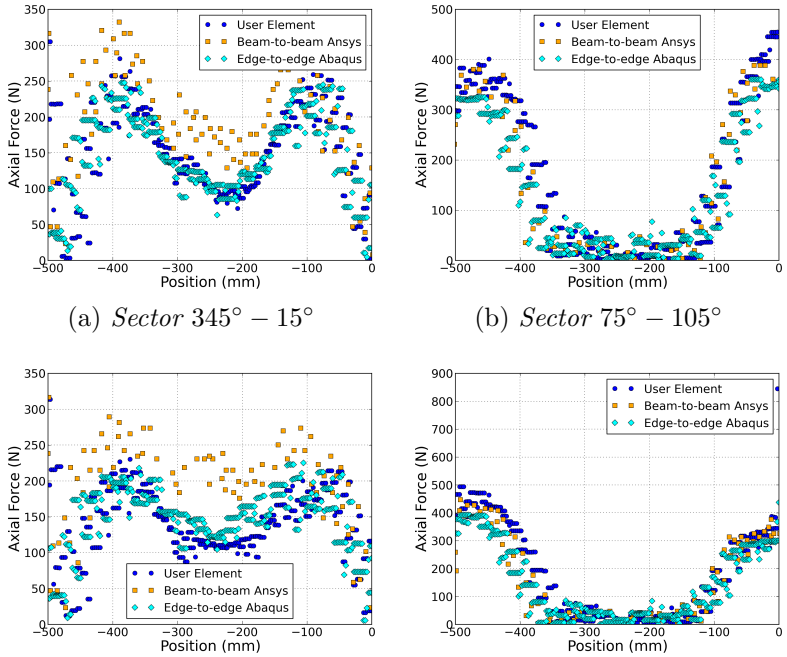

(a) *Sector* 345° − 15° (b) *Sector* 75° − 105°

(c) *Sector* 165° − 195° (d) *Sector* 255° − 285°

Figure 8.26: Axial force variation comparison, layer 4.

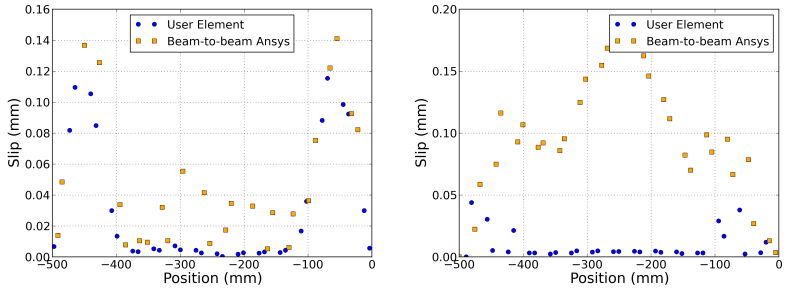

(a) *Sector* 345° − 15° (b) *Sector* 75° − 105°

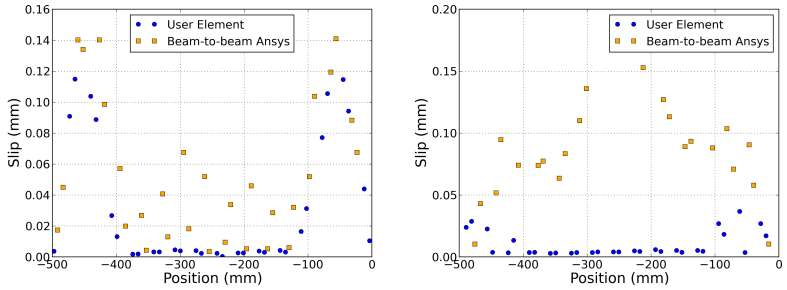

(c) *Sector* 165° − 195° (d) *Sector* 255° − 285°

Figure 8.27: Sliding comparison at $V = V_{max}$, interface between layer 1 and 2.

The sliding comparison is shown in Fig. 8.27 to 8.32. The general tendency is that the slip estimated by the ANSYS model [84] is higher than the one obtained with the user-element model. In particular the most important differences can be seen for the internal layers.

At the interface between layers 1-2 (Fig. 8.27-8.28) and layers 2-3 (Fig. 8.29-8.30), it may be seen that in the proximity of the neutral plane the sliding predicted by the user element model is confined in the zones close to the rope termination and at midspan (i.e. where the transversal load is applied). Conversely, in the beam-to-beam model of ANSYS the sliding propagates in basically the whole length of the rope. Similarly, in the user element model at the outer and inner arc sectors, the sliding is negligible along the whole rope, whereas some sliding takes place in the ANSYS model.

From these observations, we can draw the conclusions that the interwire friction in the user element model is sufficient to dissipate rapidly the effects of the transversal load. Consequently, the amount of sliding in the nearly straight wire rope portion (i.e. in between clamped end and midspan) is negligible. Moreover, at the outer and inner arc sectors we can see that the user-element model predicts an interwire sliding lower with respect to the one estimated by the beam-to-beam model.

Regarding the most external contact interface (Fig. 8.31-8.32), the sliding predictions are in a good agreement considering the neutral plane sectors. However, for the outer and inner arc sectors the same trend observed for the internal layers is noticed.

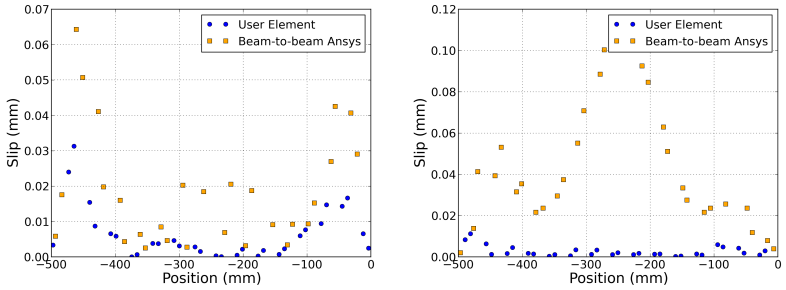

(a) *Sector* 345° − 15° (b) *Sector* 75° − 105°

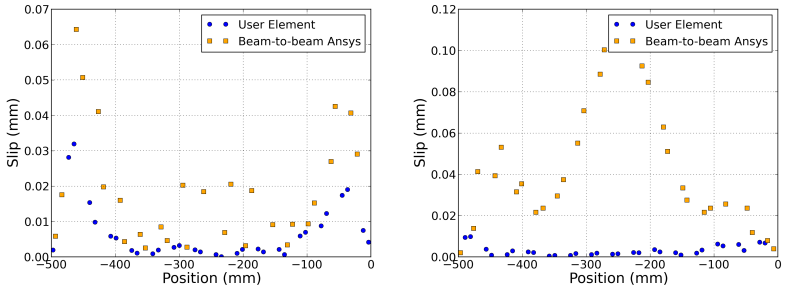

(c) *Sector* 165° − 195° (d) *Sector* 255° − 285°

Figure 8.28: Sliding variation comparison, interface between layers 1 and 2.

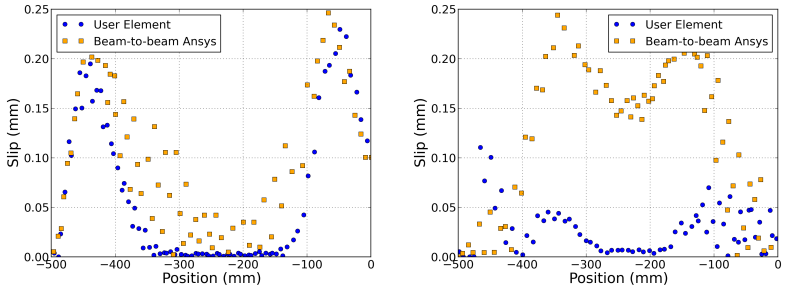

(a) *Sector* 345° − 15° (b) *Sector* 75° − 105°

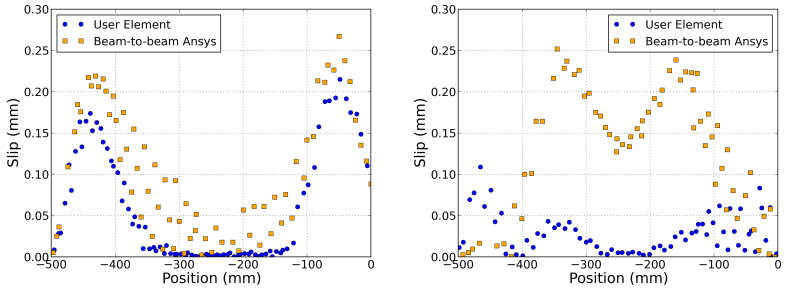

(c) *Sector* 165° − 195° (d) *Sector* 255° − 285°

Figure 8.29: Sliding comparison at $V = V_{max}$, interface between layers 2 and 3.

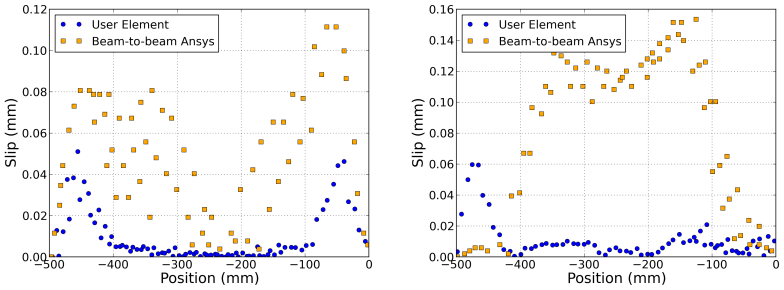

(a) *Sector* 345° – 15° (b) *Sector* 75° – 105°

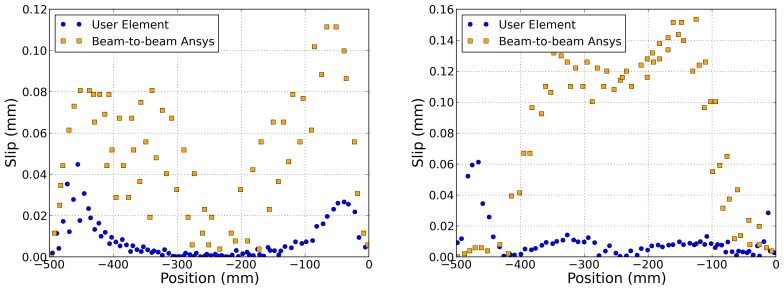

(c) *Sector* 165° – 195° (d) *Sector* 255° – 285°

Figure 8.30: Sliding variation comparison, interface between layers 2 and 3.

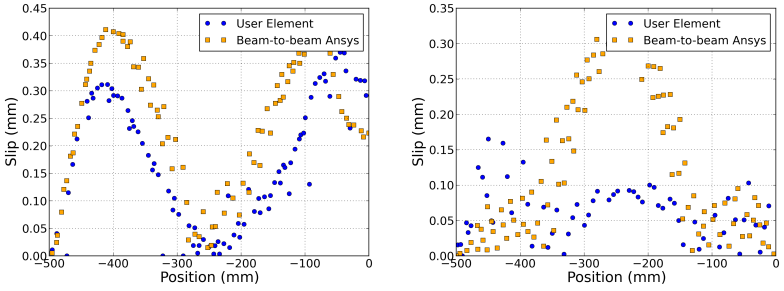

(a) *Sector* 345° – 15° (b) *Sector* 75° – 105°

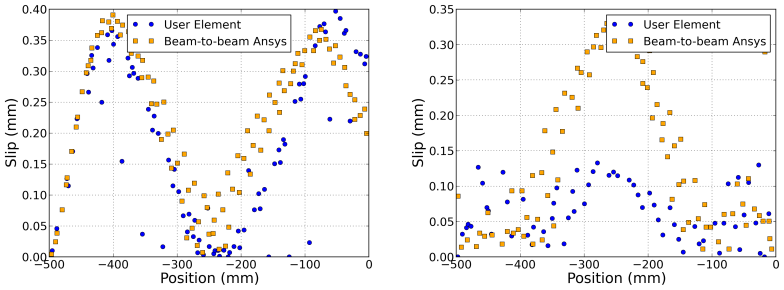

(c) *Sector* 165° – 195° (d) *Sector* 255° – 285°

Figure 8.31: Sliding comparison at $V = V_{max}$, interface between layers 3 and 4.

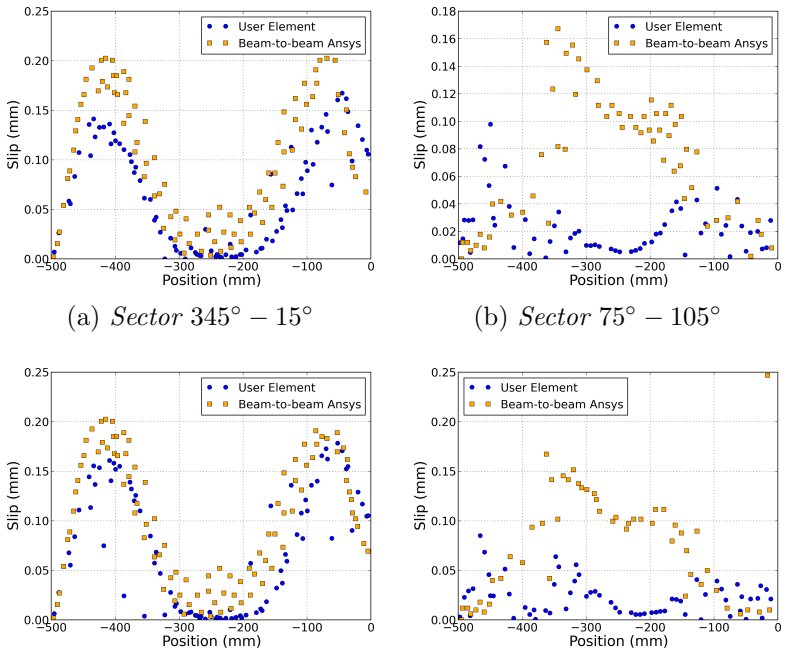

(a) *Sector* $345° - 15°$ (b) *Sector* $75° - 105°$

(c) *Sector* $165° - 195°$ (d) *Sector* $255° - 285°$

Figure 8.32: Sliding variation comparison, interface between layers 3 and 4.

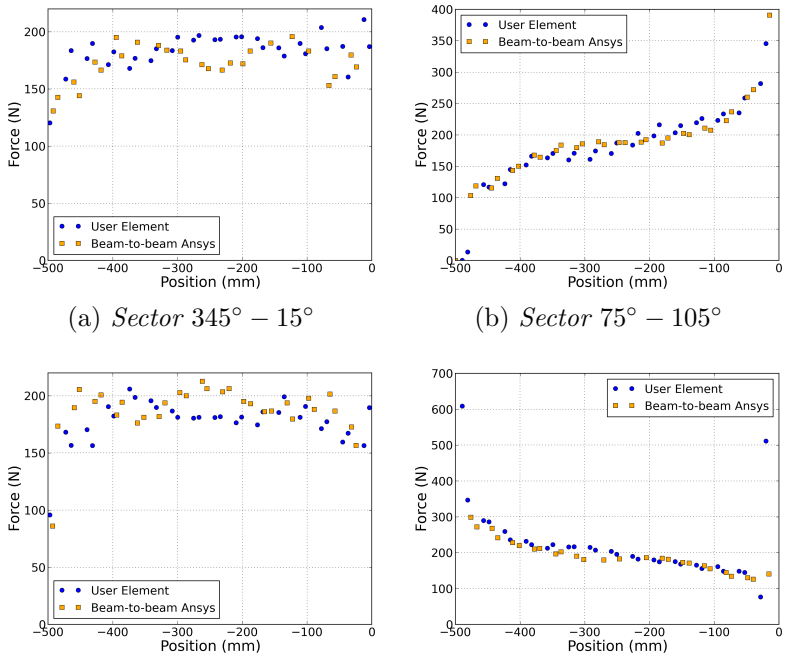

(a) *Sector* 345° − 15° (b) *Sector* 75° − 105°

(c) *Sector* 165° − 195° (d) *Sector* 255° − 285°

Figure 8.33: Normal contact force at $V = V_{max}$, interface between layers 1 and 2.

Considering the contact forces, the comparison involves the interface between layers 1 and 2. The predictions of normal contact force (Fig. 8.33-8.34) show a good agreement between the two models, expect for the variation in the neutral plane sectors, for which in any case both models give very scattered results. The estimated tangential contact forces (Fig. 8.35-8.36) have qualitatively the same distribution. It is worth mentioning that in [84] negligible tangential force variations are predicted in between the clamped-end and the midspan in the outer and inner arc sectors. However, one may see from Fig. 8.28b-8.28d that the results of the beam-to-beam model show important slip variations in this area. The results of slip and tangential contact forces seem therefore in contradiction for this model.

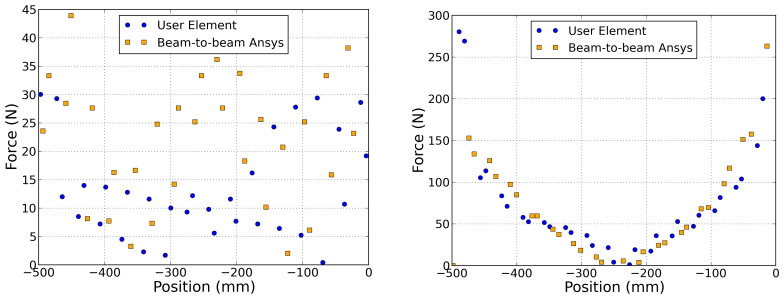

(a) *Sector* 345° − 15° (b) *Sector* 75° − 105°

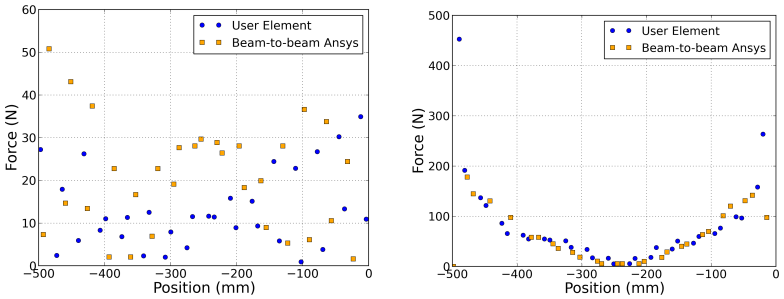

(c) *Sector* 165° − 195° (d) *Sector* 255° − 285°

Figure 8.34: Normal contact force variation, interface between layers 1 and 2.

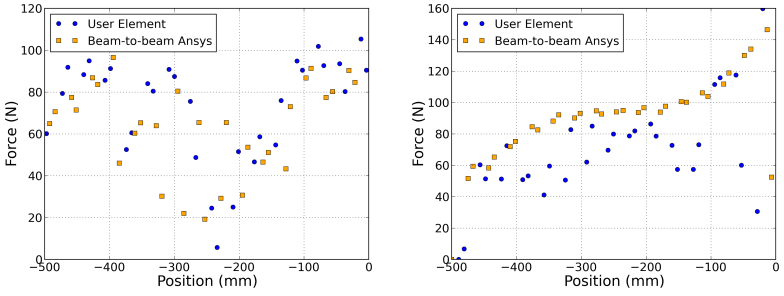

(a) *Sector* 345° − 15° (b) *Sector* 75° − 105°

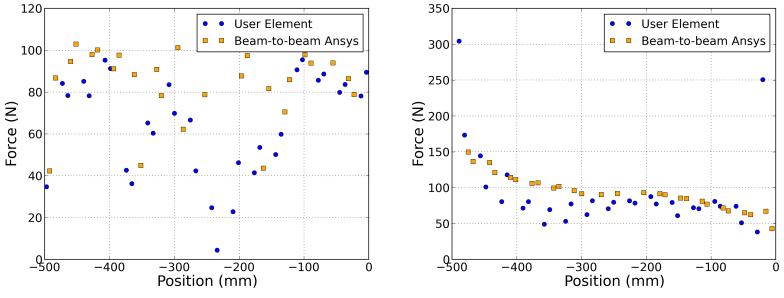

(c) *Sector* 165° − 195° (d) *Sector* 255° − 285°

Figure 8.35: Tangential contact force at $V = V_{max}$, interface between layers 1 and 2.

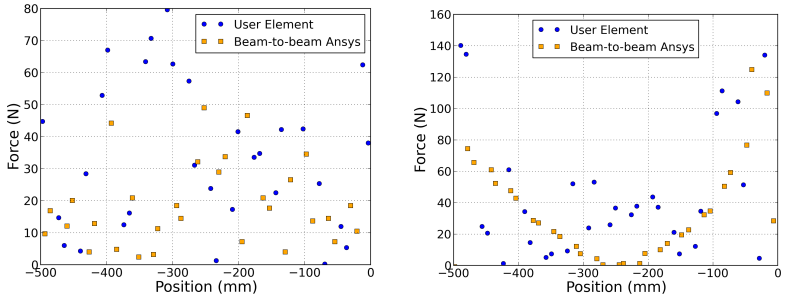

(a) *Sector* 345° − 15°

(b) *Sector* 75° − 105°

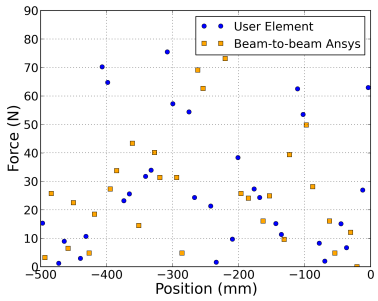

(c) *Sector* 165° − 195°

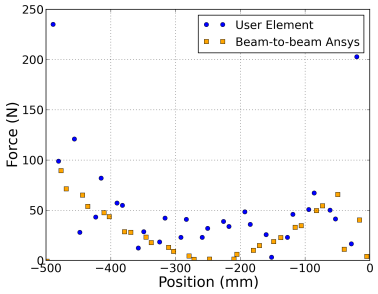

(d) *Sector* 255° − 285°

Figure 8.36: Tangential contact force variation comparison, interface between layers 1 and 2.

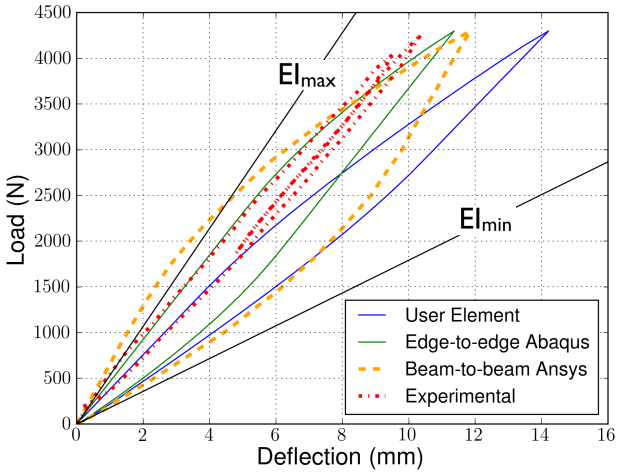

Figure 8.37: Load-deflection curve predicted by the user-element model, the other numerical models and the experimental one, obtained in [111].

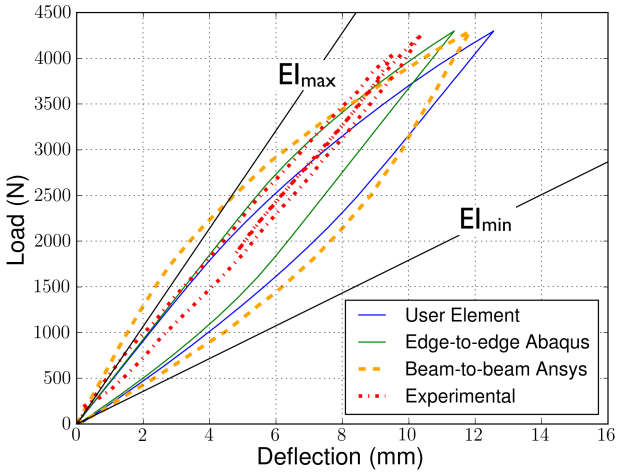

Figure 8.38: Load-deflection curve predicted by the user-element model, with the small radius formulation similar to [169], the other numerical models and the experimental one, obtained in [111].

The load-deflection curve is reported in Fig. 8.37. One may see that the user element model is less stiff with respect to the other models. The dissipated energy, which can be measured by the area of the hysteresis loop, is in agreement with the one estimated by the edge-to-edge model.

Regarding the bending stiffness of the model, it is worth mentioning that a stiffer behavior is obtained by using the small radius formulation (Fig. 8.38), similar to the one proposed in [169]. In this formulation, only the sliding along the beam axes is considered and the tangential contact forces do not produce any nodal moment. Indeed, the moments transporting the tangential forces on the beam nodes (Fig. 8.39) are responsible for the more compliant

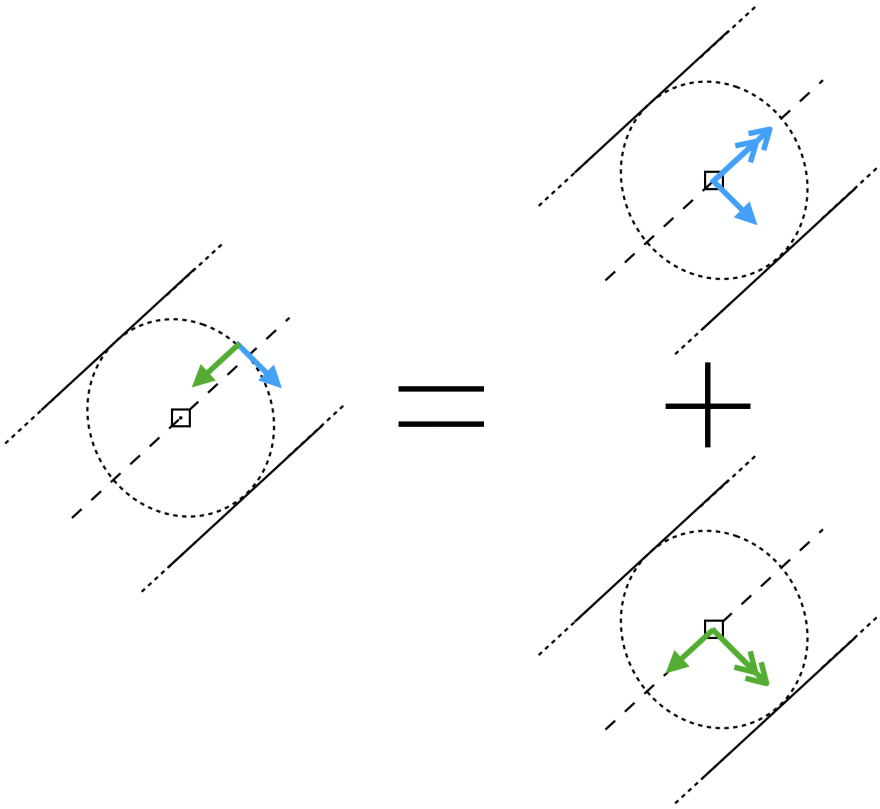

Figure 8.39: The tangential forces act at the beam surface. If the beam radius is not negligible, one needs to introduce the moments to transport the forces on the beam node. Double arrows represent moments, single arrows represent forces.

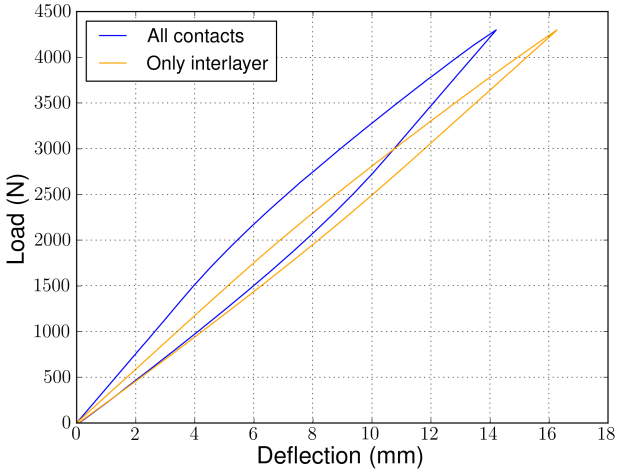

Figure 8.40: Load-deflection curve predicted by the user-element model, considering or not the contact between the wires in the same layer, which is modeled by tube-to-tube contact elements [1].

behavior. These transporting moments are absent in the edge-to-edge model, justifying the user-element model to be brought closer to the other models, from Figure 8.37 to 8.38.

Taking into account the intra-layer contact between adjacent wires also results in a stiffer response, as shown by Fig. 8.40.

As a final remark, it is worth mentioning that the real frictional behavior of the contacting wires, particularly for the aluminum ones, is probably different from the isotropic one used in the numerical models. Figure 2.15 shows that important indentation phenomena may occur at the inter-layer contact locations.

8.5 Conclusion

Some general comments can be stated regarding the capabilities of the user-element of modeling beam contact interactions.

From the pointwise contact benchmark (Sec. 8.2), it has been seen the user-element predicts correctly the normal contact forces and the stick-slip behavior, even when a high friction coefficient is used.

In the benchmark 1 (Sec. 8.3.1), the results that have been obtained are in very good agreement with the reference model concerning the helix kinematics and with the analytical results regarding the axial strain distribution. Moreover, this element allows to consider a high stiffness in the tangential direction, which is very important to capture the behavior during bending when small curvature variations are involved.

In the benchmark 2 (Sec. 8.3.2), dealing with localized contact points, the agreement concerning the helix kinematics is not as good as it is for the benchmark 1. This may be due to different reasons. In particular, it has been shown that, because of the small sliding approximation, a lack of equilibrium concerning the normal contact forces arises. Moreover, the user element lacks of a stiffness contribution concerning the rotations of the wires around the normal contact directions.

In the modeling of the tension-bending test of a multilayer spiral strand (Sec. 8.4), the axial force predictions in the wires obtained by the numerical models are generally in good agreement. Other results, concerning contact quantities and the wire rope deflection, are not in agreement with the ones of other numerical models. However, the outputs of these models seem sometimes questionable, particularly concerning the tangential contact quantities (i.e. inter-wire slip and tangential forces). Therefore, they cannot be really taken as a reference.

It should be pointed out that important speed-up factors are obtained by using the user-element. In the following, the total CPU time of the user-element is compared with the edge-to-edge model. Except when differently specified, all the calculations reported below have been performed with a Intel® Xeon® CPU E5-1620 @ 3.50 GHz.

- Pointwise contact benchmark
  - edge-to-edge: 1.57 s
  - user-element: 0.38 s (speed-up factor of about 4)
- Benchmark 1

  - edge-to-edge: $67.4\,s$
  - user-element: $6.52\,s$ (speed-up factor of about 10)
- Benchmark 2
  - edge-to-edge: $3431.9\,s$
  - user-element: $172.13\,s$ (speed-up factor of about 20)
- Tension-bending test
  - edge-to-edge: $2.8014e+5\,s$ (using 2 Intel® Xeon® CPU E5-2670 v3 @ 2.30 GHz (Haswell) with 8 processors)
  - user-element: $5120.4\,s$ (with 4 processors)

Further investigation have to be done concerning the frame invariance problem explained in Section 8.1.

Chapter 9

Application to mooring modeling

In this chapter, the developed finite element model is used for performing the analysis of a mooring line portion of the case study presented in chapter 5. In particular, the zone most subjected to curvature of the mooring line 1 is analyzed. The Dang Van criterion will be applied in order to assess the fatigue risk.

9.1 Boundary conditions

As reported in the flowchart of Fig. 4, the FOWT (i.e. global) model yields the time series of tension and curvature along the mooring lines and for each sea state. These quantities (Fig. 9.1) associated to a specific critical zone are the inputs of the wire rope model, to which constant axial strain and curvature are applied to the central wire. For the sake of simplicity, it is assumed that the bending axis remains unchanged during the analysis. Moreover, the rope torsion is prevented.
The problem consists in the imposition of the boundary conditions. The imposition of a plane-section kinematics at the end sections of the model would in fact generate important edge effects which would affect the results along the whole model length, as shown in Fig. 9.2. Therefore, a strategy has been developed to impose the boundary conditions simulating the continuity of the wire rope. In other words, the boundary conditions simulate that the rope would continue beyond the model ends with the same curvature and tension.

9.1.1 Periodic boundary conditions

These boundary conditions are imposed via a Multi-Point Constraint (MPC) user-subroutine. An important result coming from the analytical models is here exploited. When a wire rope is bent, relative displacements among the wires of adjacent layers may occur according to the curvature, the applied tension and the friction coefficient between the contacting wires [111]. Consequently, when sliding occurs, initial plane cross sections are in general not plane anymore in the bent configuration.

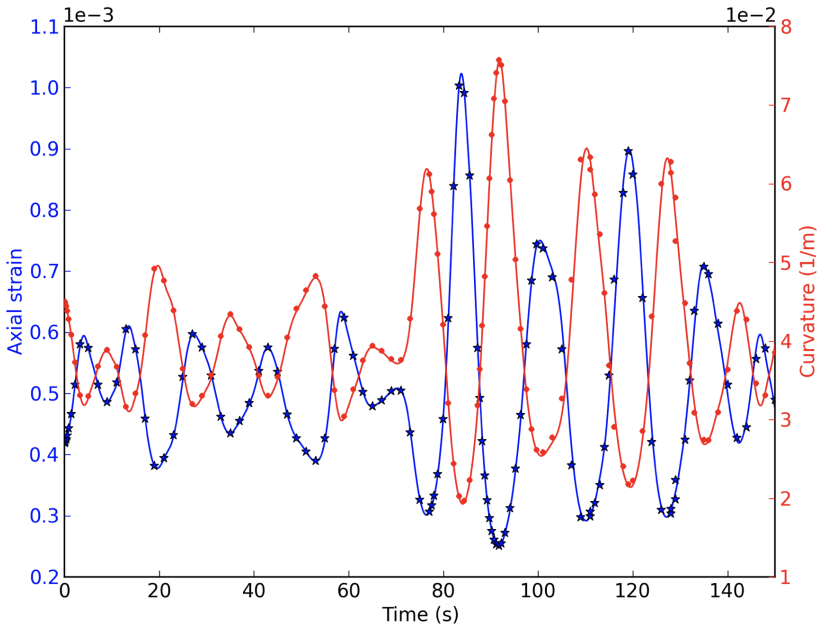

Figure 9.1: Example of time history of axial strain and curvature obtained from the global model.

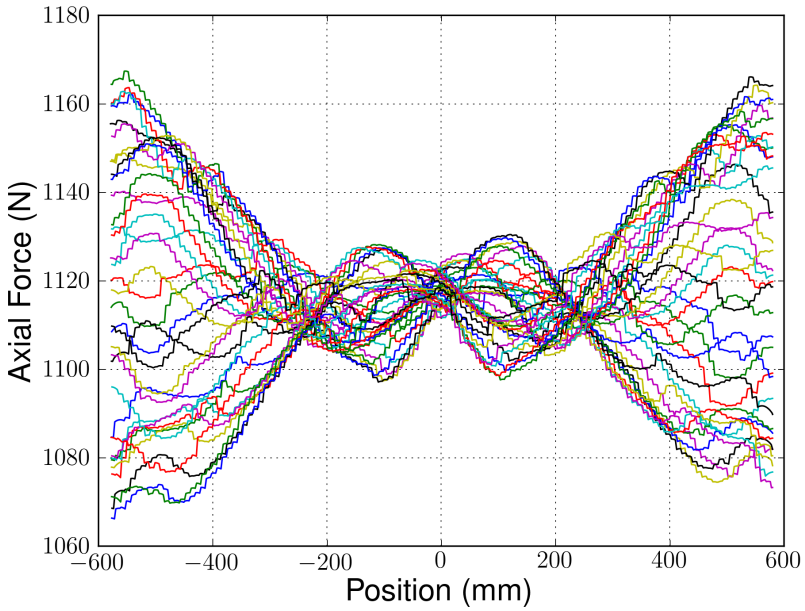

Figure 9.2: Snapshot of the axial force distribution in the wires of the last layer of the mooring wire rope along a sea state simulation. In this example the length of the model is twice the lay length of the last layer.

When bent, a position along the wire can be parameterized by a circumferential angle θ from $\pi/2$ at the outer-arc to $-\pi/2$ at the inner arc. The analytical axial force distribution in a

helical wire of a bent wire rope geometrically depends on θ. In particular, its gradient is null at the wire sections in correspondence of positions $\theta = \pm\frac{\pi}{2}$. This means that no friction forces develop at these positions and consequently no relative displacements occur. Kinematically, this means that the points at these positions follow the rotation of the rope cross section in the bent configuration.

Let us consider a wire rope portion whose axis has constant axial deformation and curvature. We consider two wires in a given layer L (Fig. 9.3): for one of these wires, two nodes at positions $\theta = \pm\frac{\pi}{2}$ are linked to the corresponding nodes of the central wire in such a way that they stay on the same wire rope cross section in the bent configuration, meaning that we impose zero relative displacement with respect to the central wire, and they keep the same position θ on this cross section (since we do not consider wire rope torsion). For this wire the boundary conditions are well imposed and consequently any computed quantity related to this wire can be considered correct. In the following we will refer to this wire as the *reference wire* of layer L. In particular we can obtain the correct profile of relative displacement with respect to the central wire. A Multi-Point constraint (MPC) allows to transfer this information to the other wires in the same layer. In this way the continuity of the wire rope is modeled correctly.

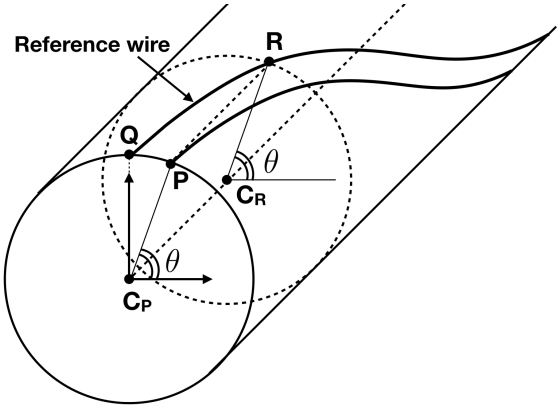

Figure 9.3: Points involved in a MPC.

The points involved in each MPC are four and are represented in Fig. 9.3:

- the point P is the one to which the constraint is imposed (i.e. the slave node), since $\theta_P \neq \pm\frac{\pi}{2}$;
- the point C_P is the node of the central wire in the cross section containing the points Q and P;
- the point R is the node on the reference wire for which $\theta_R = \theta_P$
- the point C_R is the node on the central wire in the cross section containing R.

The point Q (Fig. 9.3) is at position $\theta_Q = \frac{\pi}{2}$. It is not involved in the MPC but it is kinematically linked to C_P to stay in the same cross section and at the same angle θ.

In general, points R and C_R do not coincide with nodes in the finite element model. In this case, the degrees of freedom at these positions can be defined by using the FEM interpolation

of the beam segments to which they belong, to recover a link to the dofs of these segment nodes.

The constraint equation for displacement imposes that the relative sliding of point P with respect to C_P is the same of that for point R with respect to C_R. The relative sliding is determined for nodes P and R with respect to the wire rope cross sections defined by the rotation vectors respectively at points C_P ($\underline{\Phi}_{C_P}$) and C_R ($\underline{\Phi}_{C_R}$), i.e.

$$\underline{\underline{R}}^T_{C_P}(\underline{x}_P - \underline{x}_{C_P}) = \underline{\underline{R}}^T_{C_R}(\underline{x}_R - \underline{x}_{C_R}) \tag{9.1}$$

where $\underline{\underline{R}}$ indicates the rotation matrix and $\underline{x}$ the position vector. For the rotation vectors we simply impose

$$\underline{\Phi}_P = \underline{\Phi}_{C_P} \tag{9.2}$$

By denoting with θ_i, X^z_i and $\underline{u}_i$ respectively the angle theta (Figure 9.3), the position along the wire rope axis and the displacements of node i, we can approximate the degrees of freedom at point R by a linear interpolation of the degrees of freedom of the adjacent nodes, since these points are in practice very close. Therefore one gets

$$\xi_R = \frac{\theta_P - \theta_{R_1}}{\theta_{R_2} - \theta_{R_1}}$$

$$X^z_R = X^z_{C_R} = (1 - \xi_R)X^z_{R_1} + \xi_R X^z_{R_2}$$

$$\underline{u}_R = (1 - \xi_R)\underline{u}_{R_1} + \xi_R \underline{u}_{R_2}$$

We now consider equation (9.1). By multiplying on the left both sides by $\underline{\underline{R}}_{C_P}$ we obtain

$$\underline{f}_d = \underline{x}_P - \underline{x}_{C_P} - \underline{\underline{R}}_{C_P}\underline{\underline{R}}^T_{C_R}(\underline{x}_R - \underline{x}_{C_R}) = 0 \tag{9.3}$$

The displacements of the slave node P are hence given by

$$\underline{u}_P = \underline{\underline{R}}_{C_P}\underline{\underline{R}}^T_{C_R}(\underline{x}_R - \underline{x}_{C_R}) + \underline{x}_{C_P} - \underline{X}_P \tag{9.4}$$

We now proceed with the linearization of the constraint equations $\underline{f}_d$. Since

$$\delta\underline{v} = \delta\underline{\underline{R}}\underline{V} = \delta\underline{\widehat{\theta}}\,\underline{\underline{R}}\underline{V} = \delta\underline{\theta} \wedge (\underline{\underline{R}}\underline{V}) \quad \forall \underline{v} = \underline{\underline{R}}\underline{V}$$

with $\underline{\underline{R}}$ the rotation matrix and $\delta\underline{\theta}$ the linearized rotation vector, and

$$\delta(\underline{\underline{R}}\underline{\underline{R}}^T) = 0 \longrightarrow \delta\underline{\underline{R}}^T = -\underline{\underline{R}}^T\delta\underline{\underline{R}}\underline{\underline{R}}^T = -\underline{\underline{R}}^T\delta\underline{\widehat{\theta}}$$

we get

$$\begin{aligned} \delta\underline{f}_d \;=\; & \delta\underline{u}_P - \delta\underline{u}_{C_P} - \delta\underline{\theta}_{C_P} \wedge [\underline{\underline{R}}_{C_P}\underline{\underline{R}}^T_{C_R}(\underline{x}_R - \underline{x}_{C_R})] \\ & + \underline{\underline{R}}_{C_P}\underline{\underline{R}}^T_{C_R}[\delta\underline{\theta}_{C_R} \wedge (\underline{x}_R - \underline{x}_{C_R})] \\ & - \underline{\underline{R}}_{C_P}\underline{\underline{R}}^T_{C_R}(\delta\underline{u}_R - \delta\underline{u}_{C_R}) = 0 \end{aligned} \tag{9.5}$$

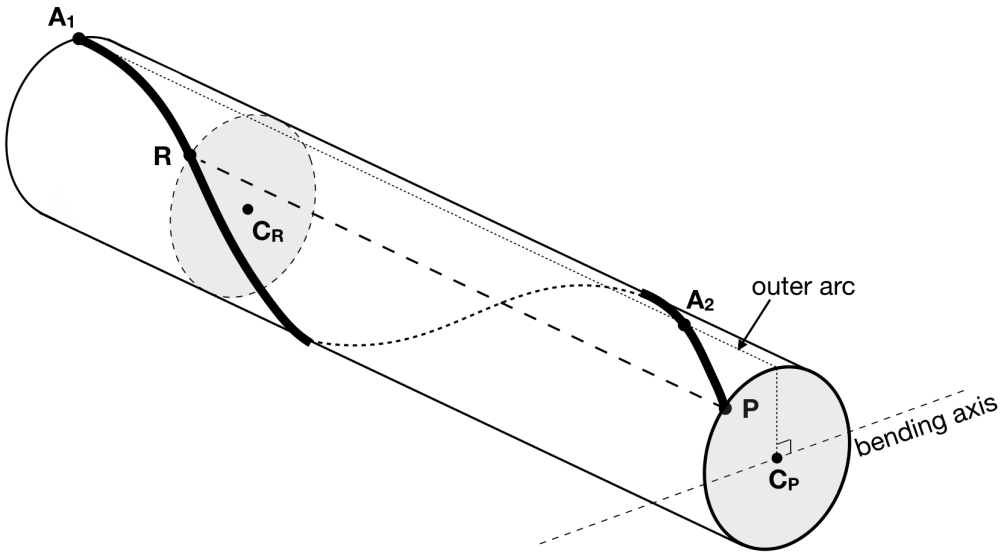

Figure 9.4: Benchmark to test the imposition of the periodic boundary conditions.

9.1.2 Implementation

A problem has been encountered in the implementation of the periodic boundary conditions. It will be explained by looking at the results obtained with the simple benchmark represented in Figure 9.4.

It is constituted by a helical wire wrapped around another wire. At A_1, the helical wire starts at the outer-arc. Hence, the plane section kinematics at this end of the wire is correct. At the other end P one has to apply the multipoint constraint (9.1), with P as slave node. This benchmark aims also to verify if the algorithm converges without imposing the plane section kinematics at node A_2, which is at the outer arc as node A_1.

The results will be shown for two different cases. In both of them the displacement of the slave node are imposed satisfying (9.1), while the difference consists in the implementation of the linearization (9.5)

- in the case *Missing terms* the terms associated to $\delta\underline{u}_R$ and $\delta\underline{u}_{C_R}$ are not implemented,
- in the case *Complete linearization* every term in (9.5) is implemented.

Figures 9.5-9.6 show the helix kinematics with respect to the reference cylinder (see Sec. 2.2.2) obtained in tension and bending, this latter both in stick and slip regimes. One can see that when the terms associated to $\delta\underline{u}_R$ and $\delta\underline{u}_{C_R}$ are absent, the kinematics of the helix is periodic, while putting these terms the displacement profile is not periodic anymore. Moreover, with the complete linearization the periodicity condition is not applied exactly, since the right end should have the same values of Δ_p and Δ_c of the master node R, which is at position $\approx -92\,mm$. This wire kinematics generates the axial strain profiles represented in Figure 9.7. In the distribution obtained with the complete linearization one can clearly see a sharp jump in correspondence of the master node. Nevertheless, the convergence rate of the incomplete linearization is lower, as one would expect since the tangent operator for

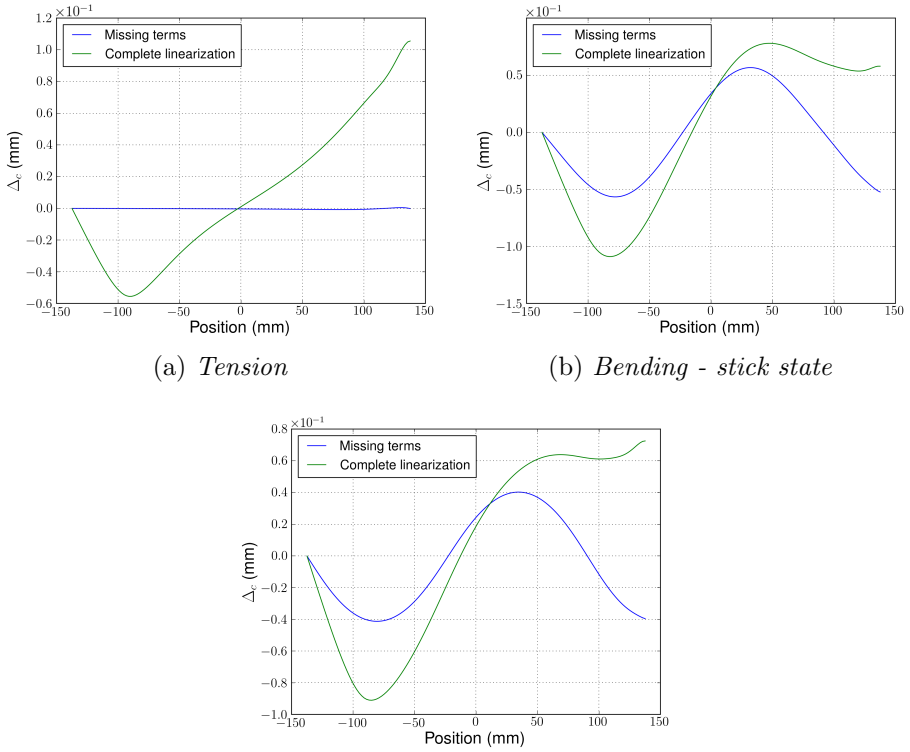

(a) *Tension* (b) *Bending - stick state*

(c) *Bending - slip state*

Figure 9.5: Distribution of Δ_c.

the Newton-Raphson algorithm is not exact.

In view of these results, we will use in the following the model with the incomplete linearization. Moreover, the imposition of a plane-section kinematics at node A_2 is avoided, since it has been observed that this would lead to the onset of a sharp gradient in the wire axial force at this position. Furthermore, the frictional contact interactions appear to be sufficient in order to avoid any rigid mode.

Putting now more wires in the same layer, a periodic axial strain distribution is recovered, as shown in Figure 9.8, with the highest and lowest axial strain respectively at the outer and at the inner arc.

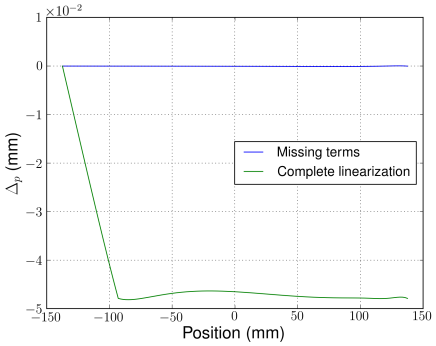

(a) *Tension*

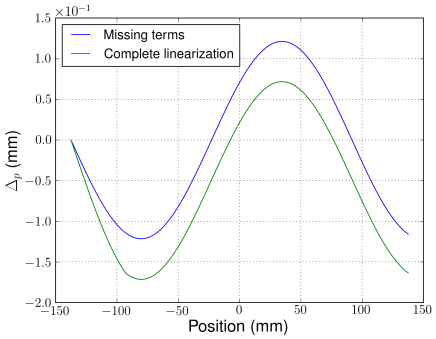

(b) *Bending - stick state*

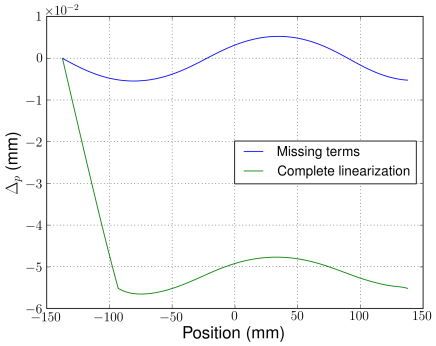

(c) *Bending - slip state*

Figure 9.6: Distribution of Δ_p.

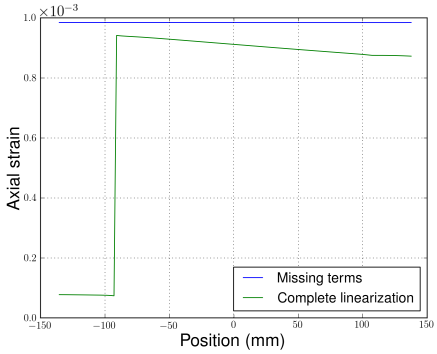

(a) *Tension*

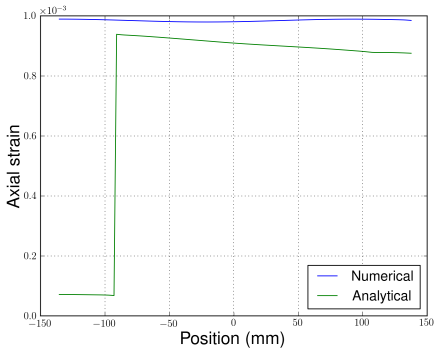

(b) *Bending - stick state*

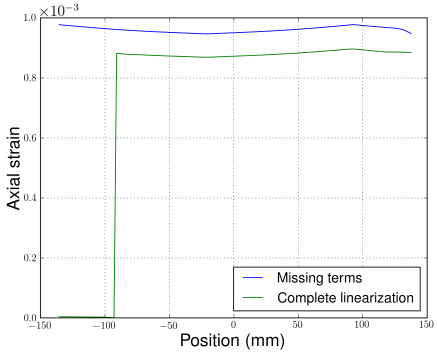

(c) *Bending - slip state*

Figure 9.7: Axial strain distribution.

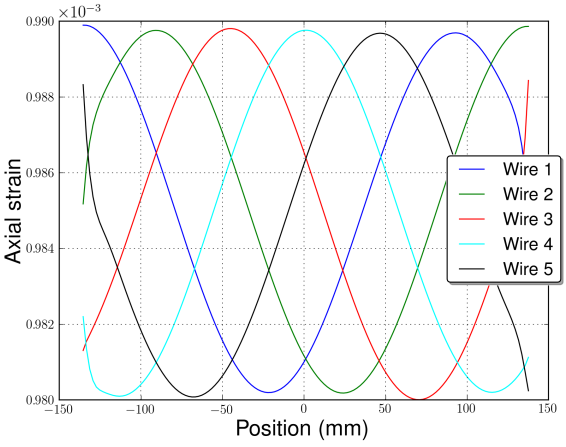

(a)

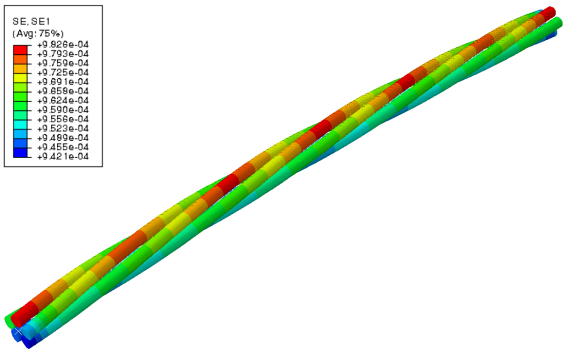

(b)

Figure 9.8: a) Axial strain distribution and b) model in the Abaqus® interface.

9.2 Mooring modeling

9.2.1 Axial stiffness of the numerical model

From the global model we obtain the time series of tension and curvature at a selected critical zone. In the local model we impose uniform axial strain and curvature. Therefore, before to proceed with the mooring line analysis one has first to evaluate the axial stiffness of the numerical model. In fact, as it has been shown in Sec. 6.2.2, even a small reduction of the helical radius can lower considerably the axial strain in the helical wire and consequently the axial stiffness of the rope. The normal stiffness of the user elements has been set to the maximum value ensuring the convergence with an elastic slip of $1.e-3\,mm$, which is $7.5e+4N/mm$. It should be pointed out that this value is lowered by the non-optimal imposition of the periodic boundary conditions shown in Sec. 9.1.2.
A tension test on the numerical model has been therefore performed in order to obtain its axial stiffness and transfer the same time series of tension of the global model into the local one. An axial stiffness of $323\,MN$ has been obtained, while the one of the real rope has been estimated from manufacturer data at $356\,MN$ and the analytical one, obtained from (2.22), is $397\,MN$.

9.2.2 Initial loading

From Figure 9.1, one can see that at the beginning of the sea state analysis the mooring portion is actually characterized by non-zero tension and curvature. It has been on-observed that a difference in the loading part before reaching this initial state can have a significant influence on the results (Fig. 9.9).
We now denote ε_0 and κ_0 respectively the initial axial strain and initial curvature. The following initial loading is imposed, whose aim is to limit the magnitude of the initial inter-wire contact forces:

1. application of a small tension $\varepsilon_{small} << \varepsilon_0$,
2. application of a curvature up to κ_0,
3. mooring tensioning up to ε_0.

9.2.3 Fatigue analysis

9.2.3.1 Calculation of the stress state

We want to perform a fatigue analysis from the results given by the local model, from which the stress resultants on the wires and the inter-wire contact interaction are evaluated. The idea is now to exploit these outputs in order to compute the 3D stress state at the inter-wire contact locations and evaluate the fatigue risk with the Dang Van criterion (Sec. 3.3.2). Namely, by denoting $\underline{\underline{\Sigma}}_b$ and $\underline{\underline{\Sigma}}_c$ the macroscopic stress tensors respectively originating from the beam stress resultants and from the contact forces, we use the superposition principle to

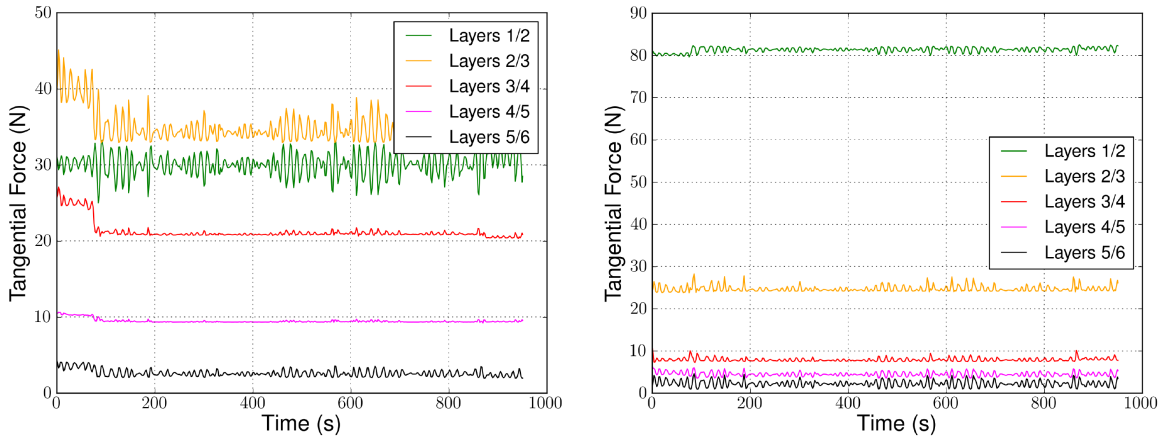

Figure 9.9: Time evolution of tangential contact force between two crossing wires in the proximity of the neutral axis with different initial loading paths : (a) the initial tension is applied before the initial bending, (b) same as (a) but an arbitrary cycle of bending/unbending is applied to get the initial curvature [10].

evaluate the complete stress state, i.e.

$$\underline{\underline{\Sigma}}^{tot} = \underline{\underline{\Sigma}}^{b} + \underline{\underline{\Sigma}}^{c} \tag{9.6}$$

The stress tensor $\underline{\underline{\Sigma}}^{b}$ can be easily obtained from well-known analytical results for beams with circular cross section. Concerning the term $\underline{\underline{\Sigma}}^{c}$, for the sake of simplicity we just consider the direction collinear with the normal contact force, that we consider acting in z direction, while x and y are respectively directed toward the the major and minor axis of the elliptical contact area. The following formulae have been used [151]:

$$\begin{cases} \dfrac{\sigma_x^c}{p_0} = \dfrac{2b}{e^2 a}\left(\Omega_x + \nu\Omega'_x\right) \\ \dfrac{\sigma_y^c}{p_0} = \dfrac{2b}{e^2 a}\left(\Omega_y + \nu\Omega'_y\right) \\ \dfrac{\sigma_z^c}{p_0} = -\dfrac{b}{e^2 a}\left(\dfrac{1-T^2}{T}\right) \end{cases} \tag{9.7}$$

where

- p_0, a and b are defined as in (2.70);
- e is the eccentricity, i.e. $e = \sqrt{1 - \left(\dfrac{b}{a}\right)^2}$;

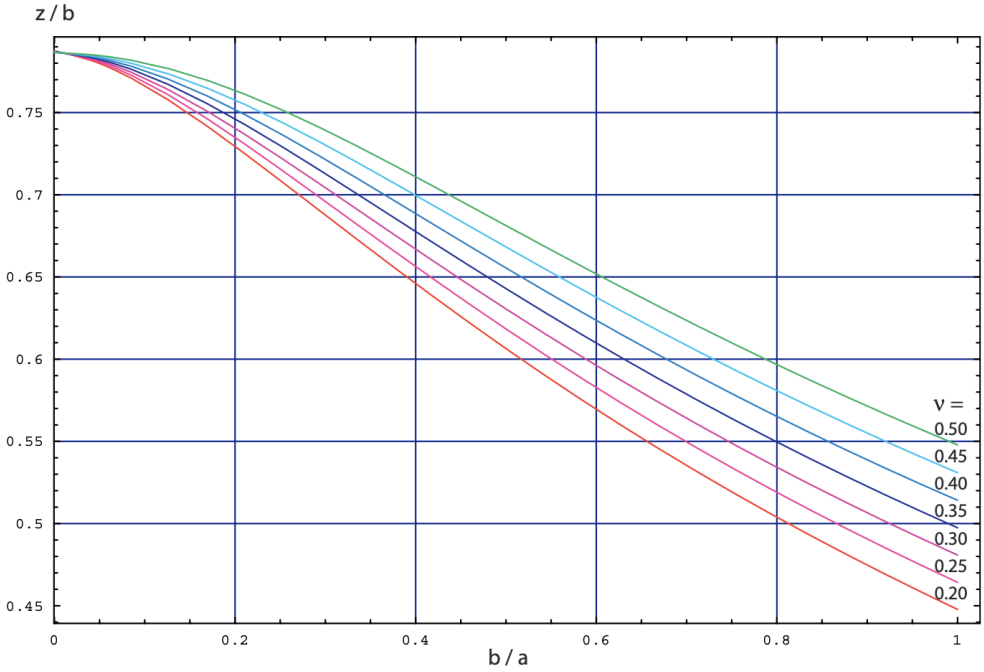

Figure 9.10: Depth correspondent to the maximum value of tangential stress, as function of the ellipticity of the contact area and for different Poisson coefficients [51].

- the other parameters are expressed by

$$\begin{cases} \Omega_x = -\dfrac{1}{2}(1-T) + \xi\left(\mathcal{F}(\Phi,e) - \mathcal{E}(\Phi,e)\right) \\ \Omega'_x = 1 - \dfrac{a^2 T}{b^2} + \xi\left(\dfrac{a^2}{b^2}\mathcal{E}(\Phi,e) - \mathcal{F}(\Phi,e)\right) \\ \Omega_y = \dfrac{1}{2} + \dfrac{1}{2T} + \xi\left(\dfrac{a^2}{b^2}\mathcal{E}(\Phi,e) - \mathcal{F}(\Phi,e)\right) \\ \Omega'_y = -1 + T + \xi\left(\mathcal{F}(\Phi,e) - \mathcal{E}(\Phi,e)\right) \\ T = \sqrt{\dfrac{b^2+z^2}{a^2+z^2}} \\ \xi = \dfrac{z}{a} = \cot\Phi \end{cases}$$

with $\mathcal{F}(\Phi,e)$ and $\mathcal{E}(\Phi,e)$ the incomplete elliptic integrals of first and second kind. The value of z is determined according to the ellipticity of the contact patch, in such a way to maximize the tangential stress (Fig. 9.10). It should be noted that this depth is independent of the contact forces, but depends on the geometry and on the Poisson coefficient of the material. Assuming that the variations of the angle between the contacting wires are negligible (as in Fig. 8.17), this depth is constant along the analysis for each contact locations. Nevertheless, this choice has been completely arbitrary and further investigations are needed in order to analyze the stress state in a region inside the material and perform a fatigue estimation in more points.

We adopt here the same strategies used in [128, 112], where the dimension of the contact area in order to take into account a contact surface flattening caused by localized plasticity. Knowing the material yield stress R_y, if the average bearing stress exceeds the yield stress, the contact area is increased with the same ellipticity. Thus one has

$$\text{if} \quad \frac{P}{A_c} > R_y \longrightarrow A_c = \frac{P}{R_y} \tag{9.8}$$

with P the normal contact force and A_c the contact area.
Before performing the summation (9.6), one has to express the two tensors with respect to the same reference system. Namely, they become coincident with a rotation around the z axis, whose magnitude can be determined from (2.69).
Once $\underline{\underline{\Sigma}}^{tot}$ is evaluated, the mesoscopic stress field $\underline{\underline{\sigma}}$ is evaluated by adding the residual stress state $\underline{\underline{\rho}}$, see Eq. (3.9). Assuming a stabilized material state, $\underline{\underline{\rho}}$ is time-independent and it is obtained as the stress state minimizing the maximum difference of $\underline{\underline{\Sigma}}^{tot}$ in the loading history ($\underline{\underline{\sigma}}_1$ in (3.13)).

9.2.3.2 Endurance limit

The Dang Van endurance limit is defined by the material parameters a and b in (3.18). They are obtained from the endurance limits in fully-reversed bending test and in fully-reversed torsion test, which we name respectively f and t. Then, the parameters a and b in (3.18) are obtained as

$$a = 3\frac{t - f/2}{f}, \qquad b = t \tag{9.9}$$

From [39], many authors showed that the ratio $\dfrac{t}{f}$ varies between 0.44 and 0.75. In [113] the values $f = 750\,MPa$ and $\dfrac{t}{f} = 0.7$ are chosen. This gives

$$a = 0.6 \qquad b = 525\,MPa$$

We add then a correction for low hydrostatic pressures, since it has been observed in [29, 19, 7] that the Dang Van criterion can be non-conservative when compressive hydrostatic stresses are present, i.e. it over-predicts the fatigue limit in this region. Based on this observation, a horizontal projection has been suggested as a conservative fatigue limit for the region of compressive hydrostatic values. Desimone [29] proposes a conservative locus which intersects the vertical axis at $y = 0.5\,f$. The same correction has been applied for instance in [155], and in our case produces the result in Fig. 9.11.

9.3 Results

We now want to apply the developed model for the analysis of a mooring line portion. In particular, we will consider the mooring line 1 at the position $s = 79\,m$, where the curvature

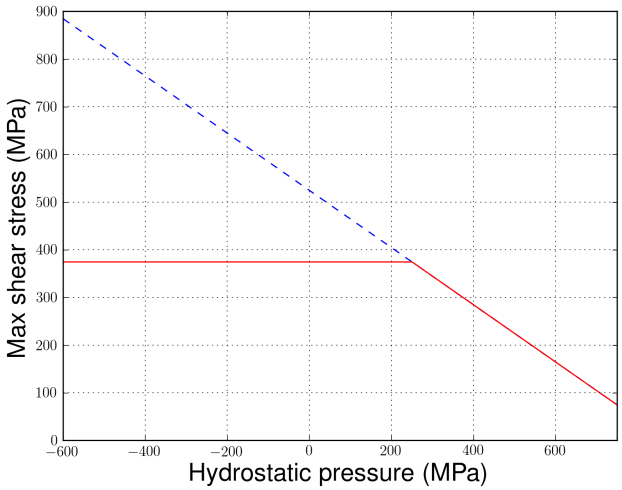

Figure 9.11: Classical Dang Van limit (in dotted blue) and the corrected criterion (in red).

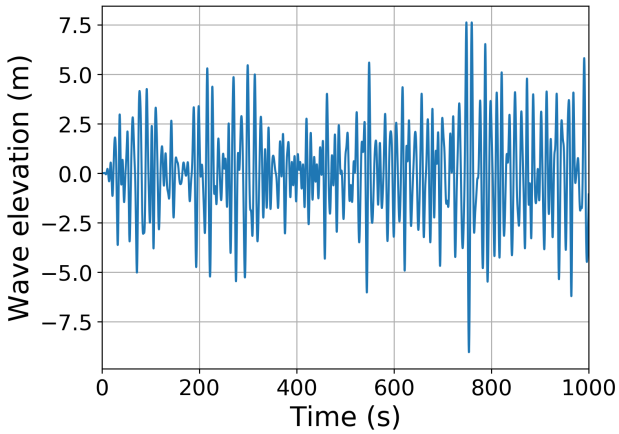

Figure 9.12: Wave elevation history considered for the fatigue analysis.

oscillations are the highest ones (see Fig. 5.9). The aim is to determine if the bending effects in this zone are sufficiently important to affect the fatigue life of the mooring line.
A 950 s long sea state (see Sec. 5.1.5) is considered, characterized by a JONSWAP spectrum with $H_s = 8.75\,m$ and $T_p = 16.5\,s$ (see Sec. 1.1.1). The wave elevation history is reported in Figure 9.12.

9.3.1 Time series of quantities of interest

Figures 9.13-9.14 show the time series of axial force and normal contact force at different locations. One can clearly see that for each layer the results do not vary much by changing the position with respect to the bending axis. This means that the variation of these forces is mainly linked to the variation of the tension force in the rope, rather than to curvature variations. Nevertheless, one can notice from Figure 9.15 that the tangential contact forces

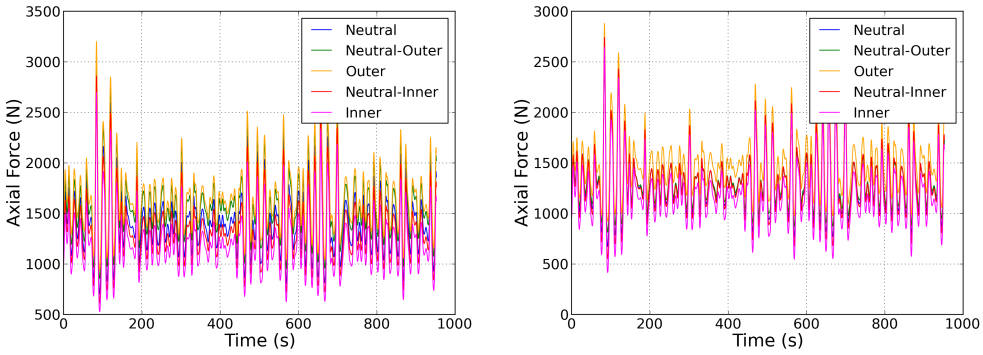

(a) *Layer 1* (b) *Layer 2*

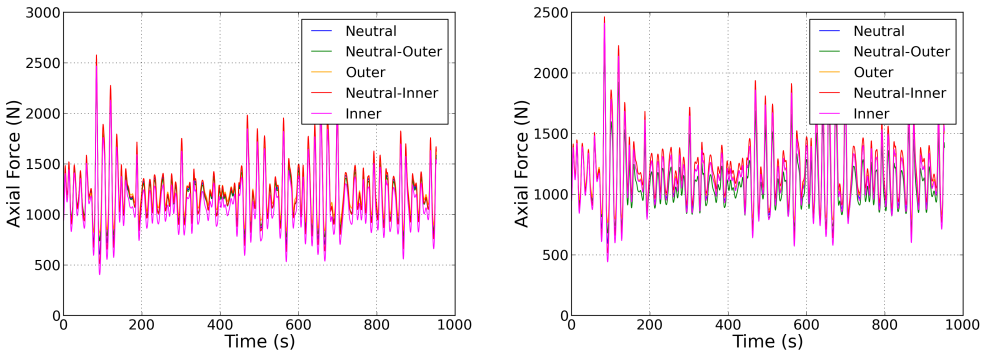

(c) *Layer 3* (d) *Layer 4*

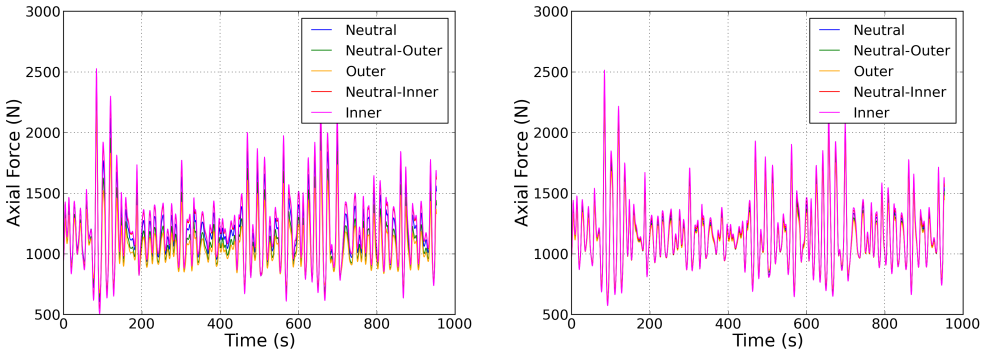

(e) *Layer 5* (f) *Layer 6*

Figure 9.13: Times series of the axial force in different layers and sectors of the cross section.

have a great variablity according to the position on the rope cross section.

The normal contact forces are higher moving from the external to the internal layers (Fig. 9.16a). This was expected, since the external layers exert a pressure on the internal ones. At higher normal forces correspond greater tangential forces as well (Fig. 9.16b).

Because of the lower tangential forces, the inter-wire slip is higher for the external layers (Fig. 9.17). One can see that the wire rope reaches a stabilized state after a time $t \approx 100\,s$,

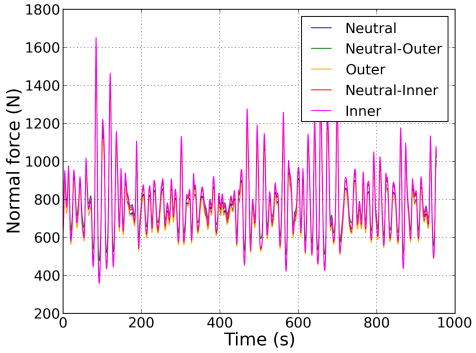

(a) *Layers 1-2*

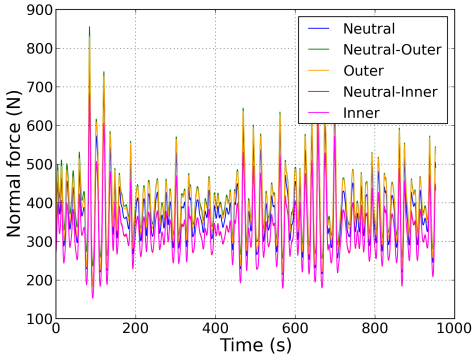

(b) *Layers 2-3*

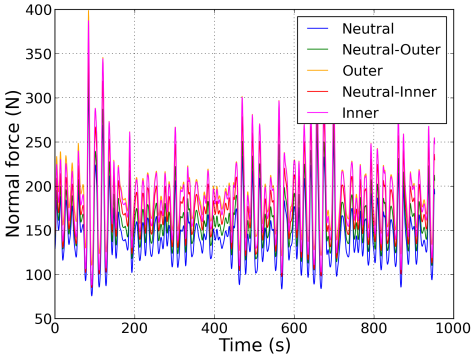

(c) *Layers 3-4*

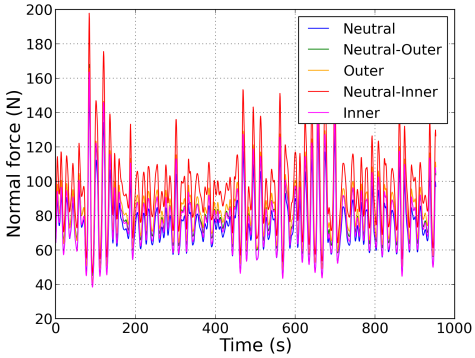

(d) *Layers 4-5*

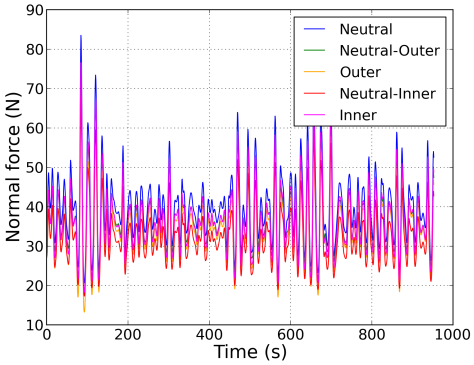

(e) *Layers 5-6*

Figure 9.14: Times series of the normal contact force at different layer interfaces and sectors of the cross section.

where shift in the sliding is observed at all the interfaces, except the most internal one. By looking at Figure 9.12, this time instant does not correspond to a particularly high wave. This actually confirms experimental evidences of tension-bending tests on wire ropes, in which the rope is loaded several times before that a stabilized response is observed. The inter-wire slip profile can be therefore considered as an indicator to reveal whether the wire rope response is stabilized ore not. Consequently, in this analysis one does not have to rely on

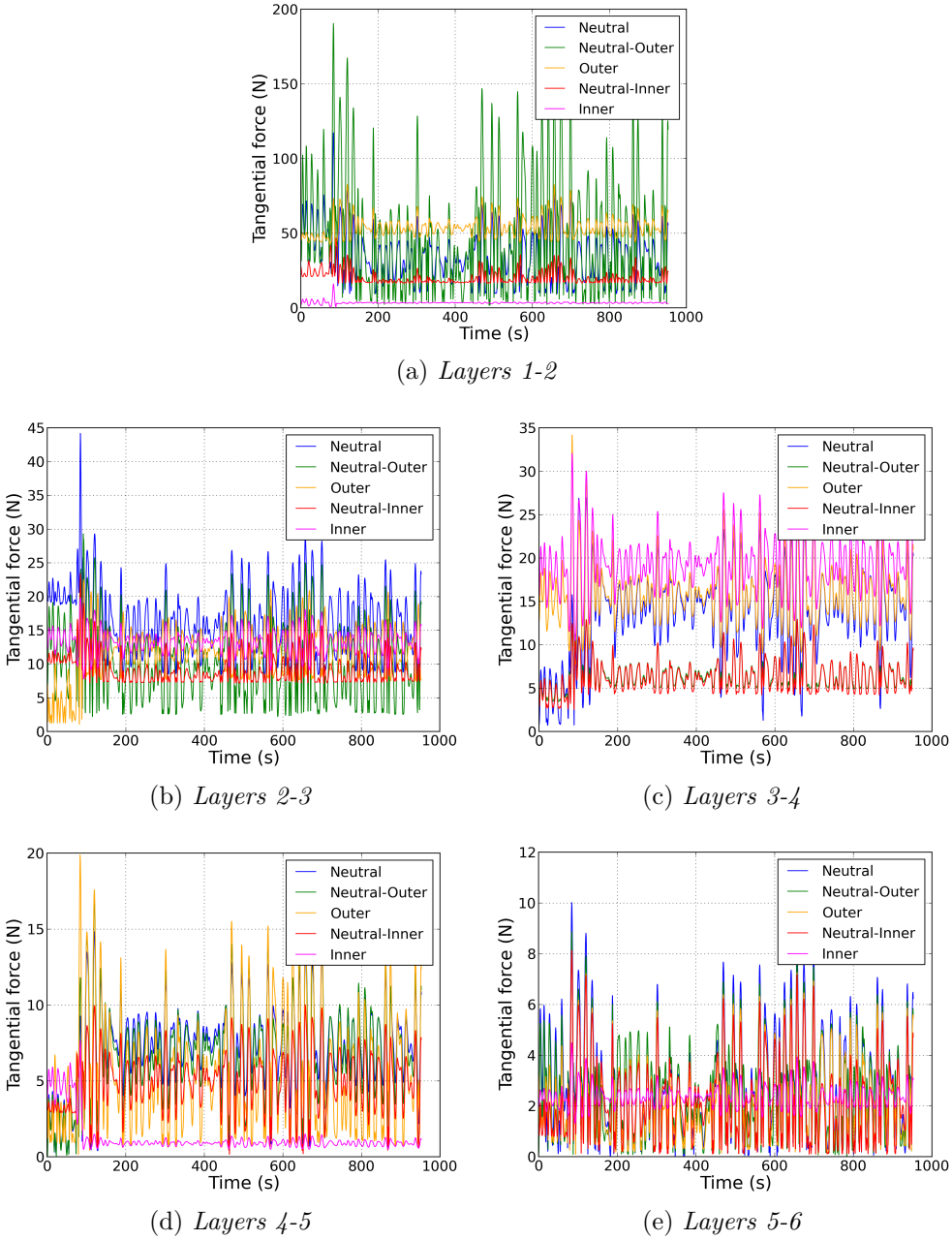

(a) *Layers 1-2*

(b) *Layers 2-3*

(c) *Layers 3-4*

(d) *Layers 4-5*

(e) *Layers 5-6*

Figure 9.15: Times series of the tangential contact force at different layer interfaces and sectors of the cross section.

the first 100 s. Other strategies to impose the initial deformations (see Sec. 9.2.2) could be considered in order to try to get rid of this issue. Concerning the slip magnitude, for the last interface, it is in the range that activates fretting fatigue (see Fig. 3.4). Nevertheless, other analyses have to be performed on less severe sea states to verify if the number of fretting cycles can be sufficient to generate fatigue cracks.

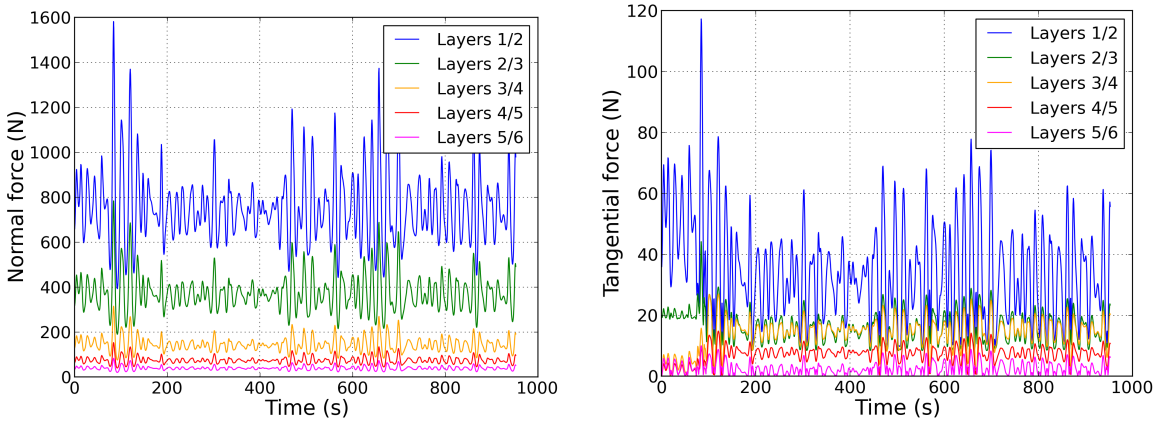

(a) *Normal* (b) *Tangential*

Figure 9.16: Time histories of the contact forces for different layers, considering positions in the proximity of the neutral plane.

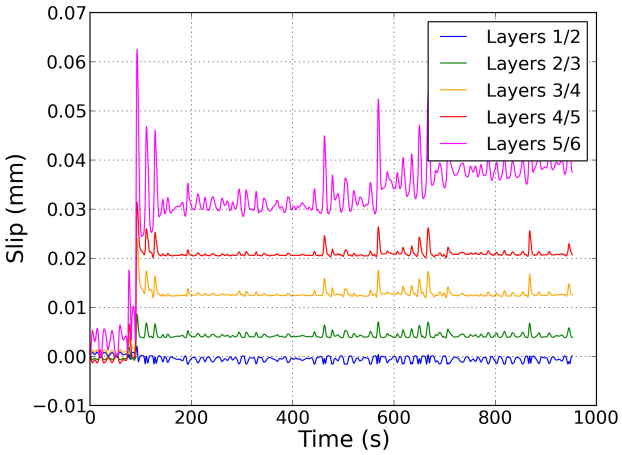

Figure 9.17: Inter-wire slip in the proximity of the neutral axis for the different layers.

9.3.2 Dang Van plots

Following the procedure detailed in Sec. 9.2.3, a fatigue analysis has been performed following the Dang Van criterion.

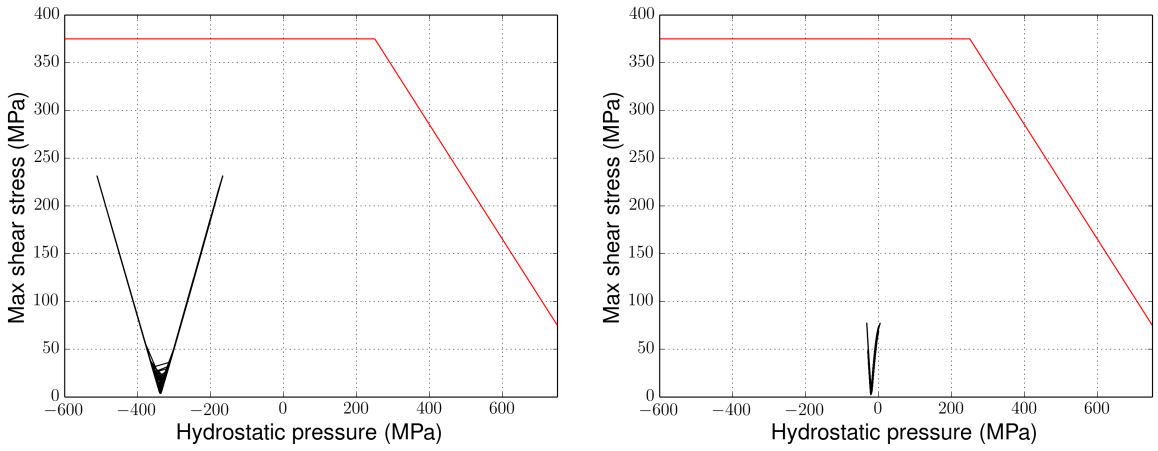

(a) *Layers 1-2* (b) *Layers 5-6*

Figure 9.18: Dang Van plots at contact position close to the neutral plane at (a) the most internal interface and (b) at the most external interface.

By calculating the residual stress tensor as detailed in Sec. 3.3.2, the results show that at all the contact points the loading path in the Dang Van Plot stays below the endurance limit, i.e. there is no fatigue risk. In particular, the loading path gets closer to the limit for the inner layers (Fig. 9.18). One can use as a metric of the fatigue risk, the parameter d defined in [46], such that

$$d = \begin{cases} \max_t \dfrac{\tau_{max}(t)}{b - a\mathcal{P}(t)} & \text{when} \quad \mathcal{P}(t) > \mathcal{P}_{kink} \\ \max_t \dfrac{\tau_{max}(t)}{0.5\, f} & \text{when} \quad \mathcal{P}(t) \leq \mathcal{P}_{kink} \end{cases} \tag{9.10}$$

where a and b are the parameters of the Dang Van limit (3.18), $\mathcal{P}$ and τ_{max} are respectively the hydrostatic pressure and the maximum shear stress and $\mathcal{P}_{kink}$ is the hydrostatic pressure at which the slope of the endurance limit changes (Fig. 9.11), that in our case $\mathcal{P}_{kink} = 250\, MPa$. The parameter d quantifies the fatigue risk, i.e. the higher it is, the greater the fatigue danger. In particular, values lower than 1 mean that the endurance limit is not exceeded. This parameter is plotted in Figure 9.19 as function of the position θ (Fig. 2.10). One can notice that its value is always lower than one.

It is worth mentioning that these results have been obtained without considering the effects of the tangential forces on the stress state. Within this limitation, the temporary conclusion would support the observation that the greater part of mooring wire ropes failures does not occur far from the line ends but near the socket, where the wire rope movements are restrained [45]. In future works, a fatigue analysis of this location should be performed.

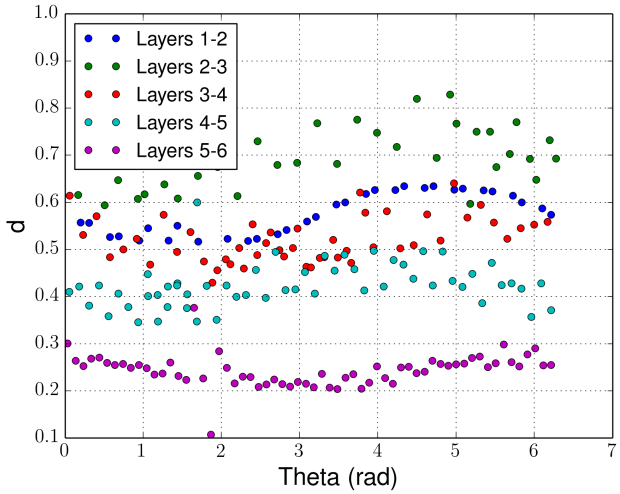

Figure 9.19: Value of the parameter d at all contact positions and at the different interfaces.

Additional investigations should be carried on considering the tangential contact interactions. In particular, it should be noticed that the Dang Van criterion (as all the other criteria reported in Sec. 3.3) is stress-based and hence it does not take into account the magnitude of slip for the determination of the fatigue risk, which has been proved to be important (see Fig. 3.4). Thus, it should be considered the use of other fatigue criteria considering also the relative displacements, as the one proposed in [133].

9.4 Conclusion

The frictional contact element developed in Chapter 7 has been used for the modeling of a multilayer spiral strand, representing a wire rope portion. The tension and curvature are determined according to times series obtained from global-scale results (see Chapter 5) and concerns a mooring portion subjected to the highest variations of curvature.

Periodic boundary conditions have been implemented in order to simulate the continuity of the rope beyond the model ends. Some problems have been encountered in the implementation of this constraints. Nevertheless, it has been proved that the correct periodic response is obtained by removing some terms in the linearization of the constraint equations, with the drawback of worsening the convergence rate.

The tension time series has been converted to an axial strain by evaluating the axial stiffness of the numerical model, which is slightly lower with respect to the one of the real rope. It has been observed in Section 6.2.2 that this more compliant behavior is linked to the use of a penalty formulation for the normal contact part.

Some observations have been made from the analysis of the time series of the axial forces and the contact quantities. It has been shown that the axial force distribution in the cross section does not vary much considering different relative positions with respect to the bending axis. The same holds for the normal contact forces. Their magnitude increases from outer to inner

layers.

The relative displacements are higher for the outer layers. By looking at their distribution it has been observed that the wire rope response in the first part of the analysis is not in a stabilized state. This is linked to the way the initial deformations are imposed, which does not represent the loading history preceding the wave elevation in Figure 9.12.

The stress state at inter-layer contact locations has been determined by superposing the stress state originating by the beam stress resultants and by the normal contact forces. The Dang Van criterion (Sec. 3.3.2) has then been applied. The results show that the endurance limit is not exceeded. Nevertheless, it is necessary to include the tangential contact force and the sliding influence in order to draw definitive conclusions on the fatigue risk.

Part III

Conclusions

The mooring systems of floating wind turbines ensure station keeping and have to be designed in order to resist the loading induced by the action of the environment on the system. The floater movements, caused by waves, current and wind, can generate high stress variations in the lines. Fatigue represents therefore one of the major concerns for mooring designers.

In this thesis we focused on the fatigue of wire ropes, in particular of multilayer spiral strands. The thesis purpose was to make feasible for a fatigue life estimate to take into account the wire contact interactions. In the literature, it has been observed that when bending is involved, these local effects can lead to wire breakages. They basically consists of fretting interactions occurring at inter-layer contact locations, producing high stresses in the contact region which can ultimately lead to a premature failure.

To accomplish this goal, an approach involving two scales has been elaborated. First, a global scale represents the global wind turbine system, in which environmental loading and cable mechanics are modeled with a dedicated hydrodynamic software (Deeplines^{TM}). Then, a local scale details the response of a small length of rope at the wire level.

Due to the random nature of the environmental loading, fatigue life assessments require to consider thousands of load cases. Consequently, the two models have to be computationally efficient in order to make them suitable for a fatigue design procedure. This requirement represented a major challenge mostly for the local model. In fact, frictional contact is a highly nonlinear phenomenon and inside commonly used spiral strand ropes for offshore mooring, there are many thousands of wire contact locations per meter.

As a result of the inter-wire friction, the bending behavior of wire ropes is highly nonlinear, with a bending stiffness that depends on the evolution of the rope curvature and on its tension. However, global scale computations showed that the bending behavior has a negligible influence on the obtained results considering a fatigue estimate. This justifies the use of a top-down scheme, i.e. the time series of tension and curvature obtained from the global model can be directly applied to the local one.

In order to characterize these interactions, a new numerical model had to be conceived. The starting point of the wire rope modeling has been the use of beam elements for the description of the wire kinematics, in order to limit the number of degrees of freedom involved. In the first part of the thesis work, solutions for beam contact modeling already available within Abaqus®/Standard implicit scheme have been investigated. The conclusion drawn after some preliminary computations was that none of these models was suitable for pursuing the goal of the thesis, in terms of robustness and CPU time.

Nevertheless, from these calculations small sliding between the wires has been noted. This observation has been exploited for the development of a new contact element between non parallel beams with circular section, implemented within Abaqus® by a user-element sub-

routine. It basically consists in adopting a node-to-node contact discretization, with the contact pairings that remain unchanged during the analysis. The contact positions in the initial configuration are determined by simple geometrical operations. The beam nodes are then placed at these locations and are linked with the user-elements. This simplification is however compensated by including finite rotations in the contact and friction contributions to the balance of momentum, with their linearization for the tangent operator of a Newton-Raphson loop. The normal definition is crucial in spiral strand applications where a smooth variation of normal is required. In this work, the normal definition depends on beam tangent directors at the two contact nodes initially in contact. Thus, the normal smoothly varies in a continuous way by simply tracking the rotations at the two contact nodes. This choice ensures a particular robustness of this model and avoids all the complications and improvement strategies of the large-sliding algorithms (see Sec. 4.2.4). Moreover, the friction is considered at the beam surfaces, inducing additional moments.

This new model has been validated by some numerical benchmarks, aiming to verify the capabilities of the new element for the simulation of inter-layer contact interactions in a wire rope. First, a simple test has been used to check the frame invariance with a rigid body rotation. A formulation considering rotation increments is invariant for a reasonable number of increments. However, it has not been used in the thesis because of convergence issues, and as it did not influence significantly the results of a wire rope tension and bending simulation. A pointwise contact benchmark has been used in order to evaluate the convergence rate of our model and the contact forces predicted, giving satisfying results. In the next series of benchmark tests, we considered a first model with one helical wire in line contact with the central wire, and a second model with an helical wire in trellis contact with all the wires of the first layer. It has been observed that the results of the new element are in a very good agreement with the ones of a reference model using surface elements to track the kinematics of the cylindrical beam surfaces, with a significant CPU time gain compared with other studied models. Concerning the modeling of a tension-bending test of a multilayer spiral strand, some obtained results are not in agreement with the ones of other numerical models. However, the outputs of these models seem questionable and cannot really be taken as a reference.

Regarding the mooring modeling, another aspect which has been investigated concerns the application of the boundary conditions to the local model. In particular, since just a portion of a longer wire rope is modeled, the idea was to apply periodic boundary conditions to simulate the continuity of the rope. Results from the analytical models in the literature have been here exploited. First results are encouraging despite the fact that the proposed linearization of the resulting kinematic constraints does not enable one to get a satisfying convergence rate. This point requires further investigations.

Finally, a mooring wire rope simulation has been performed. The results have been exploited in order to perform a multiaxial fatigue analysis employing the Dang Van criterion. Moreover, other quantities have been obtained, which can be of interest for other type of analysis (fretting, wear,...). The fatigue analysis has shown that, neglecting the tangential force con-

tribution, the endurance limit is not attained at any contact location.

The work done during this thesis can be considered as a first step toward the use of more accurate numerical modeling for fatigue estimation of wire ropes, and the main objectives have been achieved. Nevertheless, several aspects could be tackled in future research works.

- Other fatigue laws could be tested, in particular by using energy-based criteria rather than purely stress-based one. An experimental work on fretting between steel wires could be useful for the definition of a new criterion, taking into account also the influence of corrosion. Moreover, for the moment only the normal forces have been considered in the fatigue analysis. Tangential forces will have to be included as well.
- It has been observed that the compliance of the normal contact, linked to the use of the penalty method, may considerably affect the results. To get rid of this problem, the Lagrangian or Augmented Lagrangian method for the normal contact part could be implemented.
- The convergence issues affecting the frame-invariant formulation of the new element (see Sec. 8.1) require additional investigations.
- More complex friction laws could be used, exploiting also experimental works on steel wire fretting tests. These friction laws can then be used in order to fit some experimental results, namely regarding tension-bending tests.
- In order to save computational time, the use of reduced-order models (by employing for instance the Proper Orthogonal Decomposition) can be considered.
- The residual stress state originating in the wire production phase has to be taken into account. In particular, it has been proven that a compressive residual stress state increases the fatigue life. Hence, neglecting it would lead to an overly-conservative fatigue estimate.
- A refined model of contacting wires has to be conceived in order to deal with contacts with high contact forces, i.e. when important plastic strains take place and the Hertz contact theory is less valid.
- For the moment, the global model performs a dynamic analysis, while the local model is quasi-static. The importance of dynamic phenomena at the local scale has to be investigated.
- Concerning mooring portion analysis, an optimal strategy for the imposition of the initial configuration has to be identified, with the definition of a loading path for which the wire rope reaches a stabilized state.
- A micro-scale model of an inter-wire contact location could be developed, by making use of numerical models for the simulation of fatigue crack propagation, such X-FEM [3, 138]. For instance, [114] reports a number of cycles for the propagation of a crack in a wire comparable to the number of cycles for the crack initiation.

Part IV

Appendices

In this final part, all the terms related to the virtual work associated to the contact element described in Chapter 7 and its linearization will be detailed. The penalty method will be considered for the contact resolution, see Sec. 4.2.3.

In the Appendix A some basic notions on finite rotations will be given and the variations of the beam directors will be obtained. The Appendix B deals with the normal contact terms while in the Appendix C the tangential contact terms are treated. These terms will be obtained as function of $\delta\underline{d}$ and $\Delta\underline{d}$, where $\underline{d}$ is the vector gathering the nodal degrees of freedom, see Eq. (7.61). $\delta\underline{d}$ and $\Delta\underline{d}$ represents respectively the virtual variation of the degrees of freedom and its increment.

Note that, due to the geometrical nonlinearity of the finite deformation problem, the variations and linearizations often result in very complex terms (this is of course not the case when geometrically linear problems are formulated).

Appendix A

A.1 Definition of a beam tangent director

A beam tangent director $\underline{t}$ in the current configuration is defined as follows:

$$\underline{t} = \underline{\underline{R}}\,\underline{T}$$

where $\underline{T}$ is the beam tangent director in the reference configuration and $\underline{\underline{R}}$ is an (orthogonal) rotation matrix which is defined from the finite rotation vector $\underline{\Phi}$ as follows.
First one defines the skew-symmetric matrix $\underline{\underline{\hat{\Phi}}}$ associated with $\underline{\Phi}$ by the relationship:

$$\text{and} \quad \underline{\hat{\Phi}}\,\underline{v} = \underline{\Phi} \wedge \underline{v}$$

for all vectors $\underline{v}$. $\underline{\Phi}$ is called the axial vector of the skew-symmetric matrix $\underline{\underline{\hat{\Phi}}}$. In matrix components relative to the standard Euclidean basis, if $\underline{\Phi} = (\Phi_1, \Phi_2, \Phi_3)^T$, then:

$$\underline{\underline{\hat{\Phi}}} = \begin{pmatrix} 0 & -\Phi_3 & \Phi_2 \\ \Phi_3 & 0 & -\Phi_1 \\ -\Phi_2 & \Phi_1 & 0 \end{pmatrix} \tag{A.11}$$

Skew-symmetric matrix $\underline{\underline{\hat{\Phi}}}$ is often denoted by spin($\underline{\Phi}$) for spinor in the literature [42]. Conversely, the axial vector is denoted by $\underline{\Phi} = \text{axial}(\underline{\underline{\hat{\Phi}}})$. A well-known result from linear algebra is that the exponential of a skew-symmetric matrix $\underline{\underline{\hat{\Phi}}}$ is an orthogonal (rotation) matrix that produces the finite rotation $\underline{\Phi}$ (see Section 9.5.15. in [6] and [1]). Let the rotation matrix be $\underline{\underline{R}}$, such that $\underline{\underline{R}}^{-1} = \underline{\underline{R}}^T$. Then by definition,

$$\underline{\underline{R}} = \exp\,\underline{\underline{\hat{\Phi}}} = \underline{\underline{I}}_d + \underline{\underline{\hat{\Phi}}} + \frac{1}{2!}\underline{\underline{\hat{\Phi}}}^2 + \dots$$

The above infinite series has the following closed-form expression:

$$\underline{\underline{R}} = \exp\,\underline{\underline{\hat{\Phi}}} = \cos\|\underline{\Phi}\|\underline{\underline{I}}_d + \frac{\sin\|\underline{\Phi}\|}{\|\underline{\Phi}\|}\underline{\underline{\hat{\Phi}}} + \frac{1-\cos\|\underline{\Phi}\|}{\|\underline{\Phi}\|^2}\underline{\Phi}\otimes\underline{\Phi} \tag{A.12}$$

$$= \underline{\underline{I}}_d + \frac{\sin\|\underline{\Phi}\|}{\|\underline{\Phi}\|}\underline{\underline{\hat{\Phi}}} + \frac{1-\cos\|\underline{\Phi}\|}{\|\underline{\Phi}\|^2}\underline{\underline{\hat{\Phi}}}^2 \tag{A.13}$$

where second expression is obtained by noting that $\underline{\Phi} \otimes \underline{\Phi} = \|\underline{\Phi}\|^2 \underline{\underline{I}}_d + \underline{\underline{\hat{\Phi}}}^2$. The rotator $\underline{\underline{R}}$ associated with spinor $\underline{\hat{\Phi}} = \text{spin}(\underline{\Phi})$ (and axial vector $\underline{\Phi}$) is sometimes denoted by $\text{Rot}(\underline{\underline{\hat{\Phi}}})$ in the literature.

Finally, beam tangent director $\underline{t}$ can be defined explicitly from the finite rotation vector $\underline{\Phi}$. In the following, $\underline{t}_1$ and $\underline{t}_2$ denote respectively the beam tangent directors $\underline{t}_1\left(\underline{\Phi}(\underline{x}_1)\right)$ and $\underline{t}_2\left(\underline{\Phi}(\underline{x}_2)\right)$ in order to alleviate the notations.

A.2 Variations of beam directors

A beam tangent director $\underline{t}$ in the current configuration is defined as follows:

$$\underline{t} = \underline{\underline{R}} \cdot \underline{T}$$

Variation $\delta\underline{t}$ in this field is obtained as [1]:

$$\delta\underline{t} = \delta\underline{\underline{R}} \cdot \underline{T}$$

where $\delta\underline{\underline{R}}$ is the linearized rotation matrix; that is, the variation of the orthogonal rotation tensor $\underline{\underline{R}}$. On the other hand, the variation can be defined in terms of the linearized rotation field $\delta\underline{\theta}$:

$$\delta\underline{t} = \delta\underline{\theta} \wedge \underline{t} = \delta\underline{\hat{\theta}} \cdot \underline{t} = \delta\underline{\underline{\hat{\theta}}} \cdot \left(\underline{\underline{R}} \cdot \underline{T}\right)$$

Consequently, it follows that:

$$\delta\underline{\underline{R}} = \delta\underline{\underline{\hat{\theta}}} \cdot \underline{\underline{R}} \tag{A.14}$$

Since $\underline{\underline{R}}\,\underline{\underline{R}}^T = \underline{\underline{I}}_d$, the linearized rotation is defined by:

$$\delta\underline{\underline{\hat{\theta}}} = \delta\underline{\underline{R}}\,\underline{\underline{R}}^T \tag{A.15}$$

Differentiating the identity $\underline{\underline{R}}\,\underline{\underline{R}}^T = \underline{\underline{I}}_d$ one obtains $\delta\underline{\underline{\hat{\theta}}} + \delta\underline{\underline{\hat{\theta}}}^T = \underline{\underline{0}}$. Hence, $\delta\underline{\underline{\hat{\theta}}}$ is skew-symmetric. It denotes the instantaneous rate of change of the rotation of the principle axis associated with $\underline{\underline{R}}$ and when the differentiation is carried out with respect to time, $\delta\underline{\underline{\hat{\theta}}}$ represents the angular velocity tensor. It is consequently important to note that the linearized rotation $\delta\underline{\theta}$, which is analogous to the angular velocity in dynamics, is not the variation of the rotation vector $\underline{\Phi}$.

By a straightforward (but involved) calculation, it can be shown that the variation of the rotation vector $\delta\underline{\Phi}$ is related to the linearized rotation $\delta\underline{\theta}$ by [1]

$$\delta\underline{\theta} = \underline{\underline{H}}(\underline{\Phi}) \cdot \delta\underline{\Phi}$$

where:

$$\underline{\underline{H}}(\underline{\Phi}) = \frac{1}{\|\underline{\Phi}\|^2}\underline{\Phi} \otimes \underline{\Phi} + \frac{\sin\|\underline{\Phi}\|}{\|\underline{\Phi}\|}\left(\underline{\underline{I}}_d - \frac{1}{\|\underline{\Phi}\|^2}\underline{\Phi} \otimes \underline{\Phi}\right) + \frac{1-\cos\|\underline{\Phi}\|}{\|\underline{\Phi}\|^2}\underline{\underline{\hat{\Phi}}} \tag{A.16}$$

We are now capable of expressing the variation of a beam tangent director $\underline{t}$. by starting from the definition

$$\delta\underline{t} = (\widehat{\underline{\underline{H}}\delta\underline{\Phi}})\underline{t}$$

and denoting with $\underline{H}^j$ the j-th column of matrix $\underline{\underline{H}} = \underline{\underline{H}}(\underline{\Phi})$ one gets

$$\delta\underline{t} = \left(\underline{H}^1 \wedge \underline{t} \quad \underline{H}^2 \wedge \underline{t} \quad \underline{H}^3 \wedge \underline{t}\right) \delta\underline{\Phi} = \underline{\underline{W}}(\underline{\underline{H}}, \underline{t})\delta\underline{\Phi} \tag{A.17}$$

Let $\delta\underline{\theta}$ represent an infinitesimal change in the rotation field (i.e. linearized rotation field). A direct calculation of the variation of $\delta\underline{\theta}$, which is equivalent to calculation of the second variation of either $\underline{\underline{R}}$ or $\underline{t}$, leads to an expression that is not symmetric in the variations $\delta\underline{\theta}$ and the changes $\Delta\underline{\theta}$. However, it is shown in [141] that the correct definition of the Hessian operator – that is, the"covariant" derivative of the weak form of the balance equations – requires only the symmetric part (with respect to the variations) of the second variation. Thus, we write

$$\Delta\delta\underline{\underline{R}} = \frac{1}{2}\left(\delta\hat{\underline{\underline{\theta}}} \cdot \Delta\hat{\underline{\underline{\theta}}} + \Delta\hat{\underline{\underline{\theta}}} \cdot \delta\hat{\underline{\underline{\theta}}}\right) \cdot \underline{\underline{R}} \tag{A.18}$$

as proposed in [1]. Similarly, the second variation of the vector field $\underline{t}$ rotated by $\underline{\underline{R}}$ can be written as:

$$\begin{aligned}
\Delta\delta\underline{t} &= \frac{1}{2}\left[\delta\underline{\theta} \wedge (\Delta\underline{\theta} \wedge \underline{t}) + \Delta\underline{\theta} \wedge (\delta\underline{\theta} \wedge \underline{t})\right] && \text{(A.19)}\\
&= \frac{1}{2}\left[(\delta\underline{\theta} \cdot \underline{t})\,\Delta\underline{\theta} - (\delta\underline{\theta} \cdot \Delta\underline{\theta})\,\underline{t} + (\Delta\underline{\theta} \cdot \underline{t})\,\delta\underline{\theta} - (\Delta\underline{\theta} \cdot \delta\underline{\theta})\,\underline{t}\right] && \text{(A.20)}\\
&= -(\delta\underline{\theta} \cdot \Delta\underline{\theta})\,\underline{t} + \frac{1}{2}\left[(\delta\underline{\theta} \cdot \underline{t})\,\Delta\underline{\theta} + (\Delta\underline{\theta} \cdot \underline{t})\,\delta\underline{\theta}\right] && \text{(A.21)}
\end{aligned}$$

One deduces that, for a vector $\underline{n}$ perpendicular to $\underline{t}$, the following relations hold:

$$\begin{aligned}
\Delta\delta\underline{t} \cdot \underline{n} &= \frac{1}{2}\left[(\delta\underline{\theta} \cdot \underline{t})\,\Delta\underline{\theta} + (\Delta\underline{\theta} \cdot \underline{t})\,\delta\underline{\theta}\right] \cdot \underline{n} && \text{(A.22)}\\
&= \frac{1}{2}\left[(\delta\underline{\theta} \cdot \underline{t})\,(\Delta\underline{\theta} \cdot \underline{n}) + (\Delta\underline{\theta} \cdot \underline{t})\,(\delta\underline{\theta} \cdot \underline{n})\right] && \text{(A.23)}\\
&= \frac{1}{2}\delta\underline{\theta}^T\,(\underline{n} \otimes \underline{t} + \underline{t} \otimes \underline{n})\,\Delta\underline{\theta} && \text{(A.24)}\\
&= \frac{1}{2}\delta\underline{\Phi}^T\left[\underline{\underline{H}}(\underline{\Phi})^T\,(\underline{n} \otimes \underline{t} + \underline{t} \otimes \underline{n})\,\underline{\underline{H}}(\underline{\Phi})\right]\Delta\underline{\Phi} && \text{(A.25)}
\end{aligned}$$

Appendix B

B.1 Variation of normal gap

The expression of the variation of normal gap, which has been obtained in Sec. 7.1.4. is

$$\delta g_N = \left(\delta \underline{x}_2 - \delta \underline{x}_1 - \xi^i \, \delta \underline{t}_i\right) \cdot \underline{n}$$

The variation of the position vectors $\underline{x}_i$, since $\underline{x}_i = \underline{X}_i + \underline{u}_i$ with $\underline{X}_i$ the vector of the initial nodal coordinates, is trivial and reads $\delta \underline{x}_i = \delta \underline{u}_i$
Concerning the terms containing the variation of the beam tangents, they can be easily obtained from (A.17) as

$$\xi^i \delta \underline{t}_i \cdot \underline{n} = \xi^i \underline{n}^T \underline{\underline{W}}(\underline{\underline{H}}_i, \underline{t}_i) \delta \underline{\Phi}_i$$

and hence

$$\begin{pmatrix} \xi^1 \underline{n} \cdot \underline{t}_1 \\ \xi^2 \underline{n} \cdot \underline{t}_2 \end{pmatrix} = \begin{pmatrix} \xi^1 & \xi^2 \end{pmatrix} \begin{pmatrix} \underline{0}_{1\times 3} & \underline{n}^T \underline{\underline{W}}(\underline{\underline{H}}_1, \underline{t}_1) & \underline{0}_{1\times 3} & \underline{0}_{1\times 3} \\ \underline{0}_{1\times 3} & \underline{0}_{1\times 3} & \underline{0}_{1\times 3} & \underline{n}^T \underline{\underline{W}}(\underline{\underline{H}}_2, \underline{t}_2) \end{pmatrix} \delta \underline{d} \tag{B.26}$$

Equivalently, one can deduce for any vector $\underline{u}$ of $\mathbb{R}^3$ that:

$$\delta \underline{t} \cdot \underline{u} = (\delta \underline{\theta} \wedge \underline{t}) \cdot \underline{u} = (\underline{t} \wedge \underline{u}) \cdot \delta \underline{\theta} = (\underline{t} \wedge \underline{u}) \cdot \left(\underline{\underline{H}}(\underline{\Phi}) \cdot \delta \underline{\Phi}\right) \tag{B.27}$$

One obtains in matrix form:

$$\begin{pmatrix} \delta \underline{t}_1 \cdot \underline{u} \\ \delta \underline{t}_2 \cdot \underline{u} \end{pmatrix} = \begin{pmatrix} \underline{0}_{1\times 3} & (\underline{t}_1 \wedge \underline{u})^T \underline{\underline{H}}(\underline{\Phi}_1) & \underline{0}_{1\times 3} & \underline{0}_{1\times 3} \\ \underline{0}_{1\times 3} & \underline{0}_{1\times 3} & \underline{0}_{1\times 3} & (\underline{t}_2 \wedge \underline{u})^T \underline{\underline{H}}(\underline{\Phi}_2) \end{pmatrix} \begin{pmatrix} \delta \underline{x}_1 \\ \delta \underline{\Phi}_1 \\ \delta \underline{x}_2 \\ \delta \underline{\Phi}_2 \end{pmatrix} = \underline{\underline{B}}(\underline{u}) \, \delta \underline{d} \tag{B.28}$$

Moreover, following the same reasoning, we obtain

$$\delta \underline{t}_i \cdot \underline{t}_j = (\delta \underline{\theta}_i \wedge \underline{t}_i) \cdot \underline{t}_j = (\underline{t}_i \wedge \underline{t}_j) \cdot \delta \underline{\theta}_i = (\underline{t}_i \wedge \underline{t}_j) \cdot \left(\underline{\underline{H}}(\underline{\Phi}_i) \cdot \delta \underline{\Phi}_i\right) \tag{B.29}$$

without summation over all the values of the indices i and j. One easily deduces that, for $i = 1, 2$:

$$\begin{aligned} \begin{pmatrix} a^i\,\delta\underline{t}_i\cdot\underline{t}_1 \\ a^i\,\delta\underline{t}_i\cdot\underline{t}_2 \end{pmatrix} &= \begin{pmatrix} a^1\,\delta\underline{t}_1\cdot\underline{t}_1 + a^2\,\delta\underline{t}_2\cdot\underline{t}_1 \\ a^1\,\delta\underline{t}_1\cdot\underline{t}_2 + a^2\,\delta\underline{t}_2\cdot\underline{t}_2 \end{pmatrix} \\ &= \begin{pmatrix} \underline{0}_{1\times3} & a^2\,(\underline{t}_2\wedge\underline{t}_1)^T\,\underline{\underline{H}}(\underline{\Phi}_2) \\ a^1\,(\underline{t}_1\wedge\underline{t}_2)^T\,\underline{\underline{H}}(\underline{\Phi}_1) & \underline{0}_{1\times3} \end{pmatrix} \begin{pmatrix} \delta\underline{\Phi}_1 \\ \delta\underline{\Phi}_2 \end{pmatrix} \end{aligned} \tag{B.30}$$

or:

$$\begin{aligned} \begin{pmatrix} a^i\,\delta\underline{t}_i\cdot\underline{t}_1 \\ a^i\,\delta\underline{t}_i\cdot\underline{t}_2 \end{pmatrix} &= \begin{pmatrix} \underline{0}_{1\times3} & \underline{0}_{1\times3} & \underline{0}_{1\times3} & a^2\,(\underline{t}_2\wedge\underline{t}_1)^T\,\underline{\underline{H}}(\underline{\Phi}_2) \\ \underline{0}_{1\times3} & a^1\,(\underline{t}_1\wedge\underline{t}_2)^T\,\underline{\underline{H}}(\underline{\Phi}_1) & \underline{0}_{1\times3} & \underline{0}_{1\times3} \end{pmatrix} \begin{pmatrix} \delta\underline{x}_1 \\ \delta\underline{\Phi}_1 \\ \delta\underline{x}_2 \\ \delta\underline{\Phi}_2 \end{pmatrix} \\ &= \underline{\underline{\bar{B}}}(a^1, a^2)\,\delta\underline{d} \end{aligned} \tag{B.31}$$

This result will be useful in the following.
From (B.28) we get the expression of δg_N in matrix form:

$$\delta g_N = \begin{pmatrix} -\underline{n}^T & -\xi^1\,(\underline{t}_1\wedge\underline{n})^T\,\underline{\underline{H}}(\underline{\Phi}_1) & \underline{n}^T & -\xi^2\,(\underline{t}_2\wedge\underline{n})^T\,\underline{\underline{H}}(\underline{\Phi}_2) \end{pmatrix} \delta\underline{d} = \underline{\bar{N}}\delta\underline{d} \tag{B.32}$$

The normal contact contribution to the weak form (7.46) is therefore given by

$$\delta W_C^N = \epsilon_N g_N \delta g_N = \epsilon_N g_N \underline{\bar{N}}\delta\underline{d} \tag{B.33}$$

B.2 Linearization of the variation of normal gap

We now want to obtain the terms $\Delta\delta g_N$, whose expression, which has been obtained in Sec. 7.3.1, is

$$\Delta\delta g_N = -(\delta\xi^i\,\Delta\underline{t}_i + \Delta\xi^i\,\delta\underline{t}_i + \xi^i\,\Delta\delta\underline{t}_i)\cdot\underline{n} + (g_N + r_1 + r_2)(\Delta\underline{n}\cdot\delta\underline{n})$$

Its complete expression in matrix form will be obtained in the following sections. The final result is

$$\begin{aligned} \Delta\delta g_N &= \delta\underline{d}^T\left[-\underline{\underline{D}}^T\underline{\underline{M}}^{-T}\underline{\underline{B}}(\underline{n}) - \underline{\underline{B}}(\underline{n})^T\underline{\underline{M}}^{-1}\underline{\underline{D}} - \underline{\underline{\bar{C}}}(\underline{n}, \xi^1, \xi^2) + \ldots\right. \\ &\quad \left.\ldots\,(g_N + r_1 + r_2)\,\underline{\underline{B}}(\underline{n})^T\underline{\underline{M}}^{-1}\underline{\underline{B}}(\underline{n})\right]\Delta\underline{d} = \delta\underline{d}^T\,\underline{G}_N\,\Delta\underline{d} \end{aligned}$$

B.2.1 Determination of $\delta\xi^i$

The expression of $\delta\xi^i$ can be obtained from (7.18), which is

$$\delta\xi^i\,M_{ij} = \left(\delta\underline{x}_2 - \delta\underline{x}_1 - \xi^i\,\delta\underline{t}_i\right)\cdot\underline{t}_j + (g_N + r_1 + r_2)\,\underline{n}\cdot\delta\underline{t}_j$$

which leads, with (B.28) and (B.31), to:

$$\underline{\underline{M}}\begin{pmatrix} \delta\xi^1 \\ \delta\xi^2 \end{pmatrix} = \begin{pmatrix} -\underline{t}_1^T & \underline{t}_1^T \\ -\underline{t}_2^T & \underline{t}_2^T \end{pmatrix}\begin{pmatrix} \delta\underline{x}_1 \\ \delta\underline{x}_2 \end{pmatrix} - \underline{\underline{\bar{B}}}(\xi^1, \xi^2)\,\delta\underline{d} + (g_N + r_1 + r_2)\,\underline{\underline{B}}(\underline{n})\,\delta\underline{d} \tag{B.34}$$

That is to say:

$$\begin{pmatrix}\delta\xi^1\\ \delta\xi^2\end{pmatrix} = \underline{\underline{M}}^{-1}\,\underline{\underline{D}}\,\delta\underline{d} \tag{B.35}$$

with:

$$\underline{\underline{D}} = \begin{pmatrix} -\underline{t}_1^T & (g_N + r_1 + r_2)\,(\underline{t}_1 \wedge \underline{n})^T\,\underline{\underline{H}}(\underline{\Phi}_1) & \underline{t}_1^T & -\xi^2\,(\underline{t}_2 \wedge \underline{t}_1)^T\,\underline{\underline{H}}(\underline{\Phi}_2) \\ -\underline{t}_2^T & -\xi^1\,(\underline{t}_1 \wedge \underline{t}_2)^T\,\underline{\underline{H}}(\underline{\Phi}_1) & \underline{t}_2^T & (g_N + r_1 + r_2)\,(\underline{t}_2 \wedge \underline{n})^T\,\underline{\underline{H}}(\underline{\Phi}_2) \end{pmatrix} \tag{B.36}$$

B.2.2 Determination of $\delta\xi^i\,\Delta\underline{t}_i \cdot \underline{n}$

Now, one can determine term $\delta\xi^i\,\Delta\underline{t}_i \cdot \underline{n}$. From (B.28) and (B.35), one gets:

$$\delta\xi^i\,\Delta\underline{t}_i \cdot \underline{n} = \begin{pmatrix}\delta\xi^1 & \delta\xi^2\end{pmatrix}\,\underline{\underline{B}}(\underline{n})\,\Delta\underline{d} \tag{B.37}$$

With (B.35), one finally obtains:

$$\delta\xi^i\,\Delta\underline{t}_i \cdot \underline{n} = \delta\underline{d}^T\left(\underline{\underline{D}}^T\,\underline{\underline{M}}^{-T}\,\underline{\underline{B}}(\underline{n})\right)\Delta\underline{d} \tag{B.38}$$

Similarly, one deduces that:

$$\Delta\xi^i\,\delta\underline{t}_i \cdot \underline{n} = \delta\underline{d}^T\left(\underline{\underline{B}}(\underline{n})^T\,\underline{\underline{M}}^{-1}\,\underline{\underline{D}}\right)\Delta\underline{d} \tag{B.39}$$

B.2.3 Determination of $\Delta\underline{n} \cdot \delta\underline{n}$

From the orthogonality condition $\underline{n} \cdot \underline{t}_i = 0$, one gets:

$$\delta\underline{n} \cdot \underline{t}_i = -\underline{n} \cdot \delta\underline{t}_i \tag{B.40}$$

Variation $\delta\underline{n}$ can be projected on the contravariant basis $(\underline{t}^1, \underline{t}^2, \underline{n})$. With the latter equation and since $\delta\underline{n} \cdot \underline{n} = 0$, one obtains:

$$\begin{aligned}\delta\underline{n} &= (\delta\underline{n} \cdot \underline{t}_i)\,\underline{t}^i + (\delta\underline{n} \cdot \underline{n})\,\underline{n} \\ &= (\delta\underline{n} \cdot \underline{t}_i)\,\underline{t}^i = -(\underline{n} \cdot \delta\underline{t}_i)\,\underline{t}^i \\ &= -(\underline{n} \cdot \delta\underline{t}_i)\,M^{ij}\underline{t}_j\end{aligned}$$

One deduces for any vector $\underline{u}$ of $\mathbb{R}^3$ that:

$$\delta\underline{n} \cdot \underline{u} = -\begin{pmatrix}\underline{n} \cdot \delta\underline{t}_1 & \underline{n} \cdot \delta\underline{t}_2\end{pmatrix}\,\underline{\underline{M}}^{-1}\begin{pmatrix}\underline{t}_1 \cdot \underline{u}\\ \underline{t}_2 \cdot \underline{u}\end{pmatrix} \tag{B.41}$$

where $\underline{\underline{M}}$ is the metric tensor with $M_{ij} = \underline{t}_i \cdot \underline{t}_j$. Similarly to (B.40), one has $\Delta\underline{n} \cdot \underline{t}_i = -\underline{n} \cdot \Delta\underline{t}_i$. Thus, one easily deduces from (B.41) and (B.28) that:

$$\delta\underline{n} \cdot \Delta\underline{n} = \begin{pmatrix}\underline{n} \cdot \delta\underline{t}_1 & \underline{n} \cdot \delta\underline{t}_2\end{pmatrix}\,\underline{\underline{M}}^{-1}\begin{pmatrix}\underline{n} \cdot \Delta\underline{t}_1\\ \underline{n} \cdot \Delta\underline{t}_2\end{pmatrix} = \delta\underline{d}^T\left[\underline{\underline{B}}(\underline{n})^T\,\underline{\underline{M}}^{-1}\,\underline{\underline{B}}(\underline{n})\right]\Delta\underline{d} \tag{B.42}$$

B.2.4 Determination of $\Delta\delta\underline{t}\cdot\underline{n}$

One exploits (A.25) to obtain, for $i=1,2$:

$$a^i\,\Delta\delta\underline{t}_i\cdot\underline{u}=\begin{pmatrix}\delta\underline{\Phi}_1^T & \delta\underline{\Phi}_2^T\end{pmatrix}\begin{pmatrix}\dfrac{a^1}{2}\underline{\underline{C}}(\underline{\Phi}_1,\underline{u}) & \underline{\underline{0}}_{3\times3}\\ \underline{\underline{0}}_{3\times3} & \dfrac{a^2}{2}\underline{\underline{C}}(\underline{\Phi}_2,\underline{u})\end{pmatrix}\begin{pmatrix}\Delta\underline{\Phi}_1\\ \Delta\underline{\Phi}_2\end{pmatrix}\tag{B.43}$$

where $\underline{\underline{C}}(\underline{\Phi},\underline{u})=\underline{\underline{\underline{H}}}(\underline{\Phi})^T\left(\underline{u}\otimes\underline{t}(\underline{\Phi})+\underline{t}(\underline{\Phi})\otimes\underline{u}\right)\underline{\underline{\underline{H}}}(\underline{\Phi})$ is symmetric and $\underline{\underline{0}}_{3\times3}$ is a 3 by 3 null matrix. In matrix form it reads:

$$a^i\,\Delta\delta\underline{t}_i\cdot\underline{u}=\delta\underline{d}^T\,\underline{\underline{\bar{C}}}(\underline{u},a^1,a^2)\,\Delta\underline{d}\tag{B.44}$$

with:

$$\underline{\underline{\bar{C}}}(\underline{u},a^1,a^2)=\begin{pmatrix}\underline{\underline{0}}_{3\times3} & \underline{\underline{0}}_{3\times3} & \underline{\underline{0}}_{3\times3} & \underline{\underline{0}}_{3\times3}\\ \underline{\underline{0}}_{3\times3} & \dfrac{a^1}{2}\underline{\underline{C}}(\underline{\Phi}_1,\underline{u}) & \underline{\underline{0}}_{3\times3} & \underline{\underline{0}}_{3\times3}\\ \underline{\underline{0}}_{3\times3} & \underline{\underline{0}}_{3\times3} & \underline{\underline{0}}_{3\times3} & \underline{\underline{0}}_{3\times3}\\ \underline{\underline{0}}_{3\times3} & \underline{\underline{0}}_{3\times3} & \underline{\underline{0}}_{3\times3} & \dfrac{a^2}{2}\underline{\underline{C}}(\underline{\Phi}_2,\underline{u})\end{pmatrix}\tag{B.45}$$

Appendix C

C.1 Variation of tangential gap

We consider the variation of the "trial" tangential slip which has been defined in Section 7.2.2, which expressed by

$$\underline{g}_T^{e,tr} = \underline{g}_T^{\Delta} + \underline{g}^e_{T,(n,n+1)}$$

Let us consider these two terms separately.

C.1.1 Variation of the tangential gap increment

We consider Eq. (7.27), which is

$$\begin{aligned}\delta\underline{g}_T^{\Delta} = \delta\xi_i\underline{t}^i - (\xi^2_{(n)}\underline{t}^1 + \xi^1_{(n)}\underline{t}^2)\delta M_{12} + g_{Ti}^{\Delta}(M^{ij}\delta\underline{t}_j) + g_{Ti}^{\Delta}(\delta M^{ij}\underline{t}_j) - \dots \\ \dots r_2\left[\delta\underline{n}_2\cdot\underline{t}_1 + \underline{n}_2\cdot\delta\underline{t}_1\right]\underline{t}^1 - r_1\left[\delta\underline{n}_1\cdot\underline{t}_2 + \underline{n}_1\cdot\delta\underline{t}_2\right]\underline{t}^2\end{aligned} \tag{C.46}$$

The complete matrix form of $\delta\underline{g}_T^{\Delta}$ is

$$\begin{aligned}\delta\underline{g}_T^{\Delta} = \Big\{ \begin{pmatrix}\underline{t}_1 & \underline{t}_2\end{pmatrix}\underline{\underline{M}}^{-T}\underline{\underline{D}} + \underline{\underline{\widehat{B}}}(g_{Ti}^{\Delta}M^{i1}, g_{Ti}^{\Delta}M^{i2}) - \underline{\underline{\widehat{B}}}(\xi^1_{(n)},\xi^2_{(n)}) - \dots \\ \dots g_{T1}^{\Delta}[2M^{11}M^{12} + (M^{12})^2 + M^{11}M^{22}]\underline{S}_1 - \dots \\ \dots g_{T2}^{\Delta}[2M^{22}M^{12} + (M^{12})^2 + M^{11}M^{22}]\underline{S}_2 - \dots \\ \dots \begin{pmatrix}\underline{t}^1\otimes\underline{t}_1 & \underline{t}^2\otimes\underline{t}_2\end{pmatrix}\begin{pmatrix}\underline{\underline{0}}_{3\times3} & \underline{\underline{0}}_{3\times3} & \underline{\underline{0}}_{3\times3} & r_2\underline{\underline{W}}(\underline{\underline{H}}_2,\underline{n}_2) \\ \underline{\underline{0}}_{3\times3} & r_1\underline{\underline{W}}(\underline{\underline{H}}_1,\underline{n}_1) & \underline{\underline{0}}_{3\times3} & \underline{\underline{0}}_{3\times3}\end{pmatrix} - \dots \\ \begin{pmatrix}\underline{t}^1\otimes\underline{n}_2 & \underline{t}^2\otimes\underline{n}_1\end{pmatrix}\begin{pmatrix}\underline{\underline{0}}_{3\times3} & r_2\underline{\underline{W}}(\underline{\underline{H}}_1,\underline{t}_1) & \underline{\underline{0}}_{3\times3} & \underline{\underline{0}}_{3\times3} \\ \underline{\underline{0}}_{3\times3} & \underline{\underline{0}}_{3\times3} & \underline{\underline{0}}_{3\times3} & r_1\underline{\underline{W}}(\underline{\underline{H}}_2,\underline{t}_2)\end{pmatrix}\Big\}\delta\underline{d} = \underline{\underline{G}}_{\Delta}\delta\underline{d}\end{aligned} \tag{C.47}$$

C.1.1.1 Term $\delta\xi_i\underline{t}^i$

The term $\delta\xi_i\underline{t}^i$ is obtained by exploiting (B.35). Ir reads

$$\delta\xi_i\underline{t}^i = \begin{pmatrix}\underline{t}^1 & \underline{t}^2\end{pmatrix}\underline{\underline{D}}\delta\underline{d} = \begin{pmatrix}\underline{t}_1 & \underline{t}_2\end{pmatrix}\underline{\underline{M}}^{-T}\underline{\underline{D}}\delta\underline{d} \tag{C.48}$$

C.1.1.2 Term $g^{\Delta}_{Ti}(M^{ij}\delta\underline{t}_j)$

The term $g^{\Delta}_{Ti}\delta\underline{t}_i$ is obtained by starting from the definition

$$\delta\underline{t}_i = (\widehat{\underline{\underline{H}}_i\delta\underline{\Phi}_i})\underline{t}_i \tag{C.49}$$

from which one gets

$$g^{\Delta}_{Ti}(M^{ij}\delta\underline{t}_j) = \underline{\underline{\widehat{B}}}(g^{\Delta}_{Ti}M^{i1}, g^{\Delta}_{Ti}M^{i2})\delta\underline{d} \tag{C.50}$$

where

$$\begin{array}{l}\underline{\underline{\widehat{B}}}(a_1, a_2) = \\ = \begin{pmatrix}\underline{\underline{0}}_{3\times3} & a_1\underline{\underline{W}}(\underline{\underline{H}}_1, \underline{t}_1) & \underline{\underline{0}}_{3\times3} & a_2\underline{\underline{W}}(\underline{\underline{H}}_2, \underline{t}_2)\end{pmatrix}\end{array} \tag{C.51}$$

C.1.1.3 Term $(\xi^2_{(n)}\underline{t}^1 + \xi^1_{(n)}\underline{t}^2)\delta M_{12}$

Since $M_{12} = M_{21} = \underline{t}_1 \cdot \underline{t}_2$, one has

$$\delta M_{12} = \underline{t}_2 \cdot \delta\underline{t}_1 + \underline{t}_1 \cdot \delta\underline{t}_2 \tag{C.52}$$

Hence since $\underline{t}_i \cdot \underline{t}^j = \delta^j_i$ one gets

$$(\xi^2_{(n)}\underline{t}^1 + \xi^1_{(n)}\underline{t}^2)(\underline{t}_2 \cdot \delta\underline{t}_1 + \underline{t}_1 \cdot \delta\underline{t}_2) = \xi^2_{(n)}\delta\underline{t}_2 + \xi^1_{(n)}\delta\underline{t}_1 \tag{C.53}$$

and therefore

$$(\xi^2_{(n)}\underline{t}^1 + \xi^1_{(n)}\underline{t}^2)\delta M_{12} = \underline{\underline{\widehat{B}}}(\xi^1_{(n)}, \xi^2_{(n)})\delta\underline{d} \tag{C.54}$$

with $\underline{\underline{\widehat{B}}}$ defined in (C.51).

C.1.1.4 Terms $g^{\Delta}_{T1}(\delta M^{1j}\underline{t}_j)$ and $g^{\Delta}_{T2}(\delta M^{2j}\underline{t}_j)$

The variation of the metric tensor components are given by

$$\begin{array}{rcl}\delta M^{ij} = \delta(\underline{t}^i \cdot \underline{t}^j) & = & \delta(M^{ik}\underline{t}_k \cdot M^{jl}\underline{t}_l) \\ & = & \delta M^{ik}\underline{t}_k \cdot \underline{t}^j + M^{ik}\delta\underline{t}_k \cdot \underline{t}^j + \underline{t}^i \cdot \delta M^{jl}\underline{t}_l + \underline{t}^i \cdot M^{jl}\delta\underline{t}_l\end{array} \tag{C.55}$$

and therefore, after some algebra and exploiting the relationships $\underline{t}^i = M^{ij}\underline{t}_j$, $M^{ij} = M^{ji}$ and $\underline{t}_i \cdot \underline{t}^j = \delta^j_i$, one obtains

$$\begin{array}{l}\delta M^{11} = -2M^{11}M^{12}(\underline{t}_2 \cdot \delta\underline{t}_1 + \underline{t}_1 \cdot \delta\underline{t}_2) \\ \delta M^{12} = \delta M^{21} = -[(M^{12})^2 + M^{11}M^{22}](\underline{t}_2 \cdot \delta\underline{t}_1 + \underline{t}_1 \cdot \delta\underline{t}_2) \\ \delta M^{22} = -2M^{22}M^{12}(\underline{t}_2 \cdot \delta\underline{t}_1 + \underline{t}_1 \cdot \delta\underline{t}_2)\end{array} \tag{C.56}$$

Hence we have

$$\begin{array}{l}g^{\Delta}_{T1}(\delta M^{1j}\underline{t}_j) + g^{\Delta}_{T2}(\delta M^{2j}\underline{t}_j) = \\ = g^{\Delta}_{T1}(\underline{t}_1\delta M^{11} + \underline{t}_2\delta M^{12}) + g^{\Delta}_{T2}(\underline{t}_1\delta M^{21} + \underline{t}_2\delta M^{22}) = s_1 + s_2 + s_3 + s_4\end{array} \tag{C.57}$$

with

$$\begin{array}{rcl} s_1 &=& -2M^{11}M^{12}g_{T1}^{\Delta}\underline{t}_1(\underline{t}_2\cdot\delta\underline{t}_1+\underline{t}_1\cdot\delta\underline{t}_2)\\ &=& -2M^{11}M^{12}g_{T1}^{\Delta}\left(\underline{t}_1\otimes\underline{t}_2\right)\underline{\underline{W}}(\underline{\underline{H}}_1,\underline{t}_1)\delta\underline{\Phi}_1+(\underline{t}_1\otimes\underline{t}_1)\underline{\underline{W}}(\underline{\underline{H}}_2,\underline{t}_2)\delta\underline{\Phi}_2\big]\\ &=& -2M^{11}M^{12}g_{T1}^{\Delta}\underline{\underline{S}}_1\delta\underline{d}\\ s_2 &=& -[(M^{12})^2+M^{11}M^{22}]g_{T1}^{\Delta}\underline{t}_2(\underline{t}_2\cdot\delta\underline{t}_1+\underline{t}_1\cdot\delta\underline{t}_2)\\ &=& -[(M^{12})^2+M^{11}M^{22}]g_{T1}^{\Delta}\left[(\underline{t}_2\otimes\underline{t}_2)\underline{\underline{W}}(\underline{\underline{H}}_1,\underline{t}_1)\delta\underline{\Phi}_1+(\underline{t}_2\otimes\underline{t}_1)\underline{\underline{W}}(\underline{\underline{H}}_2,\underline{t}_2)\delta\underline{\Phi}_2\right]\\ &=& -[(M^{12})^2+M^{11}M^{22}]g_{T1}^{\Delta}\underline{\underline{S}}_2\delta\underline{d}\\ s_3 &=& -[(M^{12})^2+M^{11}M^{22}]g_{T2}^{\Delta}\underline{t}_1(\underline{t}_2\cdot\delta\underline{t}_1+\underline{t}_1\cdot\delta\underline{t}_2)\\ &=& -[(M^{12})^2+M^{11}M^{22}]g_{T2}^{\Delta}\left[(\underline{t}_1\otimes\underline{t}_2)\underline{\underline{W}}(\underline{\underline{H}}_1,\underline{t}_1)\delta\underline{\Phi}_1+(\underline{t}_1\otimes\underline{t}_1)\underline{\underline{W}}(\underline{\underline{H}}_2,\underline{t}_2)\delta\underline{\Phi}_2\right]\\ &=& -[(M^{12})^2+M^{11}M^{22}]g_{T2}^{\Delta}\underline{\underline{S}}_1\delta\underline{d}\\ s_4 &=& -2M^{22}M^{12}g_{T2}^{\Delta}\underline{t}_2(\underline{t}_2\cdot\delta\underline{t}_1+\underline{t}_1\cdot\delta\underline{t}_2)\\ &=& -2M^{22}M^{12}g_{T2}^{\Delta}\left[(\underline{t}_2\otimes\underline{t}_2)\underline{\underline{W}}(\underline{\underline{H}}_1,\underline{t}_1)\delta\underline{\Phi}_1+(\underline{t}_2\otimes\underline{t}_1)\underline{\underline{W}}(\underline{\underline{H}}_2,\underline{t}_2)\delta\underline{\Phi}_2\right]\\ &=& -2M^{22}M^{12}g_{T2}^{\Delta}\underline{\underline{S}}_2\delta\underline{d} \end{array} \tag{C.58}$$

$$\begin{array}{l} \underline{\underline{S}}_1=\begin{pmatrix}\underline{\underline{0}}_{3\times3} & (\underline{t}_1\otimes\underline{t}_2)\underline{\underline{W}}(\underline{\underline{H}}_1,\underline{t}_1) & \underline{\underline{0}}_{3\times3} & (\underline{t}_1\otimes\underline{t}_1)\underline{\underline{W}}(\underline{\underline{H}}_2,\underline{t}_2)\end{pmatrix}\\ \underline{\underline{S}}_2=\begin{pmatrix}\underline{\underline{0}}_{3\times3} & (\underline{t}_2\otimes\underline{t}_2)\underline{\underline{W}}(\underline{\underline{H}}_1,\underline{t}_1) & \underline{\underline{0}}_{3\times3} & (\underline{t}_2\otimes\underline{t}_1)\underline{\underline{W}}(\underline{\underline{H}}_2,\underline{t}_2)\end{pmatrix} \end{array} \tag{C.59}$$

Finally we get

$$\begin{array}{l} g_{T1}^{\Delta}(\delta M^{1j}\underline{t}_j)+g_{T2}^{\Delta}(\delta M^{2j}\underline{t}_j)=\\ =-g_{T1}^{\Delta}[2M^{11}M^{12}+(M^{12})^2+M^{11}M^{22}]\underline{\underline{S}}_1\delta\underline{d}-\ldots\\ \ldots g_{T2}^{\Delta}[2M^{22}M^{12}+(M^{12})^2+M^{11}M^{22}]\underline{\underline{S}}_2\delta\underline{d} \end{array} \tag{C.60}$$

C.1.1.5 Terms $r_2\left(\delta\underline{n}_2\cdot\underline{t}_1\right)\underline{t}^1$ and $r_1\left(\delta\underline{n}_1\cdot\underline{t}_2\right)\underline{t}^2$

First of all we have to express the variation of the rotation matrix $\delta\underline{\underline{R}}_i^{\Delta}=\delta\underline{\underline{R}}(\underline{\Phi}_i^{\Delta})$. One has:

$$\begin{array}{rcl} \underline{\underline{R}}(\underline{\Phi}_i) &=& \underline{\underline{R}}(\underline{\Phi}_i^{\Delta})\cdot\underline{\underline{R}}(\underline{\Phi}_{i,(n)})\\ \underline{\underline{R}}(\underline{\Phi}_i^{\Delta}) &=& \underline{\underline{R}}(\underline{\Phi}_i)\cdot\underline{\underline{R}}^{T}(\underline{\Phi}_{i,(n)}) \end{array} \tag{C.61}$$

with $\underline{\Phi}_i^{\Delta}$ and $\underline{\Phi}_{i,(n)}$ the current rotation vector increment and the total rotation vector at the previous increment at node i (i.e. of the beam tangent $\underline{t}_i$). Therefore, from (A.14) one obtains

$$\begin{array}{rcl} \delta\underline{\underline{R}}(\underline{\Phi}_i^{\Delta})\underline{n}_{(n)} &=& \delta\underline{\underline{R}}(\underline{\Phi}_i)\cdot\underline{\underline{R}}^{T}(\underline{\Phi}_{i,(n)})\underline{n}_{(n)}\\ &=& \widehat{\underline{\underline{H}}(\underline{\Phi}_i)\delta\underline{\Phi}_i}\cdot\underline{\underline{R}}(\underline{\Phi}_i)\underline{N}_i\\ &=& \widehat{\underline{\underline{H}}(\underline{\Phi}_i)\delta\underline{\Phi}_i}\cdot\underline{n}_i \end{array} \tag{C.62}$$

These terms are hence obtained as follows:

$$\begin{array}{rcl} \left(\delta\underline{n}_2\cdot\underline{t}_1\right)\underline{t}^1 &=& (\underline{t}^1\otimes\underline{t}_1)(\delta\underline{\underline{R}}_2^{\Delta}\underline{n}_{(n)})\\ &=& (\underline{t}^1\otimes\underline{t}_1)\,\underline{\underline{W}}(\underline{\underline{H}}_2,\underline{n}_2)\,\delta\underline{\Phi}_2 \end{array} \tag{C.63}$$

Putting together the two terms one obtains

$$\begin{array}{l} r_2\left(\delta\underline{n}_2\cdot\underline{t}_1\right)\underline{t}^1+r_1\left(\delta\underline{n}_1\cdot\underline{t}_2\right)\underline{t}^2=\\ =\begin{pmatrix}\underline{t}^1\otimes\underline{t}_1 & \underline{t}^2\otimes\underline{t}_2\end{pmatrix}\begin{pmatrix}\underline{\underline{0}}_{3\times3} & \underline{\underline{0}}_{3\times3} & \underline{\underline{0}}_{3\times3} & r_2\underline{\underline{W}}(\underline{\underline{H}}_2,\underline{n}_2)\\ \underline{\underline{0}}_{3\times3} & r_1\underline{\underline{W}}(\underline{\underline{H}}_1,\underline{n}_1) & \underline{\underline{0}}_{3\times3} & \underline{\underline{0}}_{3\times3}\end{pmatrix}\delta\underline{d} \end{array} \tag{C.64}$$

C.1.1.6 Terms $r_2\,(\underline{n}_2 \cdot \delta\underline{t}_1)\,\underline{t}^1$ and $r_1\,(\underline{n}_1 \cdot \delta\underline{t}_2)\,\underline{t}^2$

These terms are obtained following the same procedure adopted previously:

$$\begin{array}{rcl}(\underline{n}_2 \cdot \delta\underline{t}_1)\,\underline{t}^1 & = & (\underline{t}^1 \otimes \underline{n}_2)\,\delta\underline{t}_1 \\ & = & (\underline{t}^1 \otimes \underline{n}_2)\,\underline{\underline{W}}(\underline{\underline{H}}_1, \underline{t}_1)\delta\underline{\Phi}_1\end{array} \tag{C.65}$$

Putting the two terms together one gets

$$\begin{array}{l} r_2\,(\underline{n}_2 \cdot \delta\underline{t}_1)\,\underline{t}^1 + r_1\,(\underline{n}_1 \cdot \delta\underline{t}_2)\,\underline{t}^2 = \\ = \begin{pmatrix}\underline{t}^1 \otimes \underline{n}_2 & \underline{t}^2 \otimes \underline{n}_1\end{pmatrix} \begin{pmatrix}\underline{\underline{0}}_{3\times3} & r_2\underline{\underline{W}}(\underline{\underline{H}}_1, \underline{t}_1) & \underline{\underline{0}}_{3\times3} & \underline{\underline{0}}_{3\times3} \\ \underline{\underline{0}}_{3\times3} & \underline{\underline{0}}_{3\times3} & \underline{\underline{0}}_{3\times3} & r_1\underline{\underline{W}}(\underline{\underline{H}}_2, \underline{t}_2)\end{pmatrix} \delta\underline{d}\end{array} \tag{C.66}$$

C.1.2 Calculation of the variation: $\delta\underline{g}^e_{T,(n,n+1)}$

As explained in Section 7.2.2, the elastic slip at time increment n can be expressed as

$$\underline{g}^e_{T,(n)} = \xi^i_{e,(n)}\underline{t}_{i,(n)}$$

and it can be mapped in the configuration at time increment $n+1$ as

$$\underline{g}^e_{T,(n,n+1)} = \xi^i_{e,(n)}\underline{t}_i$$

Hence in matrix form one has

$$\begin{array}{rcl}\delta\underline{g}^e_{T,(n,n+1)} & = & \xi^i_{e,(n)}\delta\underline{t}_i \\ & = & \begin{pmatrix}\underline{\underline{0}}_{3\times3} & \xi^1_{e,(n)}\underline{\underline{W}}(\underline{\underline{H}}_1, \underline{t}_1) & \underline{\underline{0}}_{3\times3} & \xi^2_{e,(n)}\underline{\underline{W}}(\underline{\underline{H}}_2, \underline{t}_2)\end{pmatrix} \delta\underline{d} \\ & = & \underline{\underline{\widehat{B}}}(\xi^1_{e,(n)}, \xi^2_{e,(n)})\delta\underline{d}\end{array} \tag{C.67}$$

with $\underline{\underline{\widehat{B}}}$ defined in (C.51).

C.2 Calculation of the contribution to the weak form

The tangential contact contribution to the weak form (7.53) is given by

$$\begin{array}{rcl}\delta W^T_C = \underline{t}_T \cdot \delta\underline{g}^{e,tr}_T & = & \underline{t}_T \cdot (\delta\underline{g}^{\Delta}_T + \delta\underline{g}^e_{T,(n,n+1)}) \\ & = & \delta\underline{d}^T \left(\underline{\underline{G}}^T_{\Delta} + \underline{\underline{\widehat{B}}}^T(\xi^1_{e,(n)}, \xi^2_{e,(n)})\right) \cdot \underline{t}_T\end{array} \tag{C.68}$$

with $\underline{\underline{G}}_{\Delta}$ and $\underline{\underline{\widehat{B}}}^T(\xi^1_{e,(n)}, \xi^2_{e,(n)})$ defined respectively in (C.47) and (C.67).

Bibliography

[1] ABAQUS. v6.14 documentation. *Dassault Systemes Simulia Corporation*, 2014.

[2] J. Araujo and D. Nowell. The effect of rapidly varying contact stress fields on fretting fatigue. *International Journal of Fatigue*, 24(7):763–775, 2002.

[3] M.-C. Baietto, E. Pierres, A. Gravouil, B. Berthel, S. Fouvry, and B. Trolle. Fretting fatigue crack growth simulation based on a combined experimental and XFEM strategy. *International Journal of Fatigue*, 47:31–43, 2013.

[4] L. Barrallier, G. Barreau, and J. Barralis. Influence de l'origine de la relaxation des contraintes résiduelles dans le cas d'aciers alliés. *Revue de métallurgie*, pages 637–649, 05 1993.

[5] O. Basquin. The exponential law of endurance tests. In *Proc Am Soc Test Mater*, volume 10, pages 625–630, 1910.

[6] T. Belytschko, W. K. Liu, and B. Moran. Finite elements for nonlinear continua and structures. *J. Wiley*, 2000.

[7] S. Beretta and S. Foletti. Propagation of small cracks under RCF: a challenge to Multiaxial Fatigue Criteria. In *CP2012*, 2012.

[8] A. P. Boresi, R. J. Schmidt, and O. M. Sidebottom. *Advanced mechanics of materials*, volume 6. Wiley New York et al., 1985.

[9] P. Brevet et al. Microstructure et propriétés mécaniques des aciers pour câble. *Bulletin des laboratoires des Ponts et Chaussées*, (249-250-251), 2004.

[10] F. Bussolati, M. Guiton, P.-A. Guidault, Y. Poirette, M. Martinez, and O. Allix. A new fully-detailed finite element of spiral strand wire ropes for fatigue life estimate of a mooring line. In *ASME 2019 38th International Conference on Ocean, Offshore and Arctic Engineering*. American Society of Mechanical Engineers, 2019.

[11] S. Butterfield, W. Musial, J. Jonkman, P. Sclavounos, and L. Wayman. Engineering challenges for floating offshore wind turbines. In *Copenhagen Offshore Wind Conference, Copenhagen, Denmark*, pages 377–382. Citeseer, 2005.

[12] C. Chaplin and A. Potts. Wire rope offshore - a critical review of wire rope endurance research affecting offshore applications. 1991.

[13] A. Cardona. *An integrated approach to mechanism analysis.* PhD thesis, Université de Liège, 1990.

[14] C. Cattaneo. Sul contatto di due corpi elastici: Distribuzione locale degli sforzi. *Reconditi dell'Academia Nazionale dei Lincei*, 27:474–478, 1938.

[15] C. Chaplin. Interactive fatigue in wire rope applications. In *Symposium on Mechanics of Slender Structures (MoSS 2008)*, 2008.

[16] C. Chaplin, A. Potts, and A. Curtis. Degradation of wire rope mooring lines in SE Asian waters. In *Kuala Lumpur, Offshore Asia Conference*, 2008.

[17] C. Chaplin, G. Rebel, I. Ridge, et al. Tension/torsion interactions in multicomponent mooring lines. In *Offshore Technology Conference*. Offshore Technology Conference, 2000.

[18] Y. Chen, F. Meng, and X. Gong. Interwire wear and its influence on contact behavior of wire rope strand subjected to cyclic bending load. *Wear*, 368:470–484, 2016.

[19] M. Ciavarella and F. Monno. A comparison of multiaxial fatigue criteria as applied to rolling contact fatigue. *Tribology International*, 43(11):2139–2144, 2010.

[20] R. Claren and G. Diana. Dynamic strain distribution on loaded stranded cables. *IEEE Transactions on Power Apparatus and Systems*, (11):1678–1690, 1969.

[21] G. A. Costello. *Theory of wire rope*. Springer Science & Business Media, 1997.

[22] B. Crossland. Effect of large hydrostatic pressures on the torsional fatigue strength of an alloy steel. In *Proc. Int. Conf. on Fatigue of Metals*, volume 138, pages 12–12. Institution of Mechanical Engineers London, 1956.

[23] K. Dang-Van. Macro-micro approach in high-cycle multiaxial fatigue. In *Advances in multiaxial fatigue*. ASTM International, 1993.

[24] K. Dang-Van. Introduction to fatigue analysis in mechanical design by the multiscale approach. In *High-Cycle Metal Fatigue*, pages 57–88. Springer, 1999.

[25] K. Dang-Van and B. Griveau. On a new multiaxial fatigue limit criterion: Theory and application. *biaxial and multiaxial fatigue*, (3):479–496, 1988.

[26] K. Dang-Van and M. H. Maitournam. On a new methodology for quantitative modeling of fretting fatigue. In *Fretting fatigue: current technology and practices*. ASTM International, 2000.

[27] B. C. De Jong. *Analytical and experimental analysis of the capacity of steel wire ropes subjected to forced bending*. PhD thesis, TU Delft, Delft University of Technology, 2015.

[28] L. De Lorenzis, P. Wriggers, and G. Zavarise. A mortar formulation for 3D large deformation contact using NURBS-based isogeometric analysis and the augmented Lagrangian method. *Computational Mechanics*, 49(1):1–20, 2012.

[29] H. Desimone, A. Bernasconi, and S. Beretta. On the application of Dang Van criterion to rolling contact fatigue. *Wear*, 260(4-5):567–572, 2006.

[30] Det Norske Veritas. Position moorings. *Offshore Standard DNV-OS-E301*, 2010.

[31] Det Norske Veritas. Design of floating wind turbine structures. *Offshore Standard DNV-OS-J103*, 2013.

[32] Det Norske Veritas. Design of offshore wind turbine structures. *Offshore Standard DNV-OS-J101*, 2014.

[33] Det Norske Veritas. Classification of mooring systems for permanent and mobile offshore units. *Rule Note NR 493 DT R03 E*, 2015.

[34] D. Doyen, A. Ern, and S. Piperno. Time-integration schemes for the finite element dynamic Signorini problem. *SIAM Journal on Scientific Computing*, 33(1):223–249, 2011.

[35] T. X. Duong, L. De Lorenzis, and R. A. Sauer. A segmentation-free isogeometric extended mortar contact method. *Computational Mechanics*, 63(2):383–407, 2019.

[36] D. Durville. Contact-friction modeling within elastic beam assemblies: an application to knot tightening. *Computational Mechanics*, 49(6):687–707, 2012.

[37] D. Durville and P. Davies. Simulation du passage de câbles tressés synthétiques sur une poulie. In *CSMA 2013-11e Colloque National en Calcul des Structures*, 2013.

[38] C. Eck, J. Jarusek, and M. Krbec. *Unilateral contact problems: variational methods and existence theorems*, volume 270. CRC Press, 2005.

[39] J.-L. Engerand. *Mécanique de la rupture*. Ed. Techniques Ingénieur, 1990.

[40] J.-B. Esnault, V. Doquet, and P. Massin. A three-dimensional analysis of fatigue crack paths in thin metallic sheets. *International Journal of Fatigue*, 62:119–132, 2014.

[41] A. Fatemi and D. F. Socie. A critical plane approach to multiaxial fatigue damage including out-of-phase loading. *Fatigue & Fracture of Engineering Materials & Structures*, 11(3):149–165, 1988.

[42] C. A. Felippa and B. Haugen. A unified formulation of small-strain corotational finite elements: I. Theory. *Computer Methods in Applied Mechanics and Engineering*, 194(21-24):2285–2335, 2005.

[43] K. A. Fischer and P. Wriggers. Mortar based frictional contact formulation for higher order interpolations using the moving friction cone. *Computer methods in applied mechanics and engineering*, 195(37-40):5020–5036, 2006.

[44] E. Fontaine, J. Heurtier, D. Durville, S. Toumit, and C. Prat. Modeling of riser contact-friction problems. In *Offshore Technology Conference*. Offshore Technology Conference, 2002.

[45] E. Fontaine, A. Kilner, C. Carra, D. Washington, K. Ma, A. Phadke, D. Laskowski, and G. Kusinski. Industry survey of past failures, pre-emptive replacements and reported degradations for mooring systems of floating production units. In *Offshore Technology Conference*. Offshore Technology Conference, 2014.

[46] S. Fouvry, K. Elleuch, and G. Simeon. Prediction of crack nucleation under partial slip fretting conditions. *The Journal of Strain Analysis for Engineering Design*, 37(6):549–564, 2002.

[47] Gao Z. Stochastic response analysis of mooring systems with emphasis on frequency-domain analysis of fatigue due to wide-band response processes. Fakultet for ingeniørvitenskap og teknologi, 2008.

[48] S. Ghosh and D. Roy. A frame-invariant scheme for the geometrically exact beam using rotation vector parametrization. *Computational Mechanics*, 44(1):103, 2009.

[49] M. Giglio and A. Manes. Bending fatigue tests on a metallic wire rope for aircraft rescue hoists. *Engineering Failure Analysis*, 10(2):223–235, 2003.

[50] J. Greenwood. Formulas for moderately elliptical hertzian contacts. *ASME J. Tribol*, 107(4):501–504, 1985.

[51] P.-A. Guidault, M. Poss, and F. Louf. Modélisation avancée des interfaces mécaniques - mécanique des contacts conformes et non conformes. *ENS de Cachan*, 2014.

[52] F. Guillemin, D. di Domenico, G. Sabiron, and D. Averbuch. Using LIDAR based control to reduce loads on floating wind turbines and boost performance. In *Offshore Technology Conference*. Offshore Technology Conference, 2016.

[53] M. Hahn and P. Gilman. Offshore wind market and economic analysis. *Burlington*, (nDE-EE0005360):1–191, 2013.

[54] M. T. J. Hall. *Mooring line modelling and design optimization of floating offshore wind turbines*. PhD thesis, University of Victoria, 2013.

[55] Q.-C. He and A. Curnier. Anisotropic dry friction between two orthotropic surfaces undergoing large displacements. *European Journal of Mechanics-A/Solids*, 12(ARTICLE):631–666, 1993.

[56] H. Hertz. On the contact of elastic solids. *J. reine angew. Math*, 92(156-171):110, 1881.

[57] M. Hjiaj, G. de Saxcé, and Z. Mróz. A variational inequality-based formulation of the frictional contact law with a non-associated sliding rule. *European Journal of Mechanics-A/Solids*, 21(1):49–59, 2002.

[58] R. Hobbs and K. Ghavani. The fatigue of structural wire strands. *International Journal of Fatigue*, 4(2):69–72, 1982.

[59] R. Hobbs and M. Raoof. Interwire slippage and fatigue prediction in stranded cables for TLP tethers. *Hemisphere Publishing Corp,*, pages 77–99, 1983.

[60] R. Hobbs and M. Raoof. Mechanism of fretting fatigue in steel cables. *International journal of fatigue*, 16(4):273–280, 1994.

[61] R. Hobbs and B. Smith. Fatigue performance of socketed terminations to structural strands. *Proceedings of the Institution of Civil Engineers*, 75(1):35–48, 1983.

[62] K.-J. Hong, A. Der Kiureghian, and J. L. Sackman. Bending behavior of helically wrapped cables. *Journal of engineering mechanics*, 131(5):500–511, 2005.

[63] J.-P. Houle-Paradis. *Modélisation de la flexion libre d'un câble multicouche tenant compte de l'élasticité des contacts*. PhD thesis, Université de Sherbrooke., 2011.

[64] X. Huang and O. Vinogradov. Analysis of dry friction hysteresis in a cable under uniform bending. *Structural Engineering and Mechanics*, 2(1):63–80, 1994.

[65] X. Huang and O. G. Vinogradov. Extension of a cable in the presence of dry friction. *Structural Engineering and Mechanics*, 4(3):313–329, 1996.

[66] P. Hurricks. The mechanism of fretting - a review. *Wear*, 15(6):389–409, 1970.

[67] International Electrotechnical Commission et al. Wind turbines: Part 3: Design requirements for offshore wind turbines, 2009.

[68] J-P. Fargues. *Modélisation dynamique des risers pétroliers en grands déplacements*. PhD thesis, École Centrale Paris, 1995.

[69] K. Johnson. The effect of a tangential contact force upon the rolling motion of an elastic sphere on a plane. *Journal of Applied Mechanics*, 80(9):339–346, 1958.

[70] K. Johnson. The application of shakedown principles in rolling and sliding contact. *Eur. J. Mech. A/Solids*, 11(155-172):188, 1992.

[71] K. Johnson, J. Greenwood, and J. Higginson. The contact of elastic regular wavy surfaces. *International journal of mechanical sciences*, 27(6):383–396, 1985.

[72] C. Jolicoeur and A. Cardou. Semicontinuous mathematical model for bending of multilayered wire strands. *Journal of engineering Mechanics*, 122(7):643–650, 1996.

[73] J. Jonkman, S. Butterfield, W. Musial, and G. Scott. Definition of a 5-MW reference wind turbine for offshore system development. *National Renewable Energy Laboratory, Golden, CO, Technical Report No. NREL/TP-500-38060*, 2009.

[74] R. Judge, Z. Yang, S. Jones, and G. Beattie. Full 3D finite element modelling of spiral strand cables. *Construction and Building Materials*, 35:452–459, 2012.

[75] A. Kapoor. *Geometry changes and crack initiation in rolling and sliding contact.* PhD thesis, University of Cambridge, 1987.

[76] A. Kilner, D. Washington, C. Carra, and A. Potts. Improvements in the practices for mooring integrity management. In *OTC Brasil*. Offshore Technology Conference, 2015.

[77] H. Kim and M. Kim. Comparison of simulated platform dynamics in steady/dynamic winds and irregular waves for oc4 semi-submersible 5mw wind-turbine against deepcwind model-test results. *Ocean Syst. Eng*, 6(1):1–21, 2016.

[78] S. Kmet, E. Stanova, G. Fedorko, M. Fabian, and J. Brodniansky. Experimental investigation and finite element analysis of a four-layered spiral strand bent over a curved support. *Engineering Structures*, 57:475–483, 2013.

[79] R. Knapp. Derivation of a new stiffness matrix for helically armoured cables considering tension and torsion. *International Journal for Numerical Methods in Engineering*, 14(4):515–529, 1979.

[80] R. Knapp and E. Chiu. Tension fatigue model for helically armored cables. *Journal of energy resources technology*, 110(1):12–18, 1988.

[81] W. Koiter. General theorems of elasto-plastic solids. *Progress in Solid Mechanics. Eds. IN Sneddon and R. Hill*, 1960.

[82] A. Konyukhov and K. Schweizerhof. Geometrically exact covariant approach for contact between curves. *Computer Methods in Applied Mechanics and Engineering*, 199(37-40):2510–2531, 2010.

[83] S. Lalonde, R. Guilbault, and S. Langlois. Modeling multilayered wire strands, a strategy based on 3D finite element beam-to-beam contacts - Part II: Application to wind-induced vibration and fatigue analysis of overhead conductors. *International Journal of Mechanical Sciences*, 126:297–307, 2017.

[84] S. Lalonde, R. Guilbault, and F. Légeron. Modeling multilayered wire strands, a strategy based on 3D finite element beam-to-beam contacts - Part I: Model formulation and validation. *International Journal of Mechanical Sciences*, 126:281–296, 2017.

[85] J. Lanteigne. Theoretical estimation of the response of helically armored cables to tension, torsion, and bending. *ASME J. Appl. Mech*, 52(2):423–432, 1985.

[86] T. A. Laursen. Emerging spatial and temporal discretization methods in contact and impact mechanics. In *Computational Contact Mechanics*, pages 1–37. Springer, 2007.

[87] J. Lemaitre and J. Chaboche. Mechanics of solid mechanics. *Cambridge University, Cambridge, United Kingdom*, pages 161–241, 1990.

[88] J.-M. Leroy and P. Estrier. Calculation of stresses and slips in helical layers of dynamically bent flexible pipes. *Oil & Gas Science and Technology*, 56(6):545–554, 2001.

[89] F. Lévesque, S. Goudreau, S. Langlois, and F. Légeron. Experimental study of dynamic bending stiffness of ACSR overhead conductors. *IEEE Transactions on Power Delivery*, 30(5):2252–2259, 2015.

[90] P. Litewka and P. Wriggers. Contact between 3D beams with rectangular cross-sections. *International Journal for Numerical Methods in Engineering*, 53(9):2019–2041, 2002.

[91] P. Litewka and P. Wriggers. Frictional contact between 3D beams. *Computational mechanics*, 28(1):26–39, 2002.

[92] Lubrication Wear Group, D. Haines, and E. Ollerton. Contact stress distributions on elliptical contact surfaces subjected to radial and tangential forces. *Proceedings of the Institution of Mechanical Engineers*, 177(1):95–114, 1963.

[93] J. Mandel. Adaptation d'une structure plastique ecrouissable et approximations. *Mechanics Research Communications*, 3(6):483–488, 1976.

[94] N. Maouche. *Modélisation des phénomènes d'endommagements dus aux contacts à faible amplitude de débattement*. PhD thesis, Ecole Nationale des Ponts et Chaussées, 1997.

[95] P. Massin and A. Martin. Influence du statut des points d'intégration sur les algorithmes de contact-frottement. In *CSMA 2013-11e Colloque National en Calcul des Structures*, 2013.

[96] I. McColl, J. Ding, and S. Leen. Finite element simulation and experimental validation of fretting wear. *Wear*, 256(11-12):1114–1127, 2004.

[97] E. Melan. Theorie statisch unbestimmter systeme aus ideal-plastichem baustoff. sitzungsber. d. akad. d. wiss. *Wien, 2A (145): 195*, 218, 1936.

[98] R. Merhej. *Impact de la taille du contact sur le comportement tribologique du contact 100Cr6/100Cr soumis à des sollicitations de fretting*. PhD thesis, Ecully, Ecole centrale de Lyon, 2008.

[99] B. Molin. *Hydrodynamique des structures offshore*. Editions Technip, 2002.

[100] Z. Mroz and S. Stupkiewicz. Constitutive modeling of slip and wear in elastic frictional contact. *Contact Mechanics*, pages 237–260, 1992.

[101] Z. Mróz and S. Stupkiewicz. An anisotropic friction and wear model. *International journal of solids and structures*, 31(8):1113–1131, 1994.

[102] Y. Mutoh. Mechanisms of fretting fatigue. *JSME international journal. Ser. A, Mechanics and material engineering*, 38(4):405–415, 1995.

[103] A. G. Neto, P. M. Pimenta, and P. Wriggers. A master-surface to master-surface formulation for beam to beam contact. Part I: frictionless interaction. *Computer Methods in Applied Mechanics and Engineering*, 303:400–429, 2016.

[104] A. G. Neto, P. M. Pimenta, and P. Wriggers. A master-surface to master-surface formulation for beam to beam contact. Part II: Frictional interaction. *Computer Methods in Applied Mechanics and Engineering*, 319:146–174, 2017.

[105] N. M. Newmark et al. A method of computation for structural dynamics. American Society of Civil Engineers, 1959.

[106] Noble Denton Europe Limited. Floating production system - JIP-FPS mooring integrity. In *Research Report 444*, 2006.

[107] O. Steinkjer, N. Soødahl and G. Grytoøyr. Methodology for time domain fatigue life assessment of risers and umbilicals. In *ASME 2010 29th International Conference on Ocean, Offshore and Arctic Engineering*. American Society of Mechanical Engineers, 2010.

[108] J. Out and B. Von Morgen. Slippage of helical reinforcing on a bent cylinder. *Engineering Structures*, 19(6):507–515, 1997.

[109] A. Pantaleo, A. Pellerano, F. Ruggiero, and M. Trovato. Feasibility study of offshore wind farms: an application to Puglia region. *Solar Energy*, 79(3):321–331, 2005.

[110] P. Papadopoulos, R. E. Jones, and J. M. Solberg. A novel finite element formulation for frictionless contact problems. *International Journal for Numerical Methods in Engineering*, 38(15):2603–2617, 1995.

[111] K. O. Papailiou. Bending of helically twisted cables under variable bending stiffness due to internal friction, tensile force and cable curvature. *Doctor of Technical Sciences thesis, ETH, Zurich, Swiss*, 1995.

[112] J.-P. H. Paradis and F. Légeron. Modelling of the free bending behavior of a multilayer cable taking into account the tangential compliance of contact interfaces. In *Ninth International Symposium on Cable Dynamics*, pages 18–20, 2011.

[113] V. Perier. Etude de l'influence des conditions environnementales sur le comportement en fretting, fatigue et fretting-fatigue des câbles du génie civil. *THESE DE DOCTORAT DE L'ECOLE CENTRALE DE LYON*, 2010.

[114] V. Périer, L. Dieng, L. Gaillet, and S. Fouvry. Influence of an aqueous environment on the fretting behaviour of steel wires used in civil engineering cables. *Wear*, 271(9-10):1585–1593, 2011.

[115] V. Périer, L. Gaillet, and L. Dieng. Effet de l'environnement sur la propagation de fissures dans les fils de câbles douvrages dart. In *31èmes Journées de Printemps de la Société Française de Métallurgie et des Matériaux*, pages pp–449, 2012.

[116] Y. Poirette, T. Perdrizet, J. C. Gilloteaux, A. Pourtier, and C. Mabile. A new ballasted floating support for offshore wind turbine. In *ASME 2014 33rd International Conference on Ocean, Offshore and Arctic Engineering*. American Society of Mechanical Engineers, 2014.

[117] M. Prados-Privado, J. C. Prados-Frutos, Á. Manchón, R. Rojo, P. Felice, and J. A. Bea. Dental implants fatigue as a possible failure of implantologic treatment: the importance of randomness in fatigue behaviour. *BioMed research international*, 2015, 2015.

[118] M. A. Puso and T. A. Laursen. A mortar segment-to-segment contact method for large deformation solid mechanics. *Computer methods in applied mechanics and engineering*, 193(6-8):601–629, 2004.

[119] M. A. Puso and T. A. Laursen. A mortar segment-to-segment frictional contact method for large deformations. *Computer methods in applied mechanics and engineering*, 193(45-47):4891–4913, 2004.

[120] M. Raoof. Free bending tests on large spiral strands. *Proceedings of the Institution of Civil Engineers*, 87(4):605–626, 1989.

[121] M. Raoof. Effect of hydrostatic pressure on strand behaviour. *The Journal of Strain Analysis for Engineering Design*, 25(2):75–84, 1990.

[122] M. Raoof. Free bending fatigue of axially pre-loaded spiral strands. *The Journal of Strain Analysis for Engineering Design*, 27(3):127–136, 1992.

[123] M. Raoof. Design of sheathed spiral strands against free bending fatigue at terminations. *The Journal of Strain Analysis for Engineering Design*, 28(3):163–174, 1993.

[124] M. Raoof and T. J. Davies. The riddle of free-bending fatigue at end terminations to spiral strands. *Journal of Constructional Steel Research*, 95:256–262, 2014.

[125] M. Raoof and R. Hobbs. Torsion tests on large spiral strands. *The Journal of Strain Analysis for Engineering Design*, 23(2):97–104, 1988.

[126] M. Raoof and R. E. Hobbs. Analysis of multilayered structural strands. *Journal of engineering Mechanics*, 114(7):1166–1182, 1988.

[127] M. Raoof and Y. Huang. Wire stress calculations in helical strands undergoing bending. *Journal of Offshore Mechanics and Arctic Engineering*, 114(3):212–219, 1992.

[128] C. B. Rawlins. Flexural self-damping in overhead electrical transmission conductors. *Journal of Sound and Vibration*, 323(1-2):232–256, 2009.

[129] J. Redford, H.-P. Lieurade, M. Gueguin, F. Hafid, C. Yang, and J.-M. Ghidaglia. Modélisation numerique du phenomène de fretting-fatigue intervenant dans le viellissement des conducteurs de lignes aeriennes. *Materiaux & Techinques*, 106(3):308, 2018.

[130] I. Ridge. Torsional characterization of ropes used offshore. *The Journal of Strain Analysis for Engineering Design*, 43(2):121–139, 2008.

[131] I. Ridge. Tension–torsion fatigue behaviour of wire ropes in offshore moorings. *Ocean Engineering*, 36(9):650–660, 2009.

[132] A. Robertson, J. Jonkman, M. Masciola, H. Song, A. Goupee, A. Coulling, and C. Luan. Definition of the semisubmersible floating system for phase ii of oc4. Technical report, National Renewable Energy Lab.(NREL), Golden, CO (United States), 2014.

[133] C. Ruiz, P. Boddington, and K. Chen. An investigation of fatigue and fretting in a dovetail joint. *Experimental mechanics*, 24(3):208–217, 1984.

[134] A. Sackfield and D. Hills. Some useful results in the tangentially loaded hertzian contact problem. *The Journal of Strain Analysis for Engineering Design*, 18(2):107–110, 1983.

[135] S. Sævik. A finite element model for predicting stresses and slip in flexible pipe armouring tendons. *Computers & structures*, 46(2):219–230, 1993.

[136] R. A. Sauer and L. De Lorenzis. An unbiased computational contact formulation for 3D friction. *International Journal for Numerical Methods in Engineering*, 101(4):251–280, 2015.

[137] W. Schütz. A history of fatigue. *Engineering fracture mechanics*, 54(2):263–300, 1996.

[138] M. Siavelis, M. L. Guiton, P. Massin, and N. Moës. Large sliding contact along branched discontinuities with X-FEM. *Computational mechanics*, 52(1):201–219, 2013.

[139] D. Siegert. *Mécanismes de fatigue de contact dans les câbles de haubanage du Génie Civil*. PhD thesis, Nantes, 1997.

[140] G. Sigurdsson. Probabilistic fatigue of offshore structures. In *Reliability and Optimization of Structural Systems 88*, pages 291–309. Springer, 1989.

[141] J. Simo. The (symmetric) hessian for geometrically nonlinear models in solid mechanics: Intrinsic definition and geometric interpretation. *Computer Methods in Applied Mechanics and Engineering*, 96(2):189–200, 1992.

[142] J. C. Simo and R. L. Taylor. Consistent tangent operators for rate-independent elastoplasticity. *Computer methods in applied mechanics and engineering*, 48(1):101–118, 1985.

[143] G. Sines. Failure of materials under combined repeated stresses with superimposed static stresses. Technical report, California. Univ., Los Angeles, 1955.

[144] R. Smallwood. *Fretting fatigue of steel roping wire in seawater.* PhD thesis, University of Nottingham, 1988.

[145] K. Smith, T. Topper, and P. Watson. A stress-strain function for the fatigue of metals (stress-strain function for metal fatigue including mean stress effect). *J Materials*, 5:767–778, 01 1970.

[146] E. Stanova, G. Fedorko, M. Fabian, and S. Kmet. Computer modelling of wire strands and ropes - Part II: Finite element-based applications. *Advances in Engineering Software*, 42(6):322–331, 2011.

[147] G. M. Stewart, A. Robertson, J. Jonkman, and M. A. Lackner. The creation of a comprehensive metocean data set for offshore wind turbine simulations. *Wind Energy*, 19(6):1151–1159, 2016.

[148] N. P. Suh. The delamination theory of wear. *Wear*, 25(1):111–124, 1973.

[149] N. P. Suh. An overview of the delamination theory of wear. *Wear*, 44(1):1–16, 1977.

[150] M. P. Szolwinski and T. N. Farris. Mechanics of fretting fatigue crack formation. *Wear*, 198(1-2):93–107, 1996.

[151] H. R. Thomas and V. A. Hoersch. Stresses due to the pressure of one elastic solid upon another with special reference to railroad rails: a report. Technical report, University of Illinois at Urbana Champaign, College of Engineering. Engineering Experiment Station., 1930.

[152] G. Tilly. Performance of bridge cables. In *First Oleg Kerensky Memorial Conference*, 1988.

[153] H. Usabiaga and J. Pagalday. Analytical procedure for modelling recursively and wire by wire stranded ropes subjected to traction and torsion loads. *International Journal of Solids and Structures*, 45(21):5503–5520, 2008.

[154] W. Utting and N. Jones. The response of wire rope strands to axial tensile loads - Part I. Experimental results and theoretical predictions. *International journal of mechanical sciences*, 29(9):605–619, 1987.

[155] P. S. Van Lieshout, J. H. den Besten, and M. L. Kaminski. Validation of the corrected Dang Van multiaxial fatigue criterion applied to turret bearings of FPSO offloading buoys. *Ships and Offshore Structures*, 12(4):521–529, 2017.

[156] A. Vannes, J. Chicois, and R. Fougeres. Restauration des contraintes résiduelles induites par écrouissage, en fonction de la température de chauffage et du temps de maintien. *Mémoires Scientifiques, Métallurgie*, 70:4, 1973.

[157] P. Vermeulen and K. Johnson. Contact of nonspherical elastic bodies transmitting tangential forces. *Journal of Applied Mechanics*, 31:338, 1964.

[158] L. Vincent, Y. Berthier, and M. Godet. Testing methods in fretting fatigue: a critical appraisal. In *Standardization of fretting fatigue test methods and equipment*. ASTM International, 1992.

[159] O. Vingsbo and S. Söderberg. On fretting maps. *Wear*, 126(2):131–147, 1988.

[160] D. Wang, D. Zhang, and S. Ge. Fretting–fatigue behavior of steel wires in low cycle fatigue. *Materials & Design*, 32(10):4986–4993, 2011.

[161] J. A. Williams and R. S. Dwyer-Joyce. Contact between solid surfaces. *Modern tribology handbook*, 1:121–162, 2001.

[162] J. Witz and Z. Tan. On the flexural structural behaviour of flexible pipes, umbilicals and marine cables. *Marine structures*, 5(2-3):229–249, 1992.

[163] A. Wöhler. *Über die festigkeitsversuche mit eisen und stahl*. Ernst & Korn, 1870.

[164] S. Wong, A. Kapoor, and J. Williams. Shakedown limits on coated and engineered surfaces. *Wear*, 203:162–170, 1997.

[165] P. Wriggers and T. A. Laursen. *Computational contact mechanics*, volume 2. Springer, 2006.

[166] P. Wriggers and G. Zavarise. On contact between three-dimensional beams undergoing large deflections. *International Journal for Numerical Methods in Biomedical Engineering*, 13(6):429–438, 1997.

[167] L. Xiang, H. Wang, Y. Chen, Y. Guan, Y. Wang, and L. Dai. Modeling of multi-strand wire ropes subjected to axial tension and torsion loads. *International Journal of Solids and Structures*, 58:233–246, 2015.

[168] V. Yastrebov. *Computational contact mechanics: geometry, detection and numerical techniques*. PhD thesis, École des Mines de Paris.

[169] G. Zavarise and P. Wriggers. Contact with friction between beams in 3-D space. *International Journal for Numerical Methods in Engineering*, 49(8):977–1006, 2000.

[170] D. Zhang, S. Ge, and Y. Qiang. Research on the fatigue and fracture behavior due to the fretting wear of steel wire in hoisting rope. *Wear*, 255(7-12):1233–1237, 2003.

[171] D. Zhang and M. Ostoja-Starzewski. Finite element solutions to the bending stiffness of a single-layered helically wound cable with internal friction. *Journal of Applied Mechanics*, 83(3):031003, 2016.

université PARIS-SACLAY
ÉCOLE DOCTORALE
Sciences mécaniques et énergétiques, matériaux et géosciences (SMEMAG)

Titre : Modélisation multi-échelle de la fatigue des lignes d'ancrage pour l'éolien offshore flottant

Mots clés : Eolien offshore, câble monotoron, éléments finis, fatigue, contact, frottement

Résumé : La fonction principale des systèmes d'ancrage des éoliennes offshore flottantes est de limiter les mouvements du support. Les lignes d'ancrage qui les composent sont typiquement constituées de chaînes, de câbles aciers, de câbles synthétiques ou d'une combinaison de ces composants. Dans cette thèse, on se concentre sur les câbles en acier qui permettent de réduire le poids et d'augmenter la résistance en tension par rapport aux chaînes. Leur dimensionnement dépend des chargements en tension et flexion, liés aux mouvements du flotteur sous l'action de la mer et du vent.

L'objectif de la thèse est le développement d'un nouveau modèle numérique pour prédire la durée de vie en fatigue des câbles d'ancrage d'une éolienne offshore flottante. Il doit notamment simuler les glissements relatifs entre les fils au cours d'une flexion du câble. Des résultats d'essais de tension-flexion de la littérature ont en effet montré que la première rupture est localisée près du plan neutre de flexion, où ces déplacements relatifs sont les plus grands. Cet effet majeur sur la durée de vie du câble n'est pas pris en compte par les lois de fatigue en tension-tension des normes de design offshore actuelles.

Il faut aussi remarquer que l'utilisation d'un modèle détaillé de câble dans une démarche de dimensionnement à la fatigue représente un vrai défi. Le nombre élevé d'interactions de contact à modéliser, de l'ordre de plusieurs milliers par mètre de câble, et le grand nombre de cas de chargement rendent ce type de calculs très coûteux.

Les chargements qui sont utilisés dans le modèle local de câble sont issus de calculs globaux réalisés à l'aide d'un logiciel multiphysique (Deeplines^{TM}). Ce logiciel permet de simuler les conditions environnementales (vent, houle, courant) appliquées sur l'ensemble de la structure offshore.

Nous montrons que le comportement non linéaire en flexion du câble, lié aux interactions de contact entre les fils, n'influence pas significativement les résultats du modèle global. Cette observation justifie une démarche de type descendante, les calculs globaux pouvant être réalisés en première étape.

Les évolutions temporelles des tensions et courbures globales sont appliquées uniformément sur le fil central du modèle local du câble. La continuité du câble est représentée par des conditions de périodicité reliant les sections de bord à des points internes du modèle situés sur la même position circonférentielle. Les fils sont modélisés par des éléments poutres. On obtient les contraintes généralisées sur les fils, les forces de contact et les glissements relatifs.

Des premières analyses ont montré que les déplacements relatifs entre les fils restent petits dans notre cadre d'application. Afin de réduire le coût calcul, nous avons développé un nouvel élément de contact entre poutres non parallèles, avec un appariement fixe de contact, dans l'hypothèse de petits glissements mais en grands déplacements et grandes rotations. Des tests numériques montrent l'amélioration obtenue, avec un résultat plus proche d'un modèle de référence qui considère un contact surfacique. De plus, le nouveau modèle réduit significativement le coût calcul et se montre plus robuste en convergence, ce qui s'avère crucial pour un calcul de fatigue.

Les sorties du modèle local sont ensuite utilisées pour prédire un état de contrainte 3D, en exploitant des solutions analytiques de contact entre corps cylindriques. Finalement, un critère de fatigue multiaxial de la littérature est appliqué pour évaluer le risque en dommage.

Title : Multi-scale modeling of the fatigue of mooring wire ropes for floating offshore wind turbines

Keywords : floating wind turbine, spiral strand, finite element, fatigue, contact, friction

Abstract : The main function of mooring systems of floating offshore wind turbines is to ensure station keeping. The mooring lines can be composed of chains, wire ropes, synthetic ropes, or even a combination of them. In this thesis we focus on wire ropes, whose advantage over chain is to sustain high tension at a lower weight. Their design must consider the successive tension and bending loading induced by the floater movement for various wind and waves conditions.

The thesis purpose is to develop a new numerical model, dedicated to the prediction of fatigue damage in mooring wire ropes of a floating wind turbine. In particular it has to simulate the relative movements between the wires when the rope is bent. Results from free-bending fatigue tests in the literature show the importance of these effects, since the first rupture is localized near the neutral plane, where fretting is more important. This phenomenon affecting the fatigue life is not considered by fatigue criteria of current offshore standards, which are related to tension-tension loading.

It is worth noting that the use of a detailed model of wire rope in a fatigue design procedure represents a real challenge. The high number of contact interactions to be modeled, which are several thousands per meter of rope, and the large amount of loading cases make this type of computations extremely time-consuming.

The loading used in the developed local model of wire rope is obtained from global computations performed with a dedicated multiphysics software (Deeplines^{TM}). This software allows to simulate the environmental conditions (wind, waves, current) applied on the whole structural system.

Some preliminary computations showed that the non-linear bending behavior of the wire rope, linked to the wire contact interactions, does not significantly affect the output of the global model. This observation justifies the use of a top-down scheme, with a prior computation of the global scale.

The global scale tension and curvature are then uniformly imposed on the central wire of the local model. The continuity of the rope is represented by periodic conditions which link the end sections to points within the model, at the same circumferential locations. The wires are modeled by beam elements. The outputs at the local scale are the stress resultants on the wires, and the contact forces and relative displacements at contact locations.

Small sliding between the wires has been observed from first numerical analysis, for a representative loading case. Therefore, in order to reduce the computational cost of the wire rope model, a new node-to-node contact element has been developed, dedicated to the modeling of contact between non-parallel beams with circular cross section. It assumes fixed contact pairing and finite rotations. Numerical benchmarks and experimental tests on wire ropes show the improvement with results closer to a reference surface-to-surface model, when compared to standard algorithm for the simulation of contact between beams. Moreover, the new model reduces significantly the CPU cost and is also more robust, which is crucial for fatigue life estimates.

The outputs of the local scale model are then used to obtain the complete 3D stress state by means of analytical solutions of contact between solids with cylindrical shape. Finally, a multiaxial fatigue criterion is applied in order to assess the safety of the system.

Université Paris-Saclay
Espace Technologique / Immeuble Discovery
Route de l'Orme aux Merisiers RD 128 / 91190 Saint-Aubin, France